Stress-induced Extracellular Vesicle and Cytoophidium Biology in Breast Cancer



Hakimi Kassim

Wolfson College

University of Oxford

A thesis submitted for a degree of

Doctor of Philosophy

Department of Physiology, Anatomy and Genetics

Hilary Term 2019

Declaration of authorship

I confirmed that the work presented in this thesis was performed in the Department of Physiology, Anatomy and Genetics, University of Oxford from October 2014 to August 2019. I performed all the work within this thesis, unless otherwise stated and has not been previously submitted to this University or any other for the award of a degree.

Hakimi Kassim

(Hilary Term 2019)

Abstract

Cells respond to metabolic stresses by reprogramming gene expression, degrading unneeded proteins and altering post-translational modifications of other proteins. Herein, I reported that breast cancer (BC) cells can adapt to cellular stress by modulating the protein composition and function of extracellular vesicles (EVs) and reorganizing metabolic enzymes into filamentous structures, termed cytoophidia. Glutamine is a non-essential amino acid that activates the mechanistic target of rapamycin complex 1 (mTORC1) pathway. I confirmed that luminal and basal lineages of BC cells differ in their glutamine dependencies, and that EVs may mediate intercellular glutamine symbiosis between the two cell lineages (Chapter 3). Despite the difference in sensitivity towards INK128 (an mTOR kinase inhibitor) between lung and brain metastatic clones of basal BC cells, I demonstrated that, blocking mTOR led to secretion of EVs containing proteins associated with cell migration and activation of epithelial-mesenchymal transition (EMT) (Chapter 4). I further demonstrated that the glutamine dependency was not only variable across BC subtypes but also between lung and brain metastatic clones of basal BC cells. Furthermore, my data shows that inhibition of glutamine consumption by 6-Diazo-5-oxo-L-norleucine (DON) significantly promoted higher abundance and length of glutamine-dependent cytidine triphosphate synthase 1 (CTPS1) and inosine-5'-monophosphate dehydrogenase 1 (IMPDH1) cytoophidia in brain metastatic than lung metastatic clone of basal BC cells, highlighting the variation in glutamine dependency across different metastatic clones of basal BC (Chapter 5). The assemblies of cytoophidia of CTPS and many other metabolic enzymes is a stress adaptation strategy to maintain metabolic homeostasis during nutrient starvation, as I demonstrated by conducting a genetic screen in budding yeast (Chapter 5). In summary, my work suggests that stress-induced alteration of protein composition and function of EVs and reorganization of metabolic enzymes into cytoophidia are strategies for BC cell survival in hostile microenvironment. (294 words)

Acknowledgement

I would like to express my heartfelt gratitude to my supervisors Prof. Ji-Long Liu, Prof. Deborah Goberdhan and Dr. Imre Mäger for their continuous guidance, supports and encouragements during the course of my DPhil study. I would like to thank Prof. Clive Wilson for his ideas in firming up my experimental plans.

Special thanks to the postdoctoral scientists including Dr. Sanjay Ghosh, Dr. Shih-Jung Fan, Dr. Cleidson Alves, Dr. Anja Krueger, Dr. Ghulam Dar, Dr. Mariana Conceicao and Dr. Inna Uliyakina for sharing their ideas on my DPhil projects and also providing technical supports especially related to using a wide range of equipment including nanoparticle tracking analysis (NTA), laser-scanning confocal microscope, size-exclusion liquid chromatography machine. I would also like to thank Dr. Ashling Holland for her helps and advice on the extracellular vesicle sample preparation for label-free mass spectrometry analysis. I would also like to thank Dr. Firdaus Abdul Wahab for his inputs on my experimental plans. To the other laboratory members, thank you for your endless assistance throughout my research.

I am enormously grateful to my beloved parents, family members and wife for their understanding and unwavering supports. Not to forget the Malaysian community members in Oxford for being supportive to me and my family during my hard times. Lastly, thank you to Majlis Amanah Rakyat and Yayasan Khazanah-Oxford Centre for Islamic Studies for generously sponsoring my DPhil study.

List of abbreviation

Abbreviation	Description
4E-BP1	Eukaryotic translation initiation factor 4E-binding protein 1
a-SMA	Alpha smooth muscle actin
AAR	Amino acid response
ABCG2	ATP-binding cassette subfamily G member 2
ACGH	Array comparative genomic hybridization
ACK1	Activated CDC42 kinase 1
ACN	Acetonitrile
ADSC	Adipose tissue-derived mesenchymal stem cell
AKT	Protein kinase B
ALIX	ALG-2-interacting protein X
ARF6	ADP ribosylation factor 6
ASN	Asparagine synthetase
BBB	Blood brain barrier
BC	Breast cancer
BRCA	Breast cancer type 1 susceptibility protein
BRCT	BRCA1 C terminal
BSA	Bovine serum albumin
CARE	C/EBP-ATF response element
CD	Cluster of differentiation
CDC	Cell division control protein
CHMP4C	Charged multivesicular body protein 4C
COX2	Cyclooxygenase 2
CTP	Cytidine triphosphate
CTPS1	Cytidine triphosphate synthase 1
CXCR4	C-X-C chemokine receptor 4
DAU	Deazauridine

DEPTOR	DEP-domain containing mTOR-interacting protein
DGK	Diacylglycerol kinase
DMEM	Dulbecco’s Modified Eagle’s Medium
DMSO	Dimethyl sulfoxide
DON	6-Diazo-5-oxo-L norleucine
E2F	E2 factor
ECM	Extracellular matrix
eIF2/2B	Eukaryotic initiation factor 2/2B
EMT	Epithelial-to-mesenchymal transition
ESCRT	Endosomal sorting complexes required for transport
EV	Extracellular vesicle
FC	Fold change
FDR	False discovery rate
FE	Fold enrichment
FRAP	Fluorescence recovery after photobleaching
GAB1	GRB2-associated binder 1
GAC	Glutaminase C
GAT	Glutamine amidotransferase
GDH1	Glutamate dehydrogenase 1
GFP	Green fluorescence protein
GLS	Glutaminase
GLT1	Glutamate synthase 1
GRB2	Growth factor receptor-binding protein 2
GS	Glutamine synthetase
HBEGF	Heparin-binding EGF-like growth factor
HER2	Human epidermal growth factor receptor 2
HIF1a	Hypoxia inducing factor 1 a
HSPB8	Heat shock beta 8

HUVEC	Human umbilical vein endothelial cell
IBA1	ionized calcium binding adaptor molecule 1
ILV	Intraluminal vesicle
IMP	Inosine monophosphate
IMPDH1	Inosine-5’-monophosphate dehydrogenase 1
ITGa6b4	Integrin alpha 6 beta 4
ITS	Insulin-transferrin-selenium
KGA	Kidney-type glutaminase
LCMS	liquid chromatography mass spectrometry
LGA	Liver-type glutaminase
MCSP	Melanoma-associated chondroitin sulphate proteoglycan
miR	microRNA
MLC	Myosin light chain
MLCK	Myosin light-chain kinase
mLST8	Mammalian lethal with SEC13 protein 8
MPA	Mycophenolic acid
mSIN1	Mammalian stress-activated protein kinase interacting protein
mTORC1	Mechanistic target of rapamycin complex 1
mTORC2	Mechanistic target of rapamycin complex 2
MVB	Multivesicular body
NF-kB	Nuclear factor kappa light-chain-enhancer of activated B cell
NKG2D	Natural killer group 2 member D
NMIIA	ono-muscle myosin IIA
NTA	Nanoparticle tracking analysis
PAT4	Proton-assisted amino acid transporter 4
PBS	Phosphate buffer saline
PCA	Principal component analysis
PCD6IP	Programmed cell death 6 interacting protein

PDGF	Platlet-derived growth factor
PDGFR	PDGF receptor
PDK1	3-phosphoinositide-dependent kinase 1
PFK	Phosphofructokinase
PI3K	Phosphatidylinositol-3 kinase
PIP3	Phosphatidylinositol-3,4,5-triphosphate
PLD2	Protein phospholipase D2
PRAS40	Proline-rich AKT substrate 40 kDa
PREX	PIP3-dependent RAC exchanger 1
PROTOR1	Protein observed with RICTOR1
PRX	Peroxiredoxin
PSA1	Guanosine diphosphate-mannose pyrophosphorylase 1
PSA1	Guanosine-5'-diphospho-mannose pyrophosphorylase
PTEN	Phosphatase and tensin homolog
PYK1	Pyruvate kinase 1
RAPTOR	Regulatory-associated protein of mTOR
RHEB	Ras-homologue enriched in brain
RICTOR	Rapamycin-insensitive companion of mTOR
RIPA	Radioimmunoprecipitation assay
ROCK	Rho-associated protein kinase
ROR1	Receptor tyrosine kinase like orphan receptor 1
RTK	Receptor tyrosine kinase
S6K	S6 kinase
SEC	Size exclusion liquid chromatography
SEM	Standard error mean
SKD1	Suppressor of K+ transport growth defect 1
SNAP23	Synaptosomal-associated protein 23
SNARE	N-ethylmaleimide-sensitive factor activating protein receptor

SOS	Son of sevenless
SREBP	Sterol regulatory element binding protein
ST6GALNAC5ST6	N-acetylgalatosaminide alpha-2,6-sialyltransferase 5
STED	Stimulation emission depletion microscopy
TAM	Tumor-associated macrophages
TFA	Trifluoroacetic acid
TFF	Tangential flow filtration
TGF-b	Transforming growth factor beta
TLR2	Toll-like receptor 2
TME	Tumor microenvironment
TNBC	Triple negative breast cancer
Treg	Regulatory T-cell
TSC	Tuberous sclerosis complex
TSG101	Tumor susceptibility gene 101
ULK1	Unc51-like kinase 1
UPR	Unfolded protein response
UTP	Uridine triphosphate
VAMP7	Vesicle-associated membrane protein 7
VEGF	Vascular endothelial growth factor
VPS4B	Vacuolar protein sorting-associated protein 4 B
VTA1	Vesicle trafficking 1
WNT	Wingless/integrated
XMP	Xanthosine monophosphate
YPD	Yeast peptone dextrose

Table of content **Page**

Chapter 1.0 Introduction……1

1.1 Extracellular vesicle biogenesis and release……2

1.1.1 Implication of extracellular vesicle in breast cancer……7

1.2 Glutamine metabolism in breast cancer……9

1.3 Lung and brain metastases of breast cancer……11

1.4 mTOR pathway: activation and function……13

1.4.1 Targeting mTOR pathway in breast cancer……17

1.5 Metabolic regulation of cytoophidium……19

1.5.1 Formation of cytoophidium……22

1.5.2 Proposed functions of cytoophidium……24

1.5.3 Relevance of cytoophidia in cancer……25

1.6 Primary research objectives……28

Chapter 2.0 Material and method……29

2.1 Reagents and suppliers……29

2.2 Cell culture method……29

2.2.1 Cell lines……29

2.2.2 Cell culture condition and maintenance……29

2.2.3 Cryopreservation and retrieval of cells……30

2.3 Co-culture transwell and cell growth assays……31

2.4 Dose-dependent inhibition of mTORC1 in breast cancer cell lines……32

2.5 Protein extraction……32

2.6 BCA assay……32

2.7 Western blot……33

2.8 Immunofluorescence staining……34

2.9 Antibodies……35

2.10 Isolation of extracellular vesicle by SEC……38

2.11 Nanoparticle tracking analysis……39

2.12 MACSPlex analysis of extracellular vesicle……39

2.13 Label-free mass spectrometry……..41

2.13.1 In-solution digestion of protein……..41

2.13.2 Chloroform-methanol protein extraction……..41

2.13.3 Peptide purification……..42

2.14 Proteomic data analysis……..43

2.15 Modulation of cell growth by extracellular vesicle……43

2.16 In vivo extracellular vesicle biodistribution assay……44

2.17 Yeast strain and media……45

2.18 Screening of cytoophidium-forming proteins in *S. cerevisiae*……46

2.19 Quantification of cytoophidium-forming proteins in breast cancer and *S.cerevisiae*……..……46

2.20 Statistical analysis……..48

Chapter 3.0. Modulation of EV function and content by glutamine……49

3.1 Introduction……..49

3.2 Result……51

3.2.1 Expression of GS and GLS1 in luminal and basal BC cell lines……51

3.2.2 Glutamine deprivation differentially altered mTORC1 and ERK activities in BC cell lines……53

3.2.3 Potential glutamine symbiosis between luminal and basal cells……...55

3.2.4 Modulation of EV protein composition by glutamine……..57

3.2.5 Modulation of EV function by glutamine……62

3.2.6 MACSPlex analysis of EV protein composition……...64

3.3 Discussion……67

3.3.1 Cell lineage-specific dependency on extracellular glutamine……67

3.3.2 Intercellular glutamine symbiosis……..70

3.3.3 Extracellular vesicle-mediated intercellular glutamine symbiosis……71

3.3.4 Cell-lineage profile of EV surface markers……..75

3.4 Conclusion……78

Chapter 4.0. Modulation of EV protein composition and function by INK128……79

4.1 Introduction……..79

4.2 Result……81

4.2.1 Dose-dependent inhibition of mTORC1 by INK128……81

4.2.2 NTA analysis and EV quantification……..83

4.2.3 Data normalization and principal component analysis……...86

4.2.4 Comparative quantitation of proteins in EVs……89

4.2.5 Annotation enrichment analysis of EV proteins……...94

4.2.6 Alteration of MDA231-LG EV proteome by mTOR kinase inhibitor INK128…103

4.2.7 Alteration of MDA231-BR EV proteome by mTOR kinase inhibitor INK128…..112

4.2.8 EV-mediated modulation of human brain endothelial cell growth……...120

4.2.8.1 Basal expression of PTEN and phosphorylation level of S6 and ERK……..120

4.2.8.2 Modulation of HBEC-5i cell proliferation by EVs……..122

4.2.9 In vivo biodistribution of EVs……127

4.3 Discussion……..129

4.3.1 INK128 partially inhibited mTORC1 in MDA231-BR cells……129

4.3.2 Alteration of EV secretion by INK128……131

4.3.3 Protein composition of MDA231-LG and MDA231-BR EVs……131

4.3.4 Potential EMT-promoting function of EVs in response to INK128……..141

4.3.5 Growth-promoting function of EV on brain microvascular endothelial cell growth……...…...143

4.3.6 INK128 minimally altered EV biodistribution patterns……145

4.4 Conclusion……147

Chapter 5.0. Stress-induced assemblies of cytoophidia in breast cancer and *Saccharomyces cerevisiae*……..148

5.1 Introduction……148

5.2 Declaration of authorship……149

5.3 Result……..150

5.3.1 DON markedly suppressed mTORC1 pathway in MDA231-BR cells……150

5.3.2 DON markedly induced CTPS1 and IMPDH1 cytoophidia in MDA231-BR cells……..152

5.3.3 A widespread assembly of proteins into cytoophidia in *S. cerevisiae*…….156

5.3.4 Bioinformatics analysis of 23 cytoophidia-forming proteins…….160

5.3.5 Cytoophidia assemblies reflected nutrient status in *Saccharomyces cerevisiae*……164

5.4 Discussion……..166

5.4.1 Stress-induced CTPS1 and IMPDH1 cytoophidia assemblies in breast cancer cells……..166

5.4.2 The assembly of cytoophidium is a nutrient stress adaption strategy in budding yeast…….167

5.4.3 The abundance and length of cytoophidia reflected metabolic status of *Saccharomyces cerevisiae*……...174

5.5 Conclusion…….176

Chapter 6.0. Summary and future work……...177

6.1 EV-mediated glutamine symbiosis between luminal and basal breast cells….177

6.2 mTORC1 inhibition minimally altered EV protein composition, function and biodistribution……..180

6.3 Cytoophidium assembly reflects tumor heterogeneity in glutamine dependency ……..182

6.4 Widespread assemblies of cytoophidia in *S. cerevisiae*……..184

6.5 Conclusion…….185

Appendix A. The upregulated proteins in EVs secreted by MDA231-LG and MDA231-BR cells……..…..…186

Appendix B. Filamentation of metabolic enzymes in *Saccharomyces cerevisiae*……198

References……..210

List of figures **Page**

Figure 1.1. Exosomes and microvesicles are two well-characterized types of extracellular vesicles (EVs) that differ in the subcellular origins, mechanism of release and vesicle size……...2

Figure 1.2. The glutamine-dependent extracellular vesicle switching is regulated by reduced glutamine-mTORC1……6

Figure 1.3. mTORC1 is activated by PI3K……16

Figure 1.4. The assemblies of CTPS1 and IMPDH1 cytoophidia in human cells…….20

Figure 1.5. The assemblies of cytoophidium-forming proteins (green) in *S. cerevisiae*..22

Figure 1.6. The multiple steps of cytoophidia assembly……..23

Figure 2.1. The experimental setting for intercellular glutamine symbiosis study……31

Figure 2.2. The summary of EV isolation by SEC……39

Figure 2.3. The protocol of analyzing the expressions of EV surface markers using MACSPlex system……40

Figure 2.4. The strategy for constructing of yeast GFP strain collection……45

Figure 3.1. Comparative immunoblotting analysis of GLS1 (KGA and GAC isoforms) and GS between luminal MCF-7 and basal MDA231-LG and MDA231-BR cells……..52

Figure 3.2. Alteration of mTORC1 and ERK activities in luminal and basal BC cell lines in response to 24 hours of glutamine deprivation……54

Figure 3.3. Secretome of MCF-7 cells enhanced the growth of MDA231-LG and MDA231-BR cells in glutamine-deprived media……..56

Figure 3.4. Chromatogram profile, size distribution, secretion and protein composition of EVs in response to glutamine deprivation……61

Figure 3.5. The growth-promoting function of glutamine-derived MCF-7 EVs……63

Figure 3.6. The changes of the levels of EV surface markers in response to glutamine deprivation……66

Figure 4.1. Dose-dependent inhibition of mTORC1 by INK128 in MDA231-LG and MDA231-BR cells……82

Figure 4.2. Chromatogram profile, size distribution and secretion of EVs in response to INK128……...85

Figure 4.3. Box plots show the expression of proteins in each group is normalized to the median value and log-transformed for all four biological repeats……...87

Figure 4.4. Principal component analysis of protein level in EVs secreted by INK128-treated MDA231-LG and MDA231-BR cells……88

Figure 4.5. The upregulated proteins in EVs secreted by MDA231-LG and MDA231-BR cells……90

Figure 4.6. A heatmap showing hierarchical clustering of statistically significant upregulated proteins in EVs secreted by MDA231-LG and MDA231-BR cells……91

Figure 4.7. Annotation analysis of proteins in EVs secreted by MDA231-LG and MDA231-BR cells associated to (A) cellular component, (B) molecular function and (C) biological process using FunRich software……...100

Figure 4.8. The ontologies of interest for (A) cellular component and (B) biological process with the details of proteins in EVs secreted by MDA231-LG and MDA231-BR cells are presented……102

Figure 4.9. The upregulated and downregulated proteins in EVs secreted by INK128-treated MDA231-LG cells……..104

Figure 4.10. A hierarchical clustering of significantly upregulated and downregulated proteins in EVs secreted by MDA231-LG cells in response to INK128……...105

Figure 4.11. The upregulated and downregulated proteins in EVs secreted by INK128-treated MDA231-BR cells……113

Figure 4.12. A hierarchical clustering of significantly upregulated and downregulated proteins in EVs secreted by MDA231-BR cells in response to INK128……114

Figure 4.13. Analysis of basal PTEN expression and phosphorylation status of ERK and S6……121

Figure 4.14. Modulation of HBEC-5i cell growth by EVs……126

Figure 4.15. The systemic distribution of EVs……128

Figure 5.1. Dose-dependent inhibition of mTORC1 by DON in MDA231-LG and MDA231-BR cells……...151

Figure 5.2. Induction of CTPS1 and IMPDH1 cytoophidia by DON……153

Figure 5.3. Comparative analysis of abundance and length of CTPS1 and IMPDH1 cytoophidia in MDA231-LG and MDA231-BR cells in response to DON treatment….154

Figure 5.4. Induction of CTPS1 cytoophidia assemblies by DON retained CTPS1 protein level……..155

Figure 5.5. Novel cytoophidium-forming proteins in *S. cerevisiae*……..157

Figure 5.6. Validation of previously discovered cytoophidia in *S. cerevisiae*……158

Figure 5.7. The spatial distribution of CTPS and ASNS cytoophidia in *S. cerevisiae*……159

Figure 5.8. A map of potential protein interaction of 23 cytoophidia in *S. cerevisiae* produced by STRING database……..161

Figure 5.9. The assemblies of glutamine-dependent metabolic enzymes into cytoophidia at different growth phases……165

Figure 6.1. Modulation of intercellular glutamine symbiosis by EVs……178

Figure 6.2. Modulation of cytoophidium assembly by EVs……183

List of tables **Page**

Table 2.1. List of primary and secondary antibodies……37

Table 4.1. The summary of FC and P-value of the top 10 proteins differentially upregulated in (A) MDA231-LG EVs and (B) MDA231-BR EVs……...93

Table 4.2. The overrepresentation enrichment analysis of proteins significantly upregulated in EVs secreted by MDA231-LG and MDA231-BR cells associated with cellular component, molecular function and biological process……98

Table 4.3. The summary of log 10 FC difference and P-value of significantly upregulated and downregulated proteins in MDA231-LG EVs in response to INK128 treatment……107

Table 4.4. The summary of the involvement of significantly upregulated and downregulated proteins in MDA231-LG EVs in response to INK128 treatment in tumor development and growth……..111

Table 4.5. The summary of log 10 FC difference, P-value of significantly upregulated and downregulated proteins in MDA231-BR EVs in response to INK128 treatment.116

Table 4.6. The summary of the involvement of significantly upregulated and downregulated proteins in MDA231-BR EVs in response to INK128 treatment in tumor development and growth……...119

Table 5.1. A total of 23 cytoophidium-forming proteins identified in *S. cerevisiae*……163

Chapter 1.0. Introduction

This thesis is composed of four connected research strands which investigate stress-induced extracellular vesicle (EV) and cytoophidium biology in breast cancer (BC). The *first* in Chapter 3, focuses on the modulation of EV content and function by glutamine deprivation which highlights EV-mediated intercellular glutamine symbiosis between luminal and basal BC cells. The *second* in Chapter 4, characterizes the sensitivity of a lung and a brain metastatic triple negative breast cancer (TNBC) MDA231 cell line to a clinically tested ATP-competitive mTOR kinase inhibitor, INK128 and changes in EV protein composition and function secreted by INK128-treated cells. The *third* in Chapter 5, investigates the difference in glutamine dependency between the lung and brain metastatic MDA231 cell line, reflected by mTORC1 activity and cytidine triphosphate synthase 1 (CTPS1) and inosine-5'-monophosphate dehydrogenase 1 (IMPDH1) cytoophidia assemblies induced by glutamine analog, 6-Diaxo-5-oxo-L-norleucine (DON) which blocks the glutamine consumption. This final research strand contains extended preliminary works focussing on the large-scale screening of cytoophidium-forming proteins in the budding yeast cells, *Saccharomyces cerevisiae* and the characterization of glutamine-dependent cytoophidium-forming proteins in yeast cells grown at different growth phases. Collectively, glutamine deprivation, INK128 and DON treatments are distinct types of cellular stresses, introduced in each of my research strands which result in the suppression of the mechanistic target of rapamycin complex 1 (mTORC1) pathway, the main nutrient-sensing pathway that I studied. The findings presented in this thesis imply that distinct cellular stresses dictate EV content and function and also induce the assemblies of metabolic enzymes into cytoophidia.

1.1 Extracellular vesicle biogenesis and release

Extracellular vesicle is a generic term for a heterogeneous group of membrane-bound vesicles that mediate intercellular communication by delivering bioactive cargoes, for example, proteins, lipids and genetic materials to the cells at neighbouring and distal sites[1]. The content and function of secreted EVs are dependent on the molecular signals that modulate the phenotypes and genotypes of the EV-secreting cells[2]. Exosomes and microvesicle (MVs) are the most broadly studied subtypes of EVs which differ in subcellular origins, mechanism of release and vesicle size[3–5] (Figure 1.1).

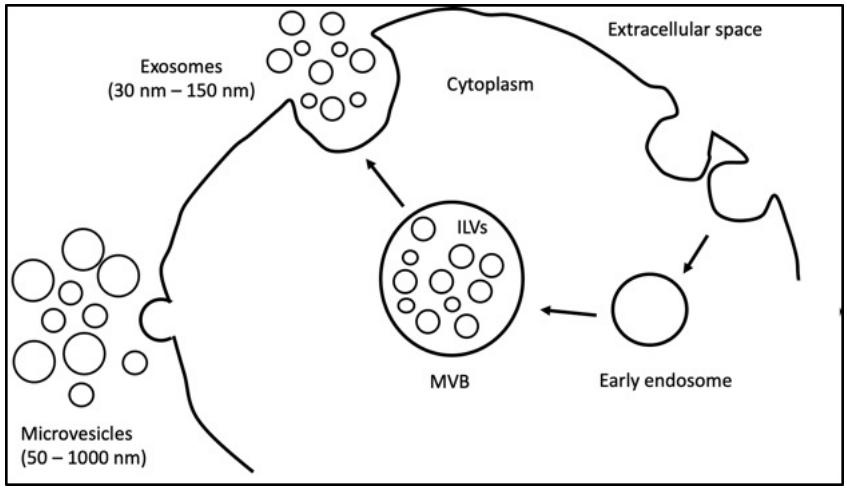


Figure 1.1. Exosomes and microvesicles are two well-characterized types of extracellular vesicles (EVs) that differ in the subcellular origins, mechanism of release and vesicle size. Exosomes (30-150 nm) are initially generated as intraluminal vesicles (ILVs) in endosomal compartment during the maturation of early endosome into late endosome known as multivesicular body (MVB). The fusion of MVB to plasma membrane releases ILVs into the extracellular space as exosomes. In contrast, microvesicles (50-1000 nm) are generated by the outward budding and fission of plasma membrane.

Exosomes (30-150 nm) are the intraluminal vesicles (ILVs) generated in the multivesicular bodies (MVBs) released into the extracellular space upon fusion of MVBs to plasma membrane. The process of ILV biogenesis requires a protein complex known as the endosomal sorting complexes required for transport (ESCRT)[6,7]. There are four components of ESCRT complex (ESCRT-0, -I, -II, -III) involved in sequestration of MVB proteins into ILVs[7,8]. The ubiquitinated proteins are recognized by ESCRT-0 on the endosomal membranes and bound by ESCRT-I, leading to the activation of ESCRT-II. Programmed cell death 6 interacting protein (PCD6IP) which is also known as ALG-2-interacting protein X (ALIX), functions in recruiting ESCRT-III and linking it to ESCRT-I complex through its interaction with ESCRT-I component, the tumor susceptibility gene 101 (TSG101). The next sequential event in ILV biogenesis is the removal of ubiquitin tag from proteins by deubiquitinating enzymes. This is followed by the dissociation of ESCRT-III mediated by AAA-ATPase suppressor of K^+ transport growth defect 1 (SKD1) and recycled for recruitment of next cargo loading. Apart from the ESCRT complex, detergent-resistant domain of tetraspanins are also involved in sorting cargoes in to ILV and this can be exemplified by incorporation of MHC class II into CD9-containing lipid microdomain[9].

In general, the RAB family of GTPases controls membrane fusions during intracellular trafficking[10]. A subset of the RAB family of small GTPases such as RAB27A, RAB27B, RAB11, RAB7 and RAB35 have been shown to facilitate the release of ILVs by fusion of limiting membrane of MVBs with the plasma membrane. Since different RAB proteins are involved in this event, it is possible that different subpopulations of exosomes could be generated by different endosomal compartments. Several studies have reported that the exosomes released through a RAB27-dependent mechanism are abundant in late endosomal proteins including MHC class II, TSG101, ALIX and CD63[8,11]. Furthermore, the secretion of flotillin-enriched exosomes containing transferrin receptor, WNT and PLP was assisted by different RABs including RAB27, RAB11 and RAB35[12,13].

The secretion of exosomes is also regulated by membrane lipids. Several studies have demonstrated that phosphatidic acid generated by diacylglycerol kinase (DGK) or phospholipase D modulated the secretion of exosomes[14,15]. The secretion of LAMP1/CD63-positive exosomes is inhibited by the activity of DGKα as it functions as a negative regulator of the formation of MVBs[16]. The release of exosomes can also be mediated through the interaction of vesicle-associated membrane protein 7 (VAMP7), a member of vesicular soluble N-ethylmaleimide-sensitive factor activating protein receptors (V-SNAREs) on MVBs with target SNAREs (T-SNAREs) such as synaptosomal-associated protein 23 (SNAP23) on the plasma membrane[17,18].

The ESCRT-independent biogenesis of exosomes has previously been defined as the inhibition of the ESCRT complex not compromising the formation of MVBs, leading to an assumption that the regulation of exosome biogenesis could involve a machinery independent of ESCRT pathway[19]. A previous study has demonstrated that neutral spingiomyelinase enzymatic product, ceramide, is required for inwards budding of the MVB limiting membrane to form ILVs due to its cone structure and ability in inducing membrane curvature[20]. Inhibition of neutral spingiomyelinase perturbs the release of exosomes in to the extracellular space.

In contrast to exosome biogenesis, MVs (50-1000 nm) are generated through the outward budding and fission of the plasma membrane into the extracellular space[1]. Apart from its involvement in endosome recycling, remodelling of actin at the cell periphery and exosome biogenesis, ARF6 has been reported to regulate MV cargo sorting by selectively loading proteins such as β1-integrin, MHC-1 and VAMP3 into MVs shed by tumor cells[21]. In BC cells, RAB22A mediates MV formation and its overexpression enhanced MV shedding[22]. This study also reported that RAB22A-dependent MV formation and selective cargo sorting is driven by hypoxia as in RAB22A-

deficient cells, MV formation is mildly affected in non-hypoxic condition. Furthermore, ceramide which involves in ESCRT-independent ILV formation also modulates MV formation[23]. Formation of MVs can also be induced by cholesterol and depletion of cholesterol abrogates the formation of this type of EV[24].

The fission and release of MVs requires ATP-dependent contraction that involve actin-myosin interaction[25,26]. ADP ribosylation factor 6 (ARF6) controls shedding machinery of MVs by activating phospholipase D which in turn leads to localization of ERK to the plasma membrane[21]. ERK-dependent phosphorylation and activation of Ca^{2+}/calmodulin-dependent kinase, myosin light-chain kinase (MLCK) induces actin-based cytoskeleton contraction by phosphorylating myosin light chain (MLC). MV shedding is also dependent on a Rho-associated protein kinase (ROCK) signaling pathway through phosphorylation of MLC by Rho GTPases particularly RhoA which occurs downstream of ARF1[27,28].

Apart from ESCRT-dependent and -independent mechanisms of exosome biogenesis, the Goberdhan Lab has recently discovered that 'exosome switching' is regulated by reduced glutamine-mTORC1 signalling in HCT116 colorectal cancer cells and other cancer cell lines. This involves a diversion of the endocytic pathway that generates exosomes, a subtype of EVs, from the classical exosome biogenesis route to the alternative recycling endosome route marked by RAB11a (Fan et al., *under revision*; Figure 1.2). This exosome switch results in the secretion of RAB11-positive exosomes which enhance the growth of recipient tumour and endothelial cells.

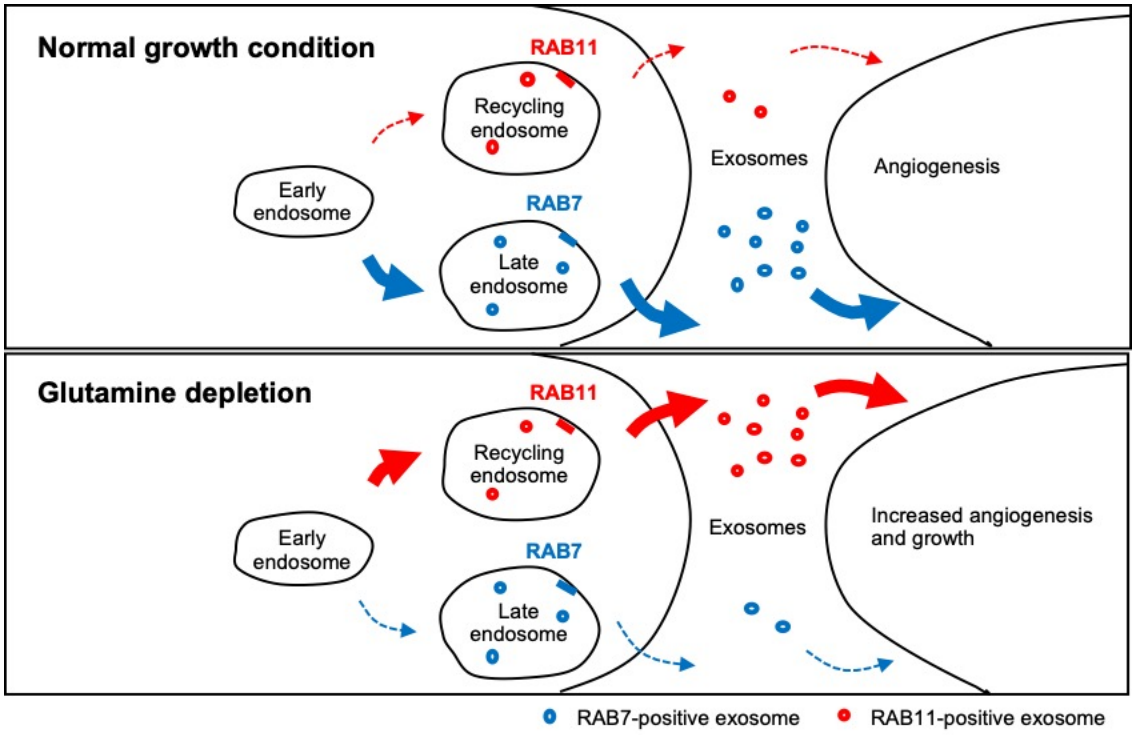


Figure 1.2. The glutamine-dependent extracellular vesicle switching is regulated by reduced glutamine-mTORC1. Under normal growth condition, exosomes are generated through the late endosome compartment, while in response to glutamine depletion, RAB11a-positive exosomes are loaded with molecular cargoes that enhance angiogenesis and growth of the recipient cells. Adapted from Fan et al., *under revision*.

Taken together, this suggests that cancer cells can adapt to microenvironmental stress by altering the exosome biogenesis site from the classical late endosomal compartment to the recycling endosome, leading to the generation of a different exosome subtypes loaded with molecular cargoes that could alter the phenotypic traits of the recipient cells in the tumor microenvironment. The involvements of EVs in tumor progression and adaptation to microenvironmental stress in the context of BC biology are further discussed in the Section 1.1.1.

1.1.1 Extracellular vesicles in breast cancer

In BC, EVs have been implicated in multiple aspects of tumor development including tumor cell extravasation, invasion, angiogenesis and evasion of immune surveillance. Tumor invasion can be modulated by EVs through degradation of extracellular matrix (ECM) and enhancing motility of tumor cells. Luga et al., 2012 demonstrated that invasiveness of BC cells can be stimulated by EVs secreted by tumor-associated fibroblast cells that activates WNT-planar cell polarity-dependent signaling process[29]. Hypoxia stimulated RAB22A-dependent secretion of EVs from BC cells that modulated several pro-survival processes including proliferation, focal adhesion, invasion and metastasis in naïve BC cells[22]. EVs derived from C-X-C chemokine receptor 4 (CXCR4)-overexpressed BC cells were enriched in mRNAs related to stemness/metastatic capacity and promoted increase in proliferation, migration and invasion of naïve recipient cells[30].

Extravasation of cancer cells mimic the physiologic process of leukocyte recruitment during the inflammation process. It is now accepted that in order for the cancer cells to cross endothelial barrier, interendothelial junctions need to be weakened by metastatic cancer cells. Integrin alpha 6 beta 4 (ITG$\alpha_6\beta_4$)-containing EVs secreted from lung-tropic BC cells activated of SRC kinase signaling and upregulated S100 proteins in lungs fibroblasts leading to vascular leakiness in lungs during pre-metastatic niche formation[31]. Moreover, Zhou et al., 2014 demonstrated that microRNA (miR) 155 secreted in BC EVs enhanced vascular permeability of endothelial cells by destructing the tight junction protein ZO1 to promote metastasis[32].

Angiogenesis is defined as the formation of new blood vessel from the pre-existing vasculature and it is one of the hallmarks of cancer. An independent study by Feng et al., 2017 demonstrated that EVs secreted from BC cells sustained the activation of

vascular endothelial growth factor (VEGF) receptor on endothelial cells through transferring of oligomeric variant of VEGF called $VEGF_{90k}$ leading to angiogenesis and ineffectiveness of VEGF antibody, Bevacizumab[33].

Evasion of immune surveillance by tumor cells is achieved by downregulating the expression of antigen-presenting proteins on the cell surface. This mechanism shields the tumor cells from being targeted for destruction by cytotoxic T-cells. EVs secreted from BC cells have been shown to inactivate the immune response by suppressing the expression of a lymphocytic homodimeric C-type lectin receptor, natural killer group 2 member D (NKG2D) leading to reduction in the cytotoxicity capacity of $CD8^+$ T-cells[34].

Cancer cells can adapt to microenvironmental stresses such as hypoxia and chemotherapeutic agent by modulating EV content and function. Tumor hypoxia is defined as an event of oxygen deprivation due to the dysregulated metabolisms and angiogenesis, resulting in inefficient oxygen and nutrient transport in tumor microenvironment[35]. King et al., 2012 has reported that hypoxic BC cells secreted exosomes enriched with miR-210[36], a molecule that promotes the evasion of apoptosis by downregulating apoptosis inducing factor mitochondrion associated 3 (AIFM3), leading to inhibition of caspase-dependent apoptosis[37].

Apart from the adaptation to hypoxia through the secretion of EVs enriched with miR-210, BC cells develop resistance to a chemotherapeutic agent by concentrating it in the EVs and that subsequent secretion leads to the reduction of drug concentration in the cytoplasm[38]. Accumulation of anti-tumor drugs in the cytoplasm can be reduced by the activity of P-glycoprotein (P-GP) transporter that mediates drug efflux[39,40]. A previous independent study has reported that dose-dependent induction of P-GP expression was induced by EVs secreted by docetaxel-resistant MCF-7 cells[41].

Nutrient deprivation is one of the phenotypic characteristics of hostile tumor microenvironment. The adaptation to depletion of specific nutrients such as glutamine by modulating EV content and function from BC cells is still unknown. The dysregulation of glutamine metabolism in different types of BC and the possible intercellular glutamine symbiosis mediated by EVs between luminal and basal breast cell are discussed in Section 1.2.

1.2 Glutamine metabolism in breast cancer

Glutamine is a non-essential amino acid endogenously generated by mammalian cells through the action of glutamine synthetase (GS) by condensing intracellular glutamate with ammonia and this reaction is reversed by glutaminase (GLS), a reaction called as glutaminolysis. In human, GLS is encoded by two different genes, GLS1 and GLS2[42]**.** GLS1 generates kidney-type glutaminase (KGA) while GLS2 generates liver-type glutaminase (LGA). Due to alternative splicing, GLS1 generates two splice variants that differs in their C-terminal regions which are KGA and its shorter variant, GAC, known as glutaminase C[43].

Glutamine metabolism is involved in the synthesis of nucleotide, lipids and tricarboxylic acid TCA cycle substrate[44]. It also regulates ATP production, redox balance and acts as an activator for mTORC1 pathway[44]. In the rapidly proliferating cancer cells, glutamine is considered as an essential metabolite required to sustain tumor growth[45]. Intracellular glutamine transport is mediated by at least 14 known amino acid transporters[46]. Nevertheless, there is no amino acid transporter selectively transport glutamine.

Upregulation of amino acid transporters have been linked to the progression of BC. Metabolic reprogramming of glutamine metabolism in BC is driven by c-MYC oncogene amplification, which is detected in approximately 15% of all breast cancer cases, in

particular in basal-like type of BC[47]. Glutamine metabolism is reprogrammed by c-MYC through its binding to the promoter of a well-characterized glutamine transporter solute carrier family 1 member 5 (SLC1A5) leading to enhanced expression of SLC1A5 that eventually causes the increase in glutamine intake[48,49]. Immunohistochemistry staining of SLC1A5, a glutamine transporter has revealed that it is highly expressed in HER2-positive BC and its expression is also markedly higher in basal-like TNBC than luminal BC cells[50]. Upregulation of SLC1A5 is also correlated to therapeutic resistant of paclitaxel[51]. Furthermore, the tumor suppressor gene known as retinoblastoma RB, modulates glutamine uptake by inhibiting SLC1A5 expression through E3F-3-dependent regulation of SLC1A5 promoter[52].

Cell-type specific metabolic profile is associated with distinct ability of different type of cells in consuming nutrients to generate energy. A previous study has demonstrated that glutamine dependency varies among BC subtypes and it is linked to mammary differentiation, with luminal breast cells were less dependent on glutamine as compared to basal breast cells due to lineage specific expression of GS and GLS[53]. This study also demonstrates that luminal MCF-7 cells manage to rescue and promote increased cell viability of basal MDA231 cells in a transwell co-culture system without glutamine. This finding led me to speculate that EVs which are one of the components in cell's secretome could facilitate this process. Intrigued by this possibility, I investigated glutamine dependency in luminal MCF-7 and distinct metastatic clones of basal MDA231 cells through characterization of basal expression of GS and GLS and also the different effect of glutamine deprivation on mTORC1 pathway in Chapter 3. I also investigated the function of EVs in mediating intercellular glutamine symbiosis between luminal and basal breast cancer cells.

As the difference in glutamine dependency exists among distinct BC subtypes which may contributes to the intercellular glutamine symbiosis mediated by EVs, little is known

about the difference in the sensitivity towards an anti-cancer agent among distinct metastatic clones originated from the same subtype of BC. The sensitivity of different metastatic clones of BC cells may be associated with the genotypic traits and potentially due to the difference in the capacity of BC cells to efflux the anti-cancer agent through EVs secretion. Firstly, the difference in molecular signatures of lung and brain metastatic clones of basal triple negative breast cancer (TNBC) are discussed in Section 1.3.

1.3 Lung and brain metastases of breast cancer

In general, organotropism of BC is caused by specific subtypes of BC, molecular features and the host organ microenvironment through cancer cell-organ cross-talk. The formation of the pre-metastatic niche is mediated by factors secreted by cancer cells before their arrival at the targeted organ. For basal-like and TNBC cells, lung and brain are the metastatic sites of choice.

A subtype of TNBC originated from invasive ductal BCs deficient of p53 is highly associated with lung metastasis. Several molecules including epiregulin, cyclooxygenase 2, matrix metalloproteinase 1 and 2 are among the identified drivers of lung metastasis by facilitating tumor angiogenesis, promoting the escape of tumor cells into systemic circulation and remodeling lung capillaries for tumor cell invasion[54].

Lung metastatic BC cells produce tenascin C that facilitates lung micrometastasis to survive and outgrow by increasing the expression of components of stem cell signaling such as a positive regulator of Notch-signaling, musashi homolog 1 and a WNT target gene, leucine-rich repeat-containing G-protein-coupled receptor 5[55]. Through secretome analysis, nidogen 1 has been identified as a marker for lung metastasis and associated with poor prognosis[56]. The prometastatic functions of nidogen 1 includes enhancing

tumor cell migration, invasion and angiogenesis through disruption of endothelium integrity[56].

Approximately, 10-30% of metastatic BC patients experienced brain or central nervous system metastasis[57,58]. Brain metastasis is associated with poor clinical outcomes and neurological damages including impairments of cognitive and sensory functions[58]. Parenchymal brain metastasis and leptomeningeal metastasis are two common patterns of brain metastasis developed in BC patients. However, parenchymal brain metastasis is more associated with hematological malignancies[59]. Leptomeningeal metastasis is majorly contributed by tumor of breast origin and the tumor cells in the leptomeningeal migrate through cerebrospinal fluid[59].

In order to reach the brain microenvironment, BC cells need to transmigrate the blood brain barrier (BBB) which is constituted by capillary endothelial cells supported by basal lamina, pericyte and astrocytic end-feet, through paracellular endothelial tight junctions[60,61]. Several molecules including cluster of differentiation 44, CXCR4 and vascular endothelial growth factor facilitate the transendothelial migration of brain-metastatic BC cells by breaching endothelial integrity[62]. The permeability of the BBB can be enhanced by angiopoietin 2 through disruption of tight junction proteins including zonula occluden 1 and claudin 5, leading to subsequent TNBC cell colonization in brain[63]. Cyclooxygenase 2 (COX2), heparin-binding EGF-like growth factor (HBEGF) and ST6 N-acetylgalatosaminide alpha-2,6-sialyltransferase 5 (ST6GALNAC5) have been identified through gene expression analysis, as molecules that facilitate BC cells transmigration across BBB[64].

One of the emerging roles of EVs is to prime the metastatic niche by transferring cargoes that could modulate the phenotypes and genotypes of local resident cells in the targeted organ in favoring their survival and formation metastatic lesions[31]. Thus, it is of

importance to characterize the content and function of EVs secreted by different metastatic clones of BC cells as this will provide a means of identifying molecules that facilitate cancer cells to metastasize to specific metastatic sites. In Chapter 4, I performed proteomic analysis and investigated function of EVs secreted from lung and brain metastatic clones of TNBC MDA231 cells.

Extending from characterization of protein composition and function of both metastatic clones of MDA231 cells, I further investigated the sensitivity of these metastatic clones towards INK128, a clinically tested ATP-competitive mTOR kinase inhibitor. The general understanding on mTOR pathway, the main cancer-related pathway studied in this thesis is discussed in Section 1.4.

1.4 mTOR pathway: activation and function

mTOR is a revolutionary conserved serine/threonine protein kinase that nucleates into two structurally and functionally distinct complexes known as mTORC1 and mTORC2. mTORC1 has 5 components which are mTOR kinase, DEP-domain containing mTOR-interacting protein (DEPTOR), proline-rich AKT substrate 40 kDa (PRAS40), mammalian lethal with SEC13 protein 8 (mLST8) and regulatory-associated protein of mTOR (RAPTOR)[65]. mTORC2 contains 6 components, 3 similar components as in mTORC1 which are mTOR kinase, mLST8 and DEPTOR. The distinct components are rapamycin-insensitive companion of mTOR (RICTOR), mammalian stress-activated protein kinase interacting protein (mSIN1) and protein observed with RICTOR1 (PROTOR1)[65].

The mTORC1 pathway integrates multiple inputs arising from local and systemic sources of nutrient and energy to coordinate cellular metabolism under physiological and pathological states[66,67]. mTORC1 is activated by different stimuli including growth

factor, amino acids, glucose, energy and oxygen[68]. For instance, mTORC1 is activated following the binding of growth factors to their cognate receptor tyrosine kinases (RTKs), which convey signals through phosphatidylinositol-3 kinase (PI3K) and protein kinase B (AKT) (Figure 1.3). Phosphatidylinositol-3,4,5-triphosphate (PIP_3) generated by the activated PI3K specifically binds to AKT and this event triggers phosphorylation of AKT at threonine 308 residue by 3-phosphoinositide-dependent kinase 1 (PDK1). The activity of AKT is further boosted by a phosphorylation event at serine 473 residue by mTORC2.

The activated AKT inhibits a protein complex called tuberous sclerosis complex (TSC) that consist of TSC1, TSC2 and TBC1D7 by phosphorylating TSC2 subunit at multiple phosphorylation subunits. This eventually leads to the activation Ras-homologue enriched in brain (RHEB), the master activator of mTORC1 kinase activity. Then, AKT and mTORC1 simultaneously phosphorylate its inhibitory subunit PRAS40 causing it to dissociate from mTORC1.

The best-characterised biological function of mTORC1 is the regulation of mRNA translation achieved by phosphorylation and suppression of the translation initiation inhibitor, eukaryotic translation initiation factor 4E-binding protein 1 (4E-BP1), in concert with the activation of S6 kinase (S6K) that regulate the transcription of a wide range of ribosome biogenesis genes[69]. Apart from targeting 4E-BP1 and S6K in regulating mRNA translation, mTORC1 promotes aerobic glycolysis by upregulating hypoxia-inducing factor 1 α (HIF1α), which in turn induces the expression of glucose transporters and the majority of enzymes involve in glycolysis[70,71].

mTORC1 also modulates lipid synthesis through sterol regulatory element binding proteins (SREBPs), a family of transcription factors that directly activates the expression of lipogenic genes to enhance lipid synthesis[72]. Moreover, c-MYC is another downstream target of mTORC1 which regulates mitochondrial glutaminolysis by

stimulating the transcription of genes required for glutamine uptake and metabolism and c-MYC-dependent glutaminolysis is also associated with glutamine addiction phenotype in cells[49]. Unc51-like kinase 1 (ULK1) is a downstream effector of mTORC1 that induces autophagy, a starvation-induced means of recycling organelles and cytosolic components into nutrients. mTORC1 inhibits autophagy by reversible phosphorylation of ULK1 in cells under favorable growth condition[73].

The mTORC1 pathway is aberrantly regulated in various types of cancers. Despite encouraging preclinical studies, inhibitors targeting this pathway have failed to provide substantial prognostic improvements in cancer patients. Therefore, a deeper understanding on the mechanisms of chemotherapeutic resistance in cancer cells treated with mTOR inhibitor is of paramount importance. In particular, the mTOR pathway has been targeted in different subtypes of BC and this context is further discussed in Section 1.4.1.

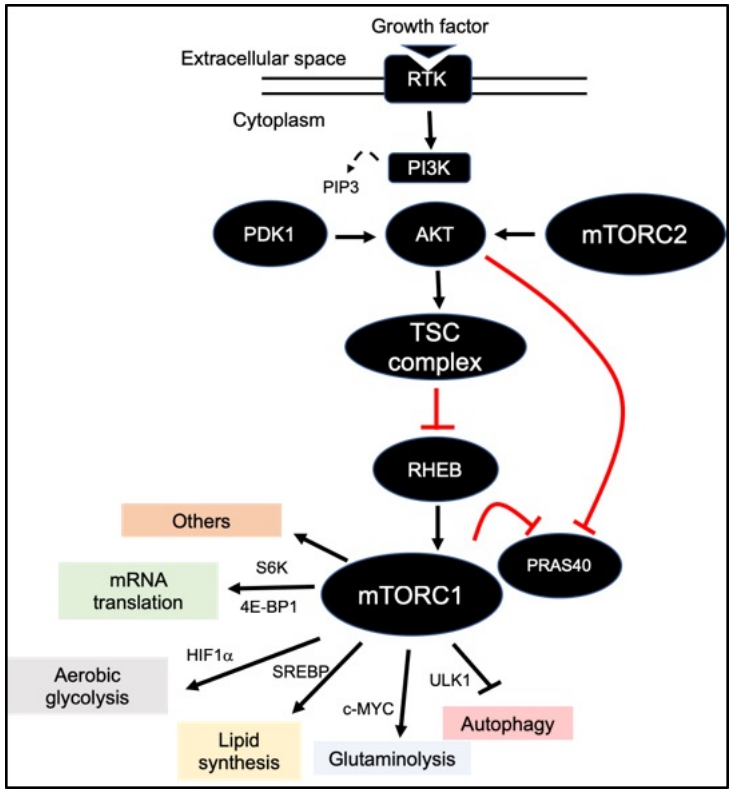


Figure 1.3. mTORC1 is activated by PI3K. The binding of growth factor to its cognate RTK activates PI3K. PIP3 generated by PI3K binds to AKT and PDK1 which in turn promotes and activates AKT through phosphorylation at threonine 308 residue. The activity of AKT is enhanced following mTORC2-dependent phosphorylation at serine 473 residue. AKT inhibits the TSC complex, the negative regulator of RHEB, by phosphorylating multiple sites on TSC2 subunit which results in the relieve of inhibition of RHEB. This leads to the activation of RHEB and subsequently stimulates mTORC1 kinase activity. PRAS40, a negative regulator of mTORC1 dissociates after phosphorylated by AKT and mTORC1. Activated mTORC1 regulates numerous biological processes through its downstream effector proteins including mRNA translation (S6K and 4E-BP1), aerobic glycolysis (HIF1α), lipid synthesis (SREBP), glutaminolysis (c-MYC) and autophagy (ULK1).

1.4.1 Targeting mTOR pathway in breast cancer

There is a growing amount of evidence that mTOR pathway is aberrantly regulated in BC, and that targeting this pathway is of therapeutic importance. Dysregulation of the PI3K-AKT-mTORC1 signaling axis in cancer is caused by loss of PTEN and activating mutations in PI3KCA (the PI3K catalytic submit alpha isoform) and mTOR kinase. mTORC1-specific rapamycin analogs (known as rapalogs) such as everolimus and temsirolimus and mTOR kinase inhibitors including AZD8055 and INK128 (also known as MLN0128 and TAK-228) that target both complexes are among the small molecules used in breast cancer research.

In hormone-receptor (HR)-positive BC with dysregulated AKT activity, sensitivity to endocrine therapy is restored by mTOR inhibitors in the preclinical studies[74,75]. Furthermore, everolimus suppressed the proliferation of estrogen-responsive BC cell lines in in vitro and synergized antitumor effect in combination with an aromatase inhibitor, letrozole[76]. In the neoadjuvant setting, the safety and efficacy of everolimus as monotherapy has been tested in a pilot study participated by 31 postmenopausal patients[77]. This study demonstrated significant reduction of Ki67 and P-S6 staining in patient samples. Furthermore, administration of everolimus has been shown to enhance the efficacy of letrozole as evidenced by marked reduction of P-S6 and Ki67 staining in 270 postmenopausal women with ER-positive BC under a randomized, double-blinded phase II trial[78].

In ER-positive BC, a small heat shock protein HSPB8 is a crucial molecule promoting resistance to tamoxifen and promotes cell proliferation by inhibiting autophagy[79]. Shi et al., 2018 has demonstrated tamoxifen resistance can be overcome by small molecule mTOR kinase inhibitor AZD8055 which led to suppression of HSPB8 expression[80]. This

work also highlighted that HSPB8 could potentially serve as an indicator for the efficacy of mTOR kinase inhibitor in ER-positive tamoxifen-resistant BC[80].

In HER2-positive BC, the recombinant humanized anti-HER2 monoclonal antibody trastuzumab has profoundly improved patient outcome[81]. However, loss of phosphatase and tensin homolog (PTEN) and activating mutations in PI3K which contribute to overactivation of mTOR promote resistance to trastuzumab[82]. Miller et al., 2009 reported that rapalogs potentially restored the sensitivity of the BC cells to trastuzumab[83]. Another preclinical trial study using patient-derived xenograft model to closely recapitulate the features of HER2-positive human BC demonstrated that the application of mTOR kinase inhibitor, INK128 sensitized the cells to trastuzumab or fulvestrant[84]. An early clinical trial evaluating the efficacy of a combination of everolimus with trastuzumab in addition to paclitaxel or vinorelbine in trastuzumab-resistant advanced HER2-positive BC reported that mTOR inhibitor potentially restore the sensitivity of the cells to trastuzumab[85–88].

Based on array comparative genomic hybridization (ACGH) studies, loss of PTEN which contributes to AKT overactivation is frequently observed in TNBC[89,90]. Among 6 molecular subtypes of TNBC, mesenchymal-like subtype is highly responsive to PI3K/mTOR inhibitors both in in vitro and in vivo settings[91]. Several studies have demonstrated that sensitization of basal-like BC to cisplatin is promoted by everolimus[92,93]. A combination of everolimus and paclitaxel was administered by 50 TNBC patients in phase II neoadjuvant study prior to a sequential administration of fluorouracil, epirubicin and cyclophosphamide for 4 cycles of every 3 weeks[94]. This study demonstrated that administration of everolimus promoted insignificant higher response rate than chemotherapy treatment alone.

However, the understanding on the sensitivity of different BC subtypes or metastatic clones to inhibitor targeting mTOR kinase is lacking. INK128, an ATP-competitive mTOR kinase inhibitor is currently under clinical trial to treat patients with metastatic TNBC in combination with other chemotherapeutic drugs (identifier number: NCT03193852). In Chapter 4, I investigated the sensitivity of lung and brain metastatic MDA231 cells to INK128, with an emphasis on the characterization EV protein composition and function. It is vital to understand the consequences of modulation of mTORC1 activity on the EV content and function as the activation of mTORC1 and exosome biogenesis share a similar subcellular compartment which is the late endosomal-lysosomal compartment.

In addition to the understanding of the biology of stress-induced EVs, I have widened the scope of research presented in this thesis by studying the stress-induced cytoophidium-forming proteins in BC cells. The general understanding of cytoophidium-forming proteins is discussed in Section 1.5.

1.5 Metabolic regulation of cytoophidium

Cellular compartmentalization is achieved, not only through membrane-bound organelles but also membrane-less structures that provides spatial regulation of distinct metabolic activities in the cells. The formations of membrane-less compartment such as stress granules, purinosome and cytoophidium are closely associated to cellular stress[95–97]. Of note, not all macromolecular assemblies under stress are due to aberrant folding and aggregation of proteins. Recent findings have demonstrated that these structures are comprised of proteins at their native states and organized in a highly ordered manner[98–101].

The cytoophidium (plural cytoophidia) is defined as a filamentous structure assembled by metabolic enzymes. Previously, several independent studies have demonstrated

IMPDH1 and CTPS1 which are involved in the de novo biosynthesis of purine and pyrimidine are able to assemble into distinct cytoophidia, respectively[100,102–104] (Figure 1.4). CTPS1 which catalyzes ATP-dependent conversion of uridine triphosphate (UTP) to cytidine triphosphate (CTP) is responsible for the rate-limiting step in de novo synthesis of CTP and salvage pyrimidine synthesis pathways whereas, IMPDH1 plays a crucial role as a regulator of purine biosynthetic pathway as it catalyzes a rate limiting step in guanine nucleotide production by converting of inosine monophosphate (IMP) to xanthosine monophosphate (XMP)[105,106].

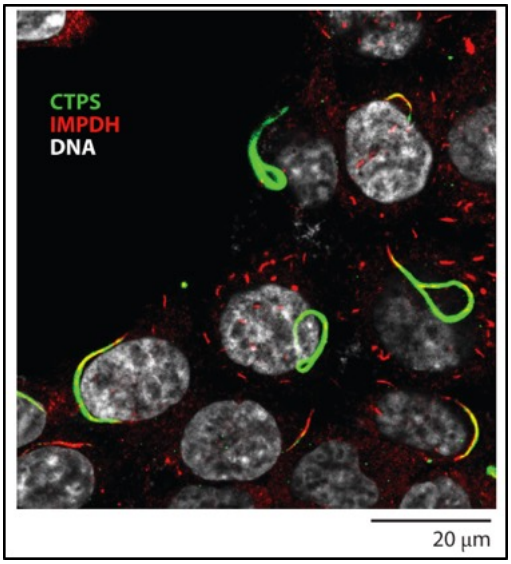


Figure 1.4. The assemblies of CTPS1 and IMPDH1 cytoophidia in human cells. CTPS (green) and IMPDH (red) cytoophidia in HEK239T cells. CTPS and IMPDH cytoophidia are in close proximity (yellow) in some of the cells. Scale bar, 20 μm. Adapted from J. Liu, 2016.

Several inhibitors of nucleotide biosynthesis have been widely used to induce cytoophidia formations in vitro. The glutamine analog, 6-Diazo-5-oxo-L norleucine (DON) induces both CTPS and IMPDH cytoophidia in many human cell lines[103,104,107]. CTPS1 and IMPDH1 can be specifically targeted by treating the cells with deazauridine

(DAU) and mycophenolic acid (MPA). DAU mediates competitive inhibition on CTPS through its conversion to a UTP analog, deaza-UTP, which in turn, suppresses pyrimidine biosynthesis pathway[108]. MPA is a reversible and non-competitive inhibitor of IMPDH. Through direct binding of MPA, the substrate turnover of both IMPDH isoforms is interfered leading to profound reduction of intracellular guanosine triphosphate (GTP) level[106]. The assemblies of CTPS1 and IMPDH2 cytoophidia can also be induced by depleting extracellular glutamine in the growth media[109].

Apart from the identification of CTPS1 and IMPDH1 as cytoophidium-forming proteins, Noree et al., 2010 identified 9 metabolic enzymes that can assembled into distinct cytoophidium by screening 1632 green fluorescence protein (GFP)-tagged *S. cerevisiae* strains equivalent to 40% of the collection[100]. These enzymes were clustered into 4 novel cytoophidium systems comprising eukaryotic initiation factor 2/2B (eIF2/2B) subunits composed of eIF2Bδ (GCD2p-GFP), eIF2Bε (GCD6p-GFP), eIF2Bβ (GCD7p-GFP), eIF2Bα (GCN3p-GFP) and eIF2α (SUI2p-GFP), URA7p-GFP and URA8p-GFP encode for CTPS, glutamate synthase 1 (GLT1p-GFP) and guanosine diphosphate-mannose pyrophosphorylase 1 (PSA1p-GFP) (Figure 1.5).

A drop in intracellular pH is associated to nutrient starvation. Petrovska et al., 2014 reported that GS assembled into cytoophidia induced by low pH induced by nutrient starvation which contributed to enzymatic inactivation[110]. This study further demonstrated that macromolecular crowding influenced cytoophidia assemblies and cytoophidium were assembled from repeated stacking of homo-decameric enzyme complex through a back-to-back mechanism. Furthermore, these researchers also demonstrated that URA8, GLT1 and GCN3 were among other metabolic enzymes assembled into cytoophidia in response to starvation-induced acidification of cytoplasm. The key finding was that the cytosolic acidification triggered cytoophidia assemblies and

acted as a storage depot for key metabolic enzymes in response to severe cellular starvation.

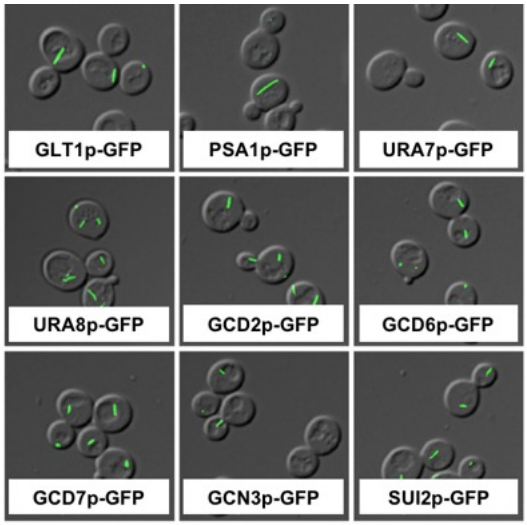


Figure 1.5. The assemblies of cytoophidium-forming proteins (green) in *S. cerevisiae*. This includes GLT1p-GFP, PSA1p-GFP, URA7p-GFP, URA8p-GFP, and eIF2/2B subunits including GCD2p-GFP, GCD6p-GFP, GCD7p-GFP, GCN3p-GFP and SUI2p-GFP. Scale bar, 5 μm. Modified from Noree et al., 2010.

Although there are many metabolic enzymes that can assemble into distinct cytoophidium, it is still unknown whether they share a similar mechanism in assembling into a cytoophidium. However, a multistep assembly of a cytoophidium has been proposed according to the CTPS cytoophidium assembly. This mechanism of assembly is discussed in Section 1.5.1.

1.5.1 Formation of cytoophidium

Gou et al., 2014 has described 5 distinct phases of CTPS cytoophidium assembly, which are: 1) nucleation, 2) elongation, 3) fusion, 4) bundling and 5) circularization through live

imaging of NIH/3T3 cells treated with DON[107] (Figure 1.6). The nucleation phase is characterized by the formation of multiple foci in the cytoplasm which gradually elongate in the second phase to form multiple small and short cytoophidia. During the fusion phase, cytoophidia can be fused with each other through two distinct ways which are head-to-head and side-by-side fusion. Head-to-head fusion leads to a longer cytoophidium with approximately similar width, while, side-by-side fusion leads to the formations of thicker cytoophidia. The bundling phase can be characterized by the continuous fusion events to form larger and thicker cytoophidia. Finally, the individual large and thick cytoophidium can form circular or ring-like structure by fusing both ends of cytoophidium.

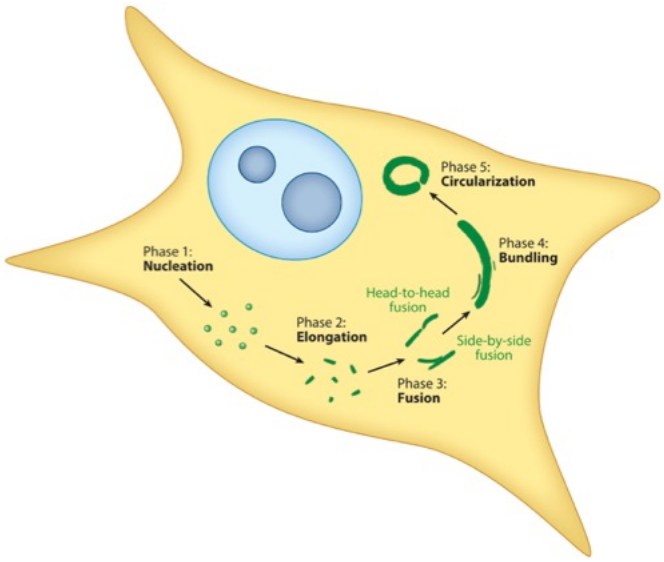


Figure 1.6. The multiple steps of cytoophidium assembly. The proposed assembly phases of cytoophidium formation include: 1) nucleation, 2) elongation, 3) fusion, 4) bundling and 5) circularization. Adapted from Liu, 2016.

The understanding of cytoophidium assembly is essential as this may provide useful information on the functional properties of cytoophidium. The functions of cytoophidium

are currently under active investigation and several biological functions of cytoophidium have been proposed and discussed in Section 1.5.2.

1.5.2 Proposed functions of cytoophidium

Cytoophidium has been proposed to serve as a storage depot for inactive enzymes which allows rapid reactivation of enzymes following its dissociation in response to the presence of growth-stimulating factors. With regards to the morphology of cytoophidium, filamentous structure of cytoophidium has an advantage in comparison with non-linear protein aggregates or membraneless compartments as this has a larger surface area which in turn provides regulatory small molecules and kinases an easier access in inducing dissociation of cytoophidium and reactivation of the enzymes.

Barry et al., 2014 has highlighted another advantage of cytoophidium structure which is being apolar, unlike various other polymers including microtubules[111]. This allows rapid transition of states between assembly and disassembly of cytoophidium. Furthermore, as CTPS constitutes the cytoophidium in the form of catalytically active tetramers, this would be beneficial to cells in fine-tuning the metabolic needs as such strategy will allow the release of active CTPS following dissociation of cytoophidium.

Ingerson-Mahar et al., 2010 proposed that CTPS cytoophidium potentially provided mechanical support analogous to cytoskeletal component, actin, in modulating cellular curve morphology by localizing to the inner curve of *C. crescentus*[112]. Nevertheless, it is still unknown whether the curve morphology was contributed directly by CTPS cytoophidium or through recruitment of other regulators.

The assembly of cytoophidia in different membrane-bound organelles is speculated to regulate compartment gating in the cells. Several studies have reported that IMPDH

shuttles between cytoplasm and nucleus as it has a crucial role as nucleic acid binding protein which regulates cell cycle progression[113,114]. Juda et al., 2014 also reported the assemblies of IMPDH into cytoophidium in the nucleus[115]. Colocalization of IMPDH to CTPS in the form of cytoophidia and the presence of unknown interacting components may confine IMPDH to the cytoplasm by hindering diffusion which in turn suppress the cell cycle progression by inhibiting its transcription factor activity.

Likewise, Gou et al., 2014 has reported that CTPS1 assembled into cytoophidia in nucleus and this finding has disputed the initial thought that CTPS1 activity is only restricted to cytoplasm[107]. This observation invited a speculation that CTPS1 may play unknown roles in nucleus which are different from its well-characterised enzymatic function in generating CTP. It is speculative that CTPS1 could modulates the transcriptional process via the production of nucleotide for RNA synthesis. As both CTPS and IMPDH enzymes are able to colocalize and assemble into cytoophidia in the nucleus, this finding suggests that the movement of these enzymes into and out of nucleus could be controlled through cytoophidia formation.

Although the general functions of cytoophidium have been proposed, the role of cytoophidium in the context of disease development and progression especially in cancer is currently unknown. However, the evidence of cytoophidium assembly in human cancer tissues has been recently reported and suggested to participate in the adaptive metabolism in cancer cells[116]. The relevance of cytoophidium assembly in cancer is further discussed in Section 1.5.3.

1.5.3 Relevance of cytoophidium assembly in cancer

The activity of CTPS has been reported to be elevated in multiple types of cancers such as renal carcinoma, hepatocellular carcinoma and lymphoma[117,118]. In this regard, the

correlation between CTPS cytoophidium and dysregulated cancer metabolism has yet been clarified. Recently, a screen of CTPS cytoophidium in an array of human hepatocellular carcinoma tissues has demonstrated that CTPS cytoophidia are only detectable in cancer tissues and not in the adjacent normal counterparts[116]. Furthermore, this study also highlights that CTPS cytoophidium assembly is highly correlated with high expression of an oncoprotein, the heat shock protein 90 (HSP90). HSP90 is known to potentiate glycolysis, cell proliferation and evasion of apoptosis through pyruvate kinase M2, a critical regulator of cell metabolism[119].

However, the correlation between the assembly of CTPS cytoophidium with glutamine dependency in different human cancer tissues was not addressed in this work. It is essential to test whether the CTPS cytoophidium assembly is closely related to the dysregulated glutamine metabolisms as several in vitro studies have reported that the suppression of glutamine metabolism through depletion of glutamine or inhibiting glutaminolysis induces CTPS1 and IMPDH2 cytoophidia assemblies[104,109,120]. In understanding the biology of cytoophidium assembly, DON is usually used to induce cytoophidia assemblies. Mechanistically, DON inhibits glutaminolysis by binding to the active sites of GLS1 (KGA and GAC)[121]. DON is a diazo compound that disrupts nucleotide and protein biosynthetic pathways which requires glutamine as a substrate[122]. Due to the chemical nature of DON, it promiscuously binds and inhibits other glutamine-utilizing enzymes including glutamine synthetase and amidotransferase[123,124].

Glutaminolysis is required for mTORC1 activation[125]. GLS plays indispensable roles for the growth of TNBC cells with dysregulated glutamine metabolism and its inhibition potentiates mTOR inhibitor[126]. Targeting glutamine metabolism by inhibiting glutaminase may provide a therapeutic window in treating glutamine addicted TNBC. Due to heterogeneity in TNBC, the difference in glutamine dependency between different

metastatic clones derived from the same parental TNBC cells is unclear. In Chapter 5, I characterized the difference in glutamine dependency between lung and brain metastatic clones of MDA231 cells reflected by the changes in the mTORC1 activity and abundance and length of CTPS1 and IMPDH1 cytoophidia based on DON treatment.

In order to understand the importance of metabolic regulation via cytoophidium assembly especially in cancer biology, it is an utmost important to identify metabolic enzymes that share similar capacity to assemble into cytoophidium. A previous partial screening of cytoophidium-forming proteins using yeast GFP collection has made an interesting finding that the assemblies of proteins into distinct cytoophidia is a widespread phenomenon associated with cellular stress[100]. Several other studies have also reported that the cytoophidium assembly is driven by the limitation of extracellular glutamine level and inhibition of nucleotide synthesis[103,109]. As most of the cytoophidium-forming proteins are implicated in the tumor development and progression, this invites a speculation that the assembly of cancer-associated proteins into cytoophidium may play a significant role in tumor biology. Hence, it is of importance to perform a complete screen of cytoophidium-forming protein at the genomic level.

To materialize this aim, the yeast GFP collection serves as the most appropriate model to screen for cytoophidium-forming protein as this system provides a tool for analyzing the effect of specific external stimuli, growth condition, genetic modification of a protein of interest on the localization of other subset of proteins[127]. Previously, the budding yeast serves as a reliable model to study integrated stress response mechanism and has improved out understanding on cancer[128–130]. This system confers several advantages including a complete genome sequence data, availability of functional genomic tools, collections of a comprehensive collection of yeast deletion mutants, genome-wide overexpression and GFP-tagged yeast strains[127,131–135].

As Noree et al, 2010 study has only screened 40% of budding yeast GFP collection at diauxic phase which is associated with glucose exhaustion and discovered a total of nine proteins with ability to assemble into distinct cytoophidia[100], I performed a collaborative works to carry out a large-scale screening of cytoophidium-forming proteins at diauxic phase using the same system to validate the findings presented in this study and also to screen for cytoophidium-forming proteins in the remaining collection presented in Chapter 5. As the assemblies of cytoophidia have been regarded as a storage depot during advanced state of nutrient starvation[110], I further investigated the abundance and length of glutamine-dependent cytoophidia in budding yeast cells cultured in different growth phases.

1.6 Primary research objectives

As discussed, the primary aim of this thesis is to focus on the biology of stress-induced EVs and cytoophidia assemblies of metabolic enzymes in BC, by pursuing the following research objectives:

1. Characterization the composition and function of EVs in establishing glutamine symbiosis between luminal and basal breast cells.
2. Comparative characterization of protein composition and function of EVs secreted by lungs and brain metastatic clones of TNBC MDA231 cells in response to clinically tested mTOR kinase inhibitor, INK128.
3. Comparative characterization of sensitivity to glutaminase inhibitor, DON between lungs and brain metastatic of TNBC MDA231 cells.
4. Large-scale identification and characterization of cytoophidium-forming proteins in budding yeast GFP collection.

Chapter 2.0 Materials and methods

2.1 Reagents and suppliers

All reagents and chemicals used were purchased from Sigma-Aldrich (UK) unless stated otherwise. The cell culture media and other solutions including Dulbecco's Modified Eagle's Medium (DMEM)-GlutaMAX™, OptiMEM, phosphate buffer saline (PBS), fetal bovine serum (FBS), penicillin, amphotericin B, insulin-transferrin-selenium (ITS) and TrypLE™ Express Enzyme were purchased from Thermo Fisher Scientific, UK.

2.2 Cell culture method

2.2.1 Cell lines

MCF-7 (ATCC® HTB-22™) and HBEC-5i (ATCC® CRL-3245™) cell lines were obtained from Professor Matthew Wood's laboratory, Department of Physiology, Anatomy and Genetics, University of Oxford, UK. Lung metastatic MDA231-LG and brain metastatic MDA231-BR cell lines were obtained from Professor Adrian Harris's laboratory, Weatherall Institute of Molecular Medicine, University of Oxford, UK.

2.2.2 Cell culture condition and maintenance

MCF-7, MDA231-LG and MDA231-BR cells were cultured in DMEM-GlutaMAX™ while HBEC-5i cells were cultured on flasks coated with 0.1% gelatin B in DMEM-F12 media. Media were supplemented with 10% heat-inactivated FBS, 100 U/mL penicillin and 250 ng/mL amphotericin B. For HBEC-5i cells, 40 μg/mL of endothelial growth supplement from bovine neural tissue was supplemented in addition to FBS, antibiotic and

antimycotic. The cells were maintained in humidified incubator (37°C and 10% CO_2) and the medium was replaced every 2 or 3 days.

Cells were passaged when they reached 70-80% confluence by discarding the old media and rinsing with sterile PBS solution. The cells were added with 2 mL of TrypLE™ Express Enzyme and kept for 5 minutes at 37°C to dissociate the cells. Then, 10 mL of complete growth media was added to neutralize the trypsin and cell suspension was mixed gently by pipetting up and down several times. The cell suspension was split at 1:6 and 25 mL of new complete growth media were added. All cell lines were subcultured within 3 months of resuscitation (<30 passage).

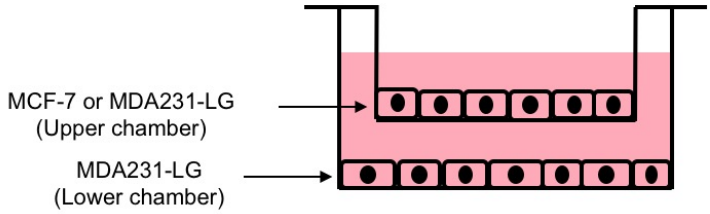
2.2.3 Cryopreservation and retrieval of cells

For cryopreservation of the cells, the cell suspension was spun down at 250 x g for 5 minutes. The cell pellets were resuspended in the freezing medium which was FBS containing 10% dimethyl sulfoxide (DMSO). Then, the cell suspension was aliquoted into several cryovial (Corning, USA) and placed in Mr Frosty freezing container (Thermo Fisher Scientific, UK) and kept in a -80°C freezer overnight. On the following day, the cryovials were transferred to a liquid nitrogen tank for storage at -196°C for long term storage. To revive the cells, 1mL of complete growth media was added to the frozen cells and resuspended until the cells were completely thawed. Then, the cell suspension was mixed with 10 mL of complete growth medium and centrifuged at 250 x g for 5 minutes. The cell pellet was resuspended in 10 mL of complete growth medium and transferred to a 25 cm^2 cell culture flask.

2.3 Co-culture transwell and cell growth assays

To study intercellular glutamine symbiosis between luminal and basal BC cells, $0.05x10^6$ of MCF-7 cells, MDA231-LG or MDA231-BR cells were seeded on the upper chamber made up of polyethylene terephthalate (Merck Millipore, UK) with a pore size of 1 μm and co-cultured with $0.05x10^6$ of MDA231-LG or MDA231-BR cells seeded on the bottom of lower chamber in 12-well plate in the complete growth media for overnight (Figure 2.1 A and B). After 16 hours, the media were then replaced by ITS-supplemented glutamine-free DMEM-F12 media to substitute FBS and provide sufficient amount of growth factor. The growth of the cells at the bottom of the plates was measured for 3 days. The growth of cells was monitored by recording phase images using Incucyte Zoom® live cell imaging system and confluence algorithm (Essence Bioscience, UK).

A



B

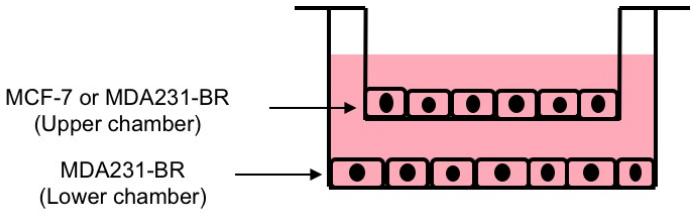


Figure 2.1. The experimental setting for intercellular glutamine symbiosis study. Co-culture transwell system to study the effect of co-culture with MCF-7 cells on the cell growth of (A) MDA-231-LG or (B) MDA 231-BR cells in glutamine-deprived media.

2.4 Dose-dependent inhibition of mTORC1 in breast cancer cell lines

In Chapter 4 and 5, both metastatic clones of MDA-231 cells were treated with INK128 (Selleckchem, UK) and DON, respectively. $0.2x10^6$ of cells per well were seeded in 6-well plates containing the complete growth media for overnight. After 16 hours, the cells were treated with INK128 or DON in a dose-dependent manner to select a dose for the downstream experiments. The inhibition of mTORC1 signaling was monitored by immunoblotting for phospho-S6, phospho-ERK, S6, ERK, 4E-BP1 and vinculin.

2.5 Protein extraction

The proteins were extracted from the cells by adding an appropriate amount of radioimmunoprecipitation assay (RIPA) buffer containing cocktails of phosphatase and protease inhibitors (Thermo Fisher Scientific, UK). The cells were removed using a cell scraper and transferred into an Eppendorf microtube by pipetting. The cell suspension was kept on ice for 15 minutes with regular vortexing every 5 minutes and followed by a centrifugation at a maximum speed of 20 000 x g for 10 minutes at 4°C. The pellet was discarded and whole cell lysate (supernatant) was collected and transferred into a new Eppendorf microtubes and stored at -20°C until use.

2.6 BCA assay

Total protein concentration was measured by the bicinchoninic assay (BCA™ Protein Assay) (Pierce Chemical Company, USA). The principle for this assay relies on the conversion of Cu^{2+} to Cu^{+} in an alkaline solution leading to the formation of purple color solution containing as Cu^{+} detected by the BCA. A vial of albumin standard at a concentration of 2 mg/mL (Pierce Chemical Company, USA) was diluted in the lysis

buffer to a range of concentration (1-2000 μg/mL) that served as protein standards. The BCA working reagent was prepared by combining solution A and B (50:1). 10 μL of each protein standard or sample (whole cell lysate or intact EV) was added to 200 μL of working reagent in the 96-well plate and incubated for 30 minutes at 37°C. The protein concentration of samples was measured spectrophotometrically at 562 nm using plate reader by comparing with the known protein standards. The amount of protein of each sample was derived by extrapolating the absorbance values from the generated standard curve.

2.7 Western blot analysis

A total of 20 μg of protein was mixed with 5X sample buffer (16% (v/v) of 2 mM Tris HCL (pH 6.8), 50% (v/v) glycerol, bromophenol blue without 2-mercaptoethanol. For a reduced condition, 2-mercaptoethanol was added to the sample mixture to a final concentration of 10% (v/v). The sample volume was equalized by adding distilled deionized water. Each sample was boiled at 37°C for 10 minutes to linearize the proteins. 10 μL of Precision Plus Protein™ Dual Color Standards (Bio-Rad, UK) and 20μL of each sample containing 20 μg of protein were loaded on the precast 10% Mini-PROTEAN® TGX™ Precast Protein Gel (Bio-Rad, UK) and electrophoresed at 150 V for 50 minutes in the 1X running buffer containing 25 mM Tris, 192 mM glycine, 0.1% (v/v) SDS at pH 8.3. Then, the SDS gel was removed from the plate and submerged in transfer buffer containing 25 mM Tris, 192 mM glycine and 20% (v/v) of 100% methanol or several minutes before immunoblotting.

For protein transfer, polyvinylidene difluoride (PVDF) membrane with 0.22 μm pore size (Amersham Biosciences, USA) was used. The membrane was activated by soaking with 100% methanol solution for 1 minutes and rinsed once with transfer buffer. Wet

electrophoresis transfer method was applied at 100V for 1 hour. After the completion of protein transfer, the membrane was incubated in blocking buffer containing 5% of bovine serum albumin (BSA) in the washing buffer containing 20 mM Tris and 500 mM NaCl at pH 7.4 for 1 hour before incubating with the primary antibody for overnight at 4 °C. Then, the primary antibody solution was discarded, and the membrane was washed with washing buffer for 10 minutes and repeated for 3 times. The secondary antibody, anti-rabbit IgG (H+L), HRP conjugate or anti-mouse IgG (H+L), HRP conjugate at a concentration of 1:10000 in 5% of bovine serum albumin (BSA) in the washing buffer was then added and kept for 1 hour at room temperature. After the incubation with secondary antibody, the blot was then washed with washing buffer for 10 minutes and repeated for 5 times. The blot was then immersed with Clarity Western Enhanced Chemiluminescence Substrate (Bio-Rad, UK) prepared according to the manufacturer's instruction and scanned using LI-COR (LI-COR Biosciences, UK) for quantitative analysis.

For detections of the total and phosphorylated of ERK and S6, two separate gels were used as the application of stripping buffer (BioRad, UK) had a variable efficiency in removing the primary antibodies from the PVDF membrane. For the internal loading control of whole cell lysate, α-tubulin was initially used. However, vinculin was later used throughout my DPhil projects as the α-tubulin antibody was out of stock in the laboratory. Furthermore, vinculin was selected as the internal loading control of choice for the detection and quantification of multiple proteins that have molecular weights lower than 50 kDa, as vinculin has a molecular weight of 130 kDa.

2.8 Immunofluorescence staining

For the induction of CTPS1 and IMPDH1 cytoophidia, $0.01x10^6$ of lungs or brain metastatic clones of MDA 231cells were cultured in μ-slide 8 well (Ibidi, Germany) overnight. After 16 hours, the media was replaced by the fresh complete growth media containing 0.5 mM DON and cultured for 24 hours. After 24 hours of treatment, the media was removed and the cells were washed with PBS twice and 200 μL of 4% paraformaldehyde was added for 15 minutes for cell fixation at room temperature. The cells were washed with PBS for 5 minutes for three times. Then, the cells were blocked with 1% BSA in PBST for 30 minutes. The cells were washed for 5 minutes for three times and then incubated in a mixture of primary antibodies for overnight at 4 °C. The cells were then washed with PBS for 5 minutes for three times and then incubated with a mixture of secondary antibodies (goat anti-mouse IgG H&L alexa fluor® 488 and goat anti-rabbit IgG H&L alexa fluor® 594) for 1 hour. The cells were washed with PBS for 5 minutes for three times and hoechst 33342 at a concentration of 0.1 μg/mL was added for 30 minutes for nuclear staining. The cells were washing with PBS for 5 minutes for three times and followed by the addition of mounting media (Ibidi, Germany).

2.9 Antibodies

The details of primary and secondary antibodies used for western blot and immunofluorescence are summarized in Table 2.1.

A

Primary antibody	Species	Supplier	Catalog number	Dilution	Molecular weight (kDa)
4E-BP1	Rabbit polyclonal	CST	53H11	WB: 1:1000	15-20
Ribosomal S6	Rabbit polyclonal	CST	5G10	WB: 1:1000	32
Phospho-ribosomalS6 (Ser240/244)	Rabbit polyclonal	CST	D68F8	WB: 1:1000	32
Phospho-p44/42 (ERK1/2) (Thr202/204)	Rabbit polyclonal	CST	9101	WB: 1:1000	42 and 44
ERK1/2 (Thr202/204)	Rabbit polyclonal	CST	9102	WB: 1:1000	42 and 44
Caveolin-1	Rabbit polyclonal	CST	D46G3	WB: 1:1000	21-24
Glutamine synthetase	Mouse monoclonal	Sigma-Aldrich	G2781	WB: 1:1000	45
Glutaminase	Rabbit monoclonal	Abcam	ab156876	WB: 1:1000	73
TSG101	Rabbit polyclonal	Abcam	ab30871	WB: 1:1000	44
Syntenin	Rabbit polyclonal	Abcam	ab19903	WB: 1:1000	32
IMPDH1	Mouse monoclonal	Abcam	ab55297	WB: 1:1000 IF: 1:200	55
CTPS1	Rabbit polyclonal	GeneTex	GTX105265	WB: 1:1000 IF: 1:200	67
CD63	Mouse monoclonal	SCBT	sc-15363	WB: 1:1000	30-60
CD81	Mouse monoclonal	SCBT	sc-70803	WB: 1:1000	22-26
α-Tubulin	Mouse monoclonal	Sigma-Aldrich	T5168	WB: 1:1000	~50
Vinculin	Mouse monoclonal	Bio- Rad	V284	WB: 1:1000	130

B

Secondary antibody	Supplier	Catalog number	Dilution
Anti-rabbit IgG (H+L), HRP conjugate	Promega	W4011	WB: 1:10000
Anti-mouse IgG (H+L), HRP conjugate	Promega	W4021	WB: 1:10000
Goat anti-mouse IgG H&L (Alexa Fluor® 488)	Abcam	ab150113	IF: 1:200
Goat anti-rabbit IgG H&L (Alexa Fluor® 594)	Abcam	ab150080	IF: 1:200

Table 2.1. List of primary and secondary antibodies. The details of (A) primary and (B) secondary antibodies used for western blot and immunofluorescence analysis.

2.10 Isolation of extracellular vesicles by SEC

Size exclusion liquid chromatography (SEC) isocratically fractionates molecules according to differences in size as they pass through the packed resin consisting of chromatography spherical beads with pores of different sizes in the column. The larger molecules are eluted in the earlier fractions while the smaller molecules are retained longer in the beads and eluted in the later fractions.

Approximately, 5-6x10^6 of cells were seeded in each 15 cm^2 petri dishes and maintained in the complete growth media for overnight. After 16 hours, the media was replaced by EV isolating media which was insulin-transferrin-selenium (ITS)-supplemented DMEM-F12 media containing either 2.5 mM or 0 mM of glutamine for glutamine deprivation condition or OptiMEM supplemented with the aforementioned concentration of antibiotic solutions (Section 2.2.2) and 25 nM of INK128 or equal volume of DMSO. After 48 hours, the media were spun down at 500 x g and 2000 x g, for 10 minutes each to pellet down cell debris and organelles from ruptured cells, respectively. The media were filtered using 0.22 μm Corning® bottom-top vacuum system, diafiltrated and concentrated using 100 kDa tangential flow filtration (TFF) system (Sartoris Products Limited, UK).

The concentrated samples were loaded on a column containing Sepharose FastFlow 4 installed on an ÄKTA prime (GE Healthcare Life Sciences, UK) equipped with a UV 280nm flow cell. Each individual fraction in PBS (2 mL) was collected based on the UV absorbance and the void volume fractions corresponded to the EV (7 to 11 mL) were pooled and concentrated using a 100-kDa MWCO Amicon Ultra spin filter (Merck Millipore, UK). The EV preparations were used for downstream analysis such as nanoparticle tracking analysis (NTA), immunoblotting, cell growth assay, mass spectrometry and MACSPlex analysis (Figure 2.2).

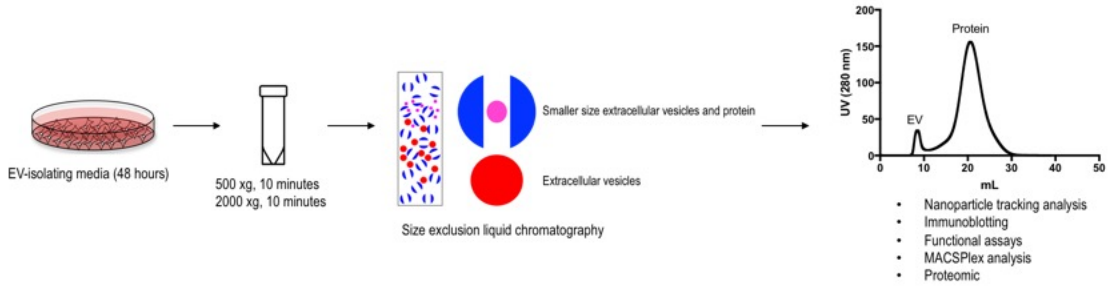


Figure 2.2. The summary of EV isolation by SEC.

2.11 Nanoparticle tracking analysis

The size distribution and concentration of EVs were analyzed by NanoSight NS500 instrument as per manufacturer's instruction (Malvern Instruments, UK). The EV preparations were mixed by vortexing and subsequently diluted in PBS at a dilution between 1:1000 to 1:5000. The NTA 2.3 software was used to generate a graph that plot EV concentration (10^8/mL) against size (nm). Further settings including the camera level, focus and detection threshold were standardized across samples.

2.12 MACSPlex analysis of extracellular vesicle

The levels of surface epitopes of EVs secreted from cells grown in glutamine-deprived and enriched media was analyzed by flow cytometry using human MACSPlex Exosome Kit (Miltenyi Biotech, Germany) in collaboration with Dr André Görgens at Karolinska Institute, Sweden.

The MACSPlex Exosome Kit contains the MACSPlex Capture Beads that are comprised of a mixture of various fluorescently labeled bead populations distinguishable by flow cytometry. A specific antibody presented on each capture bead binds to a respective exosomal surface epitope. APC-conjugated antibodies which comprise of antibodies

against tetraspanins (CD9, CD63 and CD81) stain the EVs bound to the MACSPlex Capture Beads. This forms a complex containing 3 components which are MACSPlex Capture Beads, EVs and APC-conjugated antibodies. The analysis of these complexes is in accordance to the fluorescence characteristics of both MACSPlex Capture Beads and APC-conjugated antibodies. Flow cytometric analysis is performed with MACSQuant Analyzer 10 flow cytometer (Miltenyi Biotec, UK). For each of the analyzed samples, 39 signal values corresponding to 39 MACSPlex Capture Beads are measured for each sample. The positive detected APC signal in a given sample indicates the presence of an epitope on the EV surface captured by antibody coupled to the MACSPlex Capture Bead. The protocol of MACSPlex analysis was summarized in Figure 2.3.

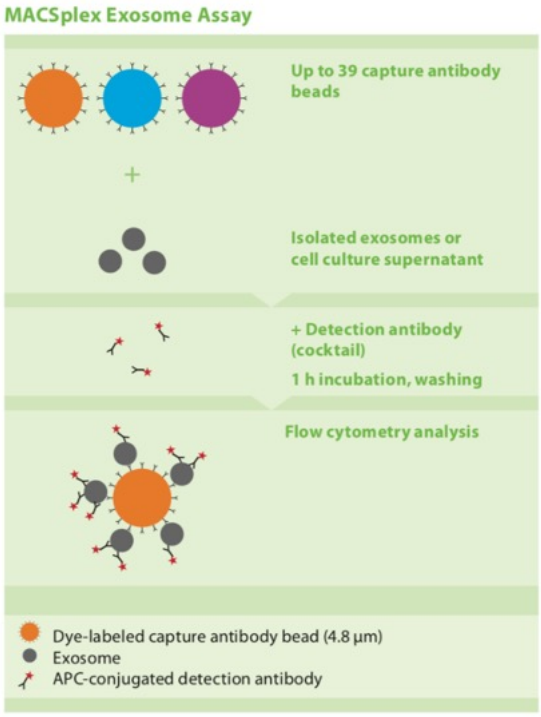


Figure 2.3. The protocol of analyzing the expressions of EV surface markers using MACSPlex system. Adapted from www.miltenyibiotech.com.

2.13 Label-free mass spectrometry

The method used for label-free mass spectrometry analysis of EV secreted from lung and brain metastatic clones of MDA-231 cells in response to mTOR kinase inhibitor, INK128 can be separated into three sections including in-solution digestion, chloroform-methanol protein extraction and peptide purification.

2.13.1 In-solution digestion of protein

The initial amount of EV used for proteomic analysis was 20 μg. For the in-dilution digestion of the sample, a reducing agent, dithiothreitol was added to each sample to a final concentration of 5 mM and vortexed. The samples were incubated for 1 hour. An alkylating agent, iodoacetamide was added to each sample to a final concentration of 20 mM and incubated for 1 hour.

2.13.2 Chloroform-methanol protein extraction

For protein extraction, 600 μL of methanol was added and followed by 150 μL of chloroform. The samples were vortexed and 450 μL of Mili-Q water was added to each sample. Then, the samples were vortexed again. The samples were centrifuged at maximum speed for 1 minute. The upper aqueous phase was carefully pipetted out without disrupting the protein precipitates at the interphase solution. Then, 450 μL of methanol was added to each sample containing precipitates in the organic phase. The samples were vortexed and centrifuged at the maximum speed for 2 minutes. The supernatant from each sample was discarded and protein precipitate was resuspended in 50 μL of 6 M urea buffer followed by vortexing and sonicating steps. The concentration of urea was reduced to a concentration less than 1 M by adding 250 μL of Mili-Q water.

Trypsin was added to digest proteins into small peptides at a ratio of 1:50 to the total protein content.

2.13.3 Peptide purification

Peptide samples were purified and concentrated using Thermo Scientific Pierce C18 Spin Column (Thermo Fisher Scientific, UK). Each column was tapped to settle resin and placed into a receiver tube. 200 μL of activation solution containing acetonitrile (ACN) was added to rinse wall of the spin columns and wet the resin. The columns were centrifuged at 1500 x g for 1 minute. The flow-through was discarded. These steps were repeated again. 200 μL of equilibrium solution containing 0.5% trifluoroacetic acid (TFA) in 5% ACN and centrifuged at 1500 x g for 1 minute. The flow-through was discarded and these steps were repeated again. For sample binding, samples were loaded on top of resin bed and the columns were placed into a receiver tube and centrifuged at 1500 x g for 1 minute. The flow-through was recovered by adding into column to ensure complete binding and centrifuged at 1500 x g for 1 minute. For sample washing, the columns were placed into receiver tubes and 200 μL of wash solution containing 0.5% TFA in 5% ACN was added to columns and centrifuged at 1500 x g for 1 minute. The flow-through was discarded and the washing steps were repeated again. For elution of samples, the columns were placed into new receivers and 20 μL of elution buffer containing 70% ACN were added to top of the resin bed and centrifuged at 1500 x g for 1 minute. The elution steps were repeated again with the same receiver tube. The samples were gently dried using vacuum evaporator. The samples were submitted to Target Discovery Institute, University of Oxford for label-free mass spectrometry analysis.

2.14 Proteomic data analysis

The expression of each protein was normalized to the median value of protein expression in each designated group for all four experimental repeats to reduce intragroup variation between biological repeats. Then, the normalized protein expression was log10-transformed to generate Gaussian data distribution required for multiple t-test statistical analysis and generating volcano and scatter plots. The volcano and scatter plots were generated by GraphPad prism software.

2.15 Modulation of cell growth by extracellular vesicles

In Chapter 3, $0.01x10^6$ recipient cells (MDA231-LG or MDA231-BR cells) per well were seeded in the 96-well plate in the complete growth medium, DMEM-GlutaMAX™ for overnight. After 16 hours, the complete growth medium was replaced by glutamine-free DMEM F12 medium supplemented with ITS, containing 10 μg/mL of EVs secreted by glutamine-deprived BC cells. The concentration of EVs used in this experiment was determined from the previous work conducted in the laboratory.

The similar experimental setting was applied in Chapter 4. $0.01x10^6$ of recipient cells (HBEC-5i cells) per well were seeded in 96-well plate, in the complete growth media DMEM F-12 for overnight. After 16 hours, the complete growth medium was replaced by serum-free DMEM F12 media containing EVs secreted by MDA231-LG or MDA231-BR cells. To investigate the growth-promoting function of these EVs on the HBEC-5i cell growth, three different concentrations of EVs (2.5 μg/mL, 5 μg/mL and 10 μg/mL) were tested. The concentration of 10 μg/mL of EVs was later selected and used to identify the changes in the phosphorylation of S6 and ERK in serum-deprived HBEC-5i cells over 24 hours. In this experiment, $0.1x10^6$ of HBEC-5i cells were seeded in the 6-well plate

in the complete growth media DMEM F-12 for overnight. After 16 hours, the complete growth media was replaced by serum-free DMEM F-12 containing 10 μg/mL of EVs secreted by the two MDA231 cell lines. After 24 hours, 80 μL of RIPA buffer was added to lyse the cells and the proteins were extracted out for the immunoblotting analysis of phospho-ERK, total ERK, phospho-S6, total S6, 4E-BP1 and tubulin. This concentration was also used to investigate the growth-promoting function of EVs secreted by the two MDA231 cell lines in response to INK128. The growth of the recipient cells in response to EV treatment was monitored by recording phase images using Incucyte Zoom® live cell imaging system and confluence algorithm (Essence Bioscience, UK).

2.16 In vivo extracellular vesicle biodistribution assay

The study on in vivo biodistribution of EVs secreted by both metastatic clones of MDA231 cells in response to INK128 was performed in collaboration with Dr. Mariana Conceicao from Professor Matthew Wood Laboratory, Department of Paediatrics, University of Oxford.

In order to fluorescently labeled the EVs with sulfo-cyanine5.5 N-hydroxysuccinimide (NHS) ester, a range of EV dose between $5x10^{11}$ to $1x10^{12}$ was incubated with the labelling agent at a final concentration of 50 μM for 2 hours at room temperature. The EVs were slowly mixed with the labelling agent using bench top orbital shaker throughout the labelling process. The unconjugated labelling agent was removed by SEC using 15 mL column packed with Sepharose FastFlow 4.

Female mice with body weight ranging between 20-22 g at the age of 13^{th} week were used in this experiment. A dose of $3x10^{9}$/g of freshly fluorescent-labeled EVs was intravenously injected through tail vein in each experimental subject. The dose of EVs

used for biodistribution assay was determined from the previous work conducted in the laboratory. After 4 hours, all mice were humanely sacrificed and the organs of interest including brain, lung, spleen, kidney and liver were collected for quantification of fluorescence intensity using IVIS Spectrum (Perkin Elmer, USA).

2.17 Yeast strain and media

S. cerevisiae strains used in the screening of cytoophidium-forming proteins were derived from a commercially available yeast GFP strain collection expressing full length proteins, tagged at the carboxy terminal end with GFP, from their endogenous promoters by inserting the coding sequence of *Aequorea victoria* GFP (S65T)[136] in-frame immediately preceding the stop codon of each ORF[127] (Figure 2.4). Each strain is originated from a parent strain with the genotype of *MATa his3Δ1 leu2Δ0 met15Δ0 ura3Δ0* (S288C). This strategy allows the screening of cytoophidium-forming proteins at the physiological level, so wild-type levels and patterns of protein expression are minimally perturbed.

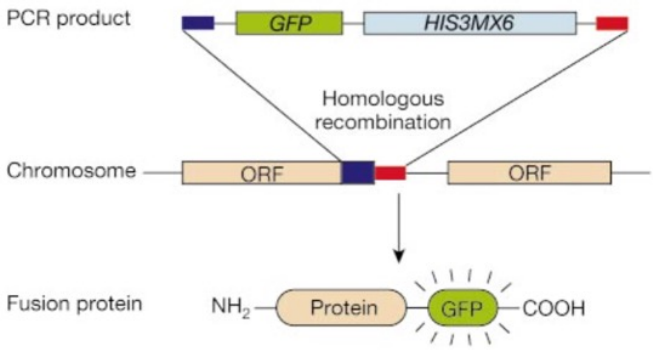


Figure 2.4. The strategy for constructing of yeast GFP strain collection. A C-terminally GFP-tagged protein is generated through an insertion of PCR product containing a GFP tag and a selectable marker gene by homologous recombination. Adapted from Huh et al., 2003[127].

2.18 Screening of cytoophidium-forming proteins in *S. cerevisiae*

The yeast strains were replicated into 96-well plates consisting of 150 μL of yeast peptone dextrose (YPD) media using a pin tool and sealed with MicroAmp™ adhesive film (Thermo Fisher Scientific, UK) to prevent well-to-well crossed contaminations. All strains were grown to reach the diauxic phase at 32 °C for 24 hours for the screening of cytoophidium-forming proteins. The yeast cells were fixed in 4% paraformaldehyde for 10 minutes. The fixed cells were washed by PBS. The cells were then visualized under 40x objective on an inverted microscope NIKON Eclipse Ti (NIKON, Japan). The cells showing filaments were selected for validation by acquiring images using a laser-scanning confocal microscope on a single focal plane. For the identification of nuclear filaments, hoechst 33342 was added to the fixed cells.

2.19 Quantification of cytoophidium-forming proteins in breast cancer cells and *S. cerevisiae*

The images of CTPS1 and IMPDH1 cytoophidia in MDA231-LG and MDA231-BR cells treated with 0.5 mM DON were acquired under 63x oil objective lens on a laser-scanning confocal microscope Olympus FV1000 (Olympus Scientific Solutions Americas Corp, USA). The abundance and length of cytoophidia in the cells were compared and quantified by capturing images in three different fields containing approximately 20-30 cells each.

In the budding yeast, the cells were cultured overnight and diluted to an OD600 of ~0.05 in 3 mL of YPD media at 32 °C in the incubator (300 r/min) and kept for 6, 24 and 168 hours which reflected the exponential, diauxic and stationary phases, respectively. The cells were transferred into 1 mL of microcentrifuge tube and spun down for 1 minute at

4000 r/min. The media were decanted and 100 μL of 4% paraformaldehyde were added to each tube for 10 minutes for cell fixation. After washing with PBS, a few microliters of cell suspension were transferred onto a slide and mixed by 1% agarose gel to avoid movement of the cells during imaging. The samples were covered by coverslips sealed with nail polish to avoid the samples from drying and ready for imaging. The abundance and length of cytoophidia in the cells cultured in different growth phases were compared and quantified by capturing images at least in four different areas containing a minimum of 100 cells each, using a laser-scanning Leica TCS SP5 II confocal microscope with a 63x oil objective lens (Leica Microsystems, Germany).

All images were taken with the extended focus projection of multiple z-levels. For the quantification of CTPS1 and IMPDH1 cytoophidia in the BC cells, the images were collected with a total of 5-6 slices at an interval of 0.45 μm between planes. For the quantification of ASN1p-GFP, ASN2p-GFP, GLT1p-GFP, URA7p-GFP and URA8p-GFP cytoophidia in the budding yeast, the images were collected with a total of 20-60 slices at an interval of 0.08μm between planes. The total number of z-level was higher for imaging of cytoophidia in the budding yeast cells because of the orientation of the cells and the thickness of 1% agarose gel across repeats. Image processing was carried out using ImageJ software.

2.20 Statistical analysis

Statistical analysis was performed either using two-tailed Student's t-test or one-way analysis of variance (ANOVA) for multiple group comparison. For proteomic analysis, the differentially expressed proteins were statistically analysed using pair-wise t-test (one per row) and 5% false discovery rate. All statistical analysis was performed using GraphPad Prism software. The error bar in the bar charts denotes the standard error

mean (SEM). A statistically significance difference was defined as *P<0.05, **P<0.01, ***P<0.001 and ****P<0.0001.

Chapter 3.0. Modulation of EV function and content by glutamine

3.1 Introduction

The first of two aspects of work presented in this chapter discusses the sensitivity of luminal (MCF-7) and basal (lungs metastatic MDA231-LG and brain metastatic MDA231-BR) BC cell lines towards extracellular glutamine level reflected by the basal expression of two key enzymes involved in glutamine metabolism which were glutamine synthetase (GS) and glutaminase 1 (GLS1). GS catalyzes glutamine synthesis from glutamate and ammonia and this reaction is reversed by glutaminolysis catalyzed by glutaminase (GLS)[137]. This chapter not only discusses glutamine sensitivity between luminal MCF-7 and both clones of basal MDA231 cells, but also demonstrates the heterogeneity of glutamine sensitivity between different metastatic clones of MDA-231 cells. Due to the close proximity between luminal and basal cells in breast tissue, both types of cells are co-cultured in glutamine-deprived media in a transwell co-culture system to validate the previous finding on the possible glutamine symbiosis established between both types of cells through cell secretome.[53]

The second aspect highlights the putative EV-mediated glutamine symbiosis through the secretion of GS-enriched EVs from glutamine-deprived MCF-7 cells that modulated the growth of both clones of MDA231 cells in glutamine-deprived media. The application of MACSPlex system, a bead-based flow cytometry technique for EV phenotyping, in the analysis of EV surface marker signature is also discussed.

The objectives of study in this chapter are stated below:

1. Comparative characterization of basal expression of GS and GLS1 between luminal MCF-7 and two basal MDA231 cell lines.

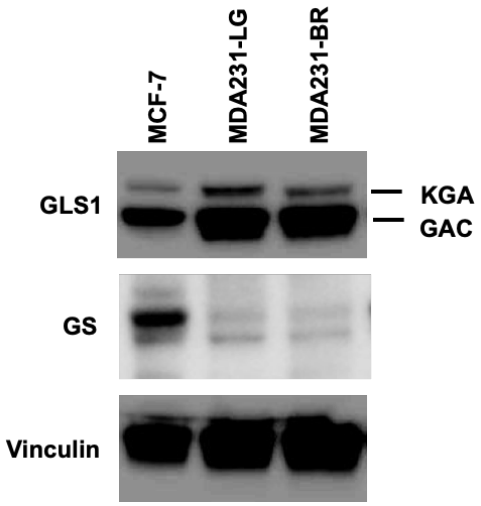
2. Comparative characterization of the differential effect of glutamine deprivation on mTORC1 and ERK pathways between luminal MCF-7 and both clones of basal MDA231 cells.
3. Investigation glutamine symbiosis between luminal MCF-7 and both clones of basal MDA231 cells through transwell co-culture system.
4. Comparative characterization of GS, TSG101, syntenin-1 and caveolin-1 levels in the EVs secreted by glutamine-deprived luminal MCF-7 and both clones of basal MDA231 cells.
5. Investigation on the functional role of EVs in establishing glutamine symbiosis between luminal MCF-7 and both clones of basal MDA231 cells in glutamine-deprived media.
6. Comparative characterization and validation of composition of exosomal surface markers in response to glutamine deprivation using MACSPlex system.

3.2 Result

3.2.1 Expression of GS and GLS1 in luminal and basal BC cell lines

The sensitivity of cells towards glutamine has been suggested to be dependent on the lineage-specific basal expression of GS and GLS.[53] In my study, immunoblotting analysis of GS demonstrated that GS expression was significantly higher in luminal MCF-7 cells as compared with both metastatic clones of basal MDA231 cells. In parallel with a previous study[53], my finding suggest that luminal MCF-7 cells have a higher capacity to resist low glutamine condition as the cells have the ability to synthesize sufficient glutamine endogenously. Immunoblotting analyses of GLS1 isoforms which were kidney-type glutaminase (KGA) and glutaminase C (GAC) basal expressions demonstrated that KGA level was significantly higher in basal MDA231-LG cells as compared with luminal MCF-7 cells while level of KAG in basal MDA231-BR cells was insignificantly higher than luminal MCF-7 cells. Nevertheless, the basal expression of KGA was significantly higher in basal MDA231-LG cells as compared to basal MDA231-BR cells. For GAC isoform, its basal expression in both metastatic clones of basal MDA231 cells was significantly higher than luminal MCF-7 cells, while there was no significant difference of GAC level between both metastatic clones of MDA231 cells. Taken together, these findings suggest that basal MDA231 cells are more dependent on glutamine than luminal MCF-7 cells due to their higher basal expression of GLS1.

A



B

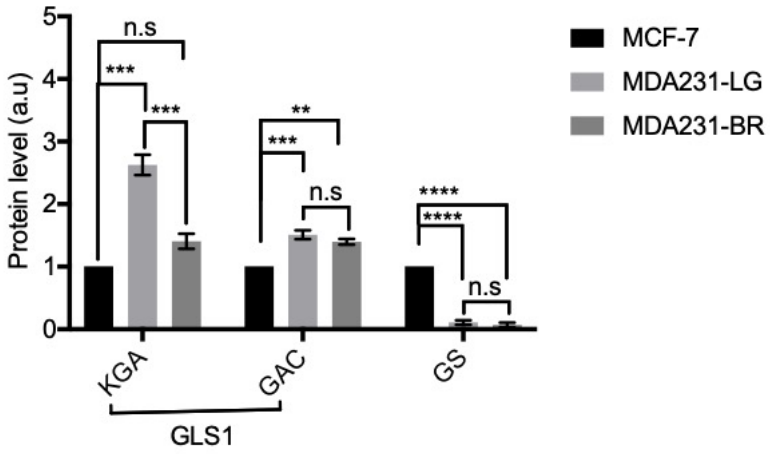


Figure 3.1. Comparative immunoblotting analysis of GLS1 (KGA and GAC isoforms) and GS between luminal MCF-7 and basal MDA231-LG and MDA231-BR cells. (A) A representative immunoblot and (B) quantitative analysis showing different expressions of GS and GLS1(KGA and GAC) in luminal MCF-7 and both clones of basal MDA231 cells. 20 μg of protein was loaded in each well of the gel. Vinculin was used as the internal loading control. Data are presented as mean ± SEM of three independent experiments, n=3. The statistical analysis was performed using one-way ANOVA. **, P ≤0.01; ***, P≤0.001 and ****, P≤0.0001. n.s: not significant.

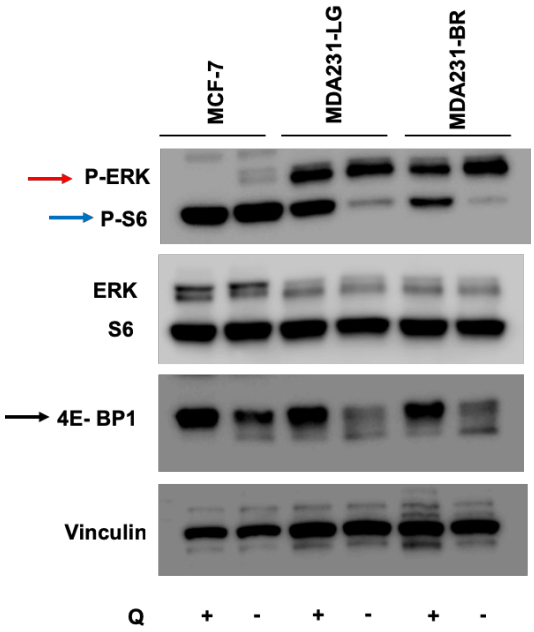
3.2.2 Glutamine deprivation differentially altered mTORC1 and ERK activities in BC cell lines

Glutamine is one of the molecules that activate mTORC1 activity in cells[138]. In order to investigate the difference in glutamine sensitivity between luminal and basal BC cell lines, immunoblotting analysis was performed to compare the changes in the phosphorylation level of mTORC1 target proteins, S6 and 4E-BP1 bands by culturing the cells in the glutamine-supplemented (2.5 mM of glutamine, Q+) and glutamine-deprived (0 mM of glutamine, Q-) media for 24 hours (Figure 3.2). These media contained ITS as the growth supplement instead of FBS, to maintain cell proliferation as FBS could interfere the experimental setting, due to the presence of small percentage of glutamine. The same growth media was used in the experiments described in the later sections, Sections 3.2.3 and 3.2.4.

As glutamine regulates the activity of mTORC1, glutamine deprivation significantly suppressed phosphorylation of S6 in both clones of basal MDA231 cells but not in luminal MCF-7 cells (blue arrow). This finding indicated that luminal MCF-7 cells are less sensitive to glutamine deprivation as opposed to both clones of basal MDA231 cells.

However, this treatment suppressed the activity of total 4E-BP1 depicted by the downshift of γ-band in all BC cell lines (black arrow). This finding also demonstrated that glutamine deprivation markedly affected mTORC1 activity through 4E-BP1 and not S6. The increase in phosphorylation of extracellular-regulated kinase (ERK) in response to suppression of mTORC1 activity mediated by glutamine deprivation was significantly increased in MCF-7 cells while this alteration was inconsistent in both metastatic clones of MDA231 cells. However, there was an increasing pattern of ERK phosphorylation in these cell lines.

A



B

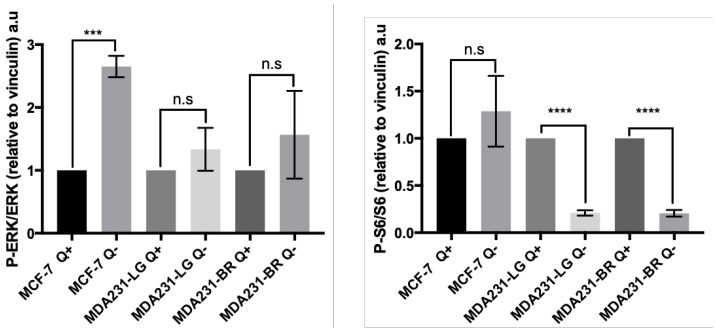


Figure 3.2. Alteration of mTORC1 and ERK activities in luminal and basal BC cell lines in response to 24 hours of glutamine deprivation. (A) A representative immunoblot and (B) quantitative analysis of phosphorylated ERK (P-ERK), total ERK, phosphorylated S6 (P-S6), total S6 and 4E-BP1. 20 μg of protein was loaded in each well of the gel. Vinculin was used as the internal loading control. Data are presented as mean ± SEM of three independent experiments, n=3. The statistical analysis was performed using one-way ANOVA. **, P ≤0.01; ***, P≤0.001 and ****, P≤0.0001. n.s: not significant. Q+: 2.5 mM glutamine. Q-: 0 mM glutamine.

3.2.3 Potential glutamine symbiosis between luminal and basal cells

As luminal MCF-7 cells expressed high basal level of GS and affected by glutamine deprivation to a milder extent than both clones of basal MDA231 cells, modulation of basal cell growth by MCF-7 cells in glutamine-deprived media supplemented with ITS in a co-culture transwell system was investigated.

As the hanging insert (upper chamber) allowed the transfer of cell secretome including paracrine soluble factors and also EVs from feeder to recipient cells, MCF-7 cell secretome promoted increase in growth of both MDA231-LG (Figure 3.3 A) and MDA231-BR cells (Figure 3.3 B) as compared to co-cultures with similar clones of MDA231 cells. The MCF-7 secretome had a greater effect on the growth of MDA231-BR cells as compared to MDA231-LG cells as evidenced by a significant increase in cell growth after 24 hours co-cultured with MCF-7 cells. This finding also indicated that MDA231-BR cells were more sensitive to the extracellular level of glutamine as compared to MDA231-LG cells. Taken together, this finding suggested that the unknown components of MCF-7 secretome activated signaling pathways that promoted cell growth.

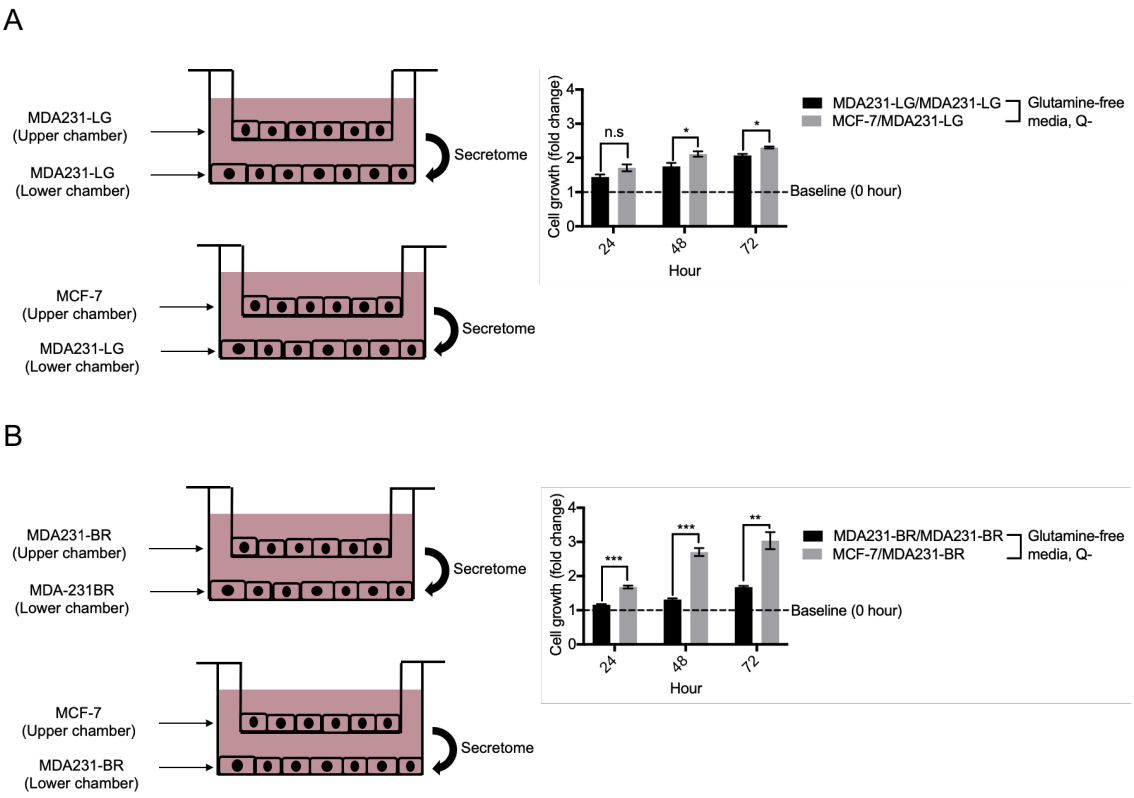


Figure 3.3. Secretome of MCF-7 cells enhanced the growth of MDA231-LG and MDA231-BR cells in glutamine-deprived media. (A) The growth of MDA231-LG and (B) MDA231-BR cells started to increase significantly after 48 and 72 hours co-cultured with MCF-7 cells, respectively. Data are presented as mean ± SEM of three independent experiments, n=3. The statistical analysis was performed using Student t-test (two-tailed). *, P≤0.05; **, P ≤0.01 and ***, P≤0.001. Q-: 0 mM glutamine. n.s: not significant.

3.2.4 Modulation of EV protein composition by glutamine

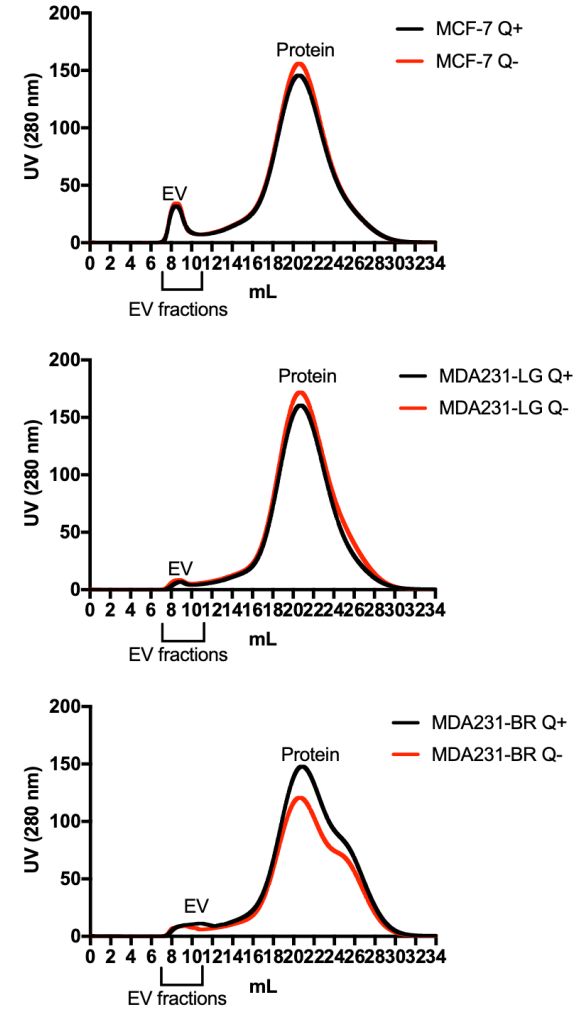
The activation of mTORC1 activity and exosome biogenesis shares a common intracellular compartment which is the late endosomal-lysosomal compartment[139,140]. As the data in Figure 3.2 indicated that glutamine deprivation suppressed mTORC1 activity, the composition and function of EVs secreted from glutamine-deprived luminal MCF-7 and both basal clones of MDA231 cells were characterized. Through size-exclusion liquid chromatography, void volume fractions corresponding to EVs (7 to 11 mL) were pooled and subjected to NTA analysis and protein quantification (Figure 3.4 A). Based on chromatogram profile, MCF-7 cells secreted a higher amount of EV s as compared to other tested cell lines. I also demonstrated that glutamine deprivation did not markedly alter the mode size of EVs secreted by all BC cell lines (Figure 3.4 B). Based on the BCA protein assay, there was a trend in my data suggesting that glutamine deprivation might have increased the secretion of EVs from MCF-7 and MDA231-BR cells, however, this change was statistically insignificant. The secretion of EVs from MDA231-LG cells was not affected by this treatment (Figure 3.4 C).

One of the proteins of interest was GS as its basal expression had been correlated to the glutamine sensitivity in breast cancer cell lines[53]. Immunoblotting analysis demonstrated that glutamine deprivation induced upregulation of GS in whole cell lysate (WCL) of luminal and basal BC cell lines (Figure 3.4 D and E). This finding suggested that upregulation of GS in response to glutamine deprivation could serve as a common mechanism to compensate the deficiency of extracellular glutamine level by synthetizing glutamine endogenously. In contrast, GS was only elevated in MCF-7 EVs in response to glutamine deprivation. GS was undetected by immunoblotting in EVs secreted by both clones of MDA231 cells, probably due to low GS abundance in EVs.

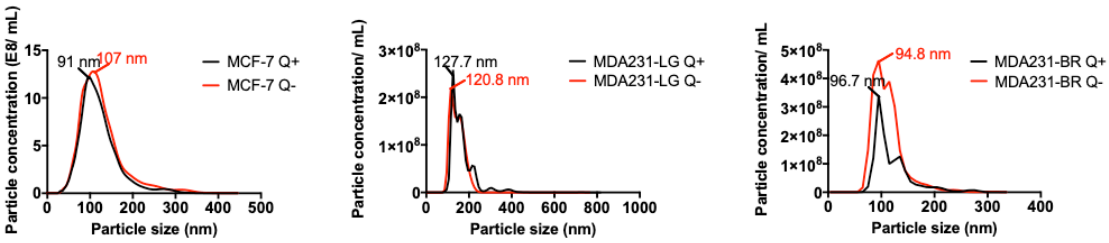
TSG101, syntenin and caveolin-1 were also selected as proteins of interest in this study due to their involvements in modulating EV biogenesis, cargo sorting and secretion[141–143]. This also allowed investigations on the effect of glutamine deprivation on the level of these proteins in WCL and EVs (Figure 3.4 D and E). Immunoblotting analysis of TSG101 demonstrated that its level remained unchanged in both WCL and EVs of all BC cell lines in response to glutamine deprivation. However, the basal level of TSG101 was higher in EVs secreted by MCF-7 cells as compared to others. The basal expression of syntenin in WCL was undetected in MCF-7 cells and low in both clones of MDA231 cells. However, glutamine deprivation only reduced its level in MDA231-LG cells. In EVs, its level was not altered by this treatment. Likewise, the basal expression of caveolin-1 in WCL was also undetected in MCF-7 cells and its expression was higher in both clones of MDA231 cells. The level of caveolin in both WCL and EVs was unchanged in response to glutamine deprivation.

For immunoblotting quantification of EV proteins, the signal of each protein was presented as an absolute intensity as there was no reliable protein that could be used as a loading control, particularly when EVs secreted from different cell lines and/or conditions are compared (Figure 3.4 E). The EVs were equally loaded based on the protein quantification using BCA protein assay for immunoblotting analysis.

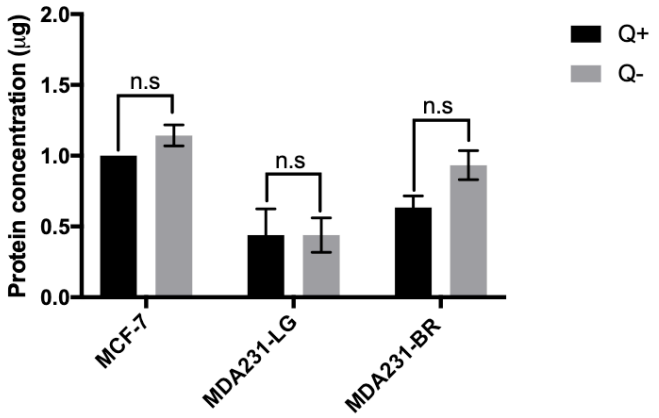
A


MCF-7 Q+
MCF-7 Q-
Protein
EV
UV (280 nm)
EV fractions
mL
MDA231-LG Q+
MDA231-LG Q-
MDA231-BR Q+
MDA231-BR Q-

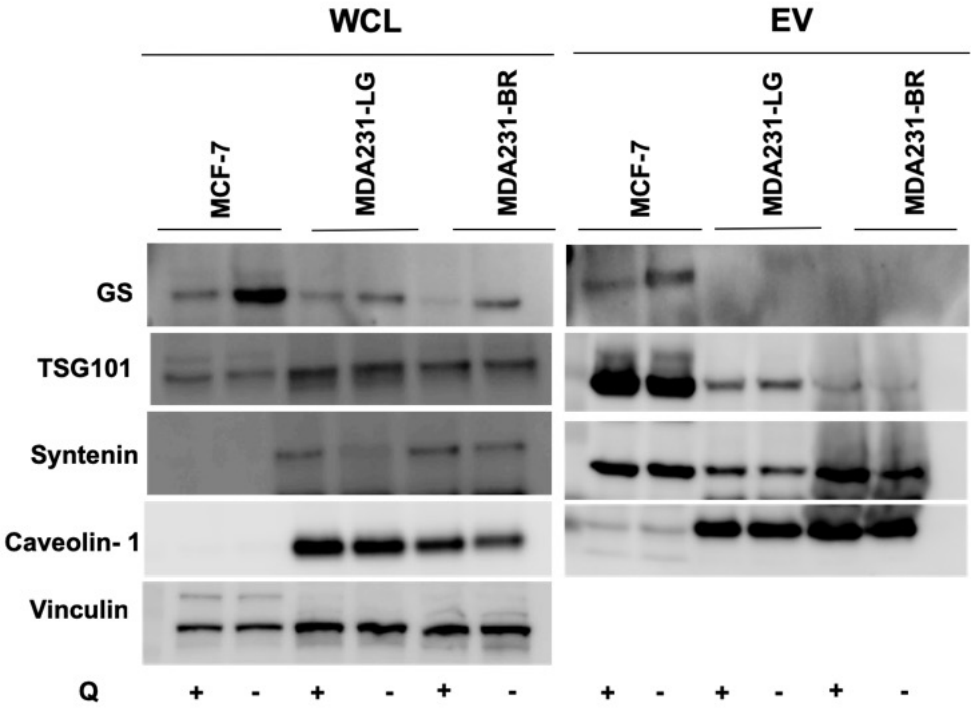
B


Particle concentration (E8/ mL)
91 nm
107 nm
MCF-7 Q+
MCF-7 Q-
Particle size (nm)
Particle concentration/ mL
127.7 nm
120.8 nm
MDA231-LG Q+
MDA231-LG Q-
96.7 nm
94.8 nm
MDA231-BR Q+
MDA231-BR Q-

C


Protein concentration (μg)
2.0
1.5
1.0
0.5
0.0
n.s
n.s
n.s
Q+
Q-
MCF-7
MDA231-LG
MDA231-BR

D


WCL
EV
MCF-7
MDA231-LG
MDA231-BR
MCF-7
MDA231-LG
MDA231-BR
GS
TSG101
Syntenin
Caveolin- 1
Vinculin
Q
+ - + - + - + - + - + -

E

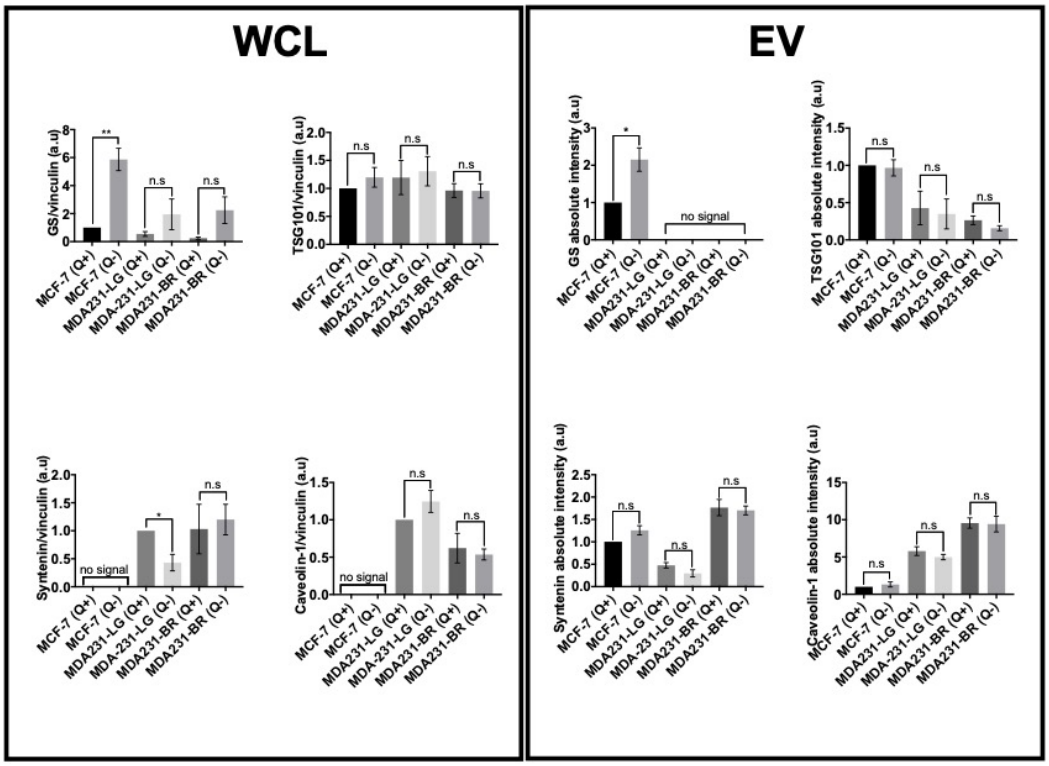
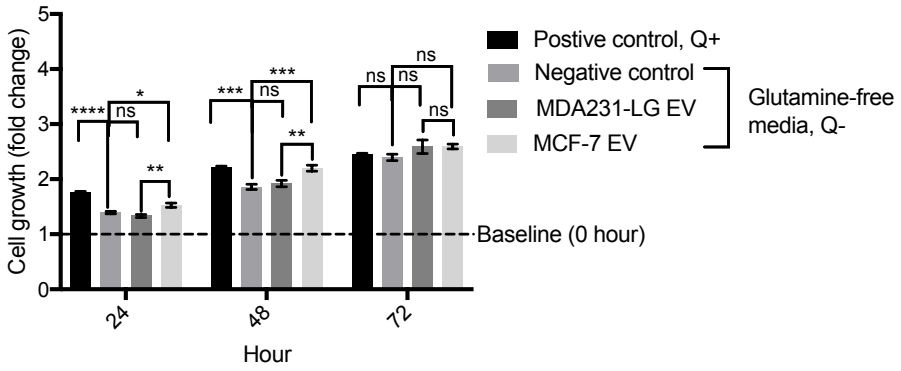


Figure 3.4. Chromatogram profile, size distribution, secretion and protein composition of EVs in response to glutamine deprivation. (A) Chromatogram profile of EVs secreted from glutamine-deprived luminal MCF-7 and both clones of basal MDA231 cells indicating MCF-7 cells secreted higher amount of EVs as compared to others. (B) NTA analysis of EV mode size and (C) protein quantification of EVs secreted from glutamine-deprived luminal MCF-7 and both clones of basal MDA231 cells. (D) Immunoblotting analysis and (E) signal quantification of GS and EV markers in WCL and secreted EVs from tested BC cell lines in response to glutamine deprivation. 20 μg of protein was loaded in each well of the gel. Vinculin was used as the internal loading control for WCL. Data are presented as mean ± SEM of three independent experiments, n=3. The statistical analysis was performed using Student t-test (two-tailed) for comparison between two conditions, Q+ and Q-, in all tested cell lines. *, P≤0.05 and **, P ≤0.01. Q+: 2.5 mM glutamine. Q-: 0 mM glutamine. n.s: not significant.

3.2.5 Modulation of EV function by glutamine

As the MCF-7 secretome increased growth of both clones of MDA231 cells and secreted MCF-7 EVs contained high level of GS in response to glutamine deprivation, the functional properties of EVs secreted by glutamine-deprived MCF-7 in modulating the growth of both clones of MDA231 cells cultured in glutamine-deprived media was investigated. The positive control in this study was the recipient cells (MDA231-LG or MDA231-BR cells) cultured in glutamine-supplemented growth media, containing 2.5 mM of glutamine, while the negative control was the recipient cells cultured in glutamine-deprived media, containing 0 mM of glutamine. As previously discussed in Section 3.2.3, these media contained ITS as the growth supplement. This experimental setting allowed the detection in the changes of recipient cell growth in response to different EV treatments (MCF-7 EV versus MDA231-LG EV, or MDA231-BR EV), as the growth of the recipient cells was significantly reduced in response to glutamine deprivation. The EVs isolated from glutamine-deprived MCF-7 but not from glutamine-deprived MDA231-LG or MDA231-BR cells, significantly increased the growth of recipient cells (MDA231-LG or MDA231-BR) cells in glutamine-deprived media as evident at 24 and 48 hours post treatment. However, there was no significant increase in growth of both clones of MDA231 cells at 72 hours as the cells had reached maximum confluency.

A



B

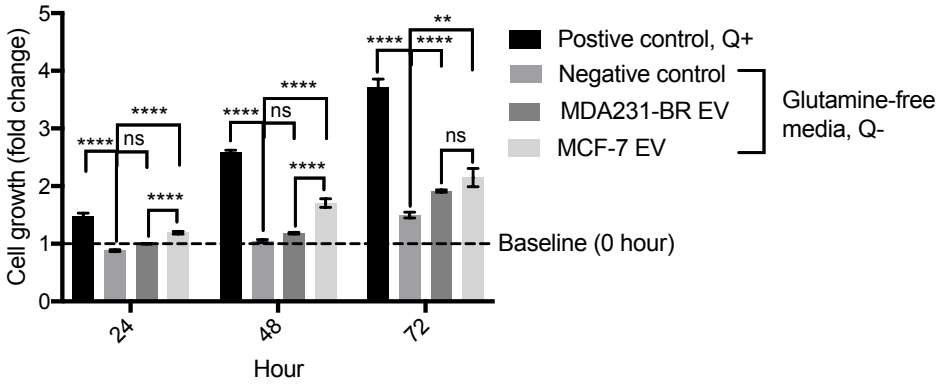


Figure 3.5. The growth-promoting function of glutamine-deprived MCF-7 EVs. EVs isolated from glutamine-deprived MCF-7 cells significantly increased the growth of (A) MDA231-LG and (B) MDA231-BR cells cultured in glutamine-free media at 24 and 48 hours post EV treatment, as compared to EVs isolated from glutamine-deprived MDA231-LG or MDA231-BR cells. The positive and negative controls in this experiment were the recipient cells (MDA231-LG or MDA231-BR cells) cultured in glutamine-supplemented (Q+) and glutamine-free (Q-) growth media, respectively. 10 μg/mL of EVs was used in this assay. Data are presented as mean ± SEM of at least, three independent experiments, n≥3. The statistical analysis was performed using one-way ANOVA. **, P ≤0.01; ***, P≤0.001 and ****, P≤0.0001.

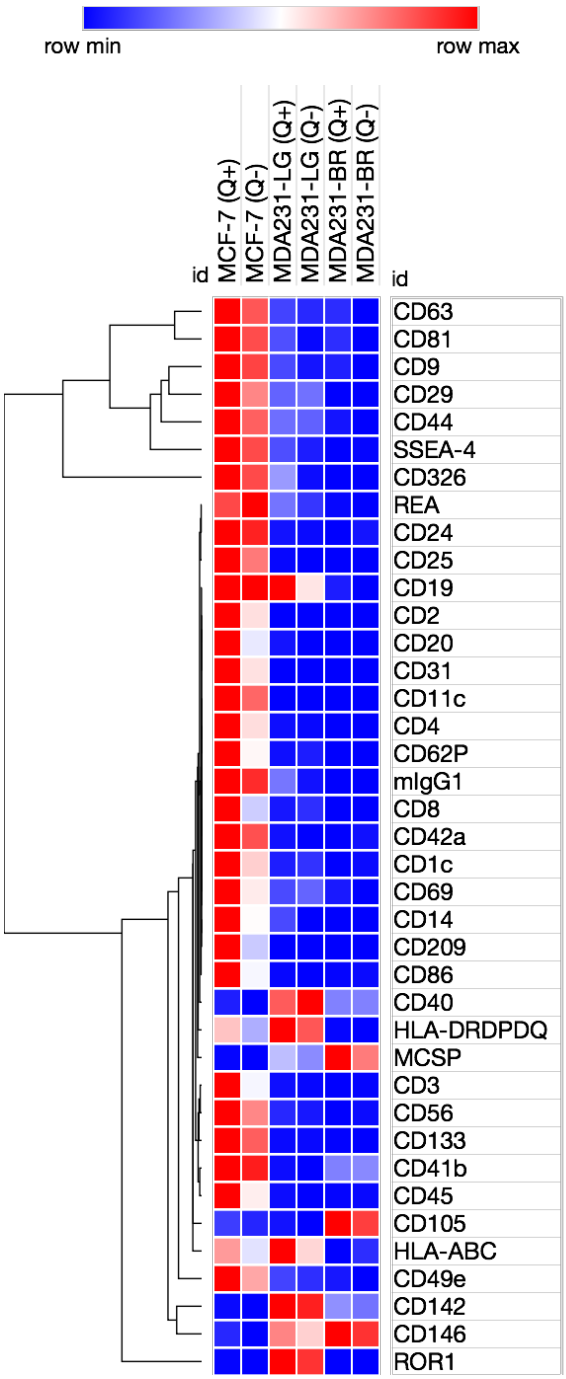
3.2.6 MACSPlex analysis of EV protein composition

The levels of 37 exosomal surface markers plus two isotype controls (mIgG1 and REA) were measured using MACSPlex system and presented in the heatmap (Figure 3.6 A). The preliminary analysis revealed that the levels of most of the surface markers were higher in EVs secreted by MCF-7 cells as compared to both clones of MDA231 cells. Based on hierarchical clustering, glutamine deprivation markedly reduced the levels of several exosomal surface markers in MCF-7 EVs including CD2, CD20, CD31, CD4, CD62p, CD8, CD1c, CD69, CD14, CD209, CD86, CD3, CD45, HLA ABC and CD49e.

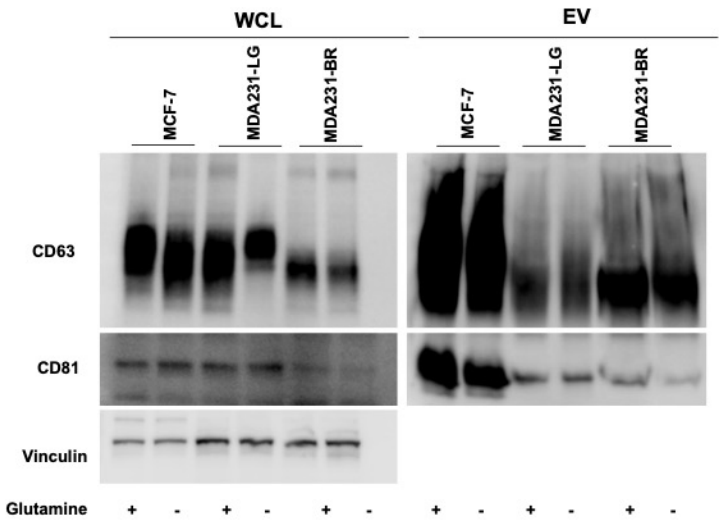
In EVs secreted by MDA231-LG cells, the highly abundant proteins were CD19, CD40, HLA- DRDPDQ, HLA- ABC, CD142, CD146 and ROR1 and among these proteins, only CD19, HLA-DRDPDQ, HLA-ABC and CD146 levels were reduced in response to glutamine deprivation. CD40 level was mildly increased and the levels of CD142 and ROR1 were unchanged. However, in the EVs secreted by MDA231-BR, there were only 3 surface markers namely MCSP, CD105 and CD146 detected by this system and the overall effect of this treatment was very mild.

CD63 and CD81 were among 37 exosomal surface markers measurable on the MACSPlex system and glutamine deprivation mildly reduced the level of these proteins in MCF-7 EVs. CD63 and CD81 were selected for data validation. Based on immunoblotting analysis, the levels of both of these proteins were higher in MCF-7 EVs as compared to EVs secreted by both clones of MDA231 cells. In WCL, glutamine deprivation significantly reduced CD63 and CD81 levels in MDA231-LG and MDA231-BR cells, respectively.

A


row min
row max
id
MCF-7 (Q+)
MCF-7 (Q-)
MDA231-LG (Q+)
MDA231-LG (Q-)
MDA231-BR (Q+)
MDA231-BR (Q-)
id
CD63
CD81
CD9
CD29
CD44
SSEA-4
CD326
REA
CD24
CD25
CD19
CD2
CD20
CD31
CD11c
CD4
CD62P
mIgG1
CD8
CD42a
CD1c
CD69
CD14
CD209
CD86
CD40
HLA-DRDPDQ
MCSP
CD3
CD56
CD133
CD41b
CD45
CD105
HLA-ABC
CD49e
CD142
CD146
ROR1

B



C

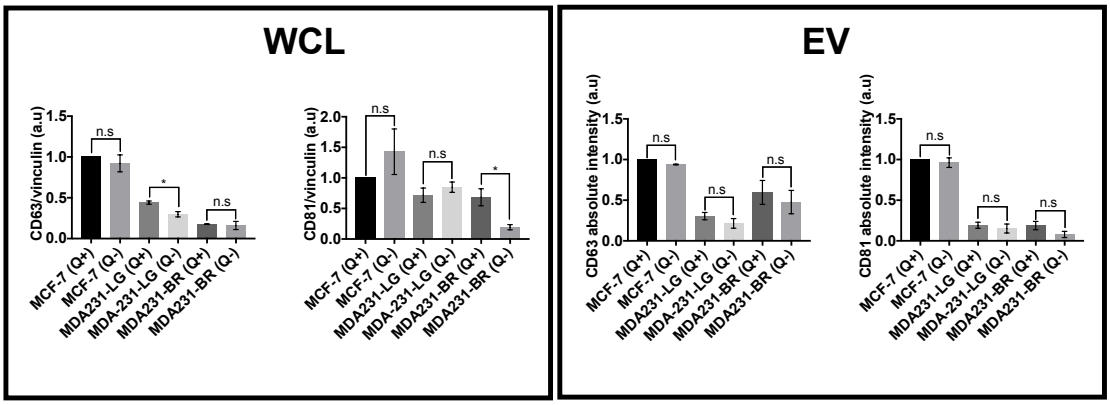


Figure 3.6. The changes of the level of EV surface markers in response to glutamine deprivation. (A) A heatmap showing hierarchical clustering of 39 EV surface epitopes of EVs secreted by different BC cell lines in response to glutamine deprivation. Data are represented as APC mean fluorescence intensity normalized to the mean signal intensity obtained with anti-CD9, anti-CD63 and anti-CD81 beads. n=1. (B) Immunoblotting and (C) signal quantifications of CD63 and CD81 in WCL and EVs. 20 μg of protein was loaded in each well of the gel. Vinculin was used as the internal loading control for WCL. Data are presented as mean ± SEM of three independent experiments, n=3. The statistical analysis was performed using Student t-test (two-tailed). *, P ≤0.05. Q+: 2.5 mM glutamine; Q-: 0 mM glutamine. n.s: not significant.

3.3 Discussion

3.3.1 Cell lineage-specific dependency on extracellular glutamine

Cancer cells are dependent on glutamine for proliferation and survival, thus displaying a unique phenotype termed as 'glutamine addiction'. In order to meet the requirement for glutamine, this molecule can be acquired by cancer cells through multiple ways including endocytosis of extracellular vesicle, micropinocytosis of extracellular fluid and de novo glutamine synthesis[144–146].

Previously, several studies reported that the dependency on glutamine varies across different types of BC cell lines[53,147]. For instance, glutamine deprivation for 48 hours has a modest effect on the proliferation and viability of luminal BC cell lines including MCF-7, T47D, BT474 and MDA-MB-361[53]. In contrast, similar treatment has a profound effect on the proliferation and viability of basal BC cell lines including BT20, MDA231 and MDA-MB-157, leading to a consensus that the basal type of BC cell lines are more dependent on the extracellular glutamine levels than luminal type of BC cell lines[53].

A previous study has demonstrated that the dependency of BC cell lines towards glutamine is dependent on the basal expressions of GS and GLS[53]. My data confirmed that such variation in glutamine dependency between luminal and basal BC cell lines was correlated to the cell-type specific basal expression of these two key enzymes involved in glutamine metabolism (Figure 3.1). The increase in GS expression in cancer cells in the tumor microenvironment enhances the intracellular production of glutamine which in turn promotes the synthesis of asparagine, nucleotides and uptake of essential amino acids[144]. Therefore, it is logical that luminal BC cell lines were more tolerant to glutamine deprivation than the basal BC cell lines.

GLS has been regarded as a promising target for inhibition in basal type TNBC cells as knockdown GLS in TNBC cells lines led to a profound growth inhibition *in vitro* and *in vivo*[126]. The strong dependency of TNBC cell lines on glutamine is more obvious when GLS knockdown has no effect on growth and metabolite levels in non-TNBC cell lines including MCF-7 cells[126]. In parallel with this study, my finding demonstrated that the basal expressions of GLS1 isoforms (KGA and GAC) in both metastatic clones of basal MDA231were higher than luminal MCF-7 cells, implying that a stronger glutamine dependency in BC cells derived from basal cell lineage (Figure 3.1). Although KGA basal expression level in basal MDA231-BR cells was lower than basal MDA231-LG cells, it is still unclear whether it is associated with lower glutaminase activity in MDA231-BR cells (Figure 3.1). A previous study has reported that both KGA and GAC protein levels were higher in breast tumor tissues as compared to normal counterpart and the similar pattern was detected in tumors of higher grade as compared to lower grade[148]. GAC isoform was reported as the key glutaminase isozyme in the tumors due to several findings that shown the elevation of GAC mRNA level in various types of cancers including BC cell lines, gliomas and colorectal cancers as compared to normal counterparts[43,149,150]. Furthermore, it was been reported that c-MYC upregulated GAC expression in prostate tumor tissues as compared to normal counterparts[48].

My study demonstrated that the dependency of BC cell lines towards extracellular level of glutamine can be reflected by the phosphorylation status of mTORC1 target proteins, 4E-BP1 and S6 (Figure 3.2). In general, the canonical function of 4E-BP1 and S6 is to regulate the translation of various ribosome biogenesis genes. Glutamine deprivation partially affected mTORC1 signaling in MCF-7 cells through inhibition of 4E-BP1 activity marked by downshift of γ-band without affecting the phosphorylation level of S6, further supporting the previous findings that this cell line was more tolerant to glutamine deprivation. As phosphorylation of S6 was not affected by glutamine deprivation, mRNA translation of ribosome biogenesis genes in MCF-7 cells could be active despite the

absence of exogenous glutamine. As expected, both clones of MDA231 cells were more affected by this treatment as marked by suppressions of phosphorylation of S6 and total 4E-BP1.

As phosphorylation of ERK was significantly increased in MCF-7 cells and the similar increasing pattern of ERK phosphorylation was observed in both metastatic clones of MDA231 cells in response to glutamine deprivation, it is important to investigate the mechanism of compensatory ERK overactivation in this context. There are three proposed mechanisms that induce the compensatory overactivation of ERK in response to mTORC1 inhibition, namely:

1. Based on a study with BC harboring PI3KCA mutant or HER2 amplification without RAS mutations highlighting PI3K mediating overactivation of ERK[151]. This result showed that PIP_3 accumulation produced by PI3K activity upregulated the activity of RAC1 (RAC1-GTP) via PIP_3-dependent RAC exchanger 1 (P-REX1) and of its effector PAK1 contributing to phosphorylation of RAF1 at the activating serine 338 residue.

2. PIP_3-independent ERK is involved. This process involves the recruitment of adaptor growth factor receptor-binding protein 2 (GRB2)-associated binder 1 (GAB1), which subsequently recruits GRB2-SOS, leading to the activation of RAS/RAF[152].

3. Through the expression of PDGF receptor (PDGFR), another target for mTORC1 negative feedback loop. A study reported that PDGFR expression was suppressed in response to activation of PI3K/AKT or PTEN deletion in mouse embryonic fibroblast cells, however, the suppression was relieved when the cells treated with rapamycin[152]. Another study reported that in hepatocellular

carcinoma cells, ERK overactivation in response to rapamycin was mediated by increase in expression and phosphorylation of PDGFRβ[153].

3.3.2 Intercellular glutamine symbiosis

In a co-culture transwell system, the investigation of glutamine symbiosis between luminal and basal BC cell lines has demonstrated that glutamine-independent luminal BC cells which expressed higher basal level of GS increased the viability of glutamine-dependent BC cells by increasing intracellular glutamine pool[53]. Recently, another study evidenced the heterogeneity in the expression of GS among glioblastoma cells within the same tumor. This cellular circumstance allowed GS-positive glioblastoma cells and astrocytes to provide glutamine to GS-deficient glioblastoma for de novo nucleotide synthesis[154].

Metabolic interdependency between different type of cells within tumor could be potentially mediated by the cancer cell secretome. The complement of macromolecules secreted from cells is termed as secretome. Analysis of cell secretome has been regarded as an important source of information to understand the hallmarks of cancer including uncontrolled proliferation, metabolic reprogramming, therapeutic resistance, invasion, evading apoptosis and metastasis[155]. As such, cancer cell secretomes are a valuable sources for biomarker discovery.

One of the components of cell secretome are EVs, a group of membrane-enclosed spherical particles mediating intercellular communication by transferring biological information between cells. EVs secreted by tumor cells transfer molecular cargos to neighbouring and distant cells, thus affecting the development, progression and metastasis.

In breast tissue, both luminal and basal cells are in a closed proximity. However, they have different sensitivity to the exogenous glutamine[53]. Although the glutamine symbiosis between luminal and basal BC cell lines has been previously studied, the roles of EVs in mediating this process has yet been investigated. In order to study EV-mediated glutamine symbiosis between luminal and basal types of breast cells, an appropriate and well- documented *in vitro* cell-culturing system which separated these two types of cell using cell culture inserts having a pore size of 1 μm was applied in my work. Although this system allowed the transfer of EVs from cells cultured in the insert to the recipient cells, other components of the cell secretome were still potentially transferred across the insert.

3.3.3 Extracellular vesicle-mediated intercellular glutamine symbiosis

Kung and colleagues have observed that the extracellular level of glutamine is higher in the glutamine-deprived media of MDA231 cells co-cultured with MCF-7 cells, indicating that the MCF-7 cell secretome may contained extracellular glutamine produced by GS in the MCF-7 cells[53]. This effect on the growth of MDA231 cells was recapitulated by growing them in the conditioned glutamine-deprived media from MCF-7 cells. In parallel with this finding, my study shown that the growth of MDA231-LG and MDA231-BR cells was significantly increased when co-cultured with MCF-7 cells in glutamine-deprived media (Figure 3.3 A and B). As the possible roles of EVs in transferring cargos in supporting the viability and growth of MDA231 cells in glutamine-deprived media was not highlighted in this article, this become the central focus of my work presented in this chapter.

Size exclusion liquid chromatography was the method of choice to isolate EVs in my experiments as this method has been shown to allow isolating high-yield and high-purity of EVs with intact biophysical and functional properties[156]. Chromatography profiles of EVs isolated from glutamine-deprived luminal MCF-7 and both clones of MDA231 cells

indicated that MCF-7 cells secreted a higher amount of EVs as compared to others (Figure 3.4 A), suggesting that luminal BC cells were more capable of secreting higher amount of EVs as compared to basal BC cells, in parallel with the amount of EV protein quantified by BCA assay (Figure 3.4 C). Glutamine deprivation did not markedly alter the mode size of EVs secreted by all tested cell lines, implying that the biogenesis of EVs with similar range of size remained unchanged, however this observation did not conclude that the compositions and functional properties of these EVs remained unchanged (Figure 3.4 B).

Based on BCA assay, I demonstrated that glutamine deprivation only affected the secretion of EVs from MCF-7 and MDA231-BR cells as reflected by an increase trend of EV concentration (Figure 3.4 C). It would be interesting to investigate the expression levels of ESCRT-III components such as ALIX, charged multivesicular body protein 4C (CHMP4C), vacuolar protein sorting-associated protein 4B (VPS4B) and vesicle trafficking 1 (VTA1) in in both WCL and EV as knockdown of these proteins has been shown to increase EV secretion[143].

Characterisation of protein compositions of EVs secreted by all three tested BC cell lines revealed that GS was significantly increased in EVs secreted by glutamine-deprived MCF-7 cells (Figure 3.4 D and E). EVs secreted by glutamine-deprived MCF-7 potentially supported the growth of both MDA231-BR cells and MDA231-LG cells by transferring of functionally active GS, in concert with other growth- promoting molecules in the EVs to the recipient cells, leading to increase in overall cell growth (Figure 3.5 A and B). The increase in GS level in EVs secreted by glutamine-deprived MCF-7 cells was also consistent with the level of GS in the WCL. Similar pattern of increase in GS protein level was also observed in both clones of MDA231 cells in response to glutamine deprivation. Upregulation of GS protein level in response to glutamine deprivation in BC

cell lines could serve as an adaptive response to compensate for the reduction of extracellular glutamine level.

TSG101 which is a component of ESCRT-0 plays an important role in the formation of MVB as a component of the endosomal sorting complex needed for machinery of protein transport[19,157]. Knockdown of ESCRT-0 components, TSG101 and HRS (hepatocyte growth factor-regulated tyrosine kinase substrate) has been demonstrated to reduce the exosome secretion[143]. In response to glutamine deprivation, my finding demonstrated that TSG101 level in both WCL EVs secreted from all tested glutamine-deprived BC cell lines was unchanged, implying that the formation of MVBs was unlikely to be affected (Figure 3.4 D and E).

Syntenin is one of the EV markers of interest in this study. It is a scaffolding-PDZ domain-containing protein involved in various biological processes such as syndecan binding and recycling, receptor clustering, signal transduction, protein trafficking and modulation of transcription factor Sox4 proteasomal degradation[158–163]. The role syndecan-syntenin pathway in regulating exosome biogenesis and vesicle cargo sorting has been recently appreciated. Through interaction of ESCRT-binding protein, Alix, syntenin-syndecan cargo is directed to the ESCRT machinery that control membrane budding and scission at the endosome[141]. Small GTPase ARF6, and lipid-modifying enzyme PLD2 are among syntenin-associated regulators that regulate the formation of ILVs[164].

Based on my finding, glutamine deprivation only significantly reduced the level of syntenin in MDA231-LG cells in WCL but remained unchanged in EVs (Figure 3.4 D and E). Another observation made in this experiment was the syntenin level in MCF-7 cells was undetectable in WCL but enriched in the secreted EVs. Although the actual reason behind this finding remains unknown, I reasoned that MDA231-LG cells probably sorted

majority of syntenin in the cells into EVs as a strategy for cell survival in response to glutamine deprivation because syntenin has been known to regulate various biological processes including cell migration, proliferation and cell cycle progression in cancer cells[165]. In EVs secreted by all tested BC cell lines, glutamine deprivation did not alter syntenin level, suggesting that the sorting of syntenin into EVs remained unperturbed.

My finding also demonstrated that basal expression of syntenin was also found to be below detectable limit in luminal MCF-7 cells as compared to both clones of basal MDA231 cells. Syntenin expression is associated with cell migration capacity[165]. MCF-7 cells have been shown to exhibit low migration capacity while MDA231 cells exhibit high mobility and invasiveness[166]. I postulated that the difference in syntenin level between luminal MCF-7 and both clones of basal MDA231 cells could be associated with their cell migration capacities, although this idea was not tested in my study.

Caveolin-1 is an oncogenic membrane protein that occupies flask-shaped plasma membrane invaginations termed as caveolae[167,168]. In the context of EV biology, a study reported that caveolin-1 negatively regulated endocytic uptake of exosomes, as caveolin-1 deficient MEF cells displayed increased level of exosome uptake as compared to wild type cells[169]. A recent study has demonstrated that caveolin-1 regulates exosome biogenesis and cargo sorting in a cholesterol-dependent manner[142]. Despite limited insights on the link between caveolin-1 expression and glutaminolysis, it has been proposed that the expression of caveolin-1 in tumor stromal compartment is inversely proportional to glutamine availability. This is evident in cancer-associated fibroblast cells cultured in high-glutamine media had decreased caveolin-1 expression and increased autophagy[170]. My finding demonstrated that the levels of caveolin-1 in WCL and EVs were not significantly altered, implying that this treatment did not elevate its expression in response to glutamine deprivation as previously reported and this could be due to cell-type specific response.

My finding demonstrated that caveolin-1 is deficient in luminal MCF-7 cells but enriched in both clones of basal MDA231 cells (Figure 3.4 D and E). Caveolin-1 functions as either tumor suppressor or oncogene, depending on the type of tumor and cellular context[171]. Caveolin-1 also serves as an important determinant for invasiveness and metastatic potential of tumor[172]. For example, in hepatocellular cancer (HCC) cell lines, caveolin-1 expression is undetectable in well-differentiated HCC cell lines but caveolin-1 is highly expressed in poorly differentiated HCC cell lines[173]. Similar explanation could be applied to different BC cell lines as luminal MCF-7 and MDA231 cells have been classified as well- and poorly differentiated BC cell, respectively[174].

3.3.4 Cell-lineage profile of EV surface markers

The MACSPlex system, a bead-based assay including 39 different antibody-coated multiplexed bead populations was recently employed to characterize the levels of EV surface markers between EVs derived from different types of blood cell using a conventional flow cytometry[175]. Based on the MACSPlex data presented as heatmap (Figure 3.6 A), the involvement of several EV surface markers of interest in the context of tumor angiogenesis and metastasis and the possible effect of glutamine deprivation are discussed in this section.

This included the detections of melanoma-associated chondroitin sulphate proteoglycan (MCSP) and cluster of differentiation (CD) 105 (CD105) which were highly detected in MDA231-BR EVs while CD146 was highly detected in both metastatic clones of MDA231 cells. Moreover, the receptor tyrosine kinase like orphan receptor 1 (ROR1) displayed a low expression in EVs secreted by BC cell lines in my study. Despite its low expression level, it is predominantly expressed in EVs secreted by MDA231-LG cells, in contrast to EVs secreted by MDA231-BR and MCF-7 cells.

MCSP is a highly glycosylated transmembrane protein-detected in TNBC primary lesions and also metastatic cancer stem cells from pleural effusions[176]. Although it is not exclusively expressed in basal-type of BC, its expression is generally associated with poor prognosis and recurrence in BCs[177]. CD105 is also known as endoglin, an accessory receptor for transforming growth factor beta (TGF-β) which is highly expressed in actively dividing endothelial cells[178–180]. Therefore, it has been suggested as a reliable marker for neovascularization and tumor-associated angiogenesis. CD146 is known as melanoma cell adhesion molecule which plays a prominent role in inducing epithelial-to-mesenchymal transition (EMT) in BC[181,182]. In BC, the expression of this molecule is associated with high grade tumors, estrogen receptor (ER)- and progesterone receptor (PR)-negative tumor and also subtypes of TNBC that are lacking ER, PR and the additional HER2[181,183,184]. Likewise, targeting ROR1 is essential as it is involvement in enhancing tumor growth, survival and metastasis by triggering EMT[185–188].

According to the MACSPlex data, deprivation of glutamine reduced the levels of MCSP, CD105, CD146 and ROR1 with various levels. As these proteins are involved in multiple processes including tumor angiogenesis, EMT activation and metastasis, downregulation of glutamine metabolism could mitigate the aggressiveness of BC cells and contributes to a better prognosis.

According to MACSPlex analysis, there were many surface markers that were relatively abundant and also affected by glutamine deprivation in MCF-7 EVs. CD14 and CD31 were among these proteins. CD14 is a glycosylphosphatidylinositol-anchored receptor expressed that plays crucial roles in bladder cancer cells in establishing the inflammatory and proliferative tumor microenvironment[189]. Thus, it is necessary to characterize the roles of CD14-expressing cancer cells in other types of solid tumors including breast cancer. As CD14 is abundant in EVs secreted from MCF-7 and not in

EVs secreted from both clones of MDA231 cells, this indicated that BC developed from luminal cells may employ similar strategy to establish inflammatory and proliferative tumor microenvironment through secretion of EVs enriched in CD14. As glutamine deprivation reduced CD14 level in MCF-7 EVs, this may indicate that targeting glutamine metabolism by blocking glutamine uptake or consumption could be essential in disrupting the establishment of inflammatory and proliferative tumor microenvironment.

CD31 is also known as platelet-endothelial cell adhesion molecule 1 serves as a robust marker for differentiation of endothelial cells in angiosarcoma[190]. A recent study has shown that a small population of $CD31^{low}$ cancer cells in human angiosarcoma that have lost their endothelial differentiation programs are more aggressive and resistant to oxidative stress and DNA damage through nuclear accumulation of YAP compared to $CD31^{high}$ population of cancer cells[191]. As glutamine deprivation reduced the level of CD31 in the EVs secreted by MCF-7 cells according to MACSPlex assay, it is therefore important to investigate whether these EVs could promote resistance in oxidative stress and DNA damage in the recipient cells.

Apart from CD14 and CD31, 3 tetraspanins including CD9, CD63 and CD81 were abundant in MCF-7 EVs and not in EVs both clones of MDA231 cells. The tetraspanin family is classified as a group of surface proteins containing 4 transmembrane domains[192]. Being as the membrane scaffold, tetraspanins activate downstream pathways by recruiting signaling molecules including integrins and cell-specific receptors[193]. There is an accumulating evidence that tetraspanins involve in tumor development and progression including growth, adhesion, invasion and metastases[194,195].

Validation of the MACSPlex data was performed by quantifying the levels of CD63 and CD81in EVs (Figure 3.6 B). My data demonstrated that glutamine deprivation selectively

reduced CD63 and CD81 levels in the WCL of MDA231-LG and MDA231-BR cells, implying a possible modulation of tetraspanins function by glutamine. However, this treatment did not markedly reduce the levels of these tetraspanin in EVs, indicating the loading of these proteins in EVs was unperturbed. In this assay, many capture bead populations were coated with antibodies against specific blood cell-related antigens leading to undetectable signals in EVs secreted by BC cell lines[196]. The absence of signal for a marker potentially implied that its abundance was under the detection threshold of the assay and did not necessarily indicate that it was not presented in the EVs. Although this data was generated from a single preliminary study, the changes of tetraspanins CD63 and CD81 expressions were reproducible and confirmed by immunoblotting.

3.4 Conclusion

In conclusion, this chapter highlighted that the characterization of protein composition and EV surface signature by immunoblotting and MACSPlex, in concert with cell growth analysis demonstrated that the changes in EV content and function modulated by glutamine deprivation are associated with cell type and metabolic status and other parameters of the EV-secreting cells.

Chapter 4.0. Modulation of EV protein composition and function by INK128

4.1 Introduction

This chapter discusses two main strands of research which include the characterization of the proteome landscape and function of EVs secreted by MDA231-LG and MDA231-BR cells and also in response to INK128, an anti-cancer drug currently tested in clinical trials acting as an ATP-competitive mTOR kinase inhibitor that blocks both mTORC1 and mTORC2 pathways. As this molecule is currently tested under clinical trials for metastatic TNBC patients in combination with other chemotherapeutic drugs (identifier number: NCT03193852), it would be important to elucidate the alteration of EV content and function upon inhibition of mTOR kinase by INK128 as EVs have been shown to be implicated in processes related to cancer cell survival.

The first strand of research presented in this chapter includes proteomic analysis of proteins in EVs secreted by both clones of MDA231 cells and also in response to INK128 treatment. The proteins that are differentially expressed are subjected to the gene ontology annotation enrichment analysis. The second strand of research presented in this chapter focusses on how these EVs might affect the site of metastasis by studying how EVs modulate the growth of the human brain microvascular endothelial cell line, HBEC-5i and also their biodistributions in the selected organs.

The objectives of study in this chapter are stated below:

1. Characterization of dose-dependent inhibition of mTORC1 by INK128 in both metastatic clones of MDA231 cells.

2. Proteomic analysis of the secreted EVs in response to INK128 and gene ontology annotation enrichment analysis of significant differentially expressed proteins in EVs.
3. Investigation on the EV function in modulating the growth of HBEC-5i cells in serum-free media.
4. Investigation on the in-vivo biodistribution of EVs secreted by both clones of MDA231 cells in response to INK128 treatment.

4.2 Result

4.2.1 Dose-dependent inhibition of mTORC1 by INK128

MDA231-LG and MDA231-BR cells were treated with INK128 in a dose-dependent manner ranging from 12.5 nM to 400 nM to determine the optimum concentration for proteomic studies of EVs (Figure 4.1). Immunoblotting analysis revealed a complete reduction of S6 phosphorylation and downshift of 4E-BP1 γ-band, indicating a complete inhibition of mTORC1 activity in MDA231-LG cells. In contrast, the inhibition of mTORC1 signaling in MDA231-BR cells was partial, as evident from incomplete suppression of S6 phosphorylation. There was, however, a marked downshift of 4E-BP1 γ-band. Taken together, MDA231-LG cells were more sensitive to INK128 inhibitor as compared to MDA231-BR cells. Inhibition of mTORC1 by INK128 also induced a compensatory upregulation of ERK phosphorylation in both cell lines. Based on this analysis a concentration of INK128, 25 nM was selected as the optimum concentration for the proteomic analysis of EVs secreted by both cell lines in response to this treatment. This concentration has been previously reported to markedly suppress mTORC1 activity in breast and colorectal cancer cell lines[197,198].

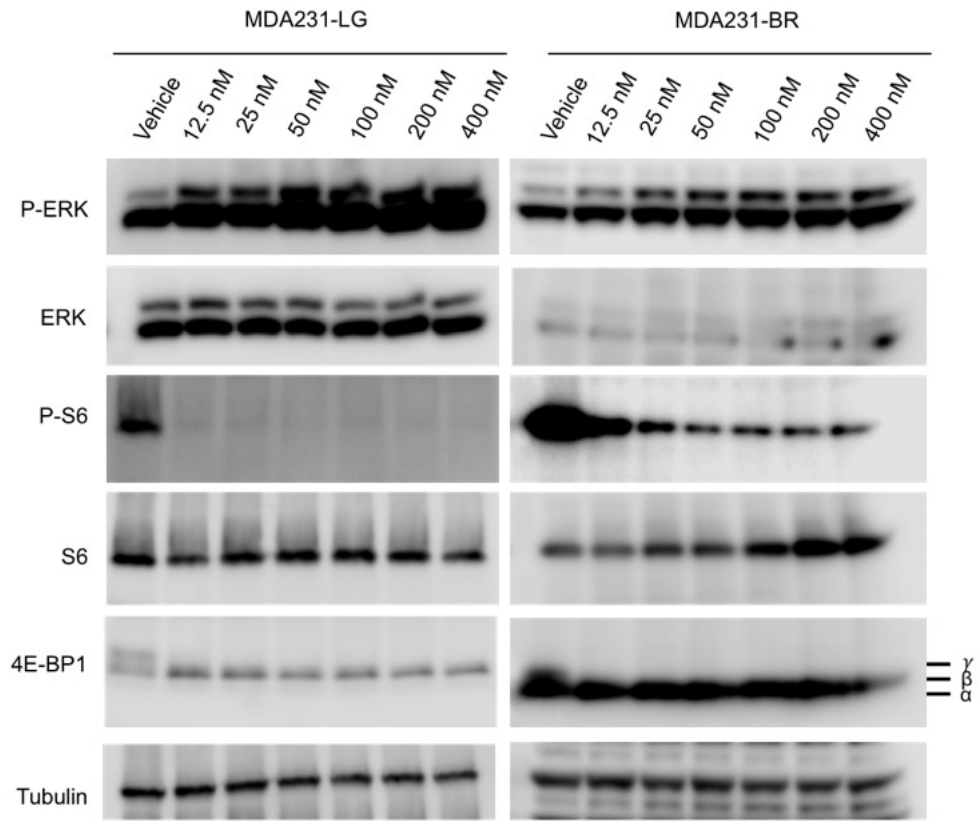
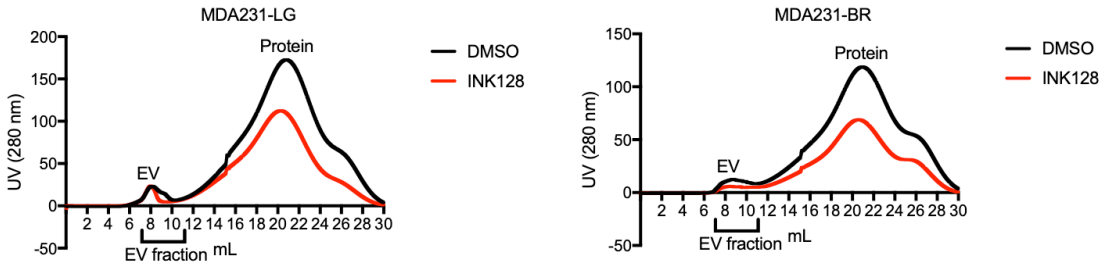


Figure 4.1. Dose-dependent inhibition of mTORC1 by INK128 in MDA231-LG and MDA231-BR cells. Reduction of S6 phosphorylation and downshift of 4E-BP1 γ-band indicates inhibition of mTORC1 activity. A compensatory upregulation of ERK phosphorylation is due to mTORC1 inhibition. 20 μg of protein was loaded in each well of the gel. Tubulin was used as the internal loading control. n=1.

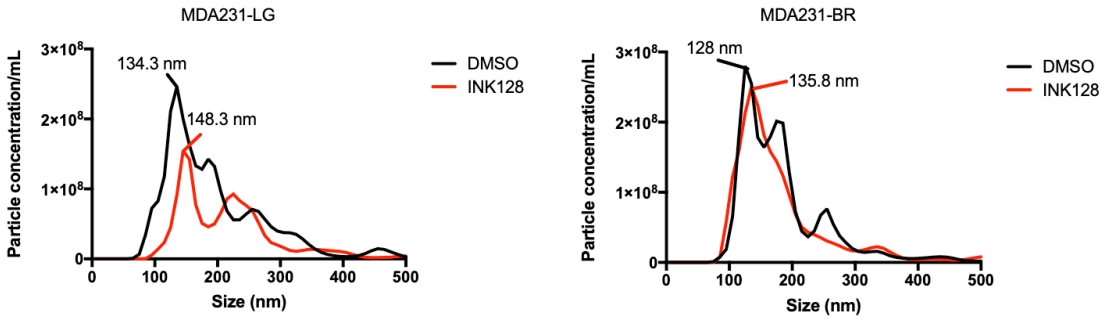
4.2.2 NTA analysis and EV quantification

For proteomic analysis, MDA231-LG and MDA231-BR cells were treated with 25 nM of INK128 or DMSO (control) for 48 hours and the EVs secreted by these cells were isolated by SEC and void volume fractions corresponding to EVs (7-11 mL) were pooled, concentrated and subjected to NTA analysis and protein quantification. According to chromatogram profile, INK128 treatment slightly reduced the amount of secreted EVs as shown by the UV 280 nm absorbance value (Figure 4.2 A). NTA analysis indicated that INK128 treatment did not alter the mode size of the secreted EVs (Figure 4.2.B). Quantification of EVs by BCA assay indicated that INK128 treatment significantly suppressed the amount of EVs secreted by MDA231-LG cells while the same treatment insignificantly promoted increase in EVs amount secreted by MDA231-BR cells (Figure 4.2 C).

A


MDA231-LG
Protein
EV
UV (280 nm)
200
150
100
50
0
-50
2 4 6 8 10 12 14 16 18 20 22 24 26 28 30
EV fraction mL
DMSO
INK128
MDA231-BR
Protein
EV
UV (280 nm)
150
100
50
0
-50
2 4 6 8 10 12 14 16 18 20 22 24 26 28 30
EV fraction mL
DMSO
INK128

B


MDA231-LG
134.3 nm
148.3 nm
Particle concentration/mL
3×10^8
2×10^8
1×10^8
0
0 100 200 300 400 500
Size (nm)
DMSO
INK128
MDA231-BR
128 nm
135.8 nm
Particle concentration/mL
3×10^8
2×10^8
1×10^8
0
0 100 200 300 400 500
Size (nm)
DMSO
INK128

C

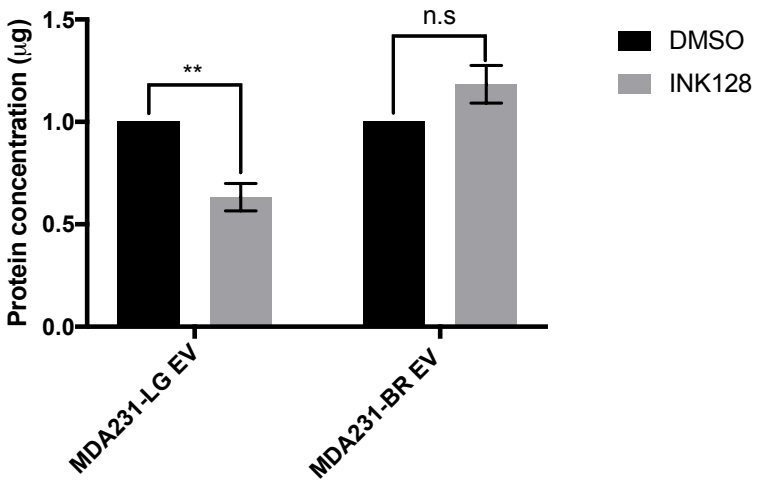

Protein concentration (μg)
1.5
1.0
0.5
0.0
**
n.s
DMSO
INK128
MDA231-LG EV
MDA231-BR EV

Figure 4.2. Chromatogram profile, size distribution and amount of secreted EVs in response to INK128. (A) Chromatogram profiles of EVs indicating a slight reduction of EV secretion measured by UV 280 nm absorbance. (B) A representative NTA graph of EVs shows the mode size of EVs remained unchanged in response to INK128 treatment. (C) INK128 treatment significantly reduced the amount of EVs secreted by MDA231-LG cells, while this treatment promoted insignificant increase in EVs secreted by MDA231-BR cells. Data are presented as mean ± SEM of three independent experiments, n=3. The statistical analysis was performed using Student t-test (two-tailed). **, $0.001 \leq P \leq 0.01$. n.s: not significant.

4.2.3 Data normalization and principal component analysis

The normalized transformed data (Figure 4.3) were subjected to principal component analysis (PCA) by Perseus software package in order to visualize the variability and the patterns of the entire data set. The majority of data variation (nearly 70%) was explained by the first three principal component PC1, PC2 and PC3 (Figure 4.4 A). The scatter plot of PCA 1 versus PCA 2 scores (Figure 4.4 B) shows the separation of proteins according to the origin of cell clones. However, the components that represented both treatments (DMSO versus INK128) for each cell line did not cluster separately, indicating the presence of experimental variability introduced by each biological repeat. In contrast, the scatter plot of PCA 1 versus PCA 3 scores (Figure 4.4 B) shows a better clustering of proteins according to treatments on the PC3 axis, indicating the treatment explains < 7% of the overall data variability. The coordinates of component that represent DMSO and INK128 treatments for each cell line are close, indicating INK128 treatment has altered the composition of proteins in the EVs to a certain extent.

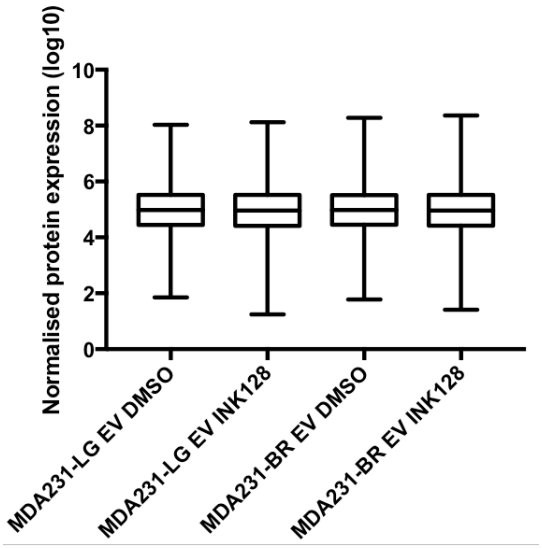
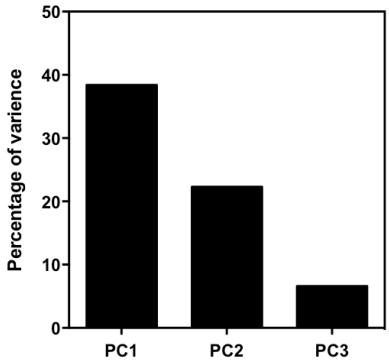


Figure 4.3. Box plots show the expression of proteins in each group is normalized to the median value and log-transformed for all four biological repeats. n=4.

A



B

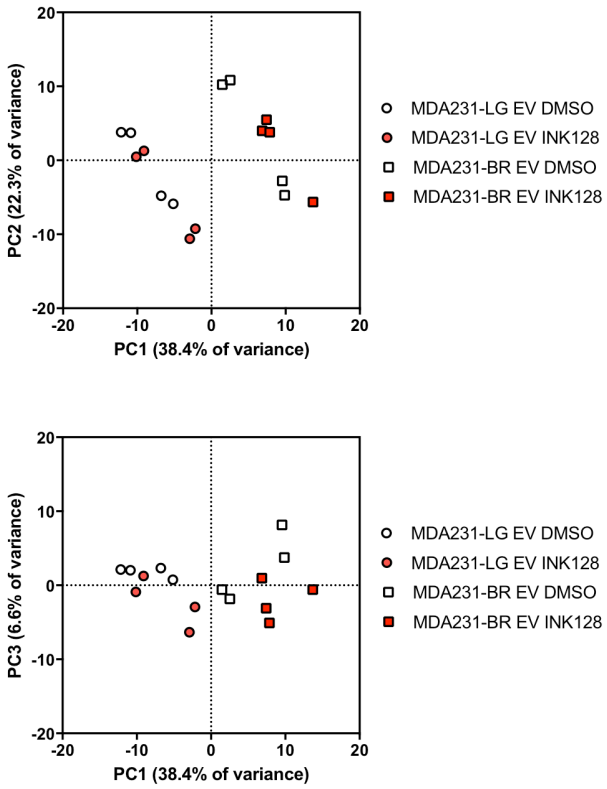
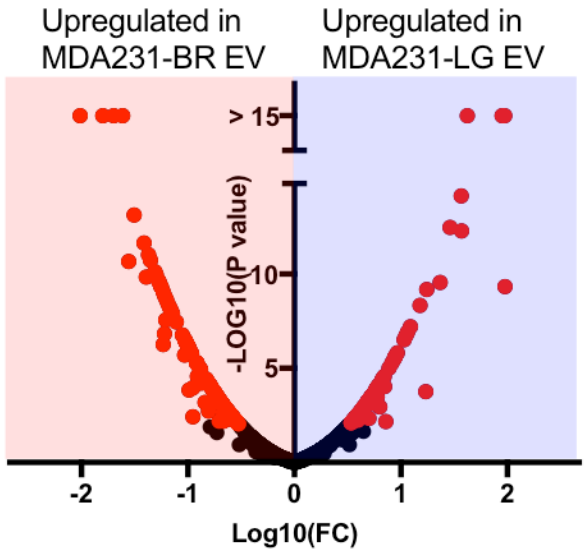


Figure 4.4. Principal component analysis of protein level in EVs secreted by INK128-treated MDA231-LG and MDA231-BR cells. (A) The percentage of variance for each principal component and (B) scatter plots of PC1 versus PC2 and PC1 versus PC3 that show the distribution of components of different cell clone derived EVs and treatments. n=4.

4.2.4 Comparative quantitation of proteins in EVs

The expressions of proteins in EVs secreted by MDA231-LG and MDA231-BR cell clones treated with DMSO (control group; n=4) was compared by conducting multiple t-tests (one for each protein) whilst correcting for multiple comparisons by using the false discovery rate (FDR) of 5%, as calculated by GraphPad Prism 7. The results of the analysis are presented on a volcano plot (Figure 4.5 A) and scatter plot (Figure 4.5 B). The volcano plot shows that 93 and 147 proteins were significantly upregulated in MDA231-LG EVs and MDA231-BR EVs, respectively, at a very low adjusted p-value, and that the change in protein expression was nearly 100-fold in some cases (Figure 4.5 A). The scatter plot suggests the majority of upregulated protein in MDA231-BR EVs had a relatively low expression level in MDA231-LG EVs. All statistically significant upregulated proteins are presented as a heatmap in order visualize the variability between individual biological replicates (Figure 4.6). The of log10 fold change (FC) difference and P-value of top 10 proteins significantly upregulated in EVs secreted by MDA231-LG and MDA231-BR cells are summarized in Table 4.1.

A



B

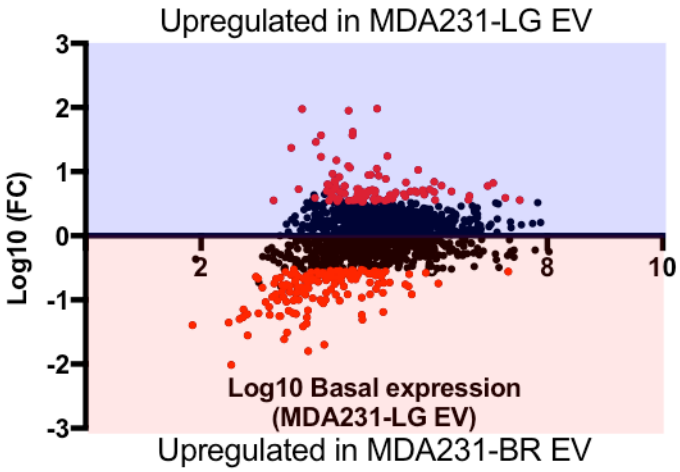
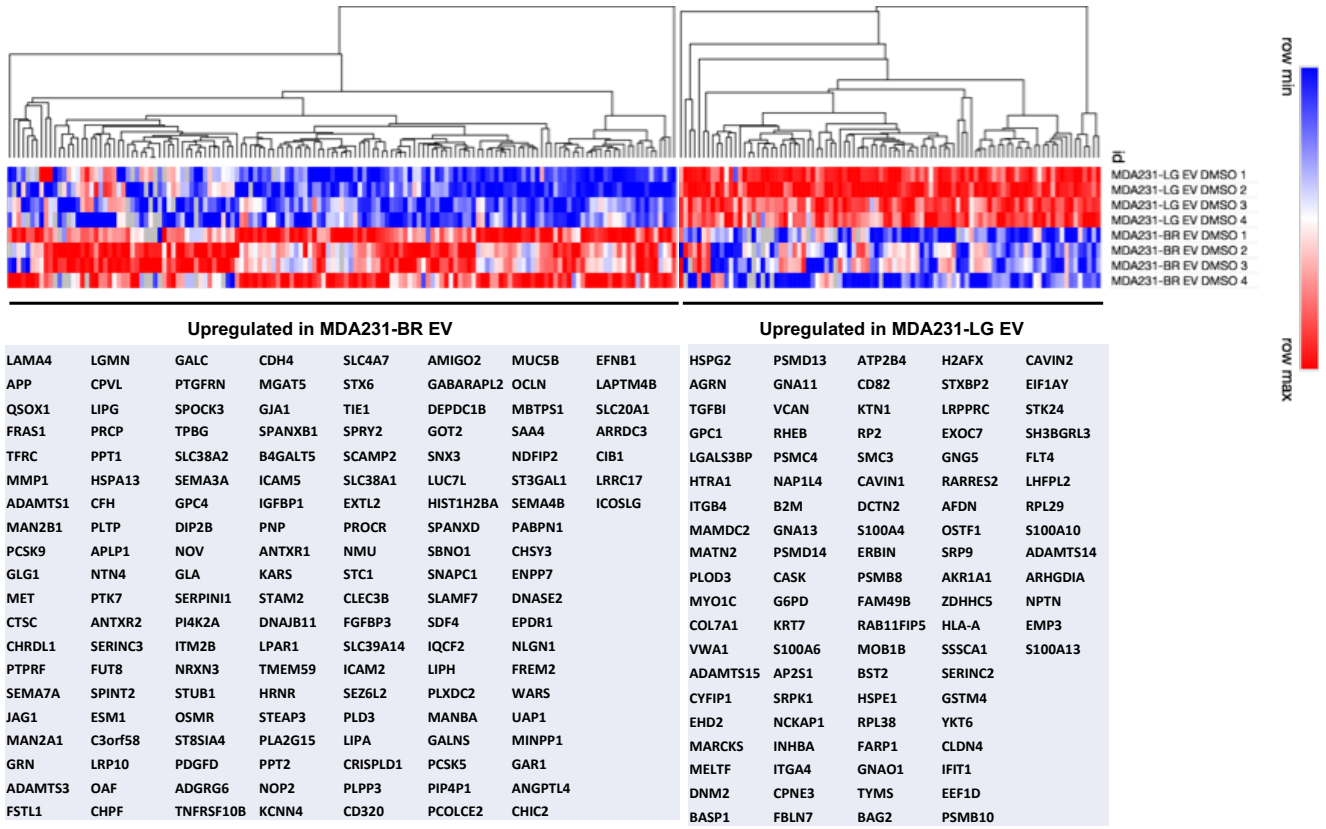


Figure 4.5. The upregulated proteins in EVs secreted by MDA231-LG and MDA231-BR cells. (A) A volcano and (B) scatter plots show significant upregulated proteins in MDA231-LG EV (purple box) and MDA231-BR EV (pink box). The red circles in the purple and pink boxes represent the significantly upregulated proteins in MDA231-LG EV and MDA231-BR EV respectively.



Upregulated in MDA231-BR EV

LAMA4	LGMN	GALC	CDH4	SLC4A7	AMIGO2	MUC5B	EFNB1
APP	CPVL	PTGFRN	MGAT5	STX6	GABARAPL2	OCLN	LAPTM4B
QSOX1	LIPG	SPOCK3	GJA1	TIE1	DEPDC1B	MBTPS1	SLC20A1
FRAS1	PRCP	TPBG	SPANXB1	SPRY2	GOT2	SAA4	ARRDC3
TFRC	PPT1	SLC38A2	B4GALT5	SCAMP2	SNX3	NDFIP2	CIB1
MMP1	HSPA13	SEMA3A	ICAM5	SLC38A1	LUC7L	ST3GAL1	LRRC17
ADAMTS1	CFH	GPC4	IGFBP1	EXTL2	HIST1H2BA	SEMA4B	ICOSLG
MAN2B1	PLTP	DIP2B	PNP	PROCR	SPANXD	PABPN1	
PCSK9	APLP1	NOV	ANTXR1	NMU	SBNO1	CHSY3	
GLG1	NTN4	GLA	KARS	STC1	SNAPC1	ENPP7	
MET	PTK7	SERPINI1	STAM2	CLEC3B	SLAMF7	DNASE2	
CTSC	ANTXR2	PI4K2A	DNAJB11	FGFBP3	SDF4	EPDR1	
CHRDL1	SERINC3	ITM2B	LPAR1	SLC39A14	IQCF2	NLGN1	
PTPRF	FUT8	NRXN3	TMEM59	ICAM2	LIPH	FREM2	
SEMA7A	SPINT2	STUB1	HRNR	SEZ6L2	PLXDC2	WARS	
JAG1	ESM1	OSMR	STEAP3	PLD3	MANBA	UAP1	
MAN2A1	C3orf58	ST8SIA4	PLA2G15	LIPA	GALNS	MINPP1	
GRN	LRP10	PDGFD	PPT2	CRISPLD1	PCSK5	GAR1	
ADAMTS3	OAF	ADGRG6	NOP2	PLPP3	PIP4P1	ANGPTL4	
FSTL1	CHPF	TNFRSF10B	KCNN4	CD320	PCOLCE2	CHIC2	

Upregulated in MDA231-LG EV

HSPG2	PSMD13	ATP2B4	H2AFX	CAVIN2
AGRN	GNA11	CD82	STXBP2	EIF1AY
TGFBI	VCAN	KTN1	LRPPRC	STK24
GPC1	RHEB	RP2	EXOC7	SH3BGRL3
LGALS3BP	PSMC4	SMC3	GNG5	FLT4
HTRA1	NAP1L4	CAVIN1	RARRES2	LHFPL2
ITGB4	B2M	DCTN2	AFDN	RPL29
MAMDC2	GNA13	S100A4	OSTF1	S100A10
MATN2	PSMD14	ERBIN	SRP9	ADAMTS14
PLOD3	CASK	PSMB8	AKR1A1	ARHGDIA
MYO1C	G6PD	FAM49B	ZDHHC5	NPTN
COL7A1	KRT7	RAB11FIP5	HLA-A	EMP3
VWA1	S100A6	MOB1B	SSSCA1	S100A13
ADAMTS15	AP2S1	BST2	SERINC2	
CYFIP1	SRPK1	HSPE1	GSTM4	
EHD2	NCKAP1	RPL38	YKT6	
MARCKS	INHBA	FARP1	CLDN4	
MELTF	ITGA4	GNAO1	IFIT1	
DNM2	CPNE3	TYMS	EEF1D	
BASP1	FBLN7	BAG2	PSMB10	

Figure 4.6. A heatmap showing hierarchical clustering of statistically significant upregulated proteins in EVs secreted by MDA231-LG and MDA231-BR cells. The details of protein description, log10 FC difference and P-value for each significantly upregulated in EVs secreted by MDA231-LG and MDA231-BR cells were summarized in Appendix A. n=4.

A

Upregulated protein in MDA231-LG EV	Description	Log 10 FC difference	P-value
S100A4	Protein S100-A4	1.98E+00	4.70E-10
TYMS	Thymidylate synthase	1.98E+00	<0.000000000000001
ADAMTS14	A disintegrin and metalloproteinase with thrombospondin motifs 14	1.95E+00	<0.000000000000001
KRT7	Keratin, type II cytoskeletal 7	1.62E+00	<0.000000000000001
EXOC7	Exocyst complex component 7	1.57E+00	5.07E-13
IFIT1	Interferon-induced protein with tetratricopeptide repeats 1	1.57E+00	7.00E-15
SRPK1	SRSF protein kinase 1	1.46E+00	3.38E-13
EIF1AY	Eukaryotic translation initiation factor 1A, Y-chromosomal	1.37E+00	2.83E-10
RPL29	60S ribosomal protein L29	1.24E+00	6.64E-10
GSTM4	Glutathione S-transferase Mu 4	1.23E+00	1.72E-04

B

Upregulated protein in MDA231-BR EV	Description	Log 10 FC difference	P-value
SLAMF7	SLAM family member 7	-2.01E+00	<0.000000000000001
ESM1	Endothelial cell-specific molecule 1	-1.80E+00	<0.000000000000001
JAG1	Protein jagged-1	-1.70E+00	<0.000000000000001
NRXN3	Neurexin-3	-1.61E+00	1.00E-15
EFNB1	Ephrin-B1	-1.55E+00	2.17E-11
CHPF	Chondroitin sulfate synthase 2	-1.51E+00	7.20E-14
PPT1	Palmitoyl-protein thioesterase 1	-1.41E+00	2.23E-12
GOT2	Aspartate aminotransferase, mitochondrial	-1.39E+00	1.45E-10
ICAM2	Intercellular adhesion molecule 2	-1.37E+00	9.53E-12
HRNR	Hornerin	-1.35E+00	1.84E-11

Table 4.1. The summary of log 10 FC difference and P-value of the top 10 proteins significantly upregulated in (A) MDA231-LG EVs and (B) MDA231-BR EVs. The positive and negative values of log 10 FC difference are derived from the subtraction of log 10 FC value of each protein from MDA231-LG EV with MDA231-BR EV. The positive value of log 10 FC difference denotes a higher median-normalized expression value of each protein in MDA231-LG EV as compared to MDA231-BR EV. The negative value of log 10 FC difference denotes a higher median-normalized expression value of each protein in MDA231-BR EV as compared to MDA231-LG EV.

4.2.5 Annotation enrichment analysis of EV proteins

Having identified individual proteins that were upregulated in EVs derived from MDA231-LG and MDA231-BR cell clones and to gain further insight, I analyzed whether these proteins were enriched in specific protein classes. The annotation overrepresentation enrichment analysis of EV proteins in cellular component, molecular function and biological process were performed using FunRich software (Table 4.2).

The upregulated proteins in MDA231-LG EVs were significantly enriched in cellular components including exosomes, lysosome, extracellular matrix, cytoplasm and proteasome complex. Similarly, certain proteins in EVs secreted from MDA231-BR cells were also significantly enriched in lysosome and exosomes, in addition to enrichments in extracellular region, Golgi apparatus and plasma membrane.

The molecular functions of upregulated proteins in EVs secreted by MDA231-LG cells were significantly enriched in extracellular matrix structural constituent and GTPase activity. In contrast, the upregulated proteins in MDA231-BR EVs were significantly involved in lipase activity and cell adhesion molecule activity.

The upregulated proteins in EVs secreted by MDA231-LG cells were significantly involved in biological process related to cell growth and/or maintenance. However, the upregulated proteins in MDA231-BR EVs were not significantly enriched in any specific biological process.

Even though the overrepresentation analysis above revealed a number of interesting differences between the proteins overexpressed in EVs of either the MDA231-LG and MDA231-BR cell clone, this analysis did not necessarily capture all important differences. Therefore, I next used the FunRich software to analyze the total number of

upregulated proteins in each annotation class (cellular component, molecular function and biological process) without performing the enrichment test compared to the whole human proteome (Figure 4.7).

I also analyzed the annotation of EV proteins based on specific biological process and cellular component ontologies (Figure 4.8). For the ontologies of cellular component of interest, this included multivesicular bodies, recycling endosome, plasma membrane raft, Golgi apparatus, cytosolic part and cell-cell junction. The biological process ontologies on interest included cell proliferation, cell adhesion, wound healing, integrin-mediated signaling pathway, metallopeptidase and amino acid transport.

The understanding of the upregulated EV proteins in MDA231-LG and MDA231-BR EVs based on the selected biological process and cellular components would allow further investigations on the possible functional properties of EVs through different activity assays such as cell growth, adhesion, wound healing and others in the future. The overrepresentation enrichment analysis as well as manual protein annotation analysis was only performed for significantly upregulated proteins in EVs secreted by both clones of MDA231 cells in the control condition (DMSO treatment) not for EV proteins significantly altered in response to INK128 treatment due to low number of significant differentially expressed proteins.

Sample ID	Cellular component	No. of protein	% of protein	FE	p-value	Proteins mapped (from input data set)
MDA231-LG EV	Exosomes	52	60.5	4.3	1.52E-20	**S100A4**, KRT7, CLDN4, MARCKS, RP2, AKR1A1, STXBP2, S100A6, HSPG2, ATP2B4, TGFBI, GPC1, RHEB, ITGA4, SH3BGRL3, CD82, SERINC2, PLOD3, DCTN2, PSMB8, VWA1, LRPPRC, HSPE1, HLA-A, EEF1D, B2M, CPNE3, S100A10, ITGB4, NAP1L4, BASP1, GNG5, BST2, HTRA1, G6PD, MYO1C, GNA13, STK24, AGRN, CYFIP1, FAM49B, GNA11, EHD2, ARHGDIA, SMC3, DNM2, LGALS3BP, MOB1B, LHFPL2, PSMD13, PSMC4, NCKAP1
	Lysosome	26	30.2	2.7	9.71E-04	EXOC7, RP2, AKR1A1, STXBP2, FARP1, ATP2B4, CD82, **YKT6**, DCTN2, AP2S1, CPNE3, PSMD14, ITGB4, BASP1, HTRA1, GNA13, CYFIP1, FAM49B, GNA11, EHD2, ARHGDIA, DNM2, LGALS3BP, KTN1, PSMC4, NCKAP1
	Extracellular matrix	7	8.1	9.9	5.34E-03	**MATN2**, HSPG2, TGFBI, VCAN, HTRA1, AGRN, LGALS3BP
	Cytoplasm	54	62.8	1.6	5.42E-03	S100A4, **TYMS**, KRT7, EXOC7, IFIT1, SRPK1, EIF1AY, RPL29, GSTM4, PSMB10, MARCKS, S100A13, AKR1A1, STXBP2, S100A6, ATP2B4, TGFBI, RHEB, SRP9, ITGA4, SH3BGRL3, CD82, GNAO1, YKT6, DCTN2, PSMB8, LRPPRC, EEF1D, B2M, CPNE3, FLT4, S100A10, OSTF1, PSMD14, NAP1L4, BASP1, G6PD, MYO1C, GNA13, STK24, CYFIP1, FAM49B, GNA11, EHD2, ARHGDIA, SMC3, DNM2, MOB1B, KTN1, CASK, PSMD13, RAB11FIP5, PSMC4, NCKAP1
	Proteasome complex	4	4.7	19.9	3.61E-02	**PSMB10, PSMB8**, PSMD14, PSMC4

Continued.

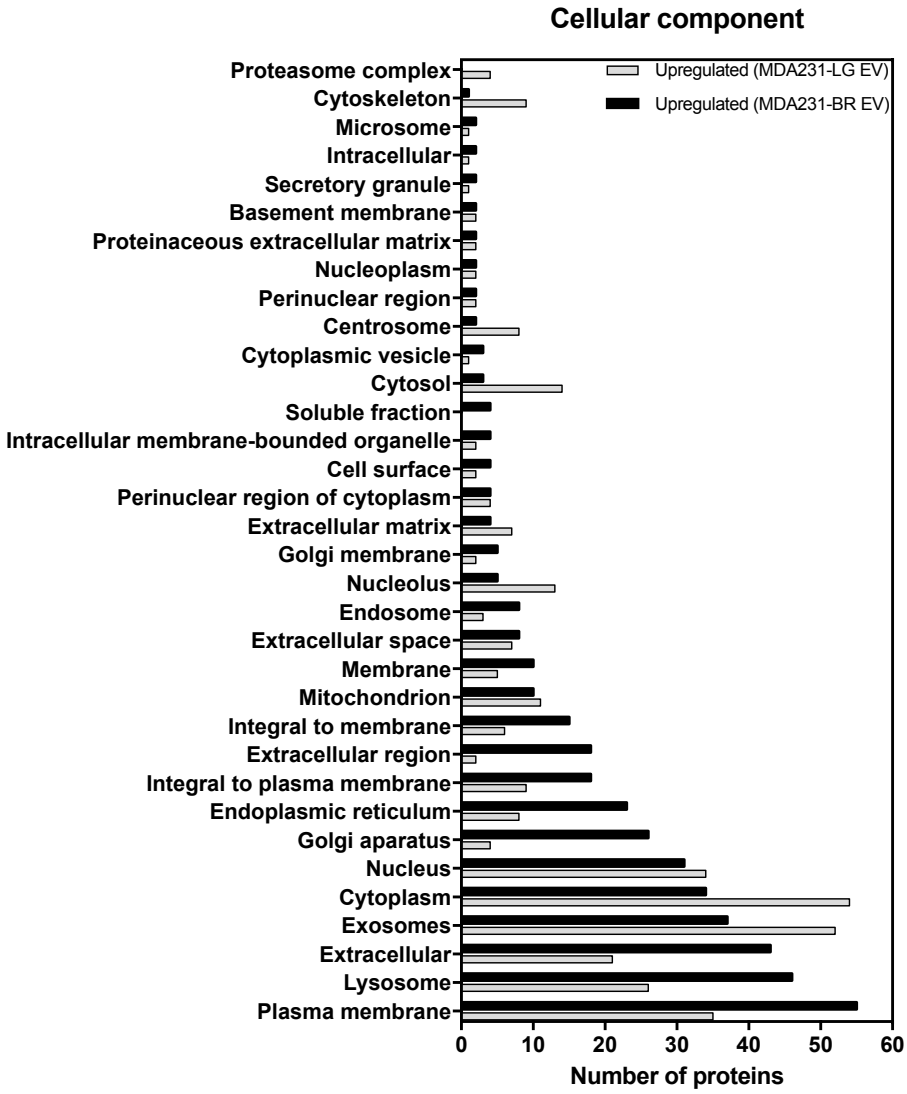
Sample ID	Cellular component	No. of protein	% of protein	FE	p-value	Proteins mapped (from input data set)
MDA231-BR EV	Lysosome	46	33.3	3.0	2.02E-09	PI4K2A, MAN2A1, LIPA, SERINC3, APP, SLC20A1, ITM2B, DIP2B, STEAP3, PLA2G15, **PROCR**, PRCP, TFRC, TPBG, DNASE2, MBTPS1, CFH, CPVL, GALNS, GLA, PTGFRN, KCNN4, LGMN, PTPRF, PNP, SCAMP2, STX6, GALC, SLC38A2, MAN2B1, SEMA7A, CIB1, MANBA, LAPTM4B, CTSC, PPT2, GLG1, ST3GAL1, PLD3, ANTXR2, SNX3, SPINT2, SPRY2, PCSK9, GOT2, PPT1,
	Extracellular	43	31.2	2.5	5.09E-06	CLEC3B, APLP1, APP, LIPH, **PDGFD**, FSTL1, STC1, ADAMTS3, PLA2G15, LIPG, TFRC, ANGPTL4, FRAS1, SPOCK3, NMU, CFH, CPVL, IGFBP1, EPDR1, PTPRF, STX6, GRN, QSOX1, SEMA7A, LAMA4, SAA4, PCOLCE2, MMP1, MGAT5, NTN4, MANBA, CTSC, ST8SIA4, PLTP, NOV, SNAPC1, SPINT2, SEMA3A, FREM2, CRISPLD1, ADAMTS1, PCSK9, ESM1,
	Extracellular region	18	13.0	4.3	1.52E-04	CLEC3B, APP, **PDGFD**, FSTL1, TFRC, ANGPTL4, GLA, SAA4, MMP1, PLTP, MUC5B, FGFBP3, SPINT2, SEMA3A, CHRDL1, PPT1, JAG1, ESM1,
	Golgi apparatus	26	18.8	3.1	2.15E-04	**PI4K2A**, MAN2A1, FUT8, APLP1, APP, C3orf58, MBTPS1, GLA, PTGFRN, NDFIP2, SCAMP2, STX6, QSOX1, MGAT5, LAPTM4B, B4GALT5, ST8SIA4, PLTP, GLG1, PLD3, GABARAPL2, ADAMTS1, PCSK5, CHIC2, ENPP7, PPT1,
	Plasma membrane	55	39.9	1.7	1.69E-02	KARS, APLP1, **MET**, SERINC3, APP, LIPH, SLC20A1, ITM2B, LPAR1, CDH4, PROCR, SLC39A14, TFRC, TPBG, ADGRG6, TNFRSF10B, PTGFRN, ICOSLG, SEMA4B, KCNN4, PTPRF, OSMR, SCAMP2, STX6, AMIGO2, SLC38A2, SEMA7A, LAMA4, PTK7, CIB1, SLC38A1, LAPTM4B, ST8SIA4, GLG1, SEZ6L2, LRP10, GJA1, SPINT2, GPC4, TIE1, NLGN1, CD320, ICAM5, CHIC2, ENPP7, SPRY2, SLC4A7, ANTXR1, HRNR, ICAM2, GOT2, EFNB1, NRXN3, JAG1, SLAMF7,
	Exosomes	37	26.8	1.9	4.34E-02	MAN2A1, **FUT8**, SDF4, WARS, APP, ITM2B, DIP2B, ADAMTS3, HSPA13, PRCP, TFRC, ANGPTL4, TPBG, CFH, CPVL, PTGFRN, HIST1H2BA, PTPRF, PNP, SCAMP2, QSOX1, TMEM59, LAMA4, CIB1, SLC38A1, CTSC, PLTP, GLG1, ST3GAL1, PLD3, SNX3, GPC4, CRISPLD1, PCSK9, HRNR, GOT2, EFNB1,

Continued.

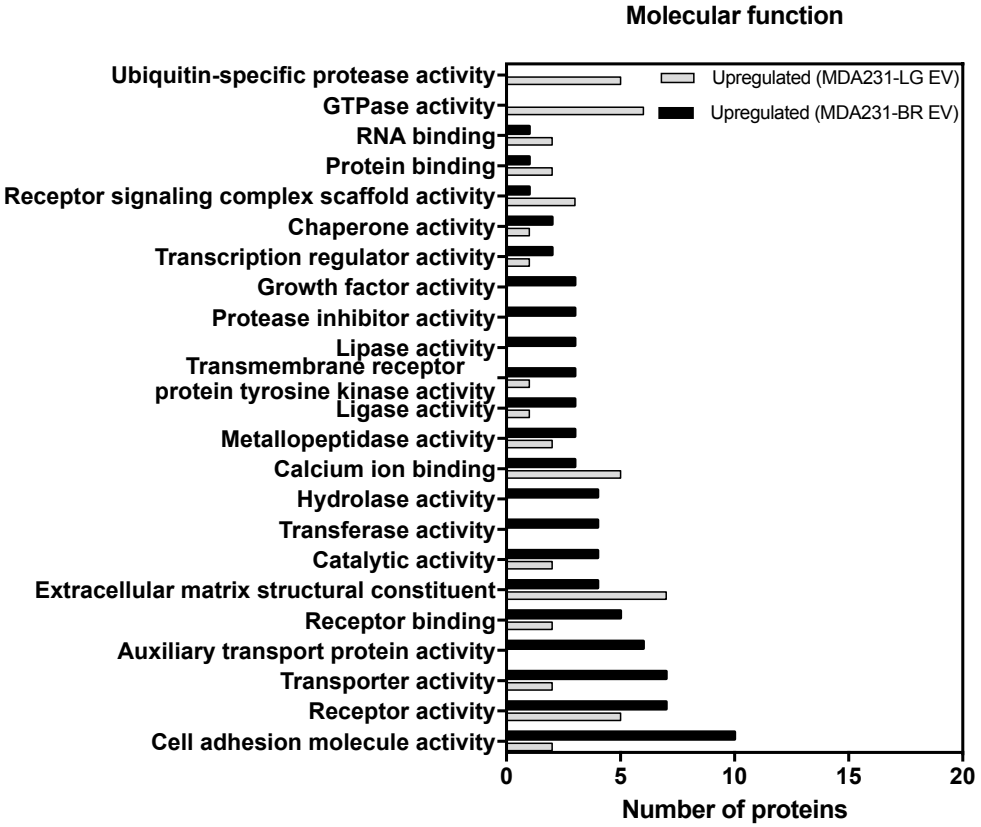
Sample ID	Molecular function	No. of protein	% of protein	FE	p-value	Proteins mapped (from input data set)
MDA231-LG EV	Extracellular matrix structural constituent	7	8.0	8.7	3.63E-03	**MATN2**; HSPG2; VCAN; VWA1; COL7A1; AGRN; LGALS3BP;
	GTPase activity	6	6.8	5.6	1.66E-01	RHEB; GNAO1; GNG5; **GNA13**; GNA11; DNM2;
MDA231-BR EV	Lipase activity	3	2.1	20.2	9.32E-02	LIPA; LIPH; **LIPG**;
	Cell adhesion molecule activity	10	7.0	3.6	1.13E-01	CDH4; IGFBP1; EPDR1; **AMIGO2**; LAMA4; NLGN1; ICAM5; ICAM2; NRXN3; ESM1;
Sample ID	**Biological process**	**No. of protein**	**% of protein**	**FE**	**p-value**	**Proteins mapped (from input data set)**
MDA231-LG EV	Cell growth and/or maintenance	16	18.2	2.9	1.62E-02	**S100A4**; KRT7; CLDN4; MARCKS; RP2; FARP1; MATN2; HSPG2; EMP3; VCAN; DCTN2; COL7A1; MYO1C; AGRN; ARHGDIA; KTN1;
MDA231-BR EV	n/a	n/a	n/a	n/a	n/a	n/a

Table 4.2. The overrepresentation enrichment analysis of proteins significantly upregulated in EVs secreted by MDA231-LG and MDA231-BR cells associated with cellular component, molecular function and biological process. The selected proteins (in bold) known to be involved in tumor progression are discussed in the Section 4.4.3.

A


Cellular component
Upregulated (MDA231-LG EV)
Upregulated (MDA231-BR EV)
Proteasome complex
Cytoskeleton
Microsome
Intracellular
Secretory granule
Basement membrane
Proteinaceous extracellular matrix
Nucleoplasm
Perinuclear region
Centrosome
Cytoplasmic vesicle
Cytosol
Soluble fraction
Intracellular membrane-bounded organelle
Cell surface
Perinuclear region of cytoplasm
Extracellular matrix
Golgi membrane
Nucleolus
Endosome
Extracellular space
Membrane
Mitochondrion
Integral to membrane
Extracellular region
Integral to plasma membrane
Endoplasmic reticulum
Golgi aparatus
Nucleus
Cytoplasm
Exosomes
Extracellular
Lysosome
Plasma membrane
0
10
20
30
40
50
60
Number of proteins

B



C

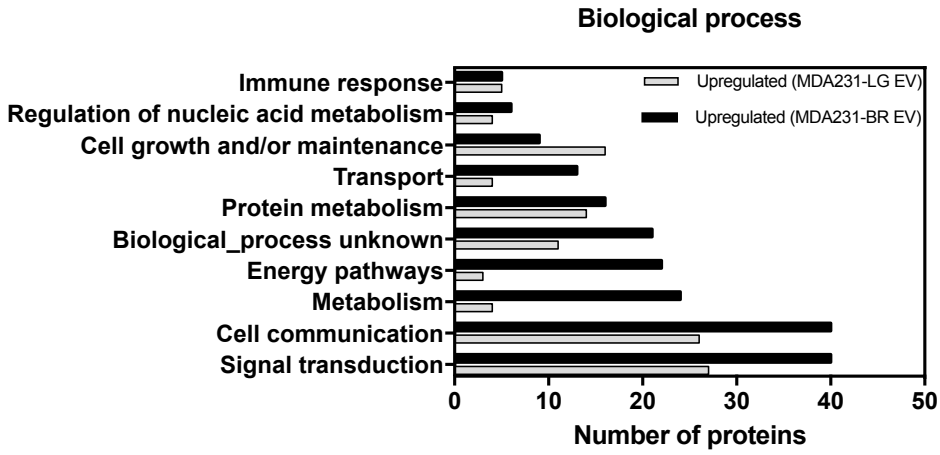
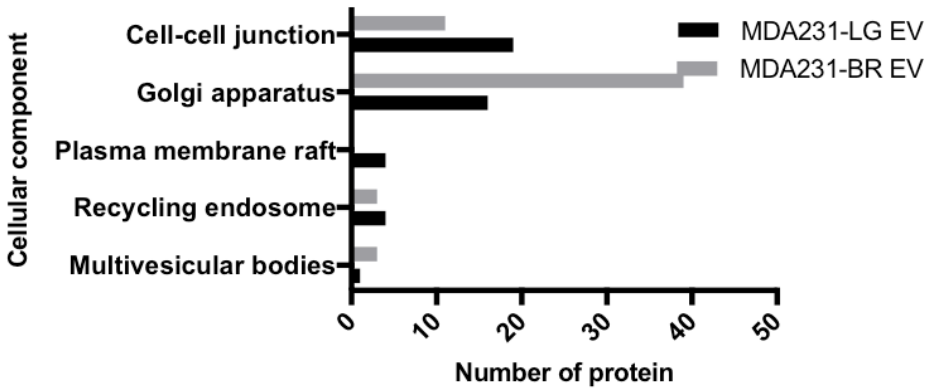


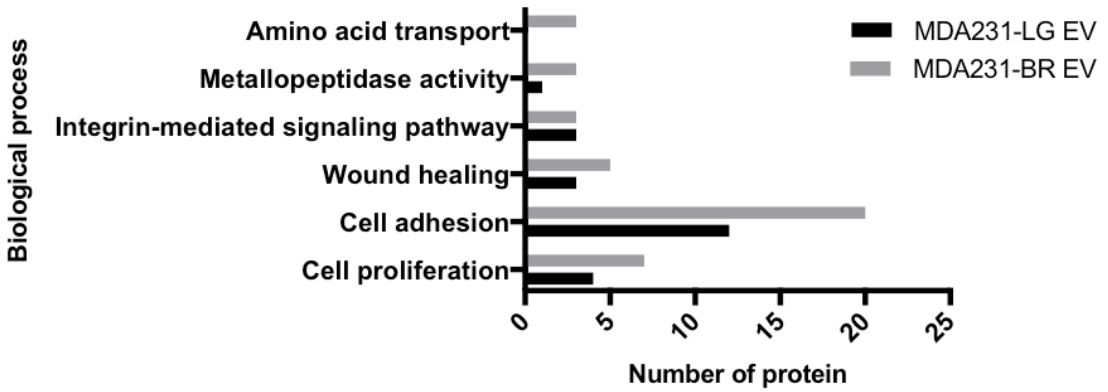
Figure 4.7. Annotation analysis of proteins in EVs secreted by MDA231-LG and MDA231-BR cells associated to (A) cellular component, (B) molecular function and (C) biological process using FunRich software.

A



MDA231-LG EV	MDA231-BR EV	MDA231-LG EV	MDA231-BR EV
Multivesicular bodies		**Recycling endosome**	
BST2	STEAP3	**EHD2**	APP
	NDFIP2	B2M	**TFRC**
	LAPTM4B	RAB11FIP5	SCAMP2
Golgi apparatus		HLA-A	
HSPG2	APP	**Plasma membrane raft**	
AGRN	QSOX1	**EHD2**	
TGFBI	PCSK9	ATP2B4	
GPC1	GLG1	CAVIN1	
PLOD3	CTSC	CAVIN2	
COL7A1	MAN2A1	**Cell-cell junction**	
DNM2	**LIPG**	HSPG2	APP
VCAN	PPT1	AGRN	JAG1
RHEB	SERINC3	**ITGB4**	PTK7
B2M	FUT8	CYFIP1	NOV
RP2	C3orf58	MARCKS	PI4K2A
RAB11FIP5	CHPF	DNM2	CDH4
BST2	PTGFRN	BASP1	GJA1
HLA-A	GPC4	B2M	**PROCR**
YKT6	GLA	GNA13	PLPP3
STK24	**PI4K2A**	CASK	OCLN
	ITM2B	NCKAP1	NLGN1
	ST8SIA4	ITGA4	
	PDGFD	CPNE3	
	MGAT5	FBLN7	
	GJA1	ERBIN	
	B4GALT5	RPL38	
	IGFBP1	FARP1	
	TMEM59	AFDN	
	STX6	CLDN4	
	SCAMP2		
	PLPP3		
	GABARAPL2		
	SDF4		
	PCSK5		
	MUC5B		
	MBTPS1		
	NDFIP2		
	ST3GAL1		
	CHSY3		
	ENPP7		
	NLGN1		
	CHIC2		
	CIB1		

B



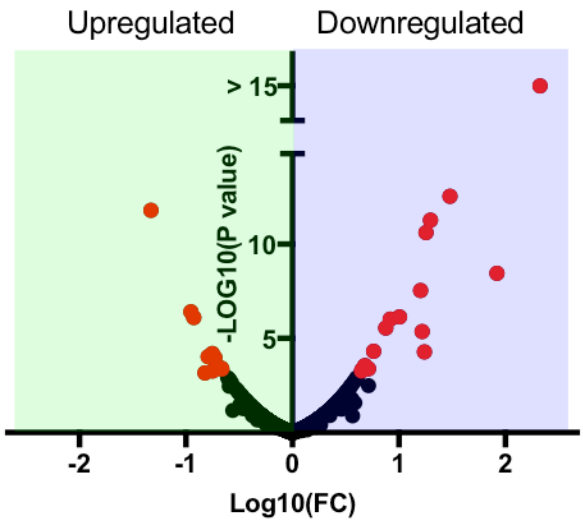
MDA231-LG EV	MDA231-BR EV	MDA231-LG EV	MDA231-BR EV
Cell proliferation		**Wound healing**	
TGFBI	**MET**	**EHD2**	PRCP
DCTN2	**LIPG**	GNA11	PTK7
BST2	C3orf58	GNA13	NOV
PSMB10	NOV		IGFBP1
	STC1		**PROCR**
	LIPA	**Integrin-mediated signaling pathway**	
	LRRC17	**ITGB4**	ADAMTS1
Cell adhesion		ITGA4	SEMA7A
TGFBI	LAMA4	ERBIN	**FUT8**
LGALS3BP	APP	**Metallopeptidase activity**	
ITGB4	PTPRF	**PSMD14**	**MMP1**
COL7A1	APLP1		ADAMTS1
VCAN	PTK7		ADAMTS3
CASK	TPBG	**Amino acid transport**	
ITGA4	NOV		SERINC3
FBLN7	NRXN3		SLC38A2
ERBIN	CDH4		**SLC38A1**
AFDN	ICAM5		
CLDN4	ANTXR1		
NPTN	ICAM2		
	PLPP3		
	AMIGO2		
	SLAMF7		
	EPDR1		
	NLGN1		
	FREM2		
	EFNB1		
	CIB1		

Figure 4.8. The ontologies of interest for (A) cellular component and (B) biological process with the details of proteins in EVs secreted by MDA231-LG and MDA231-BR cells are presented. The EV proteins highlighted in bold were discussed in Section 4.4.3.

4.2.6 Alteration of MDA231-LG EV proteome by mTOR kinase inhibitor INK128

Apart from comparative analysis of distinct proteins significantly upregulated in EVs secreted from MDA231-LG and MDA231-BR cells, the significant changes in protein composition of EVs secreted by MDA231-LG cells in response to INK128, a dual mTORC1/2 inhibitor was compared to EVs secreted by control cells. The significant upregulated (green) and downregulated (purple) proteins in EVs secreted from MDA231-LG cells in response to INK128 were shown in the volcano and scatter plots (Figure 4.9 A and B, red circles). The difference in log10 FC value of each EV protein between treatment groups (DMSO versus INK128) indicated that only 10 and 17 proteins were significantly upregulated and downregulated respectively. The significantly upregulated and downregulated proteins are shown in the heatmap in Figure 4.10. The log 10 FC difference and P-value of each protein were summarized in Table 4.3. As the number of EV proteins that was significantly altered in response to INK128 was low, I highlighted the involvement of these proteins in the context of cancer progression, based on findings reported in the literature (Table 4.4). Among these proteins, SBNO1, a highly conserved chromatin factor has yet been found to implicate in the development of any type of cancer or disease.

A



B

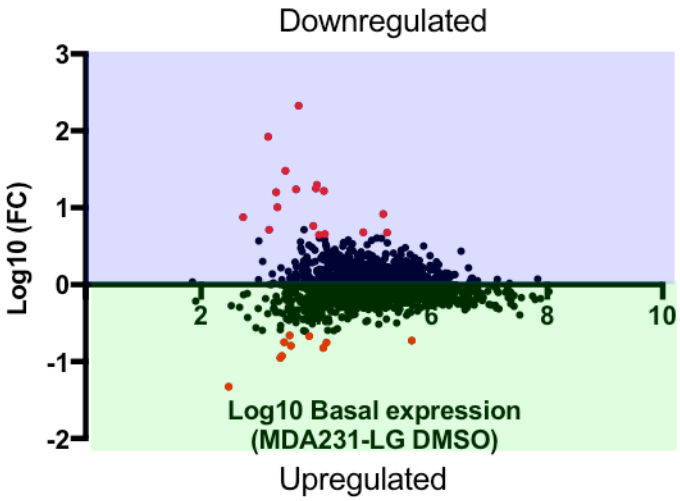


Figure 4.9. The upregulated and downregulated proteins in EVs secreted by INK128-treated MDA231-LG cells. (A) A volcano and (B) scatter plots show significant differentially expressed proteins in MDA231-LG EV in response to INK128 treatment. The red circles in the green and purple boxes represent the significantly upregulated and downregulated proteins, respectively.

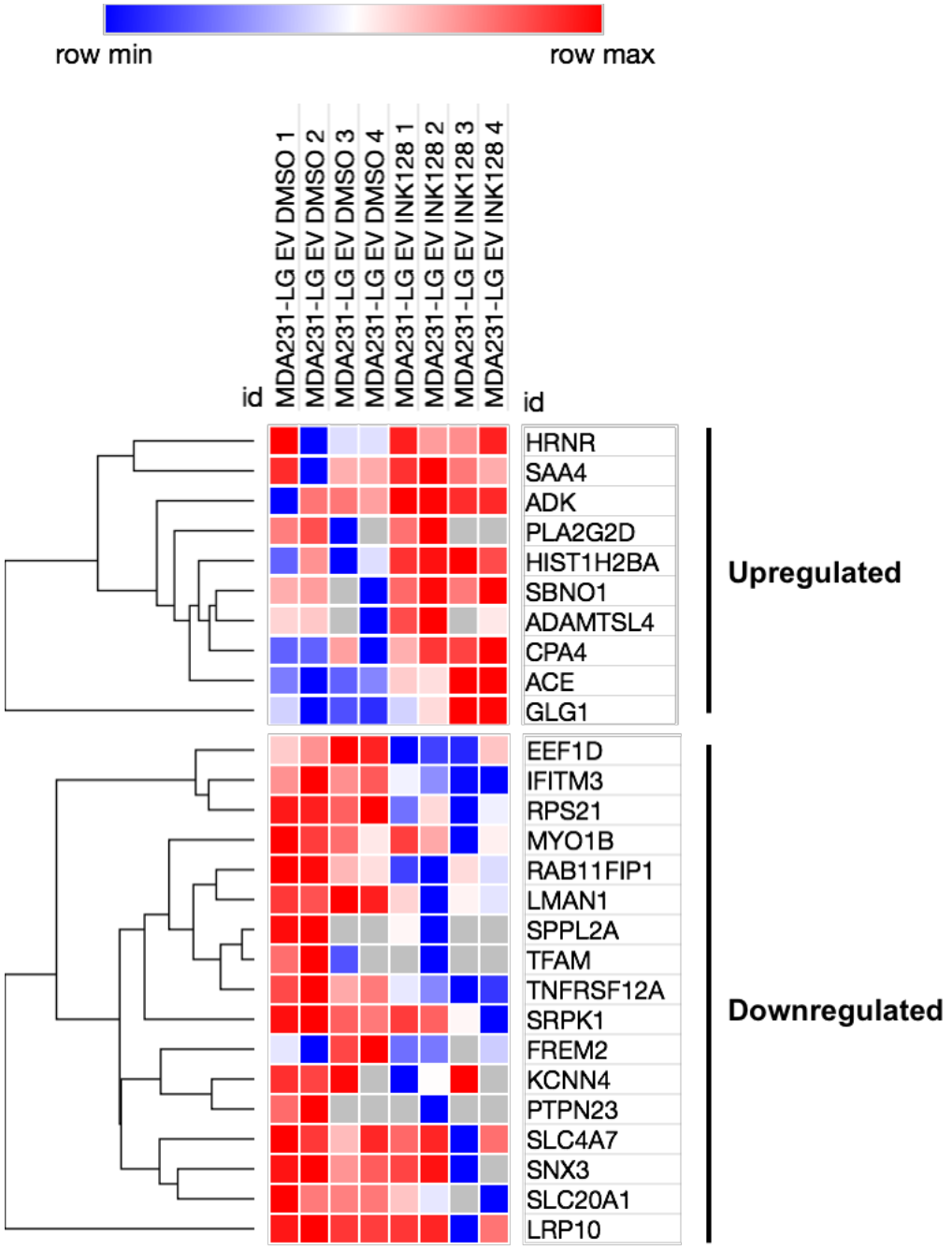


Figure 4.10. A hierarchical clustering of significantly upregulated and downregulated proteins in EVs secreted by MDA231-LG cells in response to INK128. n=4.

Upregulated protein	Description	Log 10 FC difference	P-value
HRNR	Hornerin	-1.33E+00	1.59E-12
HIST1H2BA	Histone H2B type 1-A	-9.52E-01	3.90E-07
SAA4	Serum amyloid A-4 protein	-9.27E-01	7.86E-07
PLA2G2D	Group IID secretory phospholipase A2	-8.22E-01	6.88E-04
SBNO1	Protein strawberry notch homolog 1	-7.92E-01	9.32E-05
ADK	Adenosine kinase	-7.51E-01	6.27E-05
ADAMTSL4	ADAMTS-like protein 4	-7.49E-01	5.46E-04
GLG1	Golgi apparatus protein 1	-7.28E-01	1.05E-04
ACE	Angiotensin-converting enzyme	-6.67E-01	3.74E-04
CPA4	Carboxypeptidase A4	-6.61E-01	4.28E-04
Downregulated protein	**Description**	**Log 10 FC difference**	**P-value**
RAB11FIP1	Rab11 family-interacting protein 1	6.50E-01	5.31E-04
LMAN1	Protein ERGIC-53	6.57E-01	4.63E-04
IFITM3	Interferon-induced transmembrane protein 3	6.76E-01	3.12E-04
EEF1D	Elongation factor 1-delta	6.81E-01	2.81E-04
FREM2	FRAS1-related extracellular matrix protein 2	7.15E-01	4.16E-04
MYO1B	Unconventional myosin-Ib	7.63E-01	4.76E-05
SLC4A7	Sodium bicarbonate cotransporter 3	8.78E-01	2.86E-06
RPS21	40S ribosomal protein S21	9.20E-01	9.36E-07

Continued.

Downregulated protein	Description	Log 10 FC difference	P-value
SNX3	Sorting nexin-3	1.00E+00	7.11E-07
KCNN4	Intermediate conductance calcium-activated potassium channel protein 4	1.20E+00	2.81E-08
SPPL2A	Signal peptide peptidase-like 2A	1.22E+00	4.38E-06
TFAM	Transcription factor A, mitochondrial	1.24E+00	5.25E-05
SRPK1	SRSF protein kinase 1	1.25E+00	2.41E-11
TNFRSF12A	Tumor necrosis factor receptor superfamily member 12A	1.30E+00	5.20E-12
SLC20A1	Sodium-dependent phosphate transporter 1	1.48E+00	2.90E-13
PTPN23	Tyrosine-protein phosphatase non-receptor type 23	1.92E+00	3.47E-09
LRP10	Low-density lipoprotein receptor-related protein 10	2.33E+00	<0.000000000000001

Table 4.3. The summary of log 10 FC difference and P-value of significantly upregulated and downregulated proteins in MDA231-LG EVs in response to INK128 treatment. The positive and negative values of log 10 FC difference are derived from the subtraction of log 10 FC value of each protein in the control (DMSO) group with drug treatment (INK128) group. The positive value of log 10 FC difference denotes a higher median-normalized expression value of each protein in the control (DMSO) group as compared to drug treatment (INK128) group. The negative value of log 10 FC difference denotes a higher median-normalized expression value of each protein in the drug treatment (INK128) group as compared to the control (DMSO) group.

Upregulated protein	Type of cancer or other disease	Implication in tumor progression or other disease
HRNR	Hepatocellular carcinoma	○ Overexpressed in human hepatocellular carcinoma tissues associated with poor prognosis[199]. ○ Promotes hepatocellular carcinoma progression through AKT pathway[199].
	Pancreatic ductal carcinoma	○ Highly expressed in pancreatic ductal carcinoma vascular endothelium and modulates tumor vascularity in VEGF-independent manner[200]. ○ Knockdown of HRNR suppressed tumor leakiness, growth and increased oxygenation and apoptosis[200].
HIST1H2BA	Lung cancer	○ HIST1H2BA is biomarker candidate uniquely identified in salivary EVs derived from patients with lung cancer as compared to normal counterparts[201].
SAA4	Oral squamous cell carcinoma	○ SAA4 expression is significantly upregulated in patients with oral squamous cell carcinoma[202].
PLA2G2D	Skin cancer	○ Deficiency of PLA2G2D suppresses skin tumorigenesis by boosting anti-tumor immunity.[203]
SBNO1	Unknown	○ The implication of SBNO1 in cancer or other disease is unknown. In spermatogonial stem cells, SBNO1 has been reported to modulate proliferation through WNT pathway[204].
ADK	Glioma	○ ADK expression is higher in peritumoral cortex of glioma patients with epilepsy than glioma patient without epilepsy[205].
	Primary effusion lymphoma	○ ADK is required for phosphorylation and activation of nucleoside analog 6-ethylthioinosine to induce ATP depletion and cell death in ADK-expressing primary effusion lymphoma cells.
ADAMTSL4	Nasopharyngeal carcinoma	○ The ADAMTSL4 level in serum is significantly lower in metastatic nasopharyngeal carcinoma than non-metastatic counterparts patients[206]. ○ It is proposed to function as tumor suppressor gene[206].
GLG1	Prostate cancer	○ Also known as E-selectin ligand-1. It is involved in the regulation of prostate cancer cell adhesion and metastasis[207].

Continued.

Upregulated protein	Type of cancer or other disease	Implication in tumor progression or other disease
ACE	Breast cancer	○ In population-based cohort study, the reduction of ACE activity is associated with low BC risk[208].
CPA4	Gastric cancer	○ Overexpression of CPA4 is detected in primary GC as compared to normal mucosa and its expression is correlated with unfavourable clinical outcome in GC patients. Its expression is also correlated with tumor size, stage and metastasis[209].
	Non-small-cell lung cancer	○ CPA4 mRNA level is elevated in patient tumor tissues as compared to normal lung tissue. Its expression is associated with poor prognosis and correlated with tumor size, stage, metastasis and plasma levels of VEGF and survivin[210].
Downregulated protein	**Tumor type**	**Implication in tumor development and growth**
RAB11FIP1	Breast cancer	○ It is also known as Ras-coupling protein. The overexpression of this protein in MCF10A, a normal mammary epithelial cells leads to the acquisition of malignant phenotypes including loss of contact inhibition, anchorage-independent growth and growth factor independence[211]. In mouse xenograft model, knockdown of RAB11FIP1 suppressed formation of tumor and metastasis[211].
LMAN1	Colorectal cancer	○ Inactivating mutation and aberrant expression of LMAN1, a protein that involves in the glycoprotein transport from ER to Golgi in colorectal cancer impairs the secretions of anti-angiogenic and growth-inhibiting proteins contributes to the development of microsatellite unstable (MSI-H) colorectal cancer[212].
IFITM3	Breast cancer	○ Invasive BC tissues display higher IFITM3 expression as compared to normal tissue[213]. ○ Knockdown of IFITM3 in BC cells reduces cell viability, growth and colony formation[213].

Continued.

Downregulated protein	Tumor type	Implication in tumor development and growth
EEF1D	Oral squamous cell carcinoma	○ EEF1D modulates cell proliferation via cyclin D 1 and knockdown of EEF1D induces EMT program[214].
FREM2	Glioblastoma	○ The mRNA and protein levels of FREM2 are higher in glioblastoma stem-like cell lines as compared to other glioblastoma cell lines and thus, serves as a putative biomarker for glioblastoma stem cells[215].
MYO1B	Head and neck squamous cell carcinoma	○ High MYO1B expression is detected in human tumor tissues as compared to normal counterparts and its expression in patients with tongue cancer is also correlated to lymph node metastases[216].
SLC4A7	Breast cancer	○ SLC4A7 mediates acid extrusion from BC tissue, sustains intracellular alkaline environment and contributes to aggressive tumor development.
SNX3	Epidermoid carcinoma	○ EGRF trafficking and degradation is regulated by SNX3 in epidermoid cancer treated with aspirin[217].
KCNN4	Non-small-cell lung cancer	○ Loss of KCNN4 promoter methylation and increase in expression are reported in aggressive lung cancer cells and correlated with poor prognosis in patients[218].
RPS21	Prostate cancer	○ In human prostate tissue array, the expression of RPS21 is higher in malignant tissue and may serve as a putative biomarker[219].
SPPL2A	Breast cancer	○ SPPL2A, also known as U3 small nucleolar ribonucleoprotein (IMP3), is a mRNA binding protein that modulate chemoresistance in breast cancer cells by regulating drug transporter ABCG2 expression. Silencing of IMP3 suppressed ABCG2 expression and restored sensitivity of cancer cells to doxorubicin and mitoxantrone[220].
SLC20A1	Breast cancer	○ Based on the mRNA expression and clinical information derived from cBioPortal for Cancer Genomics, SLC20A1 is identified as a prognostic biomarker for ER+ BC and high SLC20A1 expression is correlated to poor prognosis[221].
PTPN23	Breast cancer	○ PTPN23 functions as a tumor suppressor and knockdown of PTPN23 activates FYN kinase and enhances cell invasion[222,223].

Continued.

Downregulated protein	Tumor type	Implication in tumor development and growth
TNFRSF12A	Breast cancer	○ High expression of TNFRSF12A is linked to overexpression of metalloproteinase 9 which involves in remodeling of ECM and invasion[224].
LRP10	Various types of cancer	○ High LRP10 expression is associated with reduced survival in patients with hepatocellular carcinoma, lung adenocarcinoma and pancreatic adenocarcinoma[225].

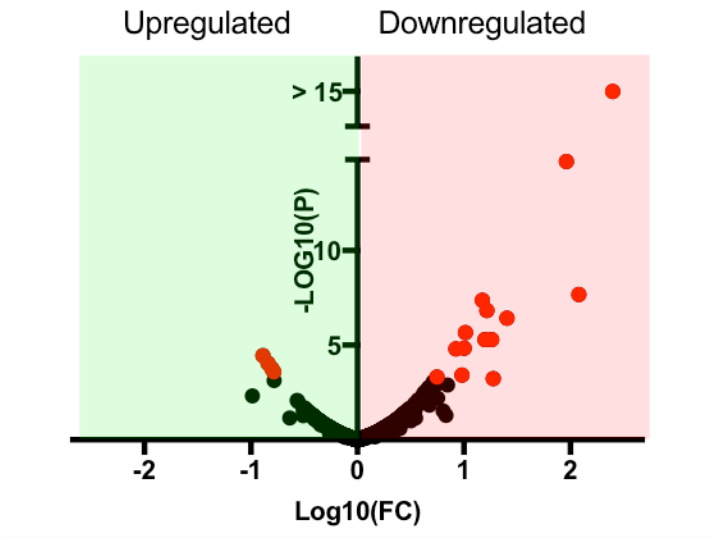
Table 4.4. The summary of the involvement of significantly upregulated and downregulated proteins in MDA231-LG EVs in response to INK128 treatment in tumor development and growth. The changes in the level of EV protein associated with enhanced in migration and EMT activation are marked in bold. The implication of SBNO1 in tumor biology is unknown.

4.2.7 Alteration of MDA231-BR EV proteome by mTOR kinase inhibitor INK128

Similarly, the changes in the protein composition of EVs secreted from INK128-treated MDA231-BR cells were also analyzed in comparison with EVs secreted by control cells. The significant upregulated (green) and downregulated (red) proteins in EVs secreted from MDA231-BR cells in response to INK128 were shown in the volcano and scatter plots (Figure 4.11 A and B, red circles). The difference in log10 FC value of each EV protein between treatment groups (DMSO versus INK128) demonstrated that only 4 and 14 proteins were significantly upregulated and downregulated, respectively. The significantly upregulated and downregulated proteins are shown in the heatmap in Figure 4.12. The log 10 FC difference and P-value of each protein were summarized in Table 4.5. Similar to EVs secreted by MDA231-LG cells, INK128 was also minimally altered the protein composition of EV secreted by MDA23-BR cells. I highlighted the involvement of these proteins in the context of cancer progression, based on findings reported in the literature (Table 4.6).

Taken together, INK128 minimally altered protein composition of EVs secreted by both metastatic clones of MDA231 cells. SRPK1, TFAM, MYO1B and PTPN23 were similarly downregulated in EVs secreted by both clones of MDA231 cells. Interestingly, HIST1H2BA was downregulated in MDA231-LG EVs but upregulated in MDA231-BR EVs. However, the role of this protein in normal physiological and pathological conditions especially in the development of cancer remains elusive as there was only one study reported that HIST1H2BA was uniquely identified in the EVs from saliva of lung cancer patients[201]. However, the involvement of this protein in tumor progression remains unexplored. In particular, the changes in expression of several proteins were association with EMT activation and enhanced in cell migration in response to INK128 treatment including: 1) downregulation of PTPN23 and EEF1D in MDA231-LG; 2) GALNS and EMP3 upregulations and downregulation of PTPN23 in MDA231-BR EVs.

A



B

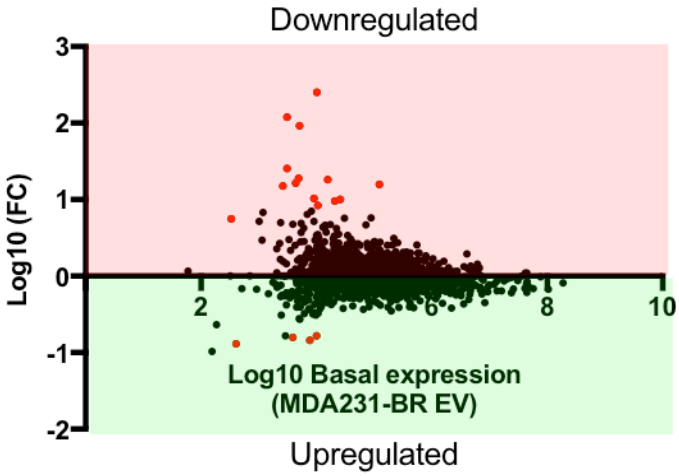


Figure 4.11. The upregulated and downregulated proteins in EVs secreted by INK128-treated MDA231-BR cells. (A) Volcano and (B) scatter plots show significant differentially expressed proteins in MDA231-BR EV in response to INK128 treatment. The red circles in the green and red boxes represent the significantly upregulated and downregulated proteins, respectively.

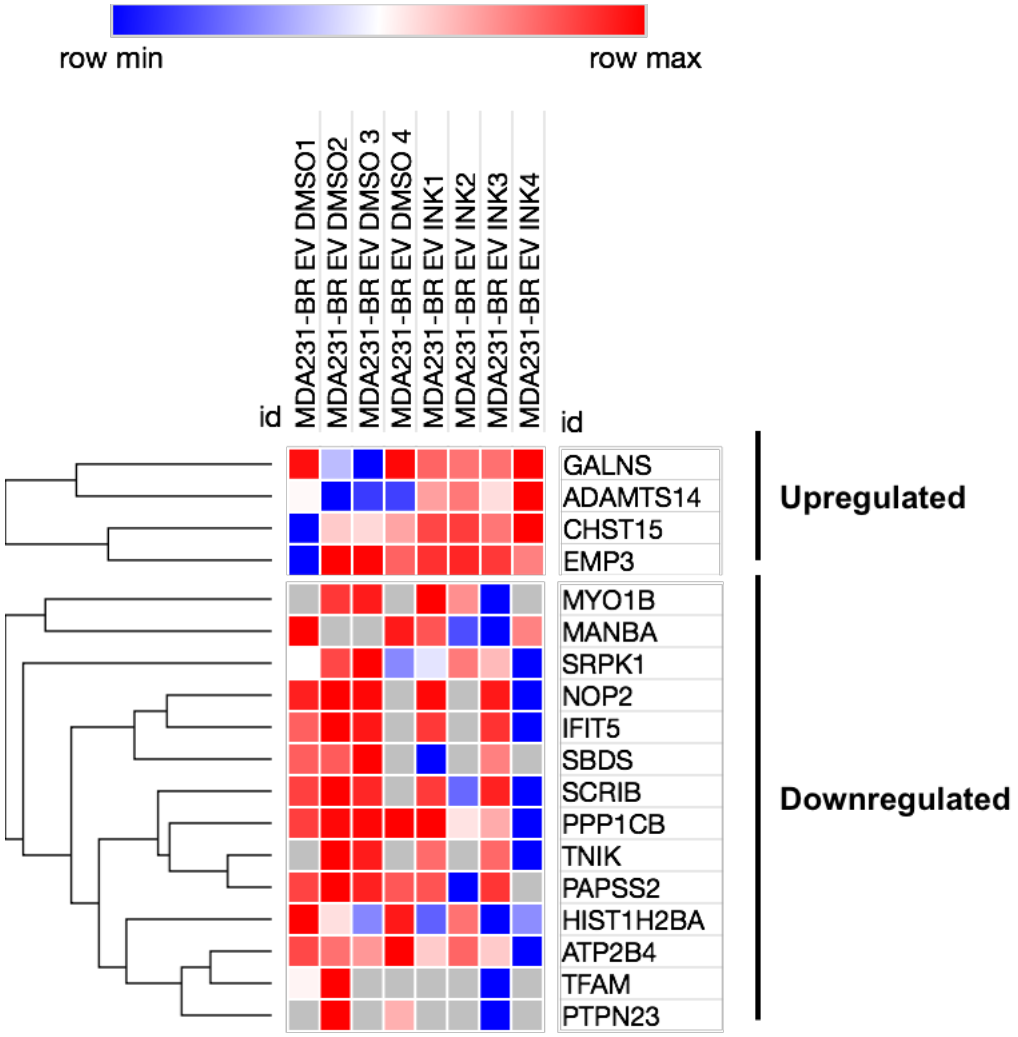


Figure 4.12. A hierarchical clustering of significantly upregulated and downregulated proteins in EVs secreted by MDA231-BR cells in response to INK128. n=4.

Upregulated protein	Description	Log 10 FC difference	P-value
ADAMTS14	A disintegrin and metalloproteinase with thrombospondin motifs 14	-8.86E-01	3.57E-05
CHST15	Carbohydrate sulfotransferase 15	-8.38E-01	9.15E-05
GALNS	N-acetylgalactosamine-6-sulfatase O	-8.04E-01	1.75E-04
EMP3	Epithelial membrane protein 3	-7.83E-01	2.56E-04
Downregulated protein	**Description**	**Log 10 FC difference**	**P-value**
SRPK1	SRSF protein kinase 1	7.47E-01	4.84E-04
HIST1H2BA	Histone H2B type 1-A	9.25E-01	1.58E-05
TNIK	TRAF2 and NCK-interacting protein kinase	9.83E-01	3.78E-04
PAPSS2	Bifunctional 3'-phosphoadenosine 5'-phosphosulfate synthase 2	1.00E+00	1.45E-05
PPP1CB	Serine/threonine-protein phosphatase PP1-beta catalytic subunit	1.01E+00	2.18E-06
ATP2B4	Plasma membrane calcium-transporting ATPase 4	1.17E+00	4.21E-08
MANBA	Beta-mannosidase	1.20E+00	5.12E-06
SCRIB	Protein scribble homolog	1.22E+00	1.48E-07
SBDS	Ribosome maturation protein SBDS	1.26E+00	5.01E-06
TFAM	Transcription factor A, mitochondrial	1.28E+00	5.79E-04
MYO1B	Unconventional myosin-Ib	1.41E+00	3.77E-07
IFIT5	Interferon-induced protein with tetratricopeptide repeats 5	1.96E+00	2.00E-15
PTPN23	Tyrosine-protein phosphatase non-receptor type 23	2.08E+00	2.13E-08
NOP2	Probable 28S rRNA (cytosine(4447)-C(5))-methyltransferase	2.40E+00	<0.000000000000001

Table 4.5. The details of log 10 FC difference and P-value of significantly upregulated and downregulated proteins in MDA231-BR EVs in response to INK128 treatment. The positive and negative values of log 10 FC difference are derived from the subtraction of log 10 FC value of each protein in the control (DMSO) group from drug treatment (INK128) group. The positive value of log 10 FC difference denotes a higher median-normalized expression value of each protein in the control (DMSO) group as compared to drug treatment (INK128) group. The negative value of log 10 FC difference denotes a higher median-normalized expression value of each protein in the drug treatment (INK128) group as compared to the control (DMSO) group.

Upregulated protein	Type of cancer or other disease	Implication in tumor progression or other disease
ADAMTS14	Hepatocellular carcinoma	○ Gene polymorphism of ADAMTS14 is associated with clinical stage and tumor size in patients with smoking behavior[226].
CHST15	Pancreatic ductal adenocarcinoma	○ The expression of CHST15 is highly expressed in human pancreatic ductal adenocarcinoma cell lines and knockdown of CHST15 suppresses cell proliferation and upregulates the expression of genes related to cell cycle inhibitor. Silencing of CHST15 also suppresses tumor growth in xenograft model[227].
GALNS	Prostate cancer	○ GALNS expression in higher in human prostate tumor tissues as compared to normal counterpart[228]. ○ Overexpression of GALNS in prostate stem cells activates WNT/β-catenin pathway, a pathway required for EMT program activation[228].
EMP3	Gastric cancer	○ In gastric cancer cells, EMP3 is the downstream target of TWIST 1/2 involved in reprogramming cells to undergo EMT and upregulation of EMT is associated with metastasis and indicates poor prognosis[229].
Downregulated protein	**Tumor type**	**Implication in tumor development and growth**
SRPK1	Prostate cancer	○ The expression of SRPK1 is higher is malignant tissues as compared to benign counterparts and its expression is correlated to disease stage and invasion[230].
HIST1H2BA	Lung cancer	○ HIST1H2BA is biomarker candidate uniquely identified in salivary EVs derived from patients with lung cancer as compared to normal counterparts[201].
TNIK	Colorectal cancer	○ Pharmacological inhibition of TNIK reduced stemness of colorectal cancer cells according to flow cytometry analysis that demonstrated a reduction of population of cells with high expression of CSC surface markers[231].
PAPSS2	Breast cancer	○ Knockdown of PAPSS2 in MDA-MB-231 cells leads to reduction lung metastasis incidences and micrometastatic nodules in nude mice[232].
PPP1CB	B-cell leukaemia	○ Silencing of PPP1CB in leukaemia cells contributed to increased cell proliferation and colony formation[233].

Continued.

Downregulated protein	Tumor type	Implication in tumor development and growth
ATP2B4	Colorectal cancer	○ In patients with rectum tumors, the expression of ATP2B4 was higher in tumor tissues as compared to normal counterparts. There was no significant difference in ATP2B4 expression in patients with colon and cecum tumors as compared to normal counterparts[234].
MANBA	Colorectal	○ Based on population cohort studies, gene polymorphism of MANBA was associated with colorectal cancer risk in Swedish population as opposed to Chinese population[235].
SCRIB	Liver cancer	○ Functioned as a tumor suppressor gene by suppressing the expression of YAP1, c-MYC and cyclin D1. SCRIB deficiency promotes tumor growth in vivo[236].
SBDS	Unknown	○ It is involved in Shwachman-Diamond syndrome development. ○ SBDS plays a role in telomere protection and deficiency or overexpressing of SBDS bearing disease-associated mutations contributes to telomere shortening[237].
TFAM	Non-small-cell lung cancer	○ Downregulation of TFAM in cancer cells leads to cell cycle arrest at G1 phase and suppresses growth and migration via the activation of reactive oxygen species (ROS)-induced c-Jun amino terminal kinase (JNK)/p38 MAPK signalling and reduces cellular bioenergetics[238].
MYO1B	Head and neck squamous cell carcinoma	○ High MYO1B expression is detected in human tumor tissues as compared to normal counterparts and its expression in patients with tongue cancer is also correlated to lymph node metastases[216].
IFIT5	Prostate cancer	○ Silencing of IFIT5 suppresses cell invasiveness induced by IFNγ, an inducer of EMT program in vitro and lung metastasis in vivo[239].
PTPN23	Breast cancer	○ PTPN23 functions as a tumor suppressor and knockdown of PTPN23 activates FYN kinase and enhances cell invasion[222,223].
NOP2	Lung cancer	○ Immunohistochemical staining of NOP2 in human lung cancer tissues of different histology types demonstrated NOP2 could serves as a marker for proliferation and it was suggested to play a pivotal function in tumor cell proliferation[240].

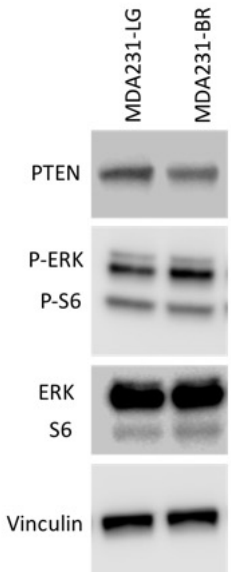
Table 4.6. The summary of the involvement of significantly upregulated and downregulated proteins in MDA231-BR EVs in response to INK128 treatment in tumor development and growth. The implication of SBDS in tumor biology is unknown. The changes in the levels of EV protein associated with enhanced in migration and EMT activation are marked in bold.

4.2.8 EV-mediated modulation of human brain endothelial cell growth

4.2.8.1 Basal expression of PTEN and phosphorylation level of S6 and ERK

In order to characterize the function of EV in modulating cell growth, I first compared the basal expression level of proteins involved in regulation of cell proliferation including ERK, PTEN and S6 in both clones of MDA231 cells (Figure 4.13). ERK was selected as a protein of interest based on a comparative analysis of proteome between MDA231-LG and MDA231-BR and this study demonstrated a significant activation of ERK in MDA231-BR cells[241]. The basal expression of PTEN and phosphorylation status of S6 were also investigated as a previous study has reported that approximately 60% of TNBC patients have low expression of PTEN, a negative regulator of PI3K proteins which control the activation of mTORC1[242]. This finding has contributed to an assumption that this cohort of patients may have higher proliferative capacity. In my study, I demonstrated that phosphorylation of ERK was not significantly increase in MDA231-BR cells as compared to MDA231-LG cells. However, PTEN expression level was significantly lower in MDA231-BR than MDA231-LG cells, suggesting that these cells potentially have higher proliferative capacity. Despite a lower basal expression of PTEN, the phosphorylation of S6 was not significantly increase in MDA231-BR cells as compared to MDA231-LG cells.

A



B

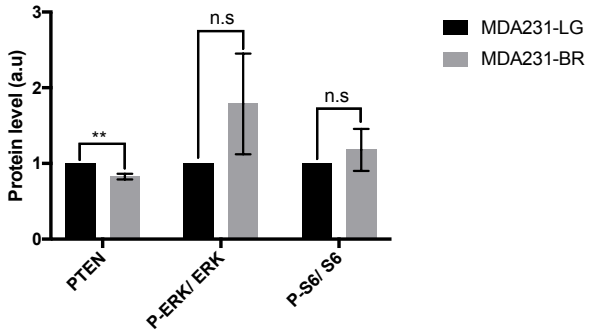


Figure 4.13. Analysis of basal PTEN expression and phosphorylation status of ERK and S6. (A) A comparative immunoblotting analysis and signal quantification (B) of basal expression of PTEN and phosphorylation levels of ERK and S6 between MDA231-LG and MDA231-BR cells. PTEN level is significantly lower in MDA231-BR cells as compared to MDA231-LG cells. The phosphorylation levels of ERK and S6 were insignificantly increased in MDA231-BR cells as compared to MDA231-LG cells. 20 μg of protein was loaded in each well of the gel. Vinculin was used as the internal loading control. Data are presented as mean ± SEM of 3 independent experiments, n=3. The statistical analysis was performed using Student t-test (two-tailed). **, $0.001 \leq P \leq 0.01$. n.s: not significant.

4.2.8.2 Modulation of HBEC-5i cell proliferation by EVs

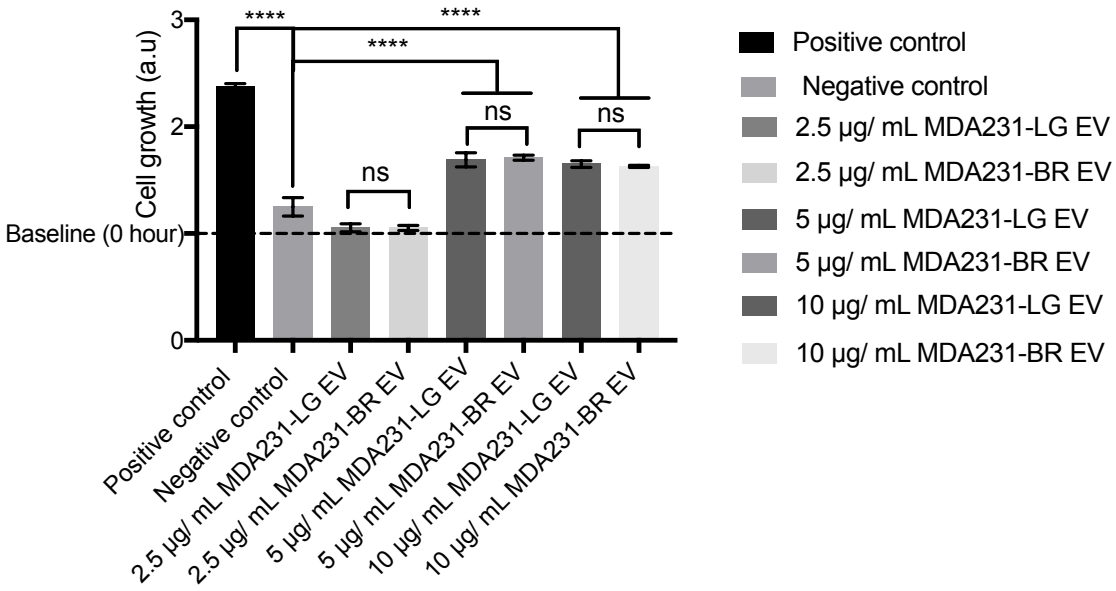
In the cell growth assay, human brain microvascular endothelial HBEC-5i cells were selected as the recipient cells. My aim was to identify selective changes contributed by EVs secreted by MDA231-BR cells. Three different concentrations of EVs (2.5 μg/ mL, 5 μg/ mL and 10 μg/ mL) were tested to detect the changes in HBEC-5i cell growth mediated by EVs secreted by both clones of MDA231 cells in serum-deprived media. In this experiment, the positive control group was a control group of HBEC-5i cells cultured in the growth media containing serum (10% FBS). In contrast, the negative control group was a control group of HBEC-5i cells cultured in the serum-deprived (0%) media.

The growth assay revealed that 5 μg/ mL and 10 μg/mL of EV significantly promoted increase in growth of the recipient cells (Figure 4.14 A). Subsequently, a concentration of 10 μg/mL of EVs secreted from either MDA231-LG EVs or MDA231-BR EVs was chosen to identify changes in the phosphorylation of S6 and ERK in the serum-starved recipient cells (Figure 4.14 B and C). Although statistically insignificant, the addition of EVs regardless of clone of origin, had a trend to promote increase in the phosphorylation of S6 level, implying an increase in cell growth. Likewise, the phosphorylation of ERK was increased indicating a compensatory action due to suppression of mTORC1 activity in the same growth condition. However, the addition of EVs did not significantly reduce the level of phosphorylated ERK back to basal level, suggesting that the addition of EVs increased the phosphorylation of S6 mildly, the downstream target of mTORC1 in the recipient cells.

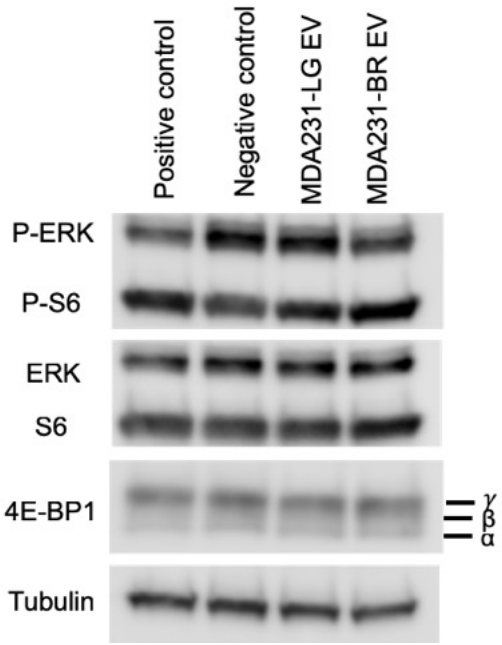
Furthermore, I have investigated whether EVs secreted from both clones of MDA231 cells treated with INK128 could differentially alter the growth of HBEC-5i cells in serum-starved media (Figure 4.14 D). My finding demonstrated that EVs secreted from both

clones of MDA231 cells treated with INK128 did not differentially altered recipient cell growth as compared to EVs from cells treated with DMSO.

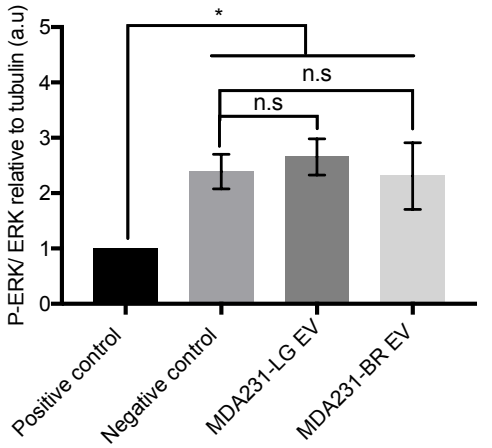
A

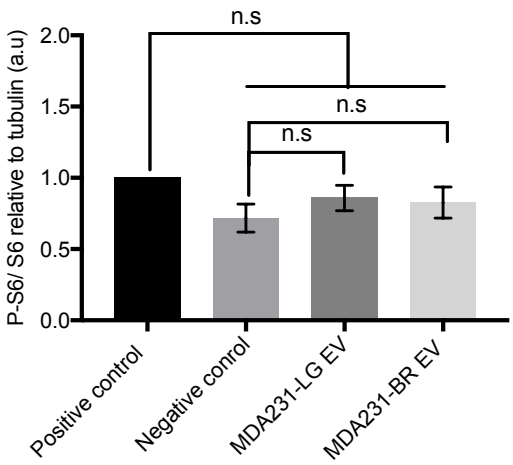

Cell growth (a.u)
3
2
0
Baseline (0 hour)
****
****
****
ns
ns
ns
Positive control
Negative control
2.5 µg/ mL MDA231-LG EV
2.5 µg/ mL MDA231-BR EV
5 µg/ mL MDA231-LG EV
5 µg/ mL MDA231-BR EV
10 µg/ mL MDA231-LG EV
10 µg/ mL MDA231-BR EV

B


Positive control
Negative control
MDA231-LG EV
MDA231-BR EV
P-ERK
P-S6
ERK
S6
4E-BP1
γ
β
α
Tubulin

C


P-ERK/ ERK relative to tubulin (a.u)
5
4
3
2
1
0
*
n.s
n.s
Positive control
Negative control
MDA231-LG EV
MDA231-BR EV


P-S6/ S6 relative to tubulin (a.u)
2.0
1.5
1.0
0.5
0.0
n.s
n.s
n.s
Positive control
Negative conrol
MDA231-LG EV
MDA231-BR EV

D

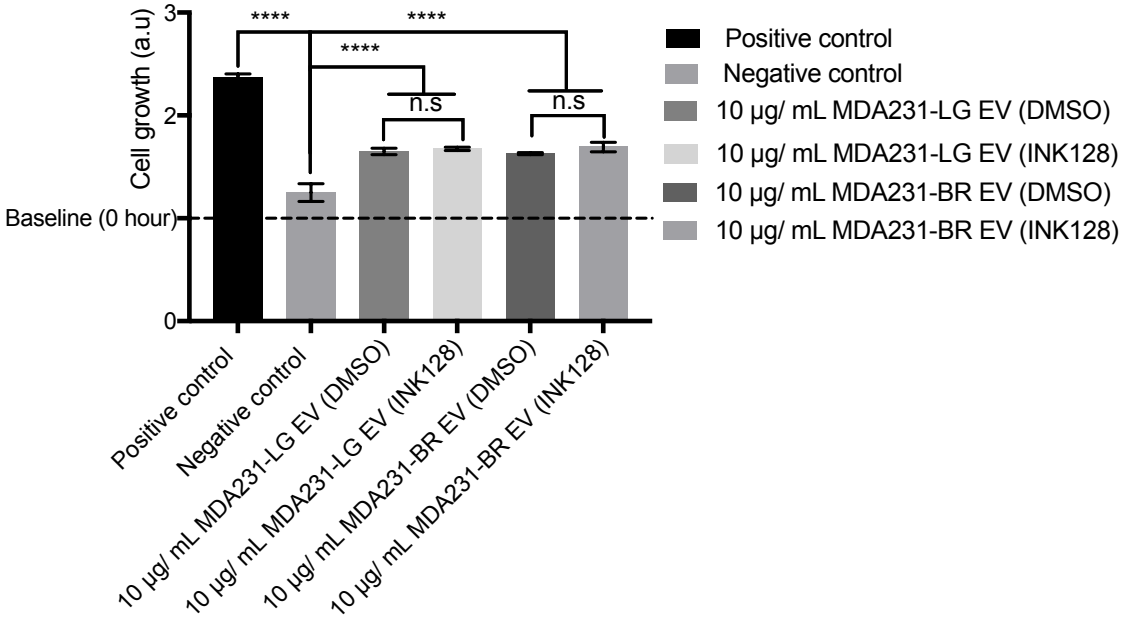

Cell growth (a.u)
3
2
0
Baseline (0 hour)
****
****
****
n.s
n.s
Positive control
Negative control
10 µg/ mL MDA231-LG EV (DMSO)
10 µg/ mL MDA231-LG EV (INK128)
10 µg/ mL MDA231-BR EV (DMSO)
10 µg/ mL MDA231-BR EV (INK128)

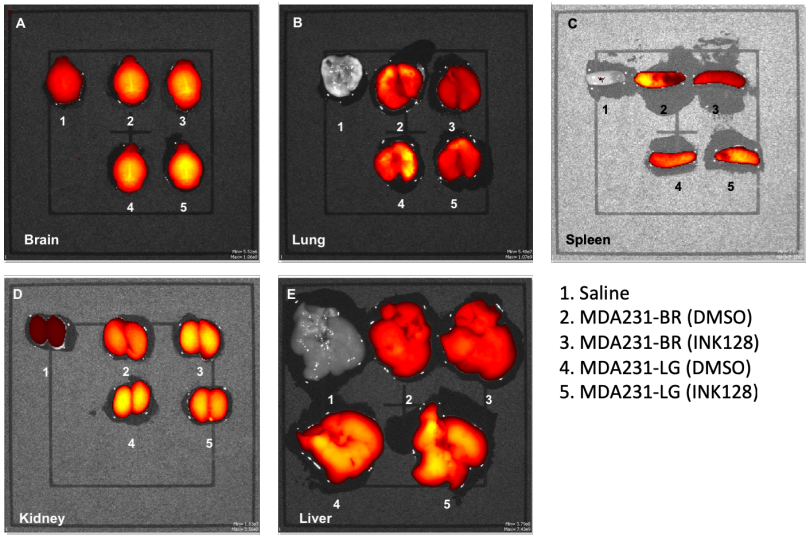
Figure 4.14. Modulation of HBEC-5i cell growth by EVs. (A) The growth of serum-deprived HBEC-5i cells measured at 96 hours post addition of 5 μg/mL and 10 μg/mL of EVs secreted from either MDA231 clones was significantly increased as compared to cells treated with PBS (vehicle), in the negative control group. The positive control group in this experiment was a control group of recipient cells cultured in standard growth media containing serum, while in the negative control group is a control group containing recipient cells cultured in the growth media without serum. The growth of the recipient cells just after the addition of EVs served as the baseline (0 hour) and 96 hours as the end point in the assay. (B) Immunoblotting analysis and (C) signal quantification of P-ERK, total ERK, P-S6, total S6 and tubulin levels in the serum-starved HBEC-5i cells treated with 10 μg/mL of EVs secreted by MDA231-LG and MDA231-BR cells for 24 hours. The EVs secreted from both clones of MDA231 cells promoted a subtle increase in phosphorylation of S6. The phosphorylation level of ERK remained unchanged in the recipient cells upon the addition of EVs either from MDA231-LG or MDA231-BR cells. 20 μg of protein was loaded in each well of the gel. Tubulin was used as the internal loading control. (D) EVs secreted from both clones of MDA231 cells treated with either DMSO or INK128 promoted a significant increase in serum-starved HBEC-5i cell growth. Data are presented as mean ± SEM of at least, 3 independent experiments, $n \geq 3$. The statistical analysis was performed using one-way ANOVA. *, $P \leq 0.05$ and ****, $P \leq 0.0001$. n.s: not significant.

4.2.9 In vivo biodistribution of EVs

A preliminary study (one mouse per group, n=1) of in vivo biodistribution of EVs secreted by both metastatic clones of MDA231 cells in response to INK128 produced two key finding which were: 1) the injected EVs at a dose of $3x10^9$ particle/g was tolerated in the mice as there was no observable behavioural changes in the mice after 4 hours post injection; and 2) the fluorescent sulfo-cyanine5.5 NHS labeled-EVs secreted from both metastatic clones treated with INK128 and drug vehicle (DMSO) were detectable in the organ of interest which was brain and other selected organ including lung, spleen, kidney and liver (Figure 4.15 A and B).

Furthermore, the EV distributions in brain and kidney of mice regardless of metastatic clone and treatment were not profoundly changed. Even though n=1 in the pilot experiment, there may have been differences in the biodistribution of different types of EVs. These findings will be focussed on in the future follow-up experiments. For example, the accumulation of EVs to the lung seems to have reduced upon INK128 treatment in case of both MDA231-LG and MDA231-BR derived EVs. The accumulation of INK128-treated MDA231-BR EVs in the spleen seemed to have reduced too, compared to controls. Correspondingly, INK128 treatment increased EV accumulation in the liver in case of both cell clones, whereas the liver accumulation of MDA231-LG EVs was higher than MDA231-BR EVs. However, it should be noted that some of the observed differences could be related to different labelling efficiency of EVs for different treatment groups. This will be thoroughly investigated in future experiments.

A



B

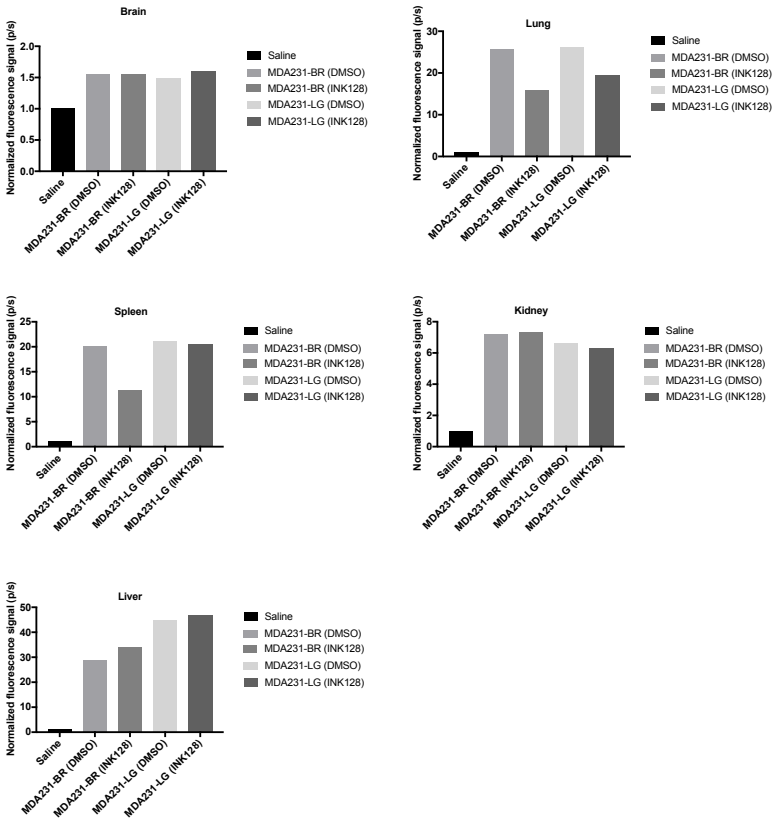


Figure 4.15. The systemic distribution of EVs. (A) A representative IVIS image of organs and (B) fluorescence signal quantification normalized to saline group after 4 hours post intravenous injection of fluorescent-labeled EVs secreted by both metastatic clones of MDA231 cells treated with INK128 or drug vehicle (DMSO). n=1.

4.3 Discussion

4.3.1 INK128 partially inhibited mTORC1 in MDA231-BR cells

Basal-like and TNBC subtypes of BC are frequently metastasized to lung, brain and distant lymph nodes. Among 177 TNBC patients studied, more than 70% of their tumors harbored phosphorylated mTOR and this significantly correlated with reduced overall and recurrence-free rates of survival for stage I and II TNBC patients[243]. The sensitivity of different metastatic clones of TNBC to INK128, an ATP-competitive mTOR kinase inhibitor which blocks both mTORC1 and 2 has not been studied. My finding demonstrated that inhibition of mTORC1 was incomplete in MDA231-BR cells as compared to MDA231-LG cells as evidenced by partial dephosphorylation of S6. This finding suggested that MDA231-BR cells were more resistant to INK128 treatment than MDA231-LG cells. My data also showed that 4E-BP1 activity was completely inhibited, evidenced by downshift of the γ-band of 4E-BP1 (Figure 4.1), supporting the idea that there may be multiple pools of mTORC1 in that respond differently to mTOR inhibition activity. The analysis of the glutamine sensor proton-assisted amino acid transporter 4 (PAT4), suggested that this is the case in HCT116 colorectal cancer cells, with the different mTORC1 complexes responding differently to the mTOR inhibitor, rapamycin[244]. The factors that contributed to INK128 resistance in MDA231-BR cells were not determined in this work. However, treatment resistant mutations of mTOR, activation of alternate proliferation pathways and intratumoral heterogeneity of mTOR kinase activity have been identified as contributing factors to the development of therapeutic resistance to mTOR inhibitor[245].

A recent study has reported that the acquired resistant mutations to mTOR inhibitors have been identified through genomic sequencing analysis of MCF-7 treated with rapamycin or AZD8055 (an ATP-competitive mTOR inhibitor) for three months[246]. This

study revealed that rapamycin-resistant clones harbored mutations in FRP domain of mTOR while AZD8055-resistant clones harbored mutations in the kinase domain of mTOR. Interestingly, these mutations have been identified in untreated patients, implying that certain types of tumors are intrinsically resistant to mTORC1 inhibitors. Thus, it would be informative to perform comparative genomic sequencing between MDA231-LG and MDA231-BR cells to determine whether intrinsic mutations in the mTOR pathway may contribute to this finding.

A second possible contributing factor to the development of resistance to mTORC1 inhibitors in tumors is the activation of an alternate proliferation pathways. For instance, increased phosphorylation of AKT at serine 473 residue in rapamycin-administered glioblastoma patients is associated rapid disease progression[247]. Furthermore, the antitumor activity of the ATP-competitive mTOR kinase inhibitor is also reduced by the activation of upstream signaling, PI3K which leads to enhanced phosphorylation of AKT at threonine 308. The compensatory activation of AKT at threonine 308 residue is sufficient to activate AKT signaling despite suppression of phosphorylation of serine 473 residue by mTORC2[248]. Apart from AKT, the overactivation of ERK in response to kinase inhibitors has been previously reported[249]. Herein, I demonstrated that in both clones of MDA231 cells treated with INK128, the overactivation of ERK was observed to compensate the inhibition of mTORC1 marked by downshift of γ-band of 4E-BP1, although phosphorylation of S6 was detectable in MDA231-BR cells. This finding further suggested that ERK overaction in response to mTORC1 inhibition was determined by the phosphorylation status of 4E-BP1.

Finally, the intratumoral heterogeneity of mTOR kinase may also contribute to the development of resistance to mTORC1 inhibitors. A recent study has demonstrated that mutation in the kinase region of mTOR is not detected in every tumor region of a renal cell carcinoma through genome sequencing analysis[250]. This finding implies that

intratumoral genetic heterogeneity of mTOR kinase determines its function and very likely its response to mTOR inhibitors. Furthermore, this study also reported that mTOR mutation is not detected in metastatic tumors, highlighting the heterogeneity between the primary and metastatic tumors. The intratumoral heterogeneity of mTOR kinase between primary and metastatic tumors or even between different metastatic clones is unknown in BC. However, my finding demonstrated that this could exist as MDA231-BR cells were resistant to INK128 as compared to MDA231-LG cells.

4.3.2 Alteration of EV secretion by INK128

Prior to proteomic analysis, the effect of mTORC1 inhibition by INK128 on the secretion of EV was determined by quantifying the amount of secreted EV using BCA assay. Inhibition of mTORC1 by INK128 suppressed the secretion of EVs by MDA231-LG cells while increased EV secretion from MDA231-BR cells (Figure 4.2 C). As initially discussed in Section 3.3.3, it would be important to investigate the expression level of ESCRT-III components including ALIX, CHMP4C, VPS4B and VTA1 in response to INK128 treatment as knockdown of these proteins has induced increase in EV secretion in HeLa cells[143]. Likewise, it would also be important to evaluate the expression level of ESCRT-0/1 component including HRS, STAM1 and TSG101 as deficiency in these proteins have been associated with decreased in EV secretion. This would give an insight whether the mechanism of INK128-induced modulation of EV secretion is ESCRT-dependent.

4.3.3 Protein composition of MDA231-LG and MDA231-BR EVs

Due to difference in sensitivity to INK128 between metastatic clones of MDA231 cells, I further characterized the protein composition of EVs secreted by INK128-treated MDA2231-LG and MDA231-BR cells by label-free liquid chromatography mass

spectrometry (LCMS) proteomic as EVs have been reported to mediate therapy resistance in cancer cells and analysis of EV proteome could leads to the identification of candidate proteins involved in the development of treatment resistance. Label-free LCMS was the method of choice as this method provided a wider dynamic range and broader proteome coverage for peptide detection[251].

Comparative proteomic analysis demonstrated that 93 and 147 proteins were upregulated in EVs secreted from MDA231-LG and MDA231-BR cells, respectively. These proteins were subjected to annotation overrepresentation enrichment analysis performed using FunRich software (Table 4.1) and also by manually referring to specific gene ontology terms (Figure 4.8). The main purpose of this analysis was to identify the putative functions of these EVs based on a bias in protein localization to specific cellular components and biological functions that will be tested using cell-based assays including cell proliferation, adhesion and others. Furthermore, the specific GO terms associated with cellular component were selected based on their involvements in EV biogenesis and membrane trafficking.

Following annotation overrepresentation enrichment analysis, selected proteins in the EVs significantly enriched in certain cellular compartment, molecular function and biological process were discussed in the following paragraphs, based on their involvements in tumor development and progression. According to overrepresentation enrichment analysis of cellular component, both upregulated proteins in MDA231-LG and MDA231-BR EVs were significantly overrepresented in exosome and lysosome. There are accumulating evidences that highlight the functional association between the lysosome status and exosome secretion, a subtype of EV that are generated upon fusion of multivesicular bodies to the plasma membrane to release intraluminal vesicles as exosomes[252]. For instance, cisplatin-resistant ovarian cancer cells with a low abundance

of lysosome, secreted high concentration of cisplatin in the EVs, leading to a speculation that the disposal of cisplatin into EVs is modulated by the lysosomal mass[253].

For example, S100A4 and FUT8 were among the proteins overrepresented in exosome, significantly upregulated in MDA231-LG and MDA231-BR EVs, respectively. In the context of tumor biology, S100A4 has been reported to increase cell migration capacity of BC cells through the formation of lamellipodia, facilitated by calcium-dependent interaction with ono-muscle myosin IIA (NMIIA)[254]. Apart from overrepresented in exosome, S100A4 was also overrepresented in biological process associated with the regulation of cell growth and/or maintenance. In the previous finding, knockdown of S100A4 thyroid cancer cells suppressed cell proliferation and invasion by downregulating MMP9 and VEGF[255].

Fucosyltransferase 8 (FUT8) catalyzes core fucosylation by transferring fucose moiety from guanosine-5'-diphosphate fucose to the innermost asparagine-linked GlcNAc through α-1,6 link, known to be associated with progression of liver cancer. A previous finding has highlighted that FUT8 is highly upregulated in TGFβ-induced EMT and correlated to invasiveness and migration capacity of BC cell lines[256]. This study also reported that overexpression of FUT8 triggered EMT while knockdown of this protein reduced the invasiveness of BC cells[256]. In liver cancer, inhibition of fucosylation by fluorofucose suppressed integrin-mediated specific downstream signaling of phosphorylated FAK required for integrin-dependent cell migration[257]. According to cellular compartment overrepresentation enrichment analysis and manual annotation analysis, FUT8 was overrepresented in exosome and associated with integrin-mediated signaling pathway, respectively.

The proteins in EVs secreted from MDA231-LG and MDA231-BR cells were also significantly overrepresented in lysosome, according to cellular component overrepresentation analysis. YKT6 and protein C receptor (PROCR) were among the identified proteins from annotation enrichment analysis that localized to lysosome. As sorted in MDA231-LG EVs, YKT6 is a SNARE protein important for cell membrane fusion, vesicular transport and it regulates the secretion of WNT3A-containing exosomes in HEK293 cells[258,259]. In an in-vitro study, the overexpression of YKT6 in BC cells has been associated with aggressive phenotype and leads to metastasis following intravenous injection in mice[260]. Apart from its association with the lysosome, it was also associated with Golgi apparatus, according to manual annotation analysis.

PROCR is a single-pass transmembrane receptor sorted in MDA231-BR EVs and it is known as a stem cell marker for vascular endothelial, hematopoietic and mammary gland cells[261–263]. A recent finding reported that PROCR triggers the activation of multiple signaling pathways such as ERK, PI3K-AKT and RhoA in BC cells[264]. According to manual annotation analysis, PROCR was associated with cell-cell junction and wound healing process. The signaling pathways mediated by endothelial PROCR have been reported to inhibit apoptosis and promote cancer cell migration, invasion and angiogenesis. Overexpression of endothelial PROCR has been reported to limit extravasation of cancer cells to liver and lung in murine B16-F10 metastasis model by enhancing vascular endothelial-cadherin-dependent vascular endothelial barrier mediated by SIP1.

Apart from PROCR, integrin β4 (ITGB4) is laminin-5 receptor is predominantly expressed in several types of cells including endothelial cells, squamous epithelial cells, Schwan cells, immature thymocytes and fibroblast of peripheral nervous system. ITGB4 was also associated with cell-cell junction according to manual cellular component

analysis. In hepatocellular carcinoma cells, ITGB4 promotes cell growth, invasiveness and EMT through Slug-dependent manner.

Based on cellular component and biological function overrepresentation enrichment analysis, MDA231-LG EVs were also significantly enriched with proteins associated with the ECM. A recent finding has reported that EV serves as a structural and functional component of ECM as this study shows EVs are bound by matrix components in the ECM bioscaffolds[265]. Moreover, the interaction of EVs with ECM also play important roles in tumor invasion. This is exemplified by the activation of EV-associated proteinases in the acidic TME such as cathepsin B which involves in the degradation of several ECM related proteins including fibronectin, type IV collagen, tenascin C and laminin, which in turn could facilitate tumor invasion[266]. Matrilin 2 (MATN2), a widely expressed ECM protein was significantly upregulated in MDA231-LG EVs and increase in MATN2 expression in hepatocellular carcinoma was associated to tumor neovascularization[267].

Apart from overrepresentation in the ECM, MDA231-LG EVs were also overrepresented in cytoplasm in the cells. One of these proteins was thymidylate synthase (TMYS) which catalyzes the synthesis of DNA-component thymidylate and is essential for DNA replication and repair[268]. A large-scale analysis of TMYS expression in clinical samples revealed that enhanced expression of TMYS was associated with adverse clinical behavior in various types of tumors including breast, lung and colorectal[269–271].

MDA231-LG EVs were also overrepresented in proteasome complex. Proteasomes are responsible for the degradation of misfolded and oxidized proteins in cells in response to stress[272]. Immunoproteasome genes including proteasome subunit beta type-8 (PSMB8), PSMB9 and PSMB10 are upregulated by IFNγ produced by tumor-infiltrating lymphocytes specific for neo-antigen[273,274]. In BC, the upregulation of

immunoproteasome genes is strongly associated with high infiltration of lymphocytes expressing interferon and good prognosis.

The proteins in EVs secreted by MDA231-BR cells were also overrepresented with extracellular region. One of the proteins identified that localized to extracellular region was platelet-derived growth factor D (PDGFD). PDGFD is newly discovered isoform of PDGF that binds and activates its cognate receptor PDGFR-β[275]. In melanoma cells, the cell proliferation, survival and development of drug resistance are mediated by zic family member 5 (ZIC5), a transcriptional suppressor of E-cadherin, by activating of FAK and STAT3 signaling pathways through PDGFD induction[276].

The EVs secreted MDA231-BR cells were overrepresented in Golgi apparatus, based on annotation overrepresentation enrichment analysis performed using FunRich software and manually referring to GO associated with Golgi apparatus. Phosphatidylinositol 4-kinases (PI4Ks) catalyze the synthesis of phosphatidylinositol 4-phosphate (PI4P) which are pivotal for the maintenance of Golgi apparatus and its well-characterized function, intracellular trafficking[277]. PI4K II alpha (PI4K2A) and PI4K II beta (PI4K2B) have been reported to localize to Golgi apparatus, regulating the membrane trafficking between trans-Golgi network to plasma membrane[278,279]. In MDA231-BR EVs, PI42KA was significantly upregulated. A previous study has reported that the level of Golgi PI4P level determine cell adhesion and invasiveness of human breast cancer[280]. For example, accumulation of Golgi PI4P decreases cell adhesion but enhance cell migration of weakly invasive cells.

Plasma membrane was another cellular component overrepresented by proteins in EVs secreted by MDA231-BR cells. As localized to plasma membrane, MET is a member of receptor tyrosine kinase family and acts as a cell surface receptor for hepatocyte growth factor[281]. It regulates tumor growth, survival and migration through effector proteins

including PI3K-AKT axis, ERK, RAS and SRC[282]. A previous study reported that MET expression is correlated to EGFR expression in human BC tissues and associated with worse disease-free survival as compared to patients that only expressed EGFR[281].

The proteins in EVs secreted by MDA231-LG cells were overrepresented in GTPase activity. This was exemplified by the presence of G protein alpha subunit 13 (GNA13). Several studies have reported that GNA13 is highly expressed in aggressive breast and prostate cancer cell lines and inhibition of GNA13 expression suppresses the invasiveness capacity of cancer cells[283,284]. Recently, GNA13 expression in head and neck squamous cell carcinoma cells has been associated with tumor-initiating capacity and developed resistance against γ-irradiation and cisplatin through NFκB and JNK/MAPK-AP1 signaling pathways[285].

The proteins in EVs secreted by MDA231-BR cells were overrepresented with lipase activities. This was exemplified by the presence of endothelial lipase G (LIPG) in MDA231-BR EVs. Based on manual cellular component annotation analysis, LIPG was also associated with Golgi apparatus. In the context of tumor biology, it has been reported to aberrantly overexpressed in basal-like TNBC and required for the tumorigenicity and metastatic capacity of TNBC cells, through its involvement in oncogenic DTX3L-ISG15 signaling pathway, known in mediating interferon signaling[286]. This signaling pathway is crucial in sustaining the expression of LIPG in basal-like TNBC cells by protecting it from proteasome-mediated protein degradation. LIPG regulates cell proliferation through lipase-dependent function and enhances the stemness, invasiveness and EMT features in a lipase-independent manner[286].

Apart from overrepresented in lipase activity, proteins in MDA231-BR EVs were also overrepresented in cell adhesion molecule activity. For instance, adhesion molecule with Ig-like domain 2 (AMIGO2) significantly upregulated in MDA231-BR EVs has been

reported to facilitate the adhesion of liver-tropic tumor cells to liver endothelial cells leading to liver metastasis. It has also been proposed that AMIGO2 mediate cell adhesion activity by modulating the expression/activation of integrins and adhesion-related kinases such as focal-adhesion kinase (FAK) and SRC[287]. The expression of AMIGO2 in human colon and gastric tumors through immunohistochemical staining demonstrated enhanced expression of this molecule in liver metastatic lesion as compared to primary tumor tissues[287].

Bone marrow stromal antigen 2 (BST2) is a type II transmembrane glycoprotein constitutively expressed on malignant cells including breast, lung and gastrointestinal tumors. It was significantly upregulated in MDA231-LG EVs and found to be associated with MVB and Golgi apparatus, according to manual cellular compartment annotation analysis. Increased BST2 expression has contributed to the development of resistance to cisplatin through the activation of NFκB signaling pathway, resulting in the upregulation of anti-apoptotic genes in nasopharyngeal cancer cells[288]. As associated with cell proliferation according to manual annotation analysis, a previous finding has reported that BST2 is required for an anchorage-independent growth in BC cells and knockdown of BST2 reduces size and colony formation of BC cells based on soft agar colony formation assay[289].

Lysosome-associated transmembrane protein-4β (LAPTM4B) gene is an oncogene that generates two isoforms which are LAPTM4B-24 and LAPTM4B-35[290]. It has been reported that LAPTM4B-35 mediates multidrug resistance in cancer cells by enhancing drug efflux via colocalization and interaction with P-glycoprotein and blocking apoptosis by activating PI3K/AKT signaling pathway through the interaction of phosphoribosyl diphosphate (PRPP) motif in the N-terminus of LAPTM4B-35 with p85α regulatory

subunit of PI3K[291]. LAPTM4B was upregulated in MDA231-BR EVs and it was associated with MVB according to manual annotation analysis.

Eps-15 homology domain-containing 2 (EHD2) involves in the regulation of plasma membrane trafficking by controlling Rac family small GTPase 1 (RAC1) activity[292]. The signals from integrins and growth factor are integrated by RAC1 and its expression is negatively correlated with EHD2 expression[293,294]. The role of EHD2 as a tumor suppressor gene has been studied and reported to be lowly expressed in the metastatic serous ovarian cancer samples in comparison with normal ovarian surface epithelial samples[295]. In breast cancer, EHD2 serves as a negative regulator of breast cancer cells motility as overexpression of EHD2 suppressed migration and invasion capacity of cells[293]. A recent study has reported that upon variations of membrane tension induced by mechanical stress, EHD2 is needed to sustain caveolae reservoir at the plasma membrane[296]. Moreover, EHD2 is translocated from caveolae to nucleus to modulate transcription of genes encoded for caveolae constituents and also those involve in K-RAS, TNFα, and receptor interacted with ECM[296]. Based on manual annotation analysis, EHD2 which significantly upregulated in MDA231-LG EVs was associated with plasma membrane raft and recycling endosome.

The recycling endosome (RE) has been well-characterized for its role in recycling cargoes to plasma membrane and in recent years, REs have been reported to involve in retrograde transport to trans-Golgi network[297,298]. Transferrin receptor 1, encoded by TFRC gene is one of the membrane proteins recycled to the plasma membrane by clathrin-coated vesicles derived from endosome in dynamin-dependent manner[299]. It is a membrane glycoprotein that mediates iron uptake by binding to plasma glycoprotein, transferrin[300]. The expression of TFRC determines BC prognosis and high TFRC expression is associated with poor prognosis[301]. In MDA231-BR EVs, TFRC was one of the proteins associated with RE that significantly upregulated.

Based on manual metallopeptidase activity annotation analysis, proteasome 26S subunit, non-ATPase 14 (PSMD14) and matrix metalloproteinase 1 (MMP1) were associated with this enzymatic activity and sorted in EVs secreted by MDA231-LG and MDA231-BR cells, respectively. PSMD14 is a deubiquitinating enzyme that plays a central function to prevent protein degradation[302]. In esophageal squamous cell carcinoma, PSMD14 stabilizes its substrate SNAIL through deubiquitination which in turn promotes tumor metastasis in vivo[302]. Furthermore, high expression of PSMD14 predicts poor prognosis in patients with esophageal cancer[302]. MMP1 is a member of matrix metalloproteinases family that involves in the breakdown of ECM under physiological and pathological conditions[303,304]. A recent finding suggested that MMP1 is aberrantly expressed upon upregulation of SLUG, an EMT-promoting transcription factor, by direct binding to the promoter region and enhances multi-drug resistance in BC cells[305].

A GO annotation related to amino acid transport was analyzed to identify glutamine metabolism-associated proteins sorted into EVs secreted by MDA231-LG and MDA231-BR cells as studies in Chapter 3 (Figure 3.2) demonstrated that MDA231-BR cells were more sensitive to glutamine deprivation as compared to MDA231-LG cells, as 24 hours glutamine deprivation completely suppressed phosphorylation of mTORC1 target proteins, 4E-BP1 and S6 without activation of ERK. The studies in Chapter 5 (Figures 5.1-5.3) also further supported the finding in Chapter 3 (Figure 3.2) that MDA231-BR cells were more sensitive to extracellular glutamine level as inhibition of glutamine consumption by the glutamine analog, DON completely suppressed mTORC1 activity and induced a significantly higher abundance and length of CTPS1 and IMPDH1 cytoophidia in MDA231-BR cells than in MDA231-LG cells.

According to manual amino acid transport annotation analysis, several proteins associated with serine and glutamine metabolism were identified only in EVs secreted

by MDA231-BR cells. Among these proteins, a system A amino acid transporter, solute carrier 38 member 1 (SLC38A1) known to transport glutamine was significantly upregulated in MDA231-BR EVs. In BC cells, the expression of SLC38A1 was associated with activation of AKT and knockdown of SLC38A1 suppressed cell growth and induced apoptosis by blocking AKT phosphorylation[306]. Besides, SLC38A1 upregulation was correlated with size of tumor, lymph node metastasis and advance stage of disease[306].

4.3.4 Potential EMT-promoting function of EVs in response to INK128

Proteomic analysis of EVs secreted by MDA231-LG and MDA231-BR cells treated with INK128 demonstrated that INK128 minimally altered EV protein composition (Figure 4.10 and 4.12). I reasoned that this could be contributed by the compensatory activation of ERK pathway. Another possible reason was INK128-induced mTORC1 inhibition specifically affected the expression of certain subsets of proteins destined to be sorted into EVs. In addition to minimal changes in the protein content of EVs secreted by both metastatic clones in response to INK, these changes were not very reproducible across repeats. Therefore, it is important to validate these results by western blotting. Here, I discussed the selected proteins that have been reported to regulate invasiveness of cancer cells.

Inhibition of mTORC1 in MDA231-LG cells led to upregulation (HRNR, SAA4, PLA2G2D, CPA4, ACE and GLG1) and downregulation (EEF1D, LMAN, KCNN4 and PTPN23) of proteins in the EVs whose functions were associated with poor prognosis, metastatic potential, suppression of anti-tumor immunity and EMT activation, according to the findings reported in the literature (Table 4.3 C and D). Likewise, similar treatment led to upregulation (GALNS and EMP3) and downregulation (SCRIB, PPP1CB and PTPN23) of proteins in MDA231-BR EVs, whose functions were also associated with EMT

activation, enhancing tumor cell growth, colony formation and cell invasion (Table 4.4 C and D).

Previously, mTORC1 signaling has been demonstrated to regulate epithelial integrity in mammary epithelial cells and genetic and pharmacological inhibition of mTORC1 activates EMT program, marked by upregulation of mesenchymal markers (fibronectin, vimentin and PAI1) and downregulation of epithelial markers (E-cadherin and ZO-3), through TGFβ-independent pathway[307]. As the overlapping putative function of EVs secreted by MDA231-LG and MDA231-BR cells treated with INK128 was related to the EMT activation and invasion, I further discussed the involvement of significantly altered EV proteins associated with these biological properties below.

For example, eukaryotic translation elongation factor 1 delta (EEF1D) was one of the significantly downregulated proteins in EVs secreted by MDA231-LG cells in response to INK128. EEF1D regulates elongation process after forming the translation initiation complex[308]. In osteosarcoma, knockdown of EEF1D suppresses proliferative and colony-forming capacities of cells by blocking G2/M cell cycle transition. EEF1D knockdown in osteosarcoma cells associates with the downregulation of AKT-mTOR and AKT-BAD signaling pathways[309]. Furthermore, knockdown EEF1D also enhances migration and invasion capacities of cancer cells by inducing EMT program as evidenced by downregulation of E-cadherin and upregulation of vimentin in oral squamous cell carcinoma[214].

My finding also demonstrated that galactosamine-N-acetyl-6-sulfatase (GALNS) level was upregulated significantly in EVs secreted by MDA231-BR cells in response to INK128. GALNS mediates the removal of 4-sulphate and 6-sulphate group from the non-reducing end of N-acetylgalactosamine sulphate residues[228]. In prostate stem cells, overexpression of GALNS upregulates the expression of GATA3 and c-MYC which are

the downstream targets of WNT/β-catenin signaling pathway[228]. The activation of WNT/β-catenin signaling pathway has been associated with the activation of EMT program in BC[310]. This finding implied that this could be one of the mechanisms to activate EMT in mTORC1-inhibited cells and the EVs secreted by these cells may possess EMT-inducing properties.

Protein tyrosine phosphatase 23 (PTPN23) is another protein associated with EMT activation and cell migration, was significantly downregulated in EVs secreted by both clones of MDA231 cells in response to INK128. PTPTN23 is a ubiquitously expressed protein containing five protein domains and its BRO1-like and V domains are crucial for ESCRT-dependent sorting of cell surface markers including integrins and EGFR[311,312]. A recent study investigating the role of PTPN23 as tumor suppressor gene has demonstrated that depletion of PTPN23 in Comma 1Dβ cells in orthotopically transplanted BALB/c mice induced the development of basal-like BC, most likely associated with mesenchymal stem-like subtype[223]. This study has also identified FYN kinase, a member of SRC family kinases as a bona-fide substrate of PTPN23 of which its activity is negatively regulated by PTPN23 by dephosphorylation at tyrosine 420 residue[223]. FYN kinase has been recently reported to induce mesenchymal phenotype in basal type breast cancer cells via STAT5/NOTCH2 signaling pathway[313]. Furthermore, a previous RNAi screen of loss-of-function of protein tyrosine kinases has revealed that PTPN23 depletion promotes cell invasion in mammary epithelial cells[222]. Collectively, downregulation of PTPN23 in EVs secreted by INK128-treated MDA231-LG and MDA231-BR cells potentially indicated that the cells acquired enhanced migration capacity.

4.3.5 Growth-promoting function of EVs on brain microvascular endothelial cell growth

A previous study has reported that the expression of PTEN, a tumor suppressor gene which acts as the negative regulator of PI3K/AKT signaling pathway is silenced in human and mouse transplanted tumor cells that metastasize to brain[314]. According to this process is mediated by intercellular transferring of exosomal PTEN-targeting microRNA by brain astrocytes and loss of PTEN in the brain-metastatic tumor cells promotes enhanced secretion of chemokine C-C motif chemokine ligand 2 resulting in the recruitment of ionized calcium binding adaptor molecule 1 (IBA1)-expressing myeloid cells, which in turn mediates tumor outgrowth by reducing apoptosis[314]. Intrigued by these findings, I compared PTEN basal expression level between MDA231-LG and MDA231-BR cells and found that PTEN level was significantly lower in MDA231-BR cells according to immunoblotting analysis (Figure 4.13). As reduction of PTEN level is associated with increased in mTORC1 signaling, characterization of phosphorylated S6 level indicated an increasing trend in MDA231-BR cells (Figure 4.13). A previous comparative proteomic analysis of lung versus brain metastatic clones of MDA231 cells has demonstrated that ERK was predicted to be activated in brain-metastatic MDA231 cells[241]. Through immunoblotting analysis, my finding confirmed that phosphorylation of ERK was in an increasing trend in MDA231-BR cells as compared to MDA231-LG cells (Figure 4.13). Taken together, these finding may imply a higher cell proliferative capacity of MDA231-BR cells and the secreted EVs could potentially promote increase in cell growth of the recipient cells.

Approximately, 10-30% of cancer patients experience brain metastases and BC is one of the common tumor metastasizing to brain[315]. Blood-brain barrier (BBB) is a semi-permeable membrane that provide a stable environment to the central nervous system (CNS) by allowing the entry of selective molecules and protecting CNS from harmful

molecules and pathogens[316]. It has been proposed that brain endothelial cells play a crucial role in the progression of brain metastasis by increasing permeability of BBB[317]. Here I performed cell growth assay to comparatively investigate the growth-promoting function of EVs secreted by MDA231-LG and MDA231-BR cells on serum-starved HBEC-5i cells as recipient cells. HBEC-5i cells were used in my study to investigate the selective growth-promoting function of MDA231-BR EVs as these cells have been previously used as a model as human BBB for drug transport study[318].

My finding demonstrated that EVs secreted by both clones of MDA231 cells similarly enhanced the growth of HBEC-5i cells by activating mTORC1 signaling through phosphorylation of S6 (Figure 4.14). As the recipient cells were grown in serum-starved growth media, any growth-promoting molecules presented either on the surface or within the lumen of EVs could promote increase in cell growth upon interaction or internalization of EVs by HBEC-5i cells. Regardless of treatment, the EVs secreted by control and INK128-treated MDA231 cells similarly enhanced the growth of serum-starved HBEC-5i cells potentially due to the compensatory activation of ERK in response to suppression of mTORC1 by INK128 in both metastatic clones of MDA231 cells (Figure 4.14).

4.3.6 INK128 minimally altered EV biodistribution patterns

A previous study has reported that the in vivo distribution pattern of fluorescently-labeled EVs is influenced by cell source, route of administration and EV dose[319]. In my study, intravenous injection was applied to deliver the fluorescently-labeled EVs as this route of administration have been regarded as more facile and well tolerated in the experimental setting[320]. Wiklander et al., 2015 has reported that fluorescently-labeled EVs were distributed in liver, gastrointestinal tract, pancreas, spleen, lung and other miscellaneous organs such as brain, heart, kidneys and quadricep muscle, in the decreasing magnitude of frequency[319].

Organotropic metastasis of BC is determined by disease subtypes and molecular features[321]. Liver, lung and brain are the most common metastatic sites in BC patients. Renal and splenic metastases from BC are less common but these events have been reported in the literature[322,323]. A previous study has reported that distinct expression of integrins in EV dictates organotropism metastasis of cancer cells[31]. As the components of integrin-mediated signaling pathway were different according to manual annotation analysis (Figure 4.8 B), it may be informative to investigate the spatial distribution of EVs secreted by lung and brain metastatic clones of MDA231 cells treated with INK128. The preliminary findings from my study (one mouse per group, n=1) were the tested dose ($3x10^9$ particle/g) was tolerated in mice regardless of EV groups and the fluorescently-labeled EVs were detectable in the brain and other selected organs including liver, lung, kidney and spleen (Figure 4.15).

In my study, the distribution pattern of fluorescently-labeled EVs secreted by both metastatic clones of MDA231 seemed to be unaltered in the all tested organs except for liver which displayed a higher distribution of MDA231-LG EVs than MDA231-BR EVs. This finding could be contributed by the molecular properties of surface proteins of MDA231-LG EVs which allow the EVs to be more efficiently taken up by liver cells.

Suppression of mTORC1 by INK128 seemed to minimally alter the distribution pattern of EVs only in lungs and spleen, while retaining it in other organs. In lungs, EVs secreted from both metastatic clones of MDA231 cells treated with INK128 displayed a lower distribution pattern as compared to the control counterparts. However, this distribution pattern in spleen seemed to be contributed only by EVs secreted by MDA231-BR cells in response to INK128. As suppression of mTORC1 activity by INK128 seemed to reduce the EV distribution especially in lungs, this may indicate that suppressing the mTORC1 activity may reduce the capacity of TNBC cells to metastasize to lungs.

Taken together, the current observation on EV distribution pattern could be partly contributed by systemic delivery by intravenous injection and also the unknown molecular drivers that dictate organ-specific distributions of EVs. Therefore, characterization of EV distribution pattern is important to improve our understanding in the role of EV in metastasis.

4.4 Conclusion

In conclusion, the annotation enrichment analysis suggests that EVs secreted by MDA231-LG and MDA231-BR cells may have different functions. INK128-induced mTORC1 inhibition in both clone of MDA231 cells, however, only minimally altered the protein composition of EVs. As EVs secreted from INK128-treated MDA231 cells may possess putative pro-survival functions, further validations using cell-based assays including cell migration, adhesion and others are required. Taken together, the findings generated from this study are still in the preliminary phase and the preclinical studies on characterization of content and function of EVs secreted by INK128-treated cells using different metastatic clones of BC cells may facilitate the understanding of clinical outcomes from INK128-treated patients with metastatic breast tumor. The fact that INK128 is usually used in combination with other anti-cancer drugs would also need to be considered.

Chapter 5.0 Stress-induced assemblies of cytoophidia in breast cancer and *Saccharomyces cerevisiae*

5.1 Introduction

In this chapter, the first strand of work discussed is the difference in glutamine dependency in lung and brain metastatic clones of the MDA231 cell line reflected by changes in the mTORC1 signalling and assemblies of CTPS1 and IMPDH1 cytoophidia in DON-treated cells. This chapter also discussed the preliminary works on the large-scale screening of cytoophidium-forming proteins in GFP collection of *S. cerevisiae* and their properties at different growth phases in order to understand the link between cytoophidium assembly and metabolic status.

The specific objectives in this research project were as followed:

1. Comparative characterization dose-dependent inhibition of mTORC1 pathway by DON.
2. Comparative characterization of CTPS1 and IMPDH1 cytoophidia assemblies and length between lung and brain metastatic clones of MDA231 cells in response to DON treatment.
3. Large-scale screening of cytoophidium-forming proteins in *S. cerevisiae*.
4. Comparative characterization of glutamine-utilizing cytoophidia abundance and length in budding yeast cells cultured at different growth phases.

5.2 Declaration of authorship

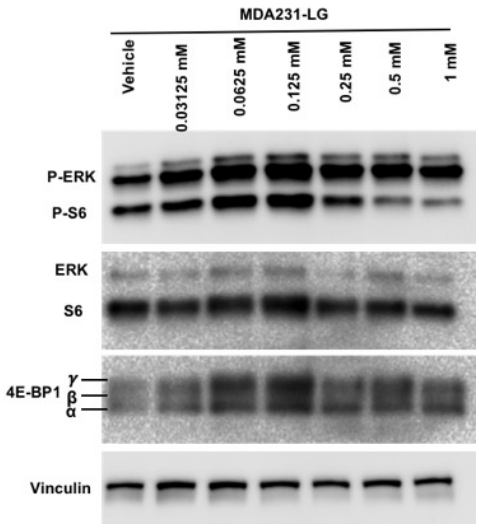
Genome-wide screening of cytoophidium-forming proteins in *S. cerevisiae* was equally performed by Dr Qingji-Shen, Hakimi Kassim and Dr Yong Huang. In my screening, I discovered 5 out of 9 novel cytoophidium-forming proteins (PFK1p-GFP, PFK2p-GFP, GCD11p-GFP, TSA1p-GFP and GDB1p-GFP). The acquisition of nuclear cytoophidia images was performed by Professor Ji- Long Liu. The revised analysis of in-silico protein-protein interaction of cytoophidium-forming proteins was performed in collaboration with Dr Ashling Holland. I solely performed the works related to characterization of abundance and length of glutamine-utilizing cytoophidia at different growth phases. The data presented in Figures 5.5, 5.6, 5.7, 5.9 and Table 5.1 have been published in Shen et al., 2016 (Appendix B).

5.3 Result

5.3.1 DON markedly suppressed mTORC1 pathway in MDA231-BR cells

The lung and brain metastatic clones of MDA231 cells were treated with the glutamine analog, DON at different doses ranging from 0.03 mM to 1 mM for 24 hours. The changes in the phosphorylation level of S6 and hyperphosphorylated γ-band of 4E-BP1 were used as the readouts for the sensitivity of cells towards DON. The tested range of DON concentration was completely dephosphorylated S6 and downshifted γ-band of 4E-BP1 in MDA231-BR cells (Figure 5.1 B) while these concentrations mildly suppressed mTORC1 in MDA231-LG cells marked by a partial reduction of S6 phosphorylation while retaining hyperphosphorylated 4E-BP1 γ-band, indicating that MDA231-BR cells were more glutamine dependent than MDA231-LG cells as mechanistically, DON blocked glutamine consumption in cells leading to mTORC1 suppression (Figure 5.1 A). The compensatory activation of ERK was also detected in response to mTORC1 suppression in both metastatic clones of MDA231 cells. As shown in Figures 5.1 A and B, 0.5 mM of DON was used to induce CTPS1 and IMPDH1 cytoophidia assemblies as this concentration partially reduced P-S6 in MDA231-LG cells while it completely suppressed phosphorylation of P-S6 and downshifted γ-band of 4E-BP1 in MDA231-BR cells. Previously, a higher dose of DON has been used to induce cytoophidia assemblies in HeLa cells without analyzing the changes in the phosphorylation status of S6 and 4E-BP1[120].

A



B

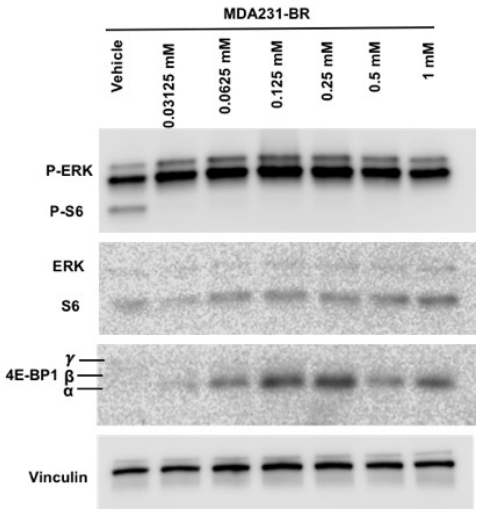


Figure 5.1. Dose-dependent inhibition of mTORC1 by DON in MDA231-LG and MDA231-BR cells. DON mildly suppressed mTORC1 pathway in (A) MDA231-LG cells marked by a partial dephosphorylation of S6 and detectable γ-band of 4E-BP1 while in (B) MDA231-BR cells, DON completely inhibited mTORC1 pathway marked by a complete dephosphorylation S6 and downshift of γ-band of 4E-BP1. A compensatory activation of ERK was detected in both metastatic clones of MDA231 cells in response to suppression of mTORC1 pathway. 20 μg of protein was loaded in each well of the gel. Vinculin was used as the internal loading control. n=1.

5.3.2 DON markedly induced CTPS1 and IMPDH1 cytoophidia in MDA231-BR cells

A concentration of 0.5 mM of DON was selected to induce CTPS1 and IMPDH1 cytoophidia for 24 hours (Figure 5.2 A and B). As mTORC1 inhibition by DON was in a greater extent in MDA231-BR cells than in MDA231-LG cells, the assemblies of CTPS1 and IMPDH1 cytoophidia were also significantly higher in MDA231-BR cells than MDA231-LG cells, highlighting a greater dependency on glutamine for MDA231-BR cells (Figure 5.3 A). In parallel, the lengths of CTPS1 and IMPDH1 cytoophidium were also significantly increased in MDA231-BR cells as compared to MDA231-LG cells in response to DON treatment (Figure 5.3 B). Immunoblotting analysis of CTPS1 and IMPDH1 demonstrated that the level of CTPS1 was unchanged in response to DON treatment while IMPDH1 protein was undetected (Figures 5.4 A and B).

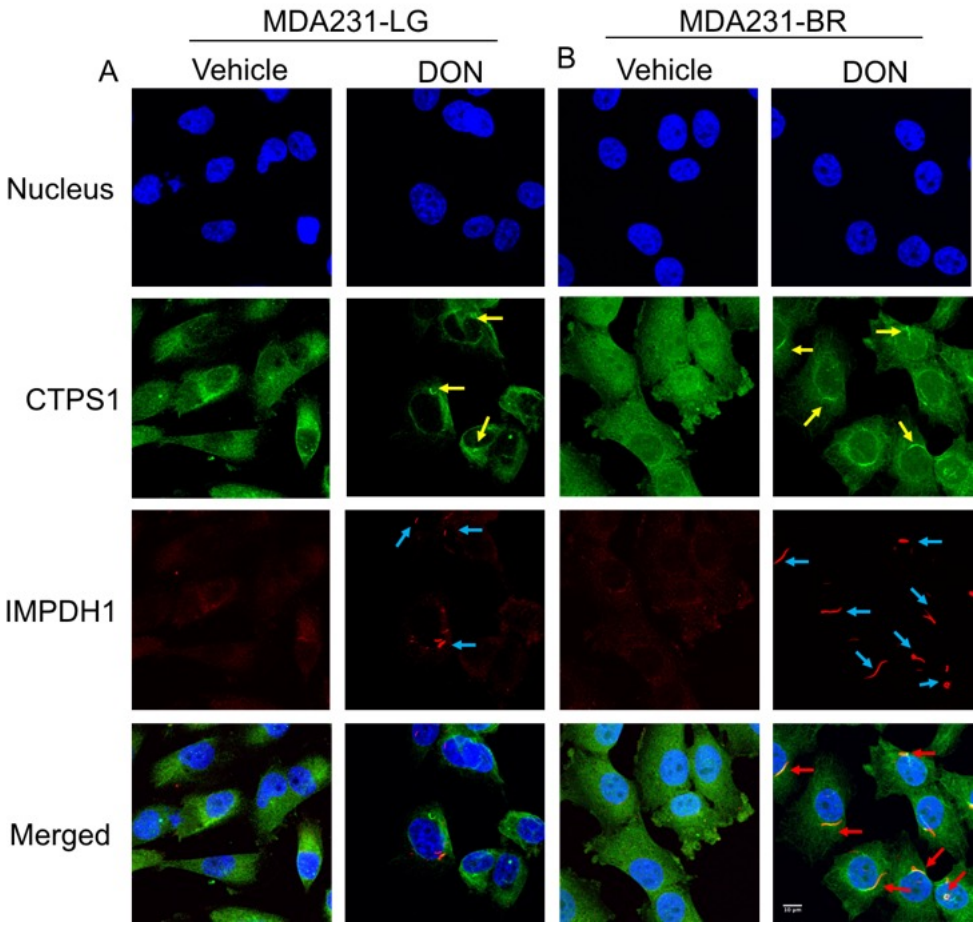
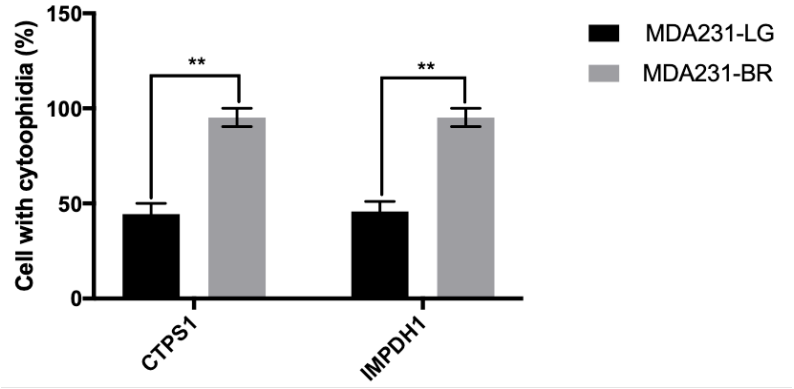


Figure 5.2. Induction of CTPS1 and IMPDH1 cytoophidia by DON. A representative image of CTPS1(yellow arrow) and IMPDH1(blue arrow) cytoophidia induced by 0.5 mM of DON for 24 hours in (A) MDA231-LG and (B) MDA231-BR cells. The length of IMPDH1 cytoophidia was greater in MDA231-BR cells than MDA231-LG cells and in some cells, IMPDH1 and CTPS1 cytoophidia were in a close proximity (red arrow). Scale bar, 10 μm.

A



B

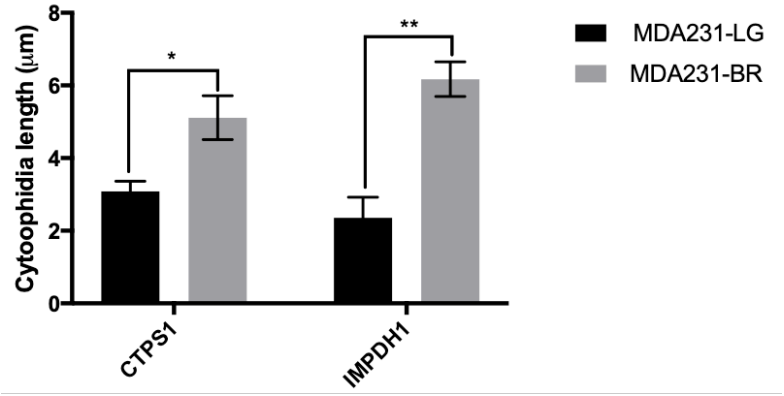
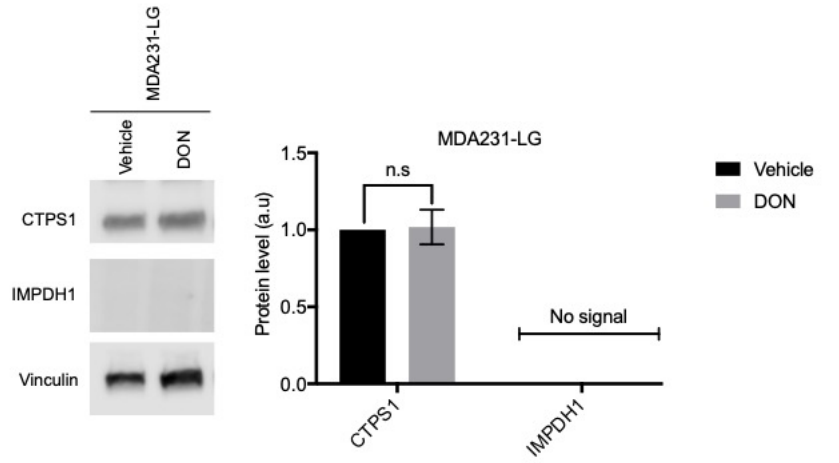


Figure 5.3. Comparative analysis of abundance and length of CTPS1 and IMPDH1 cytoophidia in MDA231-LG and MDA231-BR cells in response to DON treatment. (A) The abundance and (B) length of CTPS1 and IMPDH1 cytoophidia were significantly higher in MDA231-BR cells than MDA231-LG cells suggesting that MDA231-BR cells were more dependent on glutamine than MDA231-LG cells. Data are presented as mean ± SEM of three independent experiments, n=3. The statistical analysis was performed using Student t-test (two-tailed). *, $P \leq 0.05$; **, $P \leq 0.01$ and ***, $P \leq 0.001$.

A



B

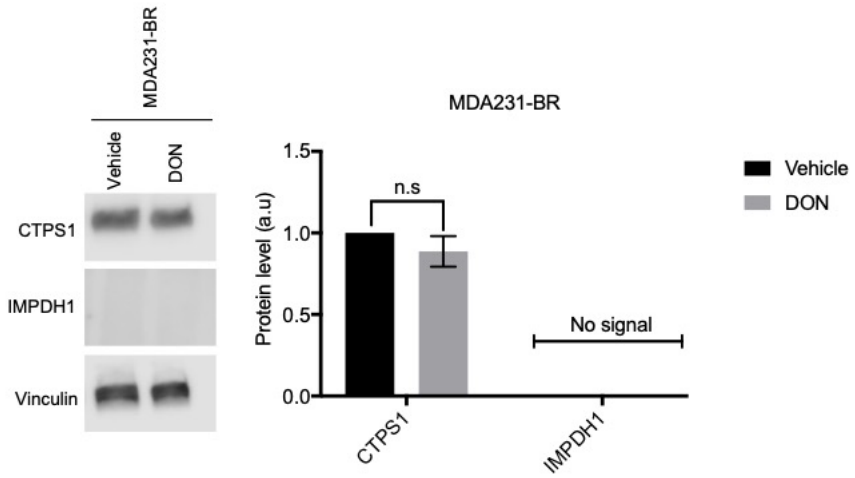


Figure 5.4. Induction of CTPS1 cytoophidia assemblies by DON retained CTPS1 protein level. A representative immunoblot and signal quantification of CTPS1 and IMPDH1 in (A) MDA231-LG and (B) MDA231-BR cells showing CTPS1 levels in both metastatic clones of MDA231 cells were unaltered while IMPDH1 protein was undetectable in response to 0.5 mM of DON for 24 hour. 20 μg of protein was loaded in each well of the gel. Vinculin was used as the internal loading control. Data are presented as mean ± SEM of three independent experiments, n=3. The statistical analysis was performed using Student t-test (two-tailed). n.s: not significant.

5.3.3 A widespread assembly of proteins into cytoophidia in *S. cerevisiae*

The large-scale screening of cytoophidium-forming proteins in *S. cerevisiae* at the diauxic phase had identified 9 novel cytoophidium-forming proteins (ACC1p-GFP, ASN1p-GFP, ASN2p-GFP, GCD1p-GFP, GDB1p-GFP, GDH2p-GFP, PFK1p-GFP, PFK2p-GFP, TSA1p-GFP) (Figure 5.5), in addition to the validation of the previously identified 14 cytoophidium-forming proteins (GCD2p-GFP, GCD6p-GFP, GCD7p-GFP, GCN3p-GFP, GLT1p-GFP, PSA1p-GFP, SUI1p-GFP, URA7p-GFP, URA8p-GFP, CDC10p-GFP, CDC11p-GFP, CDC12p-GFP, SHS1p-GFP, GLN1p-GFP) (Figure 5.6). In previous independent studies, CTPS1 and IMPDH2 have been reported to compartmentalize into both cytoplasmic and nuclear cytoophidia in *S. pombe, D. melanogaster* and human cell line[107,324,325]. However, it was not conclusive that CTPS (URA7p-GFP and URA8p-GFP) and ASNS (ASN1p-GFP and ASN2p-GFP) could potentially compartmentalized into cytoophidia both in cytoplasm and nucleus (Figure 5.7).

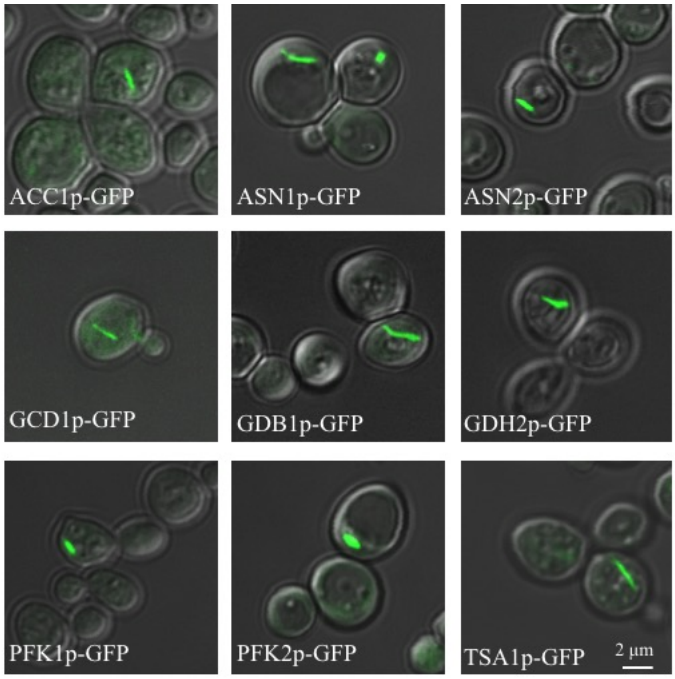


Figure 5.5. Novel cytoophidium-forming proteins in *S. cerevisiae*. A total of 9 additional cytoophidium-forming proteins including ACC1p-GFP, ASN1p-GFP, ASN2p-GFP, GCD1p-GFP, GDB1p-GFP, GDH2p-GFP, PFK1p-GFP, PFK2p-GFP and TSA1p-GFP was discovered in *S. cerevisiae*. Scale, 2 μm. Images modified from Shen et al., 2016.

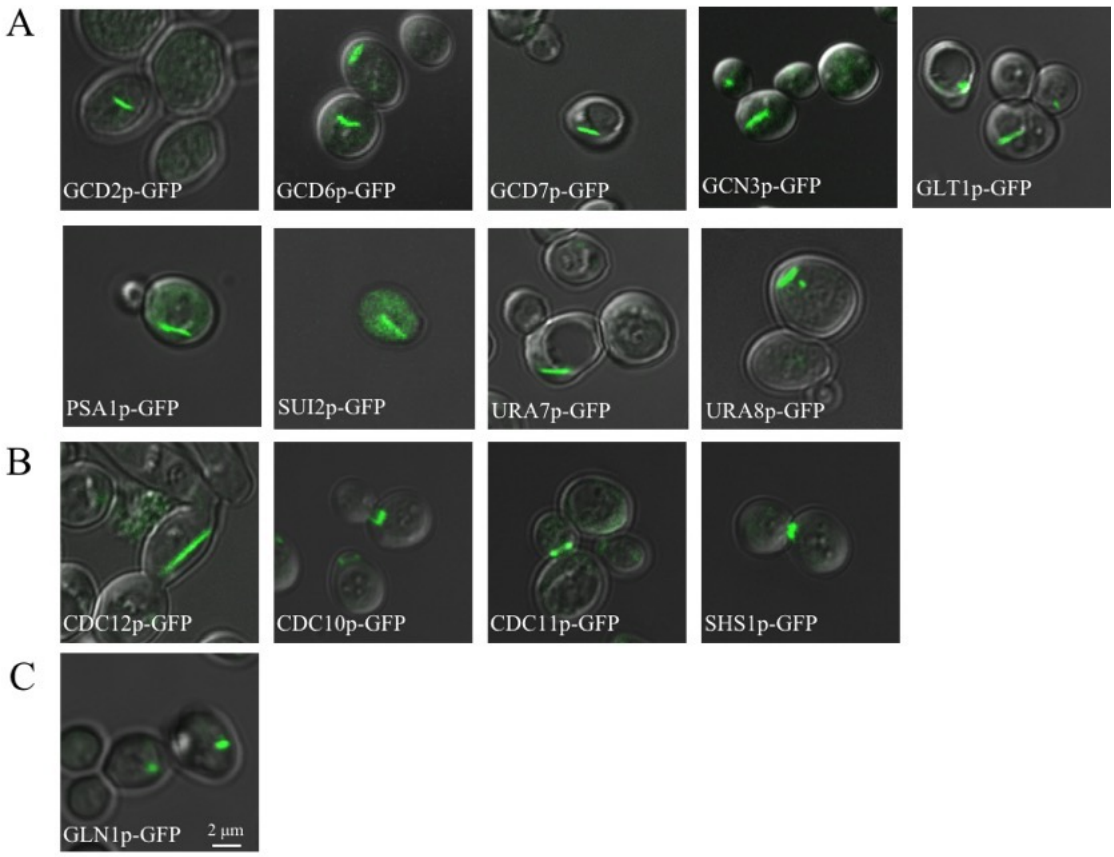


Figure 5.6. Validation of previously discovered cytoophidia in *S. cerevisiae*. (A) A total of 9 cytoophidia including GCD2p-GFP, GCD6p-GFP, GCD7p-GFP, GCN3p-GFP, GLT1p-GFP, PSA1p-GFP, SUI2p-GFP, URA7p-GFP and URA8p-GFP was confirmed in this screening and previously reported in an independent study[100]. (B) CDC10p-GFP, CDC11p-GFP, CDC12p-GFP and SHS1p-GFP are members of septin complex. (C) GLN1p-GFP formed short cytoophidia and foci, supporting a finding reported by Petrovska et al., 2014. Scale, 2 μm. Images modified from Shen et al., 2016.

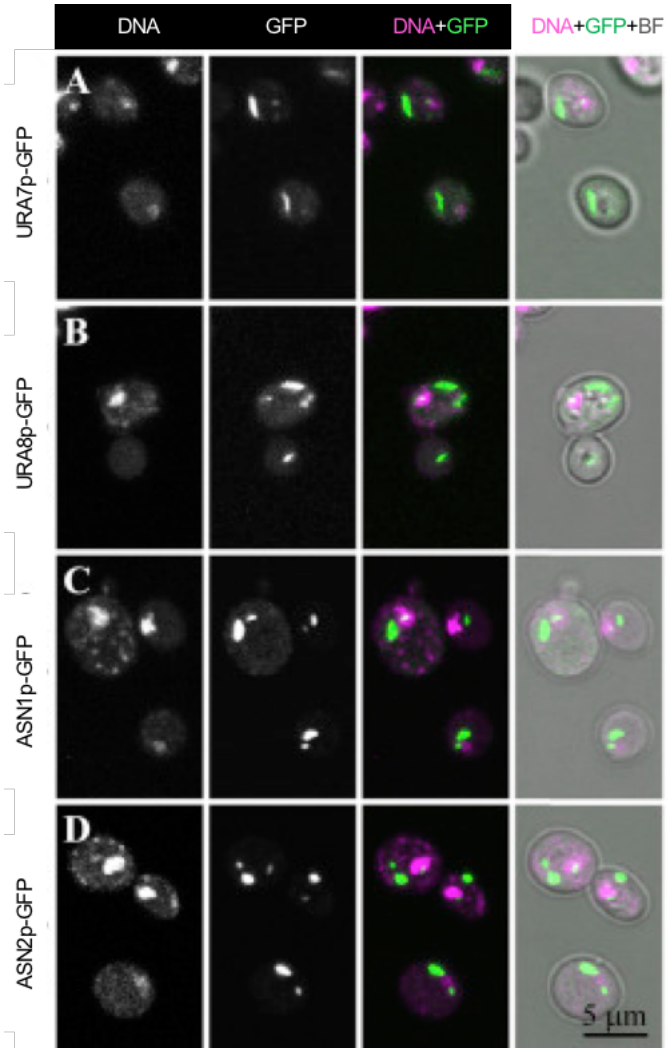


Figure 5.7. Characterization of CTPS and ASNS cytoophidia spatial distributions in *S. cerevisiae*. It is inconclusive that CTPS (URA7p-GFP and URA8p-GFP) and ASNS (ASN1p-GPP and ASN2P-GFP) could potentially assembled into cytoophidia in both nucleus and cytoplasm at diauxic phase. Scale, 5μm. Images adapted from Shen et al., 2016.

5.3.4 Bioinformatic analysis of 23 cytoophidia-forming proteins

The potential protein interactions of 23 cytoophidium-forming proteins were analyzed using STRING database (version 10.1) with highest confidence of 0.900 and based on interaction sources including textmining, experiments, databases, co-expression, gene neighborhood, gene fusion and co-occurrence (Figure 5.8). GCD1p-GFP, GCD2-GFP, GCD6p-GFP, GCD7p-GFP, GCN3p-GFP and SUI2p-GFP were clustered as they involved in a similar biological process, the regulation of translational initiation[326]. Likewise, CDC10p-GFP, CDC11p-GFP, CDC12p-GFP and SHS1p-GFP were clustered according to their functions in forming septin ring[327,328]. GLT1p-GFP, GLN1p-GFP and GDH2p-GFP were predicted to interact in regulating nitrogen metabolism. ACC1p-GFP and GLT1p-GFP were predicted to interact based on a finding reporting that glutamate was required for the activation of acetyl-CoA carboxylase[329] while the interactions between GLT1p-GFP, GLN1p-GFP and GDH2p-GFP were predicted due to their involvements in nitrogen metabolism. In *S. cerevisiae*, the paralogs of phosphofructokinase (PFK1p-GFP, PFK2p-GFP), CTP synthase (URA7p-GFP, URA8p-GFP) and asparagine synthetase (ASN1p-GFP, ASN2p-GFP) were expected to interact as they involved in catalyzing similar enzymatic reaction. For instance, URA7p-GFP and URA8p-GFP were colocalized in *S. cerevisiae*[100]. The detail of the biological function of each protein was summarized in Table 5.1.

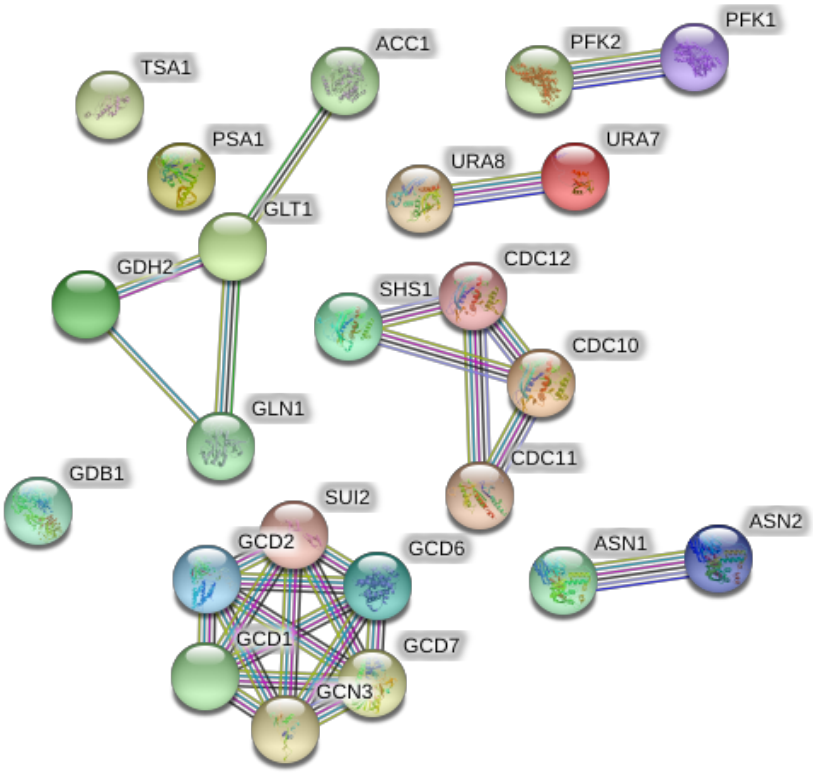


Figure 5.8. A map of potential protein interaction of 23 cytoophidia in *S. cerevisiae* produced by STRING database. Protein nodes indicates the availability of 3D protein structure and each of interaction evidence is color-coded. Modified from Shen et al., 2016.

Protein	Description	Biological process
ACC1p	**Acetyl-CoA carboxylase**	**Long chain fatty acid biosynthesis**
ASN1p	**Asparagine requiring**	**Asparagine biosynthesis**
ASN2p	**Asparagine requiring**	**Asparagine biosynthesis**
CDC10p	Cell division cycle	Septin ring assembly
CDC11p	Cell division cycle	Septin ring assembly
CDC12p	Cell division cycle	Septin ring assembly
GCD1p	**General control derepressed**	**Regulation of translational initiation**
GCD2p	General control derepressed	Regulation of translational initiation
GCD6p	General control derepressed	Regulation of translational initiation
GCD7p	General control derepressed	Regulation of translational initiation
GCN3p	General control nonderepressible	Regulation of translational initiation
GDB1p	**Glycogen debranching enzyme**	**Glycogen catabolism**
GDH2p	**Glutamate dehydrogenase**	**Nitrogen compound metabolism**
GLN1p	Glutamine synthetase	Glutamine biosynthesis

Continued.

Protein	Description	Biological process
GLT1p	Glutamate synthase	Glutamate biosynthesis
PFK1p	**Phosphofructokinase**	**Glycolytic process**
PFK2p	**Phosphofructokinase**	**Glycolytic process**
PSA1p	GDP-mannose pyrophosphorylase	GDP- mannose biosynthesis
SHS1p	Seventh homolog of septin	Septin ring assembly
SUI2p	Suppressor of initiation codon	Regulation of translational initiation
TSA1p	**Thiol- specific antioxidant**	**Cell redox homeostasis**
URA7p	Uracil- requiring	CTP biosynthesis
URA8p	Uracil- requiring	CTP biosynthesis

Table 5.1. A total of 23 cytoophidium-forming proteins identified in *S. cerevisiae*. The novel cytoophidium-forming proteins identified in this study are in bold.

5.3.5 Cytoophidia assemblies reflected nutrient status in *Saccharomyces cerevisiae*

The growth of *S. cerevisiae* can be classified into three main phases namely, exponential, diauxic and stationary[330]**.** However, the correlation of distinct growth phases to cytoophidia assemblies is unclear. To investigate the correlation between distinct growth phases and cytoophidia abundance, I selected 5 glutamine-utilizing enzymes involved in amino acid metabolism (ASN1p-GFP, ASN2p-GFP, GLT1p-GFP) and pyrimidine metabolism (URA7p-GFP, URA8p-GFP) respectively. As expected, quantitative analysis of cytoophidia abundance displayed an increasing pattern of propensity of the selected enzymes to assemble into cytoophidia from exponential to stationary phase. In the exponential phase, ASN1p-GFP and ASN2p-GFP did not form cytoophidia while the abundances of GLT1p-GFP, URA7p-GFP and URA8p-GFP were low. The lengths of GLT1p-GFP and URA7p-GFP cytoophidia were significantly increased in cells at the stationary phase while other enzymes assembled into cytoophidia with comparable lengths between diauxic and stationary phases. Collectively, the abundance of cell with cytoophidia and length of cytoophidia were gradually increased from exponential to stationary phase, implying the severity of nutrient scarcity.

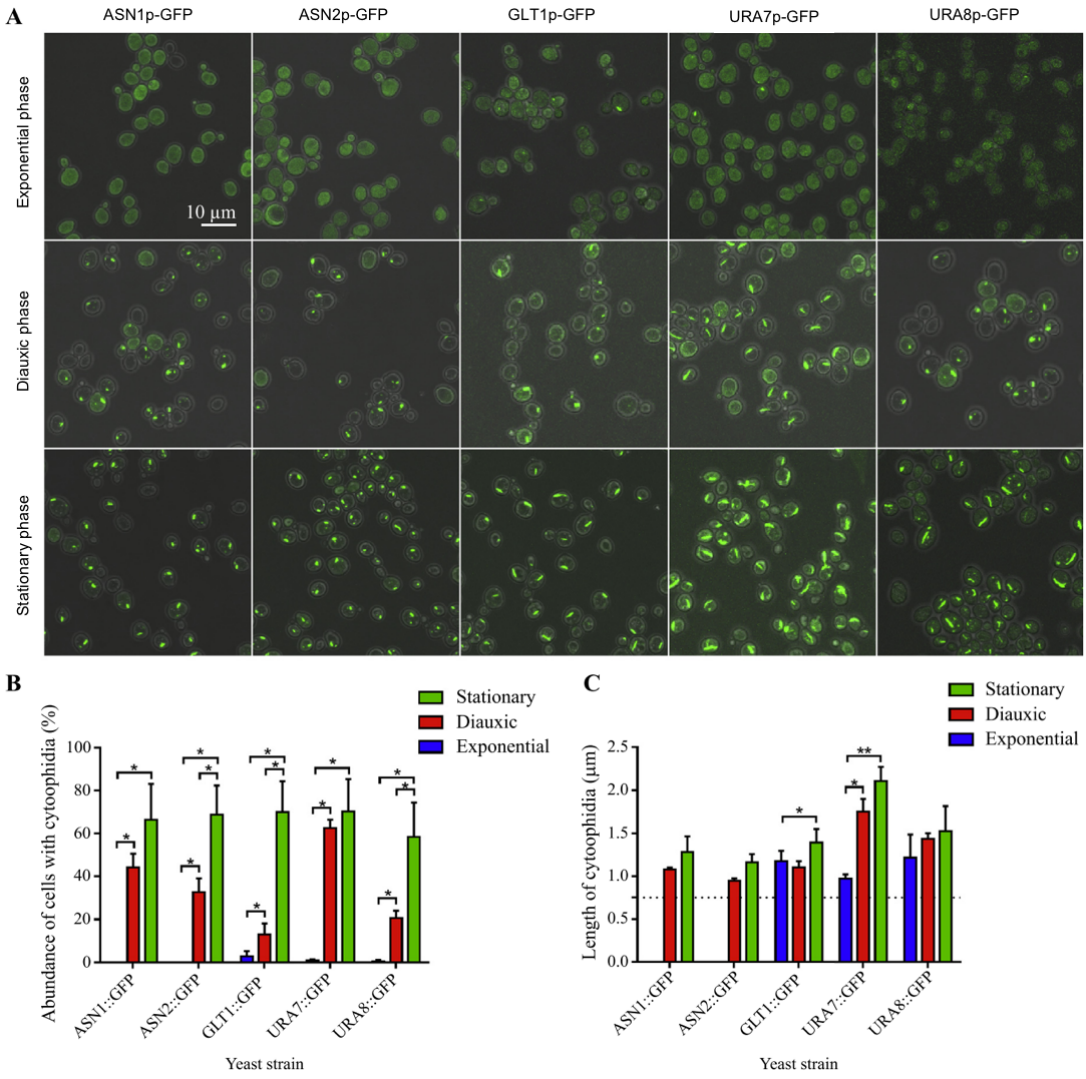


Figure 5.9. The assemblies of glutamine-dependent metabolic enzymes into cytoophidia at different growth phases. (A) Photomicrographs of yeast cells displaying gradual changes in the abundance and length of cytoophidia from exponential to stationary phase. Scale bar, 10 μm. Comparative analysis of (B) abundance and (C) length of cytoophidia at different growth phases. The cutoff value of cytoophidium length was 0.75 μm. Data are presented as mean ± SEM of three independent experiments, n=3. The statistical analyses of cytoophidium abundance and length were performed using one-way ANOVA, except for ASN1p-GFP and ASN2p-GFP, which were analyzed by Student t-test (two-tailed). Adapted from Shen et al., 2016.

5.4 Discussion

5.4.1 Stress-induced CTPS1 and IMPDH1 cytoophidia assemblies in breast cancer cells

Regulation of metabolism is tightly coordinated and achieved through compartmentalization of cell. There is an increasing realisation that the stress adaptation through reorganization of cellular architecture confers protection and pro-survival advantages to the cells. One of the examples of macromolecular assemblies of metabolic enzymes are the assemblies IMPDH and CTPS cytoophidia[107].

According to several studies, the glutamine analog, DON is frequently used to induce CTPS1 and IMPDH2 assemblies in human cells as mechanistically, this molecule blocks intracellular glutamine utilization through glutaminase inhibition by binding to the enzyme active site[331]**.** In TNBC primary tumors and cell lines, glutaminase mRNA is elevated and associated with high glutamine consumption and dependency on the exogenous glutamine availability[126]**.** Generally, TNBC is a heterogenous disease and can be classified into 6 stable subtypes including basal-like 1, basal-like 2, a mesenchymal, a mesenchymal stem-like, an immunomodulatory and a luminal androgen receptor subtype[332]**.** Therefore, it is important to assess glutamine dependency in different types or metastatic clones of TNBC cells as glutamine metabolism is considered as one of the promising targets in treating cancer[333].

Recently, a new potent, reversible and orally bioavailable glutaminase inhibitor, CB-830 is used in the clinical trial to treat advanced solid tumors (clinical trial identifier: NCT02071862). My preliminary studies demonstrated that brain metastatic MDA231-BR cells were more dependent on glutamine than lung metastatic MDA231-LG cells, marked by a complete inhibition of mTORC1 and a significant increase in CTPS1 and

IMPDH1 cytoophidia assemblies induced by DON treatment (Figure 5.1-5.3). The assemblies of CTPS1 cytoophidia did not alter CTPS1 protein level which indicated that CTPS1 protein equilibration was maintained in response to inhibition of glutamine utilization by DON treatment (Figure 5.4). Importantly, this finding suggested the presence of intrinsic heterogeneity within the same TNBC subtype as MDA231 cells had been classified as mesenchymal stem-like TNBC cells. My studies suggest that targeting glutamine metabolism should be tailored to specific subtypes or metastatic clones of TNBC cells that are addicted to glutamine.

5.4.2 The assembly of cytoophidium is a nutrient stress adaption strategy in budding yeast

Recently, a screening of CTPS1 cytoophidia in 81 human cancer tissue samples including 11 cancer types on a tumor tissue array has been performed to elucidate the possible association of CTPS1 cytoophidia abundance and aggressiveness of tumor[116]. Therefore, it is important to systematically screen for cytoophidia-forming proteins at the endogenous level as this will help us in understanding cytoophidium biology at both physiological and pathological conditions, especially in cancer.

For a comprehensive and systematic screening of cytoophidium-forming proteins, the commercially available *S. cerevisiae* GFP clone collection expressing full length open reading frames (ORFs) containing *A. victoria* green fluorescent protein (GFP) (S65T) under the control of endogenous promoter was used[127]. This system allows the identification of cytoophidium-forming proteins at the endogenous level (Figure 5.5-5.6) and at specific subcellular localization such as nucleus (Figure 5.7). However, these data should be interpreted with caution as GFP has been shown to alter protein conformation.

Acetyl-CoA carboxylase (ACC) catalyzes ATP- and biotin-dependent synthesis of malonyl-CoA which functions as an important substrate for fatty acyl chain elongation system and fatty acyl synthase[334,335]. Several previous studies have reported that ACC forms filamentous structure detectable under electron microscope and these assemblies are induced by the allosteric activator, citrate[336,337]. Importantly, the most catalytically active form of ACC is in the filamentous form[336]**.** Recently, a cryo-electron microscopy study on human ACC structure revealed that the ACC activity is regulated by at least two different types of filament: 1) ACC-citrate filaments locks ACC in its catalytically competent state; and 2) dimerization of BRCA1 C terminal (BRCT) domain of breast cancer type 1 susceptibility protein (BRCA1) with phosphosite loop of ACC locks ACC in its catalytically inactive state in the double stranded BRCT-ACC filaments[338]. ACC activity is inhibited by AMPK by phosphorylating ACC at serine 80 residue and the binding of BRCA1 to ACC through its C-terminal tandem inactivates ACC by preventing dephosphorylation of serine 80 residue[339,340]**.** At diauxic phase, the cell density still increases, despite a reduction in growth rate and glucose exhaustion[341]. At this point, the cell growth and division still require production of lipid for inclusion in the membrane of internal organelles and plasma membrane[341]. Hence, ACC1p-GFP may remain catalytically active in cytoophidia to sustain lipid production at the diauxic phase. According to in-silico protein-protein interaction analysis, GLT1p-GFP and ACC1p-GFP were predicted to be interacted and this prediction was supported by a finding that reported that glutamate was required for the polymerization of ACC into filaments and promoted phosphatase-mediated ACC activation[329] (Figure 5.8).

Asparagine synthetase (ASN) catalyse the synthesis of L-asparagine from L-aspartate and glutamine in an ATP-dependent reaction[342]**.** In response to cellular stresses including protein limitation and imbalance dietary amino acid composition, ASN transcription is activated through amino acid response (AAR), a process that is triggered upon amino acid starvation[343]. The transcription of ASN is also enhanced by

endoplasmic reticulum stress through PERK-eIF2-ATF4 arm of unfolded protein response (UPR). Both AAR and UPR increase the synthesis of ATF4 which binds to C/EBP-ATF response element (CARE), inducing ASN transcription. In tumor, ASN regulates cell proliferation through its enzymatic product, asparagine, that serves as amino acid exchange factor, which means intracellular asparagine exchanges with extracellular amino acids[344]. Several studies reported that L-asparaginase-resistant leukaemia cells displayed elevated expression of ASN[345,346]. Besides, a study reported that upregulation of ASN protected pancreatic cancer cells from apoptosis induced by glucose depletion and cisplatin treatment[347]. In our screening, we found that both ASN1p-GFP and ASN2p-GFP formed cytoophidia, however, the enzymatic activities of these enzymes in the cytoophidia at the diauxic phase remained unclear. A recent study by Zhang et al., 2018 reported several important findings on ASN cytoophidium biology in budding yeast including: 1) ASN1 and ASN2 cytoophidia can be induced by glucose depletion; 2) ASN1 and ASN2 were colocalized and this finding was in parallel with the in-silico protein-protein interaction analysis that predicted an interaction between both paralogs (Figure 5.8); 3) ASN2 cytoophidium assembly was dependent on ASN1; 4) ASN1 and URA7 colocalized either in side-by-side or head-to-head orientations[348].

In response to adverse conditions such as nutrient starvation, hypoxia or DNA damage, the mRNAs encoded for proteins essential for cell survival and stress recovery are translated, despite the repression of global protein synthesis[349]. The regulation of initiation of protein translation in eukaryotes is tightly regulated and it is mediated by recycling of eukaryotic initiation factor 2 (eIF2) by guanine nucleotide exchange factor, eIF2B[326]. A previous finding has reported that 5 subunits of eIF2/eIF2B complex can polymerized into cytoophidia at the diauxic phase of *S. cerevisiae*, namely GCD2p-GFP (eIF2B-δ), GCD6p-GFP (eIF2B-ε), GCD7p-GFP (eIF2B-β), GCN3p-GFP (eIF2B-β) and SUI2p-GFP (eIF2-α)[100]. In our screening, we found another subunit of this complex,

GCD1p-GFP (eIF2B-γ), formed cytoophidia. GCD1p-GFP has been previously reported to form foci, however, the images presented in this article showed GCD1p-GFP formed the filamentous structure, in parallel with our observation and terminology as cytoophidia[326]. A previous colocalization study has reported that GCD2p-GFP colocalized with GCD6p-GFP, GCD7p-GFP, GCN3p-GFP and SUI2p-GFP, suggesting that they are likely the components of similar cytoophidia[100]. According to in-silico protein-protein interaction analysis of cytoophidium forming proteins, GCD1p-GFP was predicted to interact with other components of eIF2/eIF2B complex (Figure 5.8). Thus, a colocalisation study between GCD1p-GFP cytoophidium with other subunits of eIF2/2B complex should be carried out to confirm its presence within similar cytoophidia.

Peroxiredoxin (PRX) is a widely conserved member of thioredoxin-dependent peroxidases that functions as antioxidant by sensing and detoxifying reactive oxygen species (ROS) including hydrogen peroxide[350]. A recent study in *S. cerevisiae* reported that TSA1 has a novel non-peroxidase function which is required for an efficient flux of gluconeogenesis by modulating pyruvate kinase 1 (PYK1) activity[351]. TSA1 not only modulates the activity of PYK1, but also other target proteins to ensure maximum biomass especially during diauxic shift by maintaining the production of catabolites, not only for growth but also for maintenance of cell integrity during stationary phase by accumulating two main glucose stores which are trehalose and glycogen essential for desiccation tolerance[351]. As TSA1p-GFP assembled into cytoophidia at the diauxic phase, it would be essential to understand how TSA1p-GFP in the cytoophidia interacts and suppresses PYK1 activity in ensuring the efficiency of transition from glycolysis to gluconeogenesis, leading to a speculation that TSA1p-GFP cytoophidium is required for the suppression of PYK1 activity.

Phosphofructokinase (PFK) catalyses the rate-limiting step in the glycolysis by phosphorylating fructose-6-fructose to fructose- 1,6-biphosphate[352]**.** In our screening,

PFK1p-GFP and PFK2p-GFP assembled into cytoophidia. In 1980, PFK has been shown to assemble into filamentous structure containing stacked tetramers according to a transmission electron microscopic study[353]. However this study lacks of information on regulation of PFK1 cytoophidia formation, the conformation of PFK tetramer subunits in filaments and its occurrence under physiological state[353]. A recent study in mammalian cells has reported that the regulation of PFK filament assembly is substrate-dependent, apolar and made of stacked tetramers with exposed catalytic sites positioned along the edge of filament[354]. This finding also suggests that PFK filaments may contain catalytically competent PFK[354]. The downregulation of PFK is one of the key events taking place during the transition from exponential growth on glucose to diauxic growth on ethanol of *S. cerevisiae*[355]**.** In parallel with this observation, it is unclear whether conformation of the PFK1p-GFP and PFK2p-GFP in the cytoophidia at the diauxic phase allows efficient substrate transfer to the catalytic sites in response to low availability substrate or inhibit the enzymatic activities by blocking the entry of substrate to the catalytic site. Thus, the similar approaches presented in Web et al., 2017 should be taken to investigate the structure-function relationship of PFK1p-GFP and PFK2p-GFP cytoophidia in order to better understand the regulation of glucose metabolism by cytoophidium assembly during transition of growth phases in yeast.

Glycogen and trehalose are two glucose stores accumulated in *S. cerevisiae*[356]. The levels of glycogen and trehalose vary in response to different environmental stresses, implying their metabolisms are tightly regulated[356]**.** Glycogen is characterised as a high molecular mass branched polysaccharide of linear α (1, 4)-glucosyl chain with α (1, 6)-linkages. Glycogen can be degraded via two pathways: (1) glycogen phosphorylase and glycogen debranching enzyme (GDB) catalyze the production of large amount of glucose-1-phosphate and free glucose which is converted to glucose 6-phosphate, entering glycolysis and TCA cycle; and (2) autophagy-dependent degradation of

glycogen through the lysosomal 1,4-α-glucosidase activity. In budding yeast, GDB1p-GFP was another enzyme assembled into cytoophidium at the diauxic phase. As glycogen is stored during cellular stress, it is speculative that the assemblies of GDB1p-GFP into cytoophidia may imply that these filamentous structures store inactive GDP1-GFP to prevent degradation of glycogen.

Septins are GTP-binding cytoskeletal proteins that play a conserved role in cytokinesis and also involved in various biological processes including apoptosis, chromosome segregation, migration and others[357–359]. They are highly conserved from yeast to human and by far, 14 members have been identified in human genome[360]. They are categorized as the fourth cytoskeletal proteins and can polymerized into high-order cytoskeletal structures including bundles, filaments and rings by heteromeric complex formation[361]. In cancer, alterations of septin proteins conferred by mutation or changes in expression is associated with tumorigenesis[362,363]. In *S. cerevisiae*, cell division control protein (CDC)3, CDC10, CDC11 and CDC12 septins associate end-to-end to form filaments consisting heterooctomer consisting of CDC11-CDC12-CDC3-CDC10-CDC10-CDC3-CDC12-CDC11[327]. The terminal subunit however, can be replaced by SHS1, leading to the formation of alternative heterooctomers[328]. In our screening of cytoophidium-forming proteins, only CDC10p-GFP, CDC11p-GFP, CDC12p-GFP and SHS1p-GFP assembled the diauxic phase and predicted to interact with each other septin proteins to regulate cytokinesis (Figure 5.8). The assemblies of septins into cytoophidia may indicate that the yeast cells still undergo cell division although the declination of cell growth during diauxic phase.

Guanosine-5'-diphospho-mannose pyrophosphorylase (PSA1) catalyzes the biosynthesis of GDP-mannose which is the precursor for mannose residues in glycoconjugates, using mannose 1-phosphate and GTP as substrates[364]. Depletion of PSA1 leads to defective cell wall, impaired cell separation and budding[365]. As the yeast

cells undergo asymmetrical division at the diauxic phase[366], this may suggest that PSA1p-GFP is still in active state as this enzyme is indispensable for cell wall integrity and budding process.

Glutamate dehydrogenase 1 (GDH1) is $NADP^+$-dependent anabolic enzyme that generates glutamate from ammonium and α-ketoglutarate[367]. In contrast, NAD^+-dependent GDH2 catalyzes the reversal reaction[368]. Alternatively, glutamate can also be synthesized by NAPDH-dependent GLT1 from glutamine and α-ketoglutarate and this process is reversed by GS. In our screening, GDH2 was one of the cytoophidium-forming proteins. Previously, two independent studies reported that GLT1 and GS were able to assemble into cytoophidia in budding yeast[100,110]. According to a previous study, the cylindrical shape of GS allows the enzymes to stack from end-to-end in forming a cytoophidium and through a zip-like mechanism, it allows fusions of neighbouring cytoophidia to form thicker cytoophidia[110]. This study also highlighted that GS cytoophidium is formed in response to acidification of the cytoplasm due to nutrient starvation, leading to a conclusion that GS cytoophidium serves as a storage depot containing inactive enzymes[110]. Taken together, the regulation of nitrogen metabolism in budding yeast during nutrient stress could be regulated through cytoophidia assemblies and interactions of key metabolic enzymes involved in this pathway (Figure 5.8).

The biology of CTPS cytoophidia has been widely studied in different organisms[103,112,325,369]. The cytoophidium assembly of CTPS inhibit its catalytic activity in bacteria while in human cells, CTPS activity is upregulated in cytoophidia[111]. Through cryo-EM studies, the divergent repercussion of CTPS cytoophidium assembly on enzymatic activity is contributed by the difference in the overall cytoophidium architecture and also CTPS protomer conformation[111]. However, the catalytic activity of

CTPS in URA7-GFP and URA8-GFP cytoophidia in budding yeast remains unexplored and requires a similar approach to elucidate the functional consequences of cytoophidium assembly on catalytic activity of budding yeast CTPS.

In *S. cerevisiae,* it was not conclusive that both CTPS and ASN paralogs could assembled into cytoophidia in the cytoplasm and nucleus (Figure 5.7). This was due to two possibilities. Firstly, if the nuclear staining did not work, it was not concluded that the cytoophidium was localized to the nucleus. Secondly, if the staining did work in which case the staining occupied the entire cell volume and from the data shown, it was not concluded that the cytoophidium was present in the cytoplasma. However, a recent study has further demonstrated that CTPS and ASN colocalized to the nucleus in budding yeast[348]. Previously, a study has reported that the nuclear IMPDH cytoophidium localizes to the nuclear envelope in mammalian cells[115]. In addition to its ability to form cytoophidium in nucleus, the function of nuclear IMPDH is known, which acts as a sequence-specific transcriptional repressor that does not requires its catalytic activity, impedes cell proliferation by binding and repressing expression of E2 factor (E2F) which is an important regulator of cell proliferation[114]. As the exact role of CTPS in nucleus remains unclear, it is speculated that the nuclear CTPS cytoophidia may assist transcription process by regulating the production of nucleotide to be incorporated into RNA *in situ* and also modulating CTPS1 transport into and out of nucleus under specific conditions[370]. Taken together, cytoophidia assemblies in the nucleus may represent a novel mechanism in regulating metabolic processes in the nucleus.

5.4.3 The abundance and length of cytoophidia reflected metabolic status of *Saccharomyces cerevisiae*

Proliferation of eukaryotic cells is controlled in concert by various growth factors and nutrients. In *S. cerevisiae*, the cells consume carbon sources such as glucose and

galactose through fermentation process, whereas non-fermentable ethanol and glycerol are consumed through respiration[371]. The ethanol produced during the exponential growth phase is consumed at the respiratory diauxic phase. Once the ethanol and other essential nutrients are fully consumed, the cells stop mitotic division and arrest within the G_1 phase of the mitotic cell cycle, a growth phase defined as stationary phase that is characterised by reduction of overall growth rate, accumulation of glycogen and acquisition of resistance to multiple environmental stresses by thickening the cell wall and the ability to remain viable in an extended period of starvation[372]. A detailed understanding of the transition of growth phases is essential as several studies on stationary phases are indeed performed with yeast cells growing in the post-diauxic phase, leading to conclusions that may be inaccurate. In this study, I defined yeast growth phases based on previously reported studies[330,373].

To understand the regulation of cytoophidia at different growth phases, I selected five cytoophidium-forming proteins involved in amino acid (ASN1p-GFP, ASN2p-GFP, GLT1p-GFP) and pyrimidine metabolisms (URA7p-GFP, URA8p-GFP). Generally, these enzymes contain a common domain which is the glutamine amidotransferase (GAT) domain[374]. GAT functions by channelling ammonia from a glutamine substrate to an acceptor substrate in the synthase site, generating different aminated products. There are two classes of GAT domains. Triad GAT (class I) which utilizes histidine and glutamate residues in activating cysteine thiol group. N-terminal nucleophile GAT is classified as class II GAT which composed of catalytic cysteine at N-terminus and α-amino group is required for the activation of thiol group. The open α/β structure fold in glutaminase is common in class I GAT whereas, the anti-parallel β-sheets are constituted in class II GAT. This implies that GAT domain could potentially play important roles in conferring the ability of a protein to assemble into cytoophidium.

As the assembly of metabolic enzymes into cytoophidia during starvation may represent a strategy to maintain metabolic homeostasis, there was an increasing pattern of abundance and length of glutamine-utilizing enzymes in budding yeast cells cultured from exponential to stationary phase, in parallel with the severity of nutrient scarcity (Figure 5.9). Although mTORC1 senses and alters cellular metabolic activities according to the availability of various nutrients, a previous study has shown that inhibition of mTORC1 by rapamycin or its upstream regulator, PI3K pathway by LY294002 suppressed IMPDH cytoophidia assemblies in HEK293T cells, suggesting that the assemblies of proteins into distinct cytoophidia are regulated in mTORC1-independent manner[375].

5.5 Conclusion

In conclusion, the intrinsic heterogeneity of glutamine dependency existed between distinct metastatic clones derived from the same tumor type and the widespread assemblies of various metabolic enzymes into cytoophidia may represent as a strategy to adjust metabolic activities with nutrient status. The structure-function studies of cytoophidium-forming proteins are essential, not only for an in-depth understanding of metabolic regulation through cytoophidium assembly, but also may open new avenues for the therapeutic development to specifically inhibit or promote the cytoophidium assembly in metabolic diseases especially cancer.

Chapter 6.0. Summary and future work

6.1 EV-mediated glutamine symbiosis between luminal and basal breast cells

In Chapter 3, my findings demonstrated that the luminal MCF-7 cells were more resistant to glutamine deprivation as compared to the two metastatic clones of basal MDA231 cells I tested. Firstly, I found that the basal expression of GS was higher in luminal MCF-7 cells which implied the ability of cells to endogenously generate intracellular glutamine in compensating the deprivation of extracellular glutamine (Figure 3.1); and secondly, my immunoblotting data showing that glutamine deprivation only suppressed 4E-BP1 activity marked by a complete downshift of γ-band while retaining the phosphorylated level of S6 in luminal MCF-7 cells, suggesting that glutamine majorly controlled mTORC1 function in mRNA translation through 4E-BP1 activity (Figure 3.2).

Due to difference in glutamine dependency, I further demonstrated that intercellular glutamine symbiosis existed between luminal and basal breast cells and this process is mediated by EVs based on three findings. Firstly, luminal glutamine-deprived MCF-7 secretome enhanced the growth of glutamine-deprived MDA231 cells regardless of the metastatic clones in co-culture transwell system, leading to a speculation that a component of cell secretome could modulate this process (Figure 3.3). Secondly, characterization of EV protein composition demonstrated that GS level was only significantly upregulated in EVs secreted by glutamine-deprived MCF-7 cells, while the upregulation of GS expression in WCL of all tested BC cell lines may implied as a general mechanism in cells to compensate the deprivation of extracellular glutamine (Figures 3.4 D and E). Thirdly, these EVs secreted by glutamine-deprived luminal MCF-7 cells enhanced the growth of glutamine-deprived MDA231 cells potentially through transferring of catalytically active GS which in turn, increased the intracellular pool of glutamine (Figure 3.5). A previous finding has reported that glutamine level was reduced

in the tumor core region due to poor organization of tumor vasculature[376]. In this regard and supported by my current findings, I hypothesized that EVs secreted from non-tumorigenic luminal cells in the mammary gland could facilitate the growth of primary TNBC originated from glutamine-dependent basal myoepithelial cells (Figure 6.1).

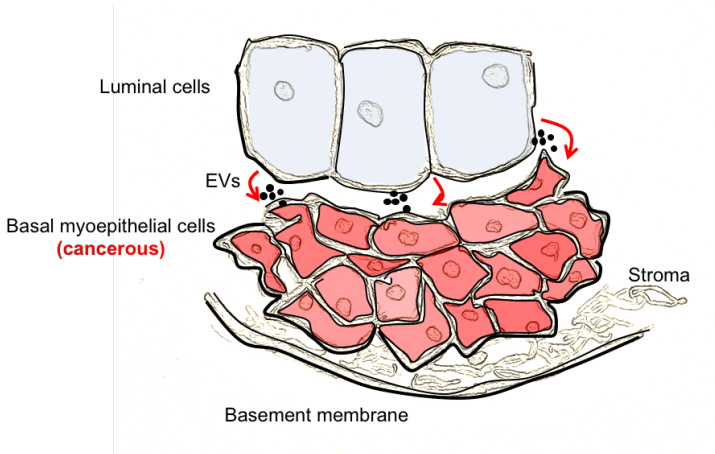


Figure 6.1. Modulation of intercellular glutamine symbiosis by EVs. A proposed model of EV-mediated glutamine symbiosis in primary basal TNBC tissue. The growth of primary basal breast cancer cells (red) in glutamine deprived region could be sustained or enhanced by EVs (black circles) secreted by the adjacent glutamine-independent luminal cells (blue) in the mammary duct.

A previous study related to intercellular glutamine symbiosis between luminal and basal breast cells reported several interesting findings. Firstly, the intracellular glutamine level in glutamine-deprived luminal MCF-7 was higher than in glutamine-deprived basal MDA231 cells, implying the capacity of glutamine-deprived MCF-7 cells to endogenously synthesize glutamine from intracellular glutamate or other sources. Secondly, the intracellular glutamine level in glutamine-deprived MDA231 cells was higher when co-cultured with MCF-7 as the feeder cells, leading to increase in growth of glutamine-deprived basal MDA231 cells. Thirdly, a stronger induction of canonical

amino acid response (AAR) program in response to glutamine deprivation through the upregulation of DNA-damage-inducible transcript 3 (DDIT3) and X-box binding protein 1 (XBP1) in basal MDA231 cells than luminal glutamine-deprived MCF-7 cells[53].

By referring to these findings, I aimed to investigate whether EVs secreted by glutamine-deprived MCF-7 cells enriched with GS could modulate several processes such as: 1) increasing intracellular glutamine level; 2) reducing the expression of AAR genes, XBP1 and DDIT3; and 3) reducing GS protein level in glutamine-deprived basal MDA231 cells of both metastatic clones. As I demonstrated that GS-enriched EVs secreted by glutamine-deprived luminal MCF-7 cells displayed growth-promoting function in the recipient cells, knockdown of GS in MCF-7 would confirm whether GS is the main protein secreted EVs responsible for the enhanced growth of glutamine-deprived basal MDA231 cells. In accordance to the findings described above, I also aim to characterized GS expression in the primary human breast tumor tissues by immunohistochemistry method to mark glutamine-deprived region in the tumor and correlate GS expression with disease stages.

Another related important finding in Chapter 3 was the deprivation of extracellular glutamine led to increasing pattern of EV secretion by MCF-7 and MDA231-BR cells while keeping MDA231-LG EV secretion unaltered (Figure 3.4 C). As initially described in Section 3.3.3, I aimed to further investigate the expression levels of ESCRT-III components such as ALIX, CHMP4C, VPS4B and VTA1 in response to glutamine deprivation as silencing of these proteins led to increase in EV secretion[377].

Lastly, a preliminary study on the expressions of EV surface markers using MACSPlex platform indicated that the majority of EV surface markers were detected in MCF-7 EVs while these markers were least detected in EVs secreted by MDA231-LG and MDA231-BR cells (Figure 3.6 A). Likewise, glutamine deprivation downregulated more surface

markers in MCF-7 EVs than in EVs secreted by both metastatic clones of MDA231 cells. Due to the EV heterogeneity, I aimed to investigate the subpopulations of EVs by coupling a custom SEC method that use Sephacryl S-1000 resin for fractionation of standard SEC-isolated EVs according to different sizes, with the MACSPlex assay for profiling EV surface markers. This will allow the characterization of surface markers and function of specific subpopulation of EVs.

6.2 mTORC1 inhibition minimally altered EV protein composition, function and biodistribution

The first major finding reported in Chapter 4 was the brain metastatic MDA231-BR cells were less sensitive to ATP-competitive mTOR kinase inhibitor as compared to lung metastatic MDA231 cells. This was evidenced by a partial inhibition of mTORC1 activity which was marked by a complete downshift of γ-band of 4E-BP1 while minimally dephosphorylating S6, suggesting that targeting mTOR kinase activity in brain-metastatic TNBC was not efficient in suppressing tumor growth (Figure 4.1).

The inhibition of mTORC1 by INK128 decreased EV secretion by MDA231-LG cells while increased EV secretion by MDA231-BR cells (Figure 4.2 C). As the secretion of EV is partly regulated by ESCRT components, I aim to measure the expression levels of ESCRT-0/1 (HRS, STAM1 and TSG101) and ESCRT-III (ALIX, CHMP4C, VPS4B and VTA1) components as silencing of ESCRT-0/1 and -III proteins have led to decrease and increase in EV secretion, respectively.

Next, the characterization of protein composition by proteomic analysis and function of EV secreted by both metastatic clones of MDA231 cells has led to several important findings. Firstly, the EVs secreted by MDA231-LG and MDA231-BR cells were likely to be functionally distinct, according to the FunRich-based annotation overrepresentation

enrichment analysis (Table 4.2 and Figure 4.7) and manual annotation analysis (Figure 4.8). Secondly, the putative function of EVs secreted by INK128-treated MDA231 cells of both metastatic clones was expected to be associated with EMT activation and migration-promoting function (Tables 4.3.and 4.4). Thirdly, the EVs secreted by both MDA231-LG and MDA231-BR cells equally enhanced the growth of HBEC-5i cells cultured in serum-free growth media (Figures 4.14 A and B), although the growth-promoting function of MDA231-BR EVs was thought to be higher due to a significant lower basal expression of PTEN in MDA231-BR cells indicating a higher proliferative capacity than MDA231-LG cells (Figure 4.13). Fourthly, the suppression of mTORC1 by INK128 minimally altered the protein composition (Figures 4.10 and 4.11) and retained the growth-promoting functions of EVs secreted by both metastatic clones of MDA231 cells potentially due to a compensatory activation of ERK pathway (Figure 4.14 D). Lastly, the preliminary in vivo study of fluorescently-labeled EV biodistribution demonstrated that the tested EV concentration was tolerated in mice and detectable in brain and other selected organs.

Given these encouraging findings, several follow-up experiments can be proposed including: 1) investigation on the difference in cell adhesion-promoting capacity of EVs secreted by both metastatic clones of MDA231 cells through MTT-based cell adhesion assay as previously described as the manual annotation analysis of cell adhesion process indicated a marked difference in protein abundance associated with cell adhesion between MDA231-LG EVs and MDA231-BR EVs[378]; 2) investigation on the migration-promoting function of EVs secreted by INK128-treated MDA231 cells on human endothelial cell migration through wound healing assay which is a conventional in vitro method to probe collective cell migration in 2 dimensions[379] and 3) a full scale in vivo biodistribution assay (4 mice per group, n=4) of fluorescently labeled EVs to reproduce the current preliminary finding and also allow investigation on how inhibition of mTORC1 by INK128 could alter the biodistribution of the secreted EVs.

6.3 Cytoophidium assembly reflects tumor heterogeneity in glutamine dependency

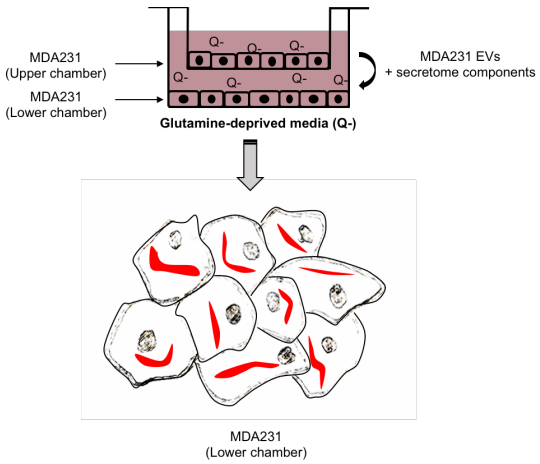
In Chapter 5, my findings demonstrated the tumor heterogeneity in glutamine dependency between different metastatic clones of TNBC cells. The brain metastatic MDA231-BR cells were more glutamine dependent than lung metastatic MDA231-LG cells based on two main findings: 1) a complete suppression of mTORC1 marked by downshift of γ-band of 4E-BP1 and dephosphorylation of S6 (Figure 5.1); and 2) the abundance of CTPS1 and IMPDH1 cytoophidia were significantly higher in MDA231-BR cells following DON treatment (Figures 5.2 and 5.3).

As CTPS1 and IMPDH1 cytoophidia assemblies were associated with glutamine deprivation, these findings may suggest that the application of CTPS1 and IMPDH1 cytoophidia to mark glutamine-deprived region of tumor which is associated with therapeutic resistance[376]. In this regard, I aimed to further investigate the spatial distributions of CTPS1 and IMPDH1 cytoophidia specifically in the periphery and core region of patient-derived TNBC tissues, co-staining with HIF1α, a marker of tumor core region induced by hypoxia.

Apart from using DON to identify the difference in glutamine dependency between different metastatic clones of MDA231 cells, I aimed to substitute this treatment with glutamine deprived growth condition as several previous findings have reported that glutamine deprivation induces CTPS1 and IMPDH2 cytoophidia[109]. As suggested by my findings in Chapter 3 on the lineage-specific glutamine dependency in breast cancer cells, I suspect that glutamine deprivation may markedly induce cytoophidium assembly in basal MDA231 cell lines as compared to luminal MCF-7 cells. If this holds true, this will allow investigation on the function of glutamine-deprived MCF-7 EVs which are

enriched with GS in reducing cytoophidium assembly in glutamine-dependent MDA231 cells cultured in glutamine-deprived growth media (Figure 6.2).

A



B

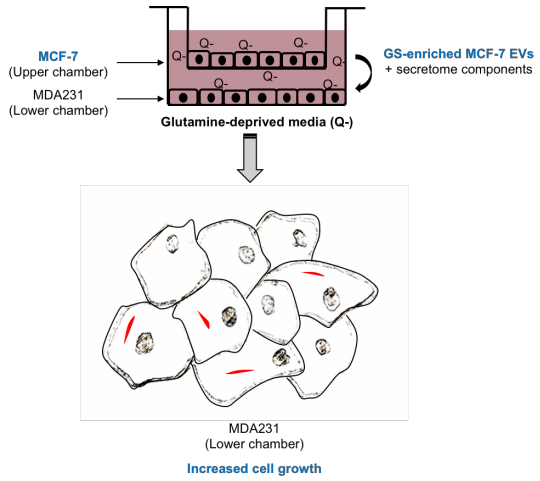


Figure 6.2. Modulation of cytoophidium assembly by EVs. A proposed model of EV-mediated regulation of cytoophidium assembly in glutamine-dependent basal TNBC MDA231 cells. GS-enriched EVs secreted from glutamine-deprived luminal MCF-7 cells may reduce assemblies of cytoophidia and enhance cell growth of basal MDA231 cells in glutamine-deprived media. Q-: 0 mM of glutamine.

6.4 Widespread assemblies of cytoophidia in *S. cerevisiae*

The assemblies of proteins into cytoophidia are a widespread cellular phenomenon potentially to preserve proteins and maintained metabolic homeostasis during nutrient starvation based on two major findings: 1) the large-scale screening of cytoophidium-forming proteins in GFP clone collection of *S. cerevisiae* identified 23 proteins involved in regulating distinct metabolic processes were assembled into distinct cytoophidia (Figures 5.5 and 5.6) and 2) the abundance and length of glutamine-utilizing cytoophidia were gradually increased from exponential to stationary phase, implying that these changes were associated with the degree of severity of nutrient scarcity (Figure 5.9).

Following up these findings, I aim to investigate whether 23 cytoophidium-forming proteins identified in *S. cerevisiae* GFP clone collection could retain their abilities to assemble into distinct cytoophidia in human cell lines. Recently, a clustered regularly interspersed short palindromic repeat associated protein 9 (CRIPSR/CAS9)-based method has been developed to allow insertion of a GFP tag at the endogenous genomic loci which in turn, permits the investigation on both subcellular localization and also the interacting partners of protein of interest in a near-native cellular background. Alternatively, the conventional immunofluorescence staining method can be applied by using commercially available monoclonal antibodies to visualize distinct cytoophidia in human cell lines.

The stationary phase culture of budding yeast cells is populated by quiescent (Q) and non-quiescent (NQ) and these populations of yeast cells are separable by gradient-density ultracentrifugation method[330]**.** The majority of Q cells are virgin daughter cells with distinct characteristics including unbudded, relatively dense and refractile by phase-contrast microscopy, reproductively competent and synchronously reenter cell-cycle upon nutrient replenishment as compared to NQ cells[380]**.** Although the abundance and

length of glutamine-utilizing cytoophidia were highest in cells cultured at the stationary phase, it is still unclear which population of yeast cells contributes to these observations. Hence, I aim to separate Q and NQ yeast cells by density-gradient ultracentrifugation method and compare the abundance and length of cytoophidia between these populations of cells.

6.5 Conclusion

mTORC1 inhibition may have unintended consequences in BC. The non-malignant cells expressing high level of GS in the tumor microenvironment might reduce the efficiency of a monotherapy that blocks glutamine consumption in the glutamine-dependent BC cells and that, potentially inhibits cytoophidia assemblies of CTPS1 and IMPDH1 in EV-dependent manner according to my hypothesis. Likewise, TNBC that are responsive to mTORC1 inhibition may become more EMT-promoting and could promote metastasis at distant sites mediated by EV secretion. In addition to a personalized therapy, additional co-therapies to mTORC1 inhibition may need to be implemented to address potential systemic rescue mechanism. Collectively, the studies presented in this thesis demonstrated that stress-induced changes in protein composition and function of EVs and cytoophidia assemblies may function as a pro-survival strategy for cancer cells grown in unfavourable conditions.

Appendix A. The upregulated proteins in EVs secreted by MDA231-LG and MDA231-BR cells.

A

Upregulated protein in MDA231-LG EV	Description	Log 10 FC difference	P-value
S100A4	Protein S100-A4	1.980360619	4.69929E-10
TYMS	Thymidylate synthase	1.976438323	<0.000000000000001
ADAMTS14	A disintegrin and metalloproteinase with thrombospondin motifs 14	1.951981449	<0.000000000000001
KRT7	Keratin, type II cytoskeletal 7	1.623085565	<0.000000000000001
EXOC7	Exocyst complex component 7	1.569493447	5.07E-13
IFIT1	Interferon-induced protein with tetratricopeptide repeats 1	1.56782984	7E-15
SRPK1	SRSF protein kinase 1	1.46412213	3.38E-13
EIF1AY	Eukaryotic translation initiation factor 1A, Y-chromosomal	1.370061597	2.82806E-10
RPL29	60S ribosomal protein L29	1.241547972	6.63582E-10
GSTM4	Glutathione S-transferase Mu 4	1.232651292	0.000172214
SSSCA1	Sjoegren syndrome/scleroderma autoantigen 1	1.178958669	4.52128E-09
ZDHHC5	Palmitoyltransferase ZDHHC5	1.088617463	6.11675E-08
PSMB10	Proteasome subunit beta type-10	1.063322755	1.22495E-07
CLDN4	Claudin-4	1.048395264	1.83234E-07
MARCKS	Myristoylated alanine-rich C-kinase substrate	1.028877593	3.07744E-07
FBLN7	Fibulin-7	0.966458887	1.52037E-06
NPTN	Neuroplastin	0.950791467	2.23758E-06
RP2	Protein XRP2	0.945707925	2.53337E-06

Continued.

Upregulated protein in MDA231-LG EV	Description	Log 10 FC difference	P-value
S100A13	Protein S100-A13	0.936818376	3.14291E-06
AKR1A1	Alcohol dehydrogenase [NADP(+)]	0.914974633	5.29622E-06
CAVIN1	Caveolae-associated protein 1	0.888130018	9.90304E-06
STXBP2	Syntaxin-binding protein 2	0.858912993	0.006850861
FARP1	FERM, ARHGEF and pleckstrin domain-containing protein 1	0.847276259	9.47184E-05
MATN2	Matrilin-2	0.843856897	2.67847E-05
S100A6	Protein S100-A6	0.830375598	3.59321E-05
HSPG2	Basement membrane-specific heparan sulfate proteoglycan core protein	0.822364883	4.26989E-05
AFDN	Afadin	0.802707068	0.001105867
ATP2B4	Plasma membrane calcium-transporting ATPase 4	0.793716159	7.81736E-05
TGFBI	Transforming growth factor-beta-induced protein ig-h3	0.782429362	9.86799E-05
RARRES2	Retinoic acid receptor responder protein 2	0.778259769	0.000335792
GPC1	Glypican-1	0.777676357	0.000108755
RHEB	GTP-binding protein Rheb	0.773818244	0.000117638
CAVIN2	Caveolae-associated protein 2	0.761576062	0.000150574
EMP3	Epithelial membrane protein 3	0.731981463	0.000269527
SRP9	Signal recognition particle 9 kDa protein	0.731643681	0.000748004
ITGA4	Integrin alpha-4	0.726881503	0.000297355
ADAMTS15	A disintegrin and metalloproteinase with thrombospondin motifs 15	0.72133629	0.00033066
SH3BGRL3	SH3 domain-binding glutamic acid-rich-like protein 3	0.719503131	0.000342414

Continued.

Upregulated protein in MDA231-LG EV	Description	Log 10 FC difference	P-value
CD82	CD82 antigen	0.714914275	0.000373579
GNAO1	Guanine nucleotide-binding protein G(o) subunit alpha	0.714175865	0.000378834
VCAN	Versican core protein	0.703905829	0.000459483
SERINC2	Serine incorporator 2	0.702264949	0.000473761
YKT6	Synaptobrevin homolog YKT6	0.699274922	0.00448338
PLOD3	Procollagen-lysine,2-oxoglutarate 5-dioxygenase 3	0.697461117	0.000517995
DCTN2	Dynactin subunit 2	0.696432437	0.000527949
MELTF	Melanotransferrin	0.69298278	0.000562661
PSMB8	Proteasome subunit beta type-8	0.692330194	0.000569464
VWA1	von Willebrand factor A domain-containing protein 1	0.691615026	0.000577001
LRPPRC	Leucine-rich PPR motif-containing protein, mitochondrial	0.68926331	0.000602463
HSPE1	10 kDa heat shock protein, mitochondrial	0.687789238	0.000618946
HLA-A	HLA class I histocompatibility antigen, A-2 alpha chain	0.683758136	0.000666209
EEF1D	Elongation factor 1-delta	0.678395788	0.000734278
B2M	Beta-2-microglobulin	0.678323089	0.000735241
COL7A1	Collagen alpha-1(VII) chain	0.677317018	0.000748723
CPNE3	Copine-3	0.663697586	0.000955399
AP2S1	AP-2 complex subunit sigma	0.666151335	0.000914632
FLT4	Vascular endothelial growth factor receptor 3	0.657851969	0.001059369
S100A10	Protein S100-A10	0.650666414	0.001201494
OSTF1	Osteoclast-stimulating factor 1	0.649664824	0.001222647
PSMD14	26S proteasome non-ATPase regulatory subunit 14	0.644953359	0.001326855

Continued.

Upregulated protein in MDA231-LG EV	Description	Log 10 FC difference	P-value
ITGB4	Integrin beta-4	0.644843432	0.001329383
NAP1L4	Nucleosome assembly protein 1-like 4	0.640050536	0.001443946
BASP1	Brain acid soluble protein 1	0.639709763	0.001452441
GNG5	Guanine nucleotide-binding protein G(I)/G(S)/G(O) subunit gamma-5	0.628150007	0.001768887
BST2	Bone marrow stromal antigen 2	0.62602715	0.001833472
HTRA1	Serine protease HTRA1	0.622885988	0.00193302
G6PD	Glucose-6-phosphate 1-dehydrogenase	0.621450967	0.00198014
MYO1C	Unconventional myosin-Ic	0.612210605	0.002309636
GNA13	Guanine nucleotide-binding protein subunit alpha-13	0.608702322	0.002447369
INHBA	Inhibin beta A chain	0.599417316	0.002848953
RPL38	60S ribosomal protein L38	0.59819638	0.005838091
STK24	Serine/threonine-protein kinase 24	0.594401085	0.003090105
AGRN	Agrin	0.591988597	0.003212615
FAM49B	Protein FAM49B	0.580118303	0.003882279
CYFIP1	Cytoplasmic FMR1-interacting protein 1	0.584022687	0.003649208
GNA11	Guanine nucleotide-binding protein subunit alpha-11	0.576838362	0.004088526
EHD2	EH domain-containing protein 2	0.576819797	0.0040897
ARHGDIA	Rho GDP-dissociation inhibitor 1	0.574780202	0.004222913
BAG2	BAG family molecular chaperone regulator 2	0.571210521	0.004465582
SMC3	Structural maintenance of chromosomes protein 3	0.564620505	0.004947008
DNM2	Dynamin-2	0.561886869	0.005160122
MAMDC2	MAM domain-containing protein 2	0.557858397	0.005489365

Continued.

Upregulated protein in MDA231-LG EV	Description	Log 10 FC difference	P-value
LGALS3BP	Galectin-3-binding protein	0.55708446	0.005554749
MOB1B	MOB kinase activator 1B	0.556459242	0.005608058
KTN1	Kinectin	0.554391045	0.005787776
H2AFX	Histone H2AX	0.553589988	0.00585874
ERBIN	Erbin	0.547768575	0.006398703
CASK	Peripheral plasma membrane protein CASK	0.547682246	0.006407053
LHFPL2	LHFPL tetraspan subfamily member 2 protein	0.546560446	0.006516179
PSMD13	26S proteasome non-ATPase regulatory subunit 13	0.541117255	0.007070071
RAB11FIP5	Rab11 family-interacting protein 5	0.536593046	0.007562236
PSMC4	26S proteasome regulatory subunit 6B	0.533368957	0.007931505
NCKAP1	Nck-associated protein 1	0.532637229	0.008017558

B

Upregulated protein in MDA231-BR EV	Description	Log 10 FC difference	P-value
SLAMF7	SLAM family member 7	-2.012721921	<0.000000000000001
ESM1	Endothelial cell-specific molecule 1	-1.799438015	<0.000000000000001
JAG1	Protein jagged-1	-1.69550143	<0.000000000000001
NRXN3	Neurexin-3	-1.612366955	1E-15
EFNB1	Ephrin-B1	-1.554515575	2.1723E-11
CHPF	Chondroitin sulfate synthase 2	-1.505618655	7.2E-14
PPT1	Palmitoyl-protein thioesterase 1	-1.41190938	2.226E-12
GOT2	Aspartate aminotransferase, mitochondrial	-1.392443638	1.44825E-10
ICAM2	Intercellular adhesion molecule 2	-1.370350155	9.528E-12
HRNR	Hornerin	-1.351188514	1.8368E-11
PCSK9	Proprotein convertase subtilisin/kexin type 9	-1.309910692	7.3319E-11
ANTXR1	Anthrax toxin receptor 1	-1.297556921	1.10076E-10
DNAJB11	DnaJ homolog subfamily B member 11	-1.274284742	2.34331E-10
SLC4A7	Sodium bicarbonate cotransporter 3	-1.269618924	2.72232E-10
LRRC17	Leucine-rich repeat-containing protein 17	-1.253102403	4.60906E-10
SPRY2	Protein sprouty homolog 2	-1.251391097	4.86563E-10
ENPP7	Ectonucleotide pyrophosphatase/phosphodiesterase family member 7	-1.232625878	5.52417E-07
CHRDL1	Chordin-like protein 1	-1.231583363	9.06343E-10
CHIC2	Cysteine-rich hydrophobic domain-containing protein 2	-1.220767434	1.44529E-07
ICAM5	Intercellular adhesion molecule 5	-1.215763927	1.47957E-09

Continued.

Upregulated protein in MDA231-BR EV	Description	Log 10 FC difference	P-value
SERPINI1	Neuroserpin	-1.20718243	2.7064E-08
PCSK5	Proprotein convertase subtilisin/kexin type 5	-1.201845976	2.26586E-09
ADAMTS1	A disintegrin and metalloproteinase with thrombospondin motifs 1	-1.185516186	3.71411E-09
CD320	CD320 antigen	-1.168484129	6.17677E-09
CRISPLD1	Cysteine-rich secretory protein LCCL domain-containing 1	-1.162736678	7.32184E-09
NLGN1	Neuroligin-1	-1.14587049	1.20062E-08
FREM2	FRAS1-related extracellular matrix protein 2	-1.108570155	3.49899E-08
SEMA3A	Semaphorin-3A	-1.05150818	1.68549E-07
GABARAPL2	Gamma-aminobutyric acid receptor-associated protein-like 2	-1.031772553	2.00645E-06
TIE1	Tyrosine-protein kinase receptor Tie-1	-1.028292841	3.12519E-07
GPC4	Glypican-4	-1.027289372	3.20879E-07
SPINT2	Kunitz-type protease inhibitor 2	-1.013663458	4.58141E-07
SNX3	Sorting nexin-3	-1.009574953	5.09362E-07
GJA1	Gap junction alpha-1 protein	-1.009192429	5.14431E-07
LRP10	Low-density lipoprotein receptor-related protein 10	-0.997086488	7.02361E-07
ANTXR2	Anthrax toxin receptor 2	-0.997011739	7.037E-07
PLD3	Phospholipase D3	-0.995338376	7.34455E-07
OCLN	Occludin	-0.987418389	0.000141
ST3GAL1	CMP-N-acetylneuraminate-beta-galactosamide-alpha-2,3-sialyltransferase 1	-0.97257681	1.30537E-06
FGFBP3	Fibroblast growth factor-binding protein 3	-0.963158428	1.65011E-06
MUC5B	Mucin-5B	-0.953332749	0.000107177

Continued.

Upregulated protein in MDA231-BR EV	Description	Log 10 FC difference	P-value
SNAPC1	snRNA-activating protein complex subunit 1	-0.95189049	0.003714203
NOV	Protein NOV homolog	-0.918343526	4.89026E-06
SEZ6L2	Seizure 6-like protein 2	-0.916803548	5.07202E-06
GLG1	Golgi apparatus protein 1	-0.912851729	5.56838E-06
OAF	Out at first protein homolog	-0.91221694	5.65236E-06
PLTP	Phospholipid transfer protein	-0.912166821	5.65902E-06
UAP1	UDP-N-acetylhexosamine pyrophosphorylase	-0.910709787	2.72014E-05
ST8SIA4	CMP-N-acetylneuraminate-poly-alpha-2,8-sialyltransferase	-0.887678578	1.00063E-05
PPT2	Lysosomal thioesterase PPT2	-0.887544176	4.33063E-05
CTSC	Dipeptidyl peptidase 1	-0.885566195	1.05036E-05
B4GALT5	Beta-1,4-galactosyltransferase 5	-0.879713044	1.2008E-05
PLXDC2	Plexin domain-containing protein 2	-0.877992577	5.22949E-05
LAPTM4B	Lysosomal-associated transmembrane protein 4B	-0.870668067	6.03561E-05
MANBA	Beta-mannosidase	-0.838723878	0.000653495
NTN4	Netrin-4	-0.828790729	3.71843E-05
SLC38A1	Sodium-coupled neutral amino acid transporter 1	-0.826449582	3.91104E-05
CHSY3	Chondroitin sulfate synthase 3	-0.817106171	4.77812E-05
CIB1	Calcium and integrin-binding protein 1	-0.806583637	0.001872505
DEPDC1B	DEP domain-containing protein 1B	-0.805975551	6.0492E-05
STAM2	Signal transducing adapter molecule 2	-0.798961752	7.00803E-05
MGAT5	Alpha-1,6-mannosylglycoprotein 6-beta-N-acetylglucosaminyltransferase A	-0.796595982	7.36264E-05
SPANXD	Sperm protein associated with the nucleus on the X chromosome D	-0.794616826	7.67234E-05

Continued.

Upregulated protein in MDA231-BR EV	Description	Log 10 FC difference	P-value
PTK7	Inactive tyrosine-protein kinase 7	-0.785989842	9.17181E-05
MMP1	Interstitial collagenase	-0.785094547	9.34242E-05
PCOLCE2	Procollagen C-endopeptidase enhancer 2	-0.784786558	9.40178E-05
SAA4	Serum amyloid A-4 protein	-0.769902006	0.000127353
IQCF2	IQ domain-containing protein F2	-0.757510236	0.00016331
LAMA4	Laminin subunit alpha-4	-0.755238576	0.000170861
TMEM59	Transmembrane protein 59	-0.75206951	0.000181945
SEMA7A	Semaphorin-7A	-0.749931793	0.000189801
QSOX1	Sulfhydryl oxidase 1	-0.74220092	0.000220948
NOP2	Probable 28S rRNA (cytosine(4447)-C(5))-methyltransferase	-0.740298347	0.000646771
GRN	Granulins	-0.730436068	0.000277689
MAN2B1	Lysosomal alpha-mannosidase	-0.729224475	0.000284253
SLC38A2	Sodium-coupled neutral amino acid transporter 2	-0.728692311	0.00028718
MINPP1	Multiple inositol polyphosphate phosphatase 1	-0.726056641	0.000302101
AMIGO2	Amphoterin-induced protein 2	-0.719913929	0.000339747
PABPN1	Polyadenylate-binding protein 2	-0.705715439	0.006507921
GALC	Galactocerebrosidase	-0.704488293	0.00045451
STX6	Syntaxin-6	-0.702773513	0.000469294
STUB1	E3 ubiquitin-protein ligase CHIP	-0.700488023	0.000489691
SCAMP2	Secretory carrier-associated membrane protein 2	-0.691380523	0.000579497
OSMR	Oncostatin-M-specific receptor subunit beta	-0.679904935	0.00071449
PNP	Purine nucleoside phosphorylase	-0.678196131	0.000736927
PTPRF	Receptor-type tyrosine-protein phosphatase F	-0.676312652	0.000762417

Continued.

Upregulated protein in MDA231-BR EV	Description	Log 10 FC difference	P-value
SPANXB1	Sperm protein associated with the nucleus on the X chromosome B1	-0.675961619	0.000767257
LGMN	Legumain	-0.670615276	0.000844592
EPDR1	Mammalian ependymin-related protein 1	-0.668401293	0.006596388
NDFIP2	NEDD4 family-interacting protein 2	-0.667705444	0.002091662
KCNN4	Intermediate conductance calcium-activated potassium channel protein 4	-0.666399338	0.004070495
SEMA4B	Semaphorin-4B	-0.666178584	0.000914189
ICOSLG	ICOS ligand	-0.664445736	0.000942787
HIST1H2BA	Histone H2B type 1-A	-0.653104924	0.001151401
EXTL2	Exostosin-like 2	-0.652232825	0.00116909
PTGFRN	Prostaglandin F2 receptor negative regulator	-0.651665865	0.001180726
IGFBP1	Insulin-like growth factor-binding protein 1	-0.650643777	0.001201971
NMU	Neuromedin-U	-0.622409265	0.001948564
ADGRG6	Adhesion G-protein coupled receptor G6	-0.617138548	0.002128137
SPOCK3	Testican-3	-0.616032678	0.002167675
FRAS1	Extracellular matrix protein FRAS1	-0.615320765	0.002193496
GAR1	H/ACA ribonucleoprotein complex subunit 1	-0.611728835	0.002328129
C3orf58	Deleted in autism protein 1	-0.610467601	0.002377153
SBNO1	Protein strawberry notch homolog 1	-0.609090856	0.005001758
DNASE2	Deoxyribonuclease-2-alpha	-0.608699223	0.00244748
TPBG	Trophoblast glycoprotein	-0.606672499	0.00253045
ANGPTL4	Angiopoietin-related protein 4	-0.604733873	0.002612208
PIP4P1	Type 1 phosphatidylinositol 4,5-bisphosphate 4-phosphatase	-0.60084103	0.002783703

Continued.

Upregulated protein in MDA231-BR EV	Description	Log 10 FC difference	P-value
TFRC	Transferrin receptor protein 1	-0.599464224	0.002846777
PRCP	Lysosomal Pro-X carboxypeptidase	-0.598288246	0.002901673
LIPG	Endothelial lipase	-0.597946867	0.002917809
SLC39A14	Zinc transporter ZIP14	-0.595807636	0.003020706
PROCR	Endothelial protein C receptor	-0.593454827	0.003137648
PLA2G15	Group XV phospholipase A2	-0.591815427	0.00322158
HSPA13	Heat shock 70 kDa protein 13	-0.589237634	0.003357718
CDH4	Cadherin-4	-0.589183415	0.003360638
ADAMTS3	A disintegrin and metalloproteinase with thrombospondin motifs 3	-0.587116235	0.003473631
STC1	Stanniocalcin-1	-0.585508798	0.003563884
STEAP3	Metalloreductase STEAP3	-0.581148676	0.003819505
LPAR1	Lysophosphatidic acid receptor 1	-0.576520431	0.004109004
DIP2B	Disco-interacting protein 2 homolog B	-0.5756173	0.004167757
ITM2B	Integral membrane protein 2B	-0.574071668	0.004270102
FSTL1	Follistatin-related protein 1	-0.572550088	0.00437308
PDGFD	Platelet-derived growth factor D	-0.571579883	0.004439907
ARRDC3	Arrestin domain-containing protein 3	-0.569679671	0.004573477
SLC20A1	Sodium-dependent phosphate transporter 1	-0.562688065	0.005096829
LIPH	Lipase member H	-0.560035285	0.00530915
APP	Amyloid-beta A4 protein	-0.559981625	0.005313575
WARS	Tryptophan--tRNA ligase, cytoplasmic	-0.559286415	0.005370554
SERINC3	Serine incorporator 3	-0.555653597	0.005677422
MET	Hepatocyte growth factor receptor	-0.551573843	0.006040955

Continued.

Upregulated protein in MDA231-BR EV	Description	Log 10 FC difference	P-value
APLP1	Amyloid-like protein 1	-0.549847279	0.006200939
SDF4	45 kDa calcium-binding protein	-0.546150378	0.006556547
CLEC3B	Tetranectin	-0.543670567	0.006805223
KARS	Lysine--tRNA ligase	-0.543277917	0.006845352
PLPP3	Phospholipid phosphatase 3	-0.541658565	0.00701316
FUT8	Alpha-(1,6)-fucosyltransferase	-0.540220434	0.007165327
LIPA	Lysosomal acid lipase/cholesteryl ester hydrolase	-0.534518822	0.007798013
MAN2A1	Alpha-mannosidase 2	-0.525052327	0.008959657
PI4K2A	Phosphatidylinositol 4-kinase type 2-alpha	-0.524895158	0.008980162

Table 1. The summary of protein description, log 10 FC difference and P-value of the upregulated proteins in (A) MDA231-LG EVs and (B) MDA231-BR EVs.

Appendix B. Filamentation of metabolic enzymes in *Saccharomyces cerevisiae*

Available online at www.sciencedirect.com
ScienceDirect
Journal of Genetics and Genomics 43 (2016) 393−404
JGG
ORIGINAL RESEARCH

Filamentation of Metabolic Enzymes in *Saccharomyces cerevisiae*

Qing-Ji Shen [a,1], Hakimi Kassim [a,1], Yong Huang [a,b,1], Hui Li [a,c,1], Jing Zhang [a], Guang Li [d], Peng-Ye Wang [c], Jun Yan [d], Fangfu Ye [c], Ji-Long Liu [a,*]

[a] *Medical Research Council Functional Genomics Unit, Department of Physiology, Anatomy and Genetics, University of Oxford, Oxford OX1 3PT, UK*
[b] *Key Laboratory of Entomology and Pest Control Engineering, College of Plant Protection, Southwest University, Chongqing 400715, China*
[c] *Key Laboratory of Soft Matter Physics, Beijing National Laboratory for Condensed Matter Physics, Institute of Physics, Chinese Academy of Sciences, Beijing 100190, China*
[d] *CAS-MPG Partner Institute for Computational Biology, Shanghai Institutes of Biological Sciences, Chinese Academy of Sciences, Shanghai 200031, China*

Received 9 February 2016; revised 9 March 2016; accepted 28 March 2016
Available online 1 April 2016

ABSTRACT

Compartmentation *via* filamentation has recently emerged as a novel mechanism for metabolic regulation. In order to identify filament-forming metabolic enzymes systematically, we performed a genome-wide screening of all strains available from an open reading frame-GFP collection in *Saccharomyces cerevisiae*. We discovered nine novel filament-forming proteins and also confirmed those identified previously. From the 4159 strains, we found 23 proteins, mostly metabolic enzymes, which are capable of forming filaments *in vivo*. *In silico* protein-protein interaction analysis suggests that these filament-forming proteins can be clustered into several groups, including translational initiation machinery and glucose and nitrogen metabolic pathways. Using glutamine-utilising enzymes as examples, we found that the culture conditions affect the occurrence and length of the metabolic filaments. Furthermore, we found that two CTP synthases (Ura7p and Ura8p) and two asparagine synthetases (Asn1p and Asn2p) form filaments both in the cytoplasm and in the nucleus. Live imaging analyses suggest that metabolic filaments undergo sub-diffusion. Taken together, our genome-wide screening identifies additional filament-forming proteins in *S. cerevisiae* and suggests that filamentation of metabolic enzymes is more general than currently appreciated.

KEYWORDS: CTP synthase; Metabolic enzyme; Cytoophidium; Glycolysis; Glutamine; Intracellular compartmentation; *Saccharomyces cerevisiae*

INTRODUCTION

Compartmentation of biological processes is a fundamental feature of the cell. One such way is to form membrane-bound organelles, which have been extensively appreciated in the past. Moreover, macromolecules can be compartmentalized through the formation of large-scale aggregates without membranes (Gall, 2000; Brangwynne et al., 2009; O'Connell et al., 2012; Hyman et al., 2014). Emerging studies have identified many membraneless organelles including cytoplasmic processing bodies (P bodies) (Sheth and Parker, 2006), histone locus bodies (HLBs) (Liu et al., 2006a, 2006b), uridine-rich small nuclear ribonucleoprotein bodies (U bodies) (Liu and Gall, 2007) and purinosomes (An et al., 2008).

In 2010, three groups independently described that the metabolic enzyme CTP synthase (CTPS) can form filamentous structures in bacteria, yeast and fruit flies (Ingerson-Mahar et al., 2010; Liu, 2010; Noree et al., 2010). These filaments have been termed as "cytoophidia" (meaning cellular snakes in Greek), "CTPS filaments", or "cytoplasmic rods and rings". Subsequent studies have shown that CTPS can form filaments in human cells as well (Carcamo et al., 2011; Chen et al., 2011). Thus cytoophidia represent a novel type of evolutionarily conserved organelles. Recent studies suggest that

* Corresponding author. Tel: +44 1865 28 5833.
E-mail address: jilong.liu@dpag.ox.ac.uk (J.-L. Liu).
[1] These authors contributed equally to this work.

http://dx.doi.org/10.1016/j.jgg.2016.03.008
1673-8527/Copyright © 2016, The Authors. Institute of Genetics and Developmental Biology, Chinese Academy of Sciences, and Genetics Society of China. Published by Elsevier Limited and Science Press. This is an open access article under the CC BY license (http://creativecommons.org/licenses/by/4.0/).

polymerisation of CTPS or other metabolic enzymes into filamentous structures serves to regulate enzymatic activity (Aughey et al., 2014a, 2014b; Barry et al., 2014; Noree et al., 2014; Petrovska et al., 2014; Strochlic et al., 2014; Chang et al., 2015). Studies in *Drosophila* indicate that the CTPS cytoophidia are involved in brain development and oogenesis (Chen et al., 2011; Azzam and Liu, 2013; Strochlic et al., 2014; Tastan and Liu, 2015a; Tastan and Liu, 2015b; Wang et al., 2015). The biology of cytoophidia emerges as a new frontier in the field of pyrimidine metabolism (Aughey et al., 2014a, 2014b; Garavito et al., 2015; Liu, 2015; Tastan and Liu, 2015a; Wang et al., 2015).

Nine filament-forming proteins including CTPS were identified *via* a screening of 1632 GFP-tagged yeast strains (Noree et al., 2010), which comprise about 40% of the budding yeast GFP-tagged open reading frame (ORF) collection (Huh et al., 2003). To identify additional novel filament-forming proteins in budding yeast, we screened the whole collection of 4159 GFP-tagged ORFs, which represents 75% the *Saccharomyces cerevisiae* proteome. From this, we identified 23 proteins (including nine novel proteins) that can form filaments *in vivo* in diauxic and stationary phases. We found that these filament-forming proteins can be clustered into several groups, including translational initiation machinery and glucose and nitrogen metabolic pathways. Further analysis of the five glutamine-utilising enzymes demonstrated that the occurrence and length of the metabolic filaments are sensitive to growth conditions. In addition, we observed that four glutamine-utilising enzymes can form filaments both in the cytoplasm and in the nucleus. Live imaging analysis of six types of filament suggests that they undergo sub-diffusion. The identification of additional filament-forming proteins from our genome-wide screening provides an opportunity to study compartmentation *via* filamentation systematically.

RESULTS

Filament-forming proteins in budding yeast

Our screening has confirmed that all nine proteins identified in Noree's study (Noree et al., 2010) (i.e., Glt1p, Psa1p, Ura7p, Ura8p, Gcd2p, Gcd6p, Gcd7p, Gcn3p and Sui2p) (Fig. S1A) and all four septin proteins (i.e., Cdc10p, Cdc11p, Cdc12p and Shs1p) (Fig. S1B) available in the budding yeast GFP-tagged ORF collection can form filaments. Short filaments and foci assembled by Gln1p (glutamine synthase) could be detected (Fig. S1C), but there were no long filaments, even after starvation treatment, in the current study, with a potential interference from the GFP tag as reported previously (Petrovska et al., 2014). In addition, nine more proteins can form large-scale filaments detectable under light microscopy (Fig. 1 and Table 1), namely Acc1p (acetyl-CoA carboxylase), Asn1p/Asn2p (asparagine synthetase), Gcd1p (eIF2B-γ), Gdb1p (glycogen debranching enzyme), Gdh2p (glutamate dehydrogenase), Pfk1p/Pfk2p (phosphofructokinase) and Tsa1p (thioredoxin peroxidase). To simplify the terminology, we refer to these metabolic enzyme-containing serpent-shaped structures as cytoophidia.

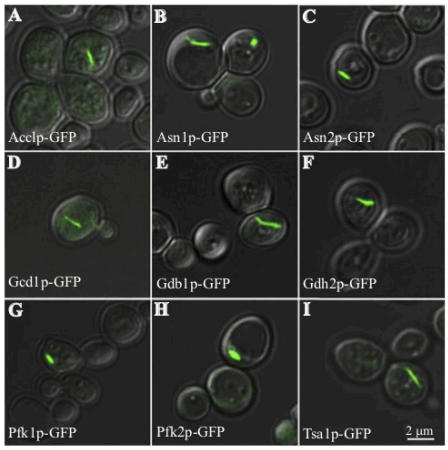


Fig. 1. Identification of filament-forming proteins in *S. cerevisiae*.
A genome-wide screening of 4159 GFP-tagged ORF collection in budding yeast identifies nine novel filament-forming proteins. **A:** Acetyl-CoA carboxylase (Acc1p). **B:** Asparagine synthetase 1 (Asn1p). **C:** Asparagine synthetase 2 (Asn2p). **D:** Gamma subunit of the translation initiation factor eIF2B (Gcd1p). **E:** Glycogen debranching enzyme (Gdb1p). **F:** Glutamate dehydrogenase (Gdh2p). **G:** Phosphofructokinase (Pfk1p). **H:** Phosphofructokinase (Pfk2p). **I:** Thioredoxin peroxidase (Tsa1p). Scale bar, 2 μm. See also Fig. S1 and Table 1.

Acetyl-CoA carboxylase catalyses the carboxylation of acetyl-CoA to produce malonyl-CoA, which provides the malonyl-CoA substrate for fatty acid biosynthesis. In mammals, acetyl-CoA carboxylase can be polymerised into tiny filaments detectable under electron microscopy (Kleinschmidt et al., 1969; Meredith and Lane, 1978). Polymerisation of acetyl-CoA carboxylase upregulates the enzymatic activity. A recent study reported that Acc1p has diffused distribution under normal growth conditions, while prolonged starvation can drive Acc1p to form rod-like structures in budding yeast (Suresh et al., 2015). Our screening revealed that Acc1p is capable of forming large-scale filaments under normal growth conditions.

Using aspartate and glutamine as the substrates, asparagine synthetase catalyses an ATP-dependent reaction to produce asparagine. In budding yeast, there are two genes, *ASN1* and *ASN2*, which encode asparagine synthetase (Dang et al., 1996). We found that Asn1p and Asn2p have very similar distributions and both can form filaments *in vivo*. Studies in *Escherichia coli* and beef pancreas suggest that asparagine synthetase functions as a dimeric enzyme (Gantt and Arfin, 1981; Larsen et al., 2000). Lack of asparagine synthetase may cause cell apoptosis (Zhang et al., 2014a). Due to its important role in amino acid synthesis, asparagine synthetase is a common target in the treatment of acute lymphoblastic leukaemia as well as prostate cancer and other kinds of cancer (Aslanian et al., 2001; Sircar et al., 2012; Panosyan et al., 2014).

Table 1
Filament-forming proteins in *S. cerevisiae*

Protein	Name description	Biological process
Acc1p	**Acetyl-CoA carboxylase**	**Long-chain fatty acid biosynthetic process**
Asn1p	**Asparagine requiring**	**Asparagine biosynthetic process**
Asn2p	**Asparagine requiring**	**Asparagine biosynthetic process**
Cdc10p	Cell division cycle	Septin ring assembly
Cdc11p	Cell division cycle	Septin ring assembly
Cdc12p	Cell division cycle	Septin ring assembly
Gcd1p	**General control derepressed**	**Regulation of translational initiation**
Gcd2p	General control derepressed	Regulation of translational initiation
Gcd6p	General control derepressed	Regulation of translational initiation
Gcd7p	General control derepressed	Regulation of translational initiation
Gcn3p	General control nonderepressible	Regulation of translational initiation
Gdb1p	**Glycogen debranching enzyme**	**Glycogen catabolic process**
Gdh2p	**Glutamate dehydrogenase**	**Nitrogen compound metabolic process**
Gln1p	Glutamine metabolism	Glutamine biosynthetic process
Glt1p	Glutamate synthase	Glutamate biosynthetic process
Pfk1p	**Phosphofructokinase**	**Glycolytic process**
Pfk2p	**Phosphofructokinase**	**Glycolytic process**
Psa1p	GDP-mannose pyrophosphorylase	GDP-mannose biosynthetic process
Shs1p	Seventh homolog of septin	Septin ring assembly
Sui2p	Suppressor of initiator codon	Regulation of translational initiation
Tsa1p	**Thiol-specific antioxidant**	**Cell redox homeostasis**
Ura7p	Uracil requiring	CTP biosynthetic process
Ura8p	Uracil requiring	CTP biosynthetic process

The novel proteins identified in this study are in bold.

Noree et al. (2010) have shown that five subunits of the eIF2 and eIF2B complexes, Gcd2p (eIF2B-δ), Gcd6p (eIF2B-ε), Gcd7p (eIF2B-β), Gcn3p (eIF2B-α), and Sui2p (eIF2-α), are present in the same filament. In this study, we identified an additional subunit of the eIF2/2B complex, Gcd1p (eIF2B-γ), which can form a similar filamentous structure. Although GFP-tagged Gcd1p (eIF2B-γ) was previously reported as foci in budding yeast (Campbell et al., 2005), the images in that paper showed filament-like structures which are in line with the results of the current study.

Glycogen is a multibranched polysaccharide of glucose residues, which acts for the energy storage in animals and yeast. The accumulation of glycogen responds to nutrient restriction, and to heat, osmotic and saline stress. Glycogen is rapidly mobilised by two enzymes, glycogen phosphorylase and glycogen debranching enzyme when non-proliferating yeast cells resume growth. The glycogen debranching enzyme Gdb1p was identified by Noree et al. (2010) as a foci-forming protein that is incapable of forming filaments. However, our screening indicated that Gdb1p is able to form filaments under normal growth conditions. Gdb1p contains two enzymatic activities, α-1,4-glucanotransferase and α-1,6-glucosidase. It is interesting to point out that filamentation of β-glucosidase was first observed in electron micrographs of oat plastids in 1965 (Gunning, 1965). More recently, biochemical analyses have suggested that the filament is the active form of the β-glucosidase (Kim et al., 2005).

In budding yeast, *GDH1* and *GDH3* encode two $NADP^+$-dependent glutamate dehydrogenases (NADP-GDHs) which catalyse the synthesis of glutamate from ammonium and α-ketoglutarate. *GDH2* encodes NAD^+-dependent glutamate dehydrogenase (NAD-GDH), which degrades glutamate and produces ammonium and α-ketoglutarate (DeLuna et al., 2001). Our screening identified that Gdh2p, but not Gdh1p or Gdh3p, can form filaments *in vivo*.

Phosphofructokinase 1 catalyses the phosphorylation of fructose 6-phosphate to fructose 1,6-bisphosphate. This reaction is the principal regulatory step in glycolysis. The yeast ortholog of human phosphofructokinase-1 consists of hetero-octamers $\alpha_4\beta_4$. Pfk1p (α subunit) and Pfk2p (β subunit) are homologous to each other. Under electron microscopy, cross-linked rabbit muscle Pfk1p has been observed to form dimeric, tetrameric, octameric and filamentous forms *in vitro* (Telford et al., 1975). Immunofluorescence images have shown the filamentous arrangement of Pfk1p in budding yeast (Schwock et al., 2004). In this study, we found that both Pfk1p and Pfk2p could form filaments in budding yeast *in vivo*. It appears that the filament-forming property of phosphofructokinase is evolutionarily conserved and ancient.

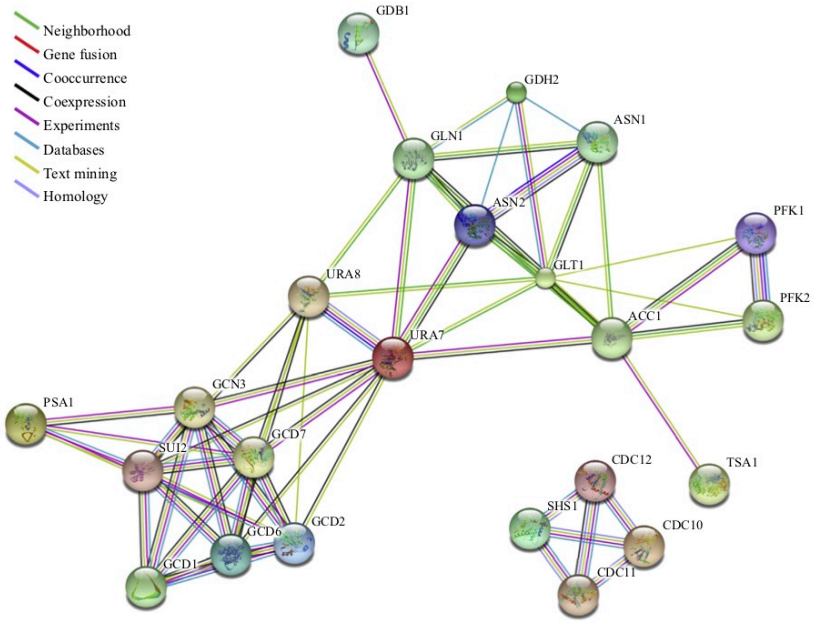


Fig. 2. Protein-protein analysis of filament-forming proteins in budding yeast.
The high-resolution evidence-view of networks was obtained with STRING under medium confidence 0.400. Protein nodes indicate the availability of 3D protein structure information and coloured lines between the proteins indicate the various types of interaction evidence. See also Table 2.

Table 2
KEGG pathways analysis of filament-forming proteins in STRING 10

KEGG pathway ID	Term	Number of genes	Gene name	*P*-value	*P*-value_FDR
sce250	Alanine, aspartate and glutamate metabolism	5	*ASN1, GLN1, ASN2, GDH2, GLT1*	4.06E-08	4.34E-06
sce3013	RNA transport	6	*GCD2, GCD1, GCN3, GCD7, GCD6, SUI2*	2.07E-07	1.11E-05
sce1100	Metabolic pathways	12	*ASN2, ACC1, ASN1, GLN1, PSA1, GLT1, GDH2, PFK2, URA7, GDB1, PFK1, URA8*	5.19E-07	1.85E-05
sce910	Nitrogen metabolism	3	*GLN1, GDH2, GLT1*	7.05E-07	1.89E-05
sce1120	Microbial metabolism in diverse environments	6	*ASN1, ASN2, GLN1, PFK1, PFK2, GLT1*	1.23E-05	2.62E-04
sce51	Fructose and mannose metabolism	3	*PFK1, PFK2, PSA1*	6.85E-05	1.22E-03
sce1110	Biosynthesis of secondary metabolites	6	*ASN2, PFK2, ASN1, PSA1, PFK1, GLT1*	2.12E-04	3.25E-03
sce1230	Biosynthesis of amino acids	4	*GLN1, PFK1, PFK2, GLT1*	6.90E-04	9.23E-03
sce52	Galactose metabolism	2	*PFK1, PFK2*	2.50E-03	2.98E-02
sce30	Pentose phosphate pathway	2	*PFK1, PFK2*	4.05E-03	3.94E-02
sce680	Methane metabolism	2	*PFK1, PFK2*	4.05E-03	3.94E-02
sce330	Arginine and proline metabolism	2	*GLN1, GDH2*	4.95E-03	4.41E-02

Oxidative stress results from oxygen metabolism and occurs in the cells of all aerobic organisms. Oxygen-utilising cells have evolved defence mechanisms called the oxidative stress response (OSR), to protect against the damage caused by oxidative stress. Thioredoxin peroxidase, Tsa1p, plays an important role in OSR. Our screening revealed that Tsa1p can form filaments *in vivo*.

Clusters of filament-forming proteins

Network analysis of proteins is useful to know how these proteins interplay with other key proteins and pathways. To assess the relationships among these 23 filament-forming proteins (Table 1), the protein-protein interaction analysis was performed by utilising the STRING database version 10 (Szklarczyk et al., 2015). Coloured lines between the proteins represent the different types of interaction evidence, and neighbourhood, cooccurrence, experiments, text mining, coexpression, databases and homology were utilised in the analysis (Fig. 2). The results illustrate the STRING gene set enrichments for those filament-forming proteins against related KEGG pathways with significance rank $P < 0.05$ after correction by false discovery rate (FDR). As expected, the septin complex proteins Cdc10p, Cdc11p, Cdc12p and Shs1p are clustered together. Enrichments on the eIF2/2B complex (Gcd1p, Gcd6p, Gcd2p, Gcd7p, Gcn3p and Sui2p) indicate the strong association with the pathway of RNA transport ($P = 1.11 \times 10^{-5}$). Five proteins (Asn1p, Asn2p, Gdh2p,

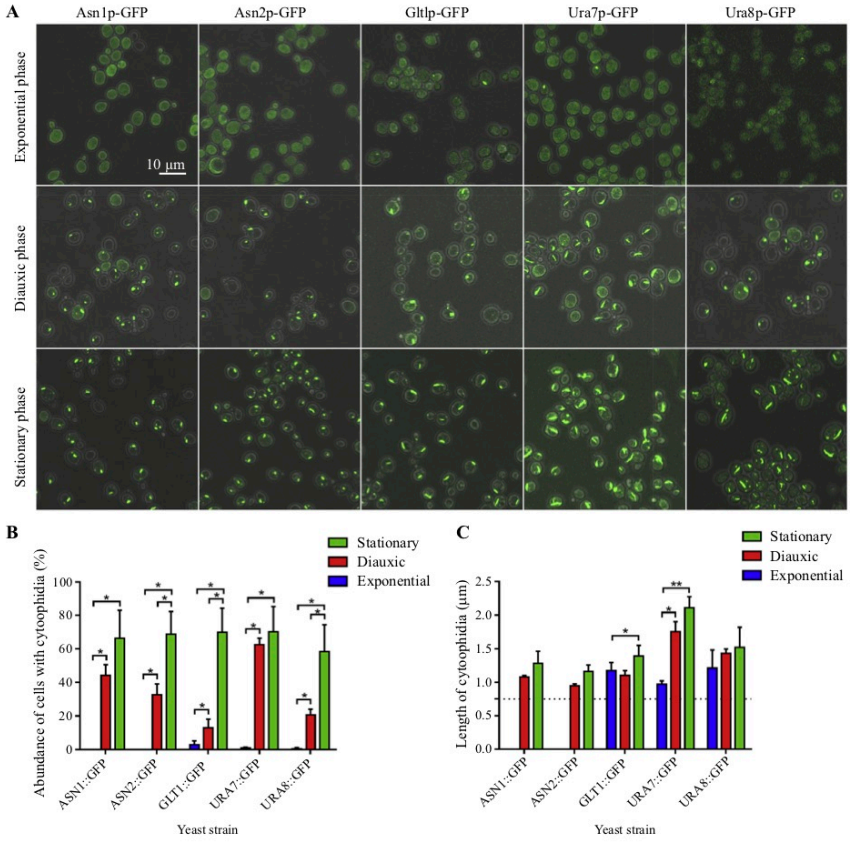


Fig. 3. The assemblies of glutamine-dependent metabolic enzymes into cytoophidia at different growth phases.
A: Photomicrographs of yeast cells displaying gradual changes in the abundance and length of cytoophidia in exponential phase, diauxic phase and stationary phase. Scale bar, 10 μm. **B:** Averaged abundance of cytoophidia formed by each enzyme. **C:** Averaged length of cytoophidia with the cutoff value of 0.75 μm. Data are represented as mean ± SD. *, $P \leq 0.05$ and **, $P \leq 0.01$.

Gln1p and Glt1p) were found to be associated with alanine, aspartate and glutamate metabolism ($P = 4.34 \times 10^{-6}$). Amongst these five proteins, Gdh2p, Gln1 and Glt1 were closely related to nitrogen metabolism ($P = 7.54 \times 10^{-5}$). Apart from the septin proteins and eIF2/2B complex, 12 of the other 13 proteins were enriched in metabolic pathways ($P = 5.55 \times 10^{-5}$), with Pfk1p, Pfk2p and Psa1p associated with fructose and mannose metabolism ($p = 7.33 \times 10^{-3}$) (Table 2).

Heterogeneities of cytoophidia in *S. cerevisiae*

In budding yeast, there are three distinct growth phases that are coupled with different metabolic signatures. However, the correlation between distinct growth phases and the regulation of cytoophidia in yeast cells remains unclear. To investigate the relationship between these two parameters, we cumulatively selected five cytoophidium-forming enzymes that are involved in amino acid (Asn1p, Asn2p and Glt1p) and pyrimidine (Ura7p and Ura8p) metabolisms, respectively. As expected, the formation of cytoophidia was gradually elevated from exponential to stationary phases (Fig. 3A).

Quantitative analyses of cytoophidia abundance displayed an increasing pattern of propensity of all five metabolic enzymes to form cytoophidia from exponential to diauxic and stationary phases (Fig. 3B). In exponential phase cultures, Asn1p and Asn2p did not coalesce into cytoophidia, whereas there was only a very low abundance of cytoophidia formed by Glt1p, Ura7p and Ura8p, respectively. These five enzymes form obvious filamentous structures in the diauxic phase. The abundance of cytoophidia increases significantly from the exponential phase to the diauxic phase and from the diauxic phase to the stationary phase. In general, all five enzymes displayed highest abundance of cytoophidia in stationary phase as compared to other growth phases.

The length of cytoophidia formed by Glt1p or Ura7p was evidently increased as the cells rested in the stationary phases, while Asn1p, Asn2p and Ura8p form cytoophidia with comparable length between the diauxic phase and the stationary phase (Fig. 3C). Collectively, these data indicated that enzymes involved in amino acids (Asn1p, Asn2p and Glt1p) and pyrimidine (Ura7p and Ura8p) biosynthetic pathways orchestrated heterogeneity in terms of the regulations of cytoophidia in different growth phases.

Filamentation in the nucleus

We previously found that CTPS can form both cytoplasmic cytoophidia (C-cytoophidia) and nuclear cytoophidia (N-cytoophidia) in mammalian cells (Gou et al., 2014). In addition, we observed that CTPS can form C- and N-cytoophidia in the fission yeast *Schizosaccharomyces pombe* (Zhang et al., 2014b). Noree et al. (2010) observed that the two CTPS proteins, Ura7p and Ura8p, can form filaments in budding yeast. However, whether Ura7p and Ura8p form structures in the nucleus remained unexplored. To address this issue, we closely looked at Ura7p-GFP and Ura8p-GFP cells counterstained with the DNA dye Hoechst 33342. Our examination suggests that both Ura7p-GFP and Ura8p-GFP can form filamentous structures in the nucleus, as well as in the cytoplasm (Fig. 4A and B). Our results regarding the subcellular distribution of CTPS in *S. cerevisiae, S. pombe* and mammalian cells indicate that both C- and N-cytoophidia are highly conserved during evolution. Encouraged by these observations, we carefully checked other filament-forming proteins in budding yeast. We found that both Asn1p and Asn2p can form nuclear filaments as well as cytoplasmic filaments (Fig. 4C and D).

Dynamics of metabolic filaments

To understand the behaviour of these filaments, we performed live imaging with *S. cerevisiae* cells expressing various filament-forming proteins fused with GFP. As was shown above, only in the diauxic and stationary phases of budding yeasts the cytoophidia were abundant and apt to be studied, therefore, we chose the budding yeasts in diauxic and stationary phases and diluted with PBS to maintain the state of cytoophidia for the following experiments. The live cells were recorded every 1.29 s for 10 min. For example, tracking of the Glt1p filaments showed that these structures are motile and located preferentially at the cell

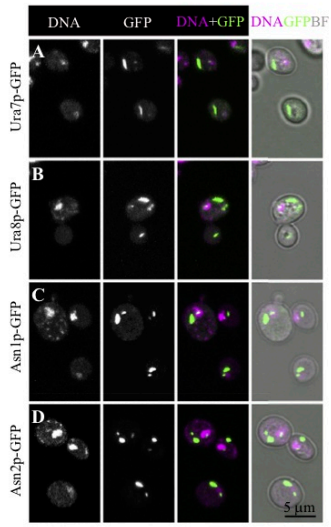


Fig. 4. Filaments formed in the cytoplasm and nucleus.
Budding yeast cells expressing GFP-tagged ORFs were observed under confocal microscopy. Both isoforms of CTPS, Ura7p (**A**) and Ura8p (**B**), can form cytoophidia in the cytoplasm and in the nucleus, consistent with our previous findings in *S. pombe* (Zhang et al., 2014b) and mammalian cells (Gou et al., 2014). Both isoforms of asparagine synthetase, Asn1p (**C**) and Asn2p (**D**), can also form cytoophidia in the cytoplasm and in the nucleus. Note that cytoplasmic cytoophidia are longer and thicker than nuclear cytoophidia. Scale bar, 5 μm.

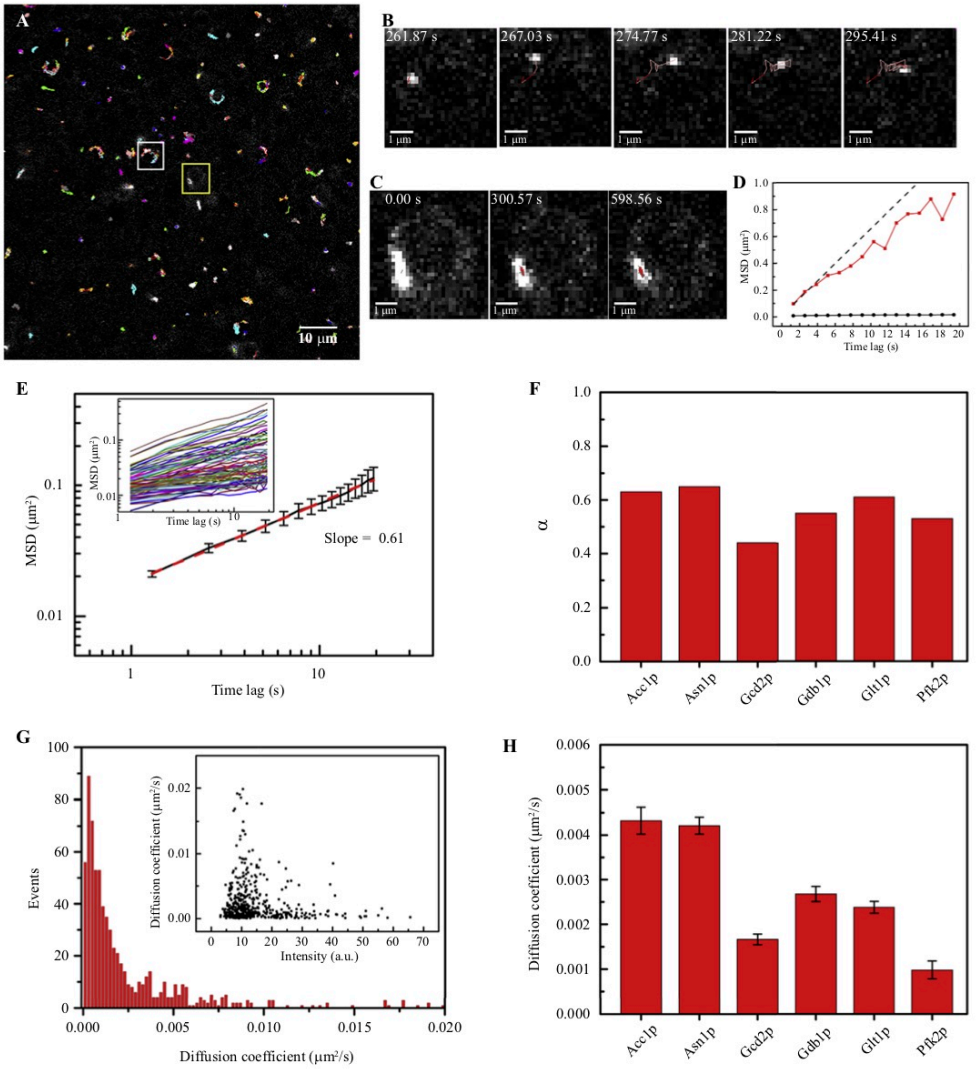


Fig. 5. Dynamic analysis of cytoophidia.

A: Representative trajectories of the Glt1p cytoophidia in budding yeast from 10 min time-lapse movies at room temperature. The paths are marked by colour lines. **B** and **C:** Image series of the Glt1p cytoophidia in the rectangular regions (white box (**B**), yellow box (**C**)) marked in (**A**). **D:** Plots of the mean square displacement (MSD) curves for the trajectories in (**B**) and (**C**). The red solid line (corresponding to the cytoophidium in (**B**)) is lower than that of a free diffusion (indicated by the dash line), showing that the cytoophidium movement in (**B**) is sub-diffusion. The black solid line (corresponding to (**C**)) remains almost unchanged over time lag, showing the cytoophidium in (**C**) is confined. **E:** Averaged MSD of ~700 Glt1p cytoophidia as a function of time lag has an exponent α about 0.61 (given by the slope of the plot), suggesting the motion type of Glt1p cytoophidia is sub-diffusion. Inset, ~100 samples of MSD curves. **F:** Comparison of averaged α values for six kinds of cytoophidia: Acc1p ($n = 122$), Asn1p ($n = 376$), Gcd2p ($n = 289$), Gdb1p ($n = 266$), Glt1p ($n = 700$), and Pfk2p ($n = 64$). **G:** Distribution of the diffusion coefficients for the trajectories of Glt1p cytoophidia ($n = 700$). The inset shows the relation between the diffusion coefficients and the fluorescence intensities for Glt1p cytoophidia. Most Glt1p cytoophidia have diffusion coefficient <0.0025 μm²/s, whereas only a few ones with relatively low intensities have larger coefficients. **H:** Comparison of diffusion coefficients of six kinds of cytoophidia, with the same sample size as (**F**). See also Data in Brief (Li et al., 2016).

cortex (Fig. 5A). A closer look at these filaments shows that some of them are highly dynamic (Fig. 5B), whereas others are relatively slow (Fig. 5C).

Generally, we selected six types of filament-forming proteins for further in-depth analysis (Fig. 5; Data in Brief see Li et al., 2016). We investigated how the mean square displacement (MSD) of the filaments varies with time lag τ. For a free random thermal diffusion, a linear relationship between the MSD and τ is expected, i.e., $\mathrm{MSD} \propto \tau^{\alpha}$, with $\alpha = 1$; for a thermal diffusion confined in certain areas, the value of α is expected to be smaller than 1; if the motion of the filaments is driven by motor proteins, the filaments would exhibit active transport, yielding an α of value larger than 1. We started by analysing the MSD curves of the two filaments shown in Fig. 5B and C and found that they were both downward compared with the dashed line (corresponding to pure random diffusion), suggesting the filaments underwent sub-diffusion, i.e., random diffusion within confined areas (Fig. 5D). The averaged MSD of the ~700 Glt1p filaments as a function of time lag was shown in Fig. 5E, whose exponent α is 0.61 (given by the slope of the plot), supporting the theory that the motion type of the Glt1p filaments is sub-diffusion. For all six types of filament-forming proteins analysed, we found that their α values were comparable (between 0.38 and 0.65) (Fig. 5F), implying that the dynamics of these filaments formed by different proteins all exhibit sub-diffusion behaviour, and are not driven by motor proteins. This conclusion support a previous study on protein aggregates in budding yeast (Zhou et al., 2011). We are, however, aware that this conclusion is based on our time resolution (1.29 s/frame) and that burst active transports (e.g., based on the actin cytoskeleton) shorter than this time resolution cannot be ruled out. Also, it should be noted that the dynamic results are acquired in the diauxic and stationary phases of budding yeasts, which is essential for cytoophidium imaging but may affect the mobility of cytoophidia.

From the MSD analysis, we could also obtain the distribution of the diffusion coefficients D for the trajectories of the filaments. For the Glt1p filaments ($n = 700$), we found that most have a very low diffusion coefficient (<0.0025 $\mu m^2/s$) (Fig. 5G), although some filaments with low intensities have relatively large coefficients (Fig. 5G, inset). This observation is reasonable because the filaments with low intensities had smaller Stoke radii and thus diffused faster in the viscoelastic cytoplasm crowded with macromolecules, which is illustrated by the fast diffusion of Fig. 5B (in contrast to Fig. 5C). For all six types of filament, we found that their diffusion coefficients ranged from 0.001 to 0.005 $\mu m^2/s$ (Fig. 5H) and are comparable with those reported by Zhou et al. (2011).

DISCUSSION

Regulation of metabolism *via* filamentation

Filamentation appears to regulate CTPS enzymatic activity as suggested in previous studies (Aughey et al., 2014a, 2014b; Barry et al., 2014; Noree et al., 2014). Thus, forming cytoophidia might serve as a complementary regulatory strategy for CTPS other than allosteric regulators or phosphorylation (Aughey et al., 2014a, 2014b).

More metabolic enzymes have been verified to form filaments by our screening. Thus, further study of the regulation of these filaments may answer questions such as whether filamentation is a common way of enzyme regulation, and whether filamentation is an indicator of a different form of cell metabolism.

Take asparagine synthetase for example. It has already been documented that under amino acid deprivation or endoplasmic reticulum stress, asparagine synthetase expression is upregulated *via* putative ATF4 transcription regulation (Chen et al., 2004). Expression level change may result in a change to filament formation. Meanwhile, the other way around, it is worth identifying whether filament formation can regulate asparagine synthetase activity under amino acid deprivation. Filament formation may either be an indicator or an active regulator of a different metabolism situation. Since the upregulation of asparagine synthetase resulted in drug resistance in acute lymphoblastic leukaemia during chemotherapy (Aslanian et al., 2001), and a high asparagine synthetase expression level was detected in prostate cancer and was also related to aggressiveness of gliomas (Sircar et al., 2012; Panosyan et al., 2014), the detailed study of the regulation of asparagine synthetase may have important clinic implications.

Growth conditions of budding yeast

Eukaryotic cell cycle is controlled in concert by specific growth factors and essential nutrients. In brief, *S. cerevisiae* utilises carbon sources (e.g., glucose or galactose) *via* fermentation and non-fermentable carbon sources (e.g., glycerol or ethanol) *via* respiration, respectively (Stahl et al., 2004). In the exponentially fermentative growth phase, ethanol produced is consumed during the second respiratory growth phase, post glucose exhaustion which is termed the diauxic shift. Once the ethanol is fully consumed, the yeast cells cease growing and shift into the stationary phase (Herman, 2002). Understanding of the growth phase transitions is vital as many studies of stationary phase are in fact conducted with cultures that are actually in the post-diauxic phase and thus, the conclusions made from these data might be misleading (Herman, 2002).

In our studies, we defined different growth phases of budding yeast based on previously documented studies (Allen et al., 2006; Davidson et al., 2011). In fact, there are two distinct fractions of cells, i.e., non-quiescence (NQ) and quiescence (Q) cells, in the stationary phase (Allen et al., 2006). Q cells can be characterised as dense, unbudded daughter cells; they are highly refractive by phase-contrast microscopy, thermotolerant, uniform in size and synchronously enter the mitotic cell cycle as compared to the NQ cells (Allen et al., 2006).

To decipher the regulation of cytoophidia in different growth phases, we analysed metabolic enzymes that involved

in the biosynthetic pathways of amino acids (Asn1p, Asn2p and Glt1p) and pyrimidine (Ura7p and Ura8p). In common, these proteins shared a common domain that is composed of glutamine amidotransferase (GAT). GATs channel ammonia from a glutamine substrate to an acceptor substrate at the synthase site to produce an array of different aminated products (Mouilleron and Golinelli-Pimpaneau, 2007). GATs are grouped into distinct classes. Triad GATs (Class I) utilise histidine and glutamate residues to activate the cysteine thiol group. N-terminal nucleophile (NTN) (Class II) GATs contain the catalytic cysteine at the N-terminus and the α-amino group is required for the activation of thiol group. The open α/β structure fold in the glutaminase domain is common in most triad GATs, whereas, anti-parallel β-sheets are the main constituent in the NTN GAT counterpart. In budding yeast, CTPS (Ura7p and Ura8p) are categorised as Class I GATs, whereas asparagine synthetases (Asn1p and Asn2p) and glutamate synthase (Glt1p) are regarded as NTN GATs. Our data indicate that proteins grouped into different GAT classes can share the common ability to coalesce into cytoophidia.

The abilities of cells to detect detrimental changes in the environment and generate specific responses by reprogramming physiological and metabolic processes are pivotal for cell survival. Budding yeast has served as a good experimental model to investigate this biological feature under nutrient starvation (Broach, 2012). Is assembly of metabolic enzyme into cytoophidium a strategy for cell survival? As suggested in the previous study that cytoophidia serve as the storage depot of metabolic enzymes under nutrient stress (Petrovska et al., 2014), the changes in the abundance of yeast cells with glutamine-utilising cytoophidia and the length of this subcellular structure in these distinct growth phases remain as a major question. In this study, an increasing pattern of the abundance and length of cytoophidia were observed as the growth phase shifted from exponential to stationary phases. These observations illustrate that cytoophidium assembly serves as a mechanism to store metabolic enzymes when the cellular conditions are not favourable for growth. However, specific pathways that regulate the formation of cytoophidia remain unknown. Target of rapamycin (TOR) protein is a serine-threonine kinase that integrates various signals from intracellular and extracellular for the regulations of metabolism, growth and even survival of cell (Laplante and Sabatini, 2009). Speculatively, this central integrator of the availabilities of nutrients and growth factors might involve in the regulation of cytoophidium formation. As cytoophidia can be formed by enzymes regulating diverse metabolic processes and displayed heterogeneities, we proposed that the reorganizations of metabolic enzymes into cytoophidia are regulated by multiple signaling pathways.

Implication of cytoophidia in human diseases

Within cells, metabolism is a highly coordinated and regulated process, which involves cooperation of many enzymes to accomplish critical functions. Metabolic enzymes are regulated at multiple levels. Abnormal metabolism contributes to several human diseases, including cancer, diabetes and obesity. Recently, we and other groups have demonstrated that the compartmentation *via* filamentation of the metabolic enzyme CTPS provides a novel mechanism for regulation of metabolic processes. We have shown that cytoophidium formation is regulated by its protein levels, glutamine availability, developmental cues and nutritional stress. Nevertheless, the finding of additional filament-forming proteins in this study highlights the complexity of intracellular compartmentation.

Nuclear cytoophidia

It is unknown if Asn1p and Asn2p form the same structures, although their patterns in the cytoplasm and nucleus are very similar to each other. Given that both Ura7p/Ura8p and Asn1p/Asn2p are glutamine-utilising enzymes, it would be interesting to see whether the Asn1p/Asn2p filaments are similar to the Ura7p/Ura8p filaments, which are sensitive to glutamine deprivation or glutamine analogue treatment. Key questions include whether and how the Asn1p/Asn2p cytoophidia interact with the Ura7p/Ura8p cytoophidia, and whether and how all of these cytoophidia regulate glutamine metabolism *via* a common mechanism.

In summary, we perform a genome-wide screening of a GFP-tagged ORF collection in budding yeast and identify novel filament-forming proteins. We also demonstrate that filamentation of metabolic enzymes is very sensitive to growth condition. Since our large-scale screening is limited in a specific growth condition, this raises the possibility that many more filament-forming proteins might escape our detection. Moreover, we demonstrate that a few glutamine-utilising enzymes form cytoophidia both in the cytoplasm and the nucleus. Therefore, the identification of the cytoophidium and its kind provides a good opportunity to link metabolic pathways and subcellular organisation.

MATERIALS AND METHODS

Yeast strains and media

S. cerevisiae strains used in this study were derived from the yeast GFP clone collection comprising 4159 GFP-tagged ORFs (Huh et al., 2003). Each strain originates from a parent strain with the genotype *MATα his3Δ1 leuΔ0 met15Δ0 ura3Δ0* (*S288c*). All yeast strains were replicated into 96-well plates consisting of 150 μL of YPD media using a pin tool and sealed with MicroAmp™ adhesive film (Applied Biosystems, Foster City, CA, USA) to reduce well-to-well contaminations. All strains were grown at 32°C for 24 h for the screening of filament-forming proteins.

Screening of filament-forming proteins

Cells were fixed in 4% paraformaldehyde for 10 min. The fixed cells were washed by PBS. Then cells were visualised under 40× objective on an inverted microscope (Nikon Eclipse Ti, Japan). Cells showing filaments were picked out

for confocal imaging. For nucleus visualisation, Hoechst 33342 was added. Imaging of fixed samples was acquired under 63× objective on a laser-scanning confocal microscope (Leica TCS SP5 II confocal microscope, Germany).

Quantification of filament-forming proteins

All yeast strains were grown overnight and diluted to an OD_{600} of ~0.05 in 3 mL of YPD at 32°C in the incubator (300 r/min) and kept for 6, 24 and 168 h which reflected the exponential phase, diauxic phase and stationary phase, respectively. Cells were transferred into 1 mL microcentrifuge tubes and spun down for 1 min at 4000 r/min. The media were decanted and 100 μL of 4% paraformaldehyde were added to each tube to fix the cells for 10 min, and then the cells were washed once with PBS. A few microlitres of cell suspension were transferred onto the slides, followed by agarose gel to avoid movement of the cells during live imaging. The samples were covered with coverslips and inverted, and some pressure was applied to remove excess liquid. The coverslips were further sealed with nail polish to avoid the samples from drying. Once the nail polish had dried, the samples were ready for microscopic analysis.

The abundance (%) and averaged length (μm) of filaments-in cells in all three growth phases were compared and quantified by capturing images in at least four different areas containing a minimum of 100 cells each, using a laser-scanning Leica TCS SP5 II confocal microscope with a 63× oil objective lens. All images were taken at multiple focal planes and each of them was deconvolved and compressed into a single image. Image processing was carried out using ImageJ software. The experiments were repeated three times independently and data were presented as mean ± SD in the bar graph. The abundance and length of cytoophidia for all metabolic enzymes were analysed by One-Way Anova (multiple comparisons), except for Asn1p and Asn2p, which were analysed by Student's *t*-test (two-tailed).

Protein-protein interaction analysis

Protein-protein interaction analysis was carried out by using the Search Tool for the Retrieval of Interacting Genes/Proteins (STRING) database version 10 (http://string-db.org/) (Szklarczyk et al., 2015). In the networks from STRING, nodes are proteins and edges are the predicted functional associations between proteins based on primary databases containing KEGG and GO, and primary literature. Various active prediction methods, such as neighbourhood, gene fusion, co-occurrence, coexpression, experiments, databases, homology and text mining, can be chosen for STRING analysis. In the current study, all of the prediction methods were used with medium confidence score 0.400.

Live imaging

For time-lapse fluorescence imaging, cells were pipetted onto Glass Bottom Microwell Dishes (MatTek Corporation, Ashland, MA, USA) at stationary stage with appropriate dilution in PBS for the cells to be a single layer on the bottom. After incubating the cells at room temperature for 30 min, time-lapse videos were taken at 1.29 s intervals between each frame over 10 min of real time. Three videos for each sample have been taken with random fields containing filaments.

Particle tracking and dynamic analysis

Tracking of the cytoophidia was performed by using the ImageJ plugin Particle Tracker (Sbalzarini and Koumoutsakos, 2005). In each frame, the cytoophidia were localized by adjusting the parameter radius and percentile in Particle Tracker software. A radius of 5–7 pixels and a percentile of 0.3%–0.5% were selected to capture the greatest number of cytoophidia that were clearly visible. The parameters of linking range and displacement were set to 2 frames and 5 pixels, respectively, to link the detected particles between frames. All the linking parameters for each kind of cytoophidia were checked and optimized manually.

For further dynamic analysis, only the trajectories longer than 15 frames (approximately 20 s) were selected. The MSD was calculated by the equation $\mathrm{MSD}(\tau) = \langle |r(t+\tau) - r(t)|^2 \rangle$, where τ is the time lag. Then the first 15 points of MSD were fitted by the power law $\mathrm{MSD}(\tau) = \mathrm{A} \cdot \tau^{\alpha}$. The exponent α indicates the nonlinear relationship of MSD with time, carrying information about the motion modes (Saxton and Jacobson, 1997): $\alpha \approx 1$ corresponds to free Brownian motion (i.e., free diffusion), $\alpha < 1$ sub-diffusion (i.e., diffusion within a crowded medium), $\alpha > 1$ super-diffusion (i.e., diffusion overlaid with deterministic motion), and $\alpha \approx 2$ directed motion. Similarly, the diffusion coefficient D is determined by fitting the 3 initial points of the MSD curves with $\mathrm{MSD}(\tau) = 4D \cdot \tau + c$. All the analyses were performed using a user-defined program in Matlab.

ACKNOWLEDGMENTS

We would like to thank the Liu group for discussion. This work was supported by the UK Medical Research Council (to J.L.L.), China Scholarship Council-University of Oxford Scholarship (to Q.J.S), Chinese Scholarship Council Studentship (to Y.H.), Malaysia Government Scholarship (to H.K.), the National Natural Science Foundation of China (No. 11304372) (to H.L., F. Y and P.Y.W.) and anonymous donation (to J.L.L.).

SUPPLEMENTARY DATA

Fig. S1. Confirmation of filament-forming proteins in *Saccharomyces cerevisiae*.

Supplementary data related to this article can be found at http://dx.doi.org/10.1016/j.jgg.2016.03.008.

REFERENCES

Allen, C., Buttner, S., Aragon, A.D., Thomas, J.A., Meirelles, O., Jaetao, J.E., Benn, D., Ruby, S.W., Veenhuis, M., Madeo, F., Werner-Washburne, M.,

2006. Isolation of quiescent and nonquiescent cells from yeast stationary-phase cultures. J. Cell Biol. 174, 89−100.

An, S., Kumar, R., Sheets, E.D., Benkovic, S.J., 2008. Reversible compartmentalization of *de novo* purine biosynthetic complexes in living cells. Science 320, 103−106.

Aslanian, A.M., Fletcher, B.S., Kilberg, M.S., 2001. Asparagine synthetase expression alone is sufficient to induce l-asparaginase resistance in MOLT-4 human leukaemia cells. Biochem. J. 357, 321−328.

Aughey, G.N., Grice, S.J., Shen, Q.J., Xu, Y., Chang, C.C., Azzam, G., Wang, P.Y., Freeman-Mills, L., Pai, L.M., Sung, L.Y., Yan, J., Liu, J.L., 2014a. Nucleotide synthesis is regulated by cytoophidium formation during neurodevelopment and adaptive metabolism. Biol. Open 3, 1045−1056.

Aughey, G.N., Tastan, Ö.Y., Liu, J.L., 2014b. Cellular serpents and dreaming spires: new frontiers in arginine and pyrimidine biology. J. Genet. Genomics 41, 561−565.

Azzam, G., Liu, J.L., 2013. Only one isoform of *Drosophila melanogaster* CTP synthase forms the cytoophidium. PLoS Genet. 9 e1003256.

Barry, R.M., Bitbol, A.F., Lorestani, A., Charles, E.J., Habrian, C.H., Hansen, J.M., Li, H.J., Baldwin, E.P., Wingreen, N.S., Kollman, J.M., Gitai, Z., 2014. Large-scale filament formation inhibits the activity of CTP synthetase. eLife 3, e03638.

Brangwynne, C.P., Eckmann, C.R., Courson, D.S., Rybarska, A., Hoege, C., Gharakhani, J., Julicher, F., Hyman, A.A., 2009. Germline P granules are liquid droplets that localize by controlled dissolution/condensation. Science 324, 1729−1732.

Broach, J.R., 2012. Nutritional control of growth and development in yeast. Genetics 192, 73−105.

Campbell, S.G., Hoyle, N.P., Ashe, M.P., 2005. Dynamic cycling of eIF2 through a large eIF2B-containing cytoplasmic body: implications for translation control. J. Cell Biol. 170, 925−934.

Carcamo, W.C., Satoh, M., Kasahara, H., Terada, N., Hamazaki, T., Chan, J.Y., Yao, B., Tamayo, S., Covini, G., von Muhlen, C.A., Chan, E.K., 2011. Induction of cytoplasmic rods and rings structures by inhibition of the CTP and GTP synthetic pathway in mammalian cells. PLoS One 6, e29690.

Chang, C.C., Lin, W.C., Pai, L.M., Lee, H.S., Wu, S.C., Ding, S.T., Liu, J.L., Sung, L.Y., 2015. Cytoophidium assembly reflects upregulation of IMPDH activity. J. Cell Sci. 128, 3550−3555.

Chen, H., Pan, Y.X., Dudenhausen, E.E., Kilberg, M.S., 2004. Amino acid deprivation induces the transcription rate of the human asparagine synthetase gene through a timed program of expression and promoter binding of nutrient-responsive basic region/leucine zipper transcription factors as well as localized histone acetylation. J. Biol. Chem. 279, 50829−50839.

Chen, K., Zhang, J., Tastan, O.Y., Deussen, Z.A., Siswick, M.Y., Liu, J.L., 2011. Glutamine analogs promote cytoophidium assembly in human and *Drosophila* cells. J. Genet. Genomics 38, 391−402.

Dang, V.D., Valens, M., Bolotin-Fukuhara, M., Daignan-Fornier, B., 1996. Cloning of the *ASN1* and *ASN2* genes encoding asparagine synthetases in *Saccharomyces cerevisiae*: differential regulation by the CCAAT-box-binding factor. Mol. Microbiol. 22, 681−692.

Davidson, G.S., Joe, R.M., Roy, S., Meirelles, O., Allen, C.P., Wilson, M.R., Tapia, P.H., Manzanilla, E.E., Dodson, A.E., Chakraborty, S., Carter, M., Young, S., Edwards, B., Sklar, L., Werner-Washburne, M., 2011. The proteomics of quiescent and nonquiescent cell differentiation in yeast stationary-phase cultures. Mol. Biol. Cell 22, 988−998.

DeLuna, A., Avendano, A., Riego, L., Gonzalez, A., 2001. NADP-glutamate dehydrogenase isoenzymes of *Saccharomyces cerevisiae*. Purification, kinetic properties, and physiological roles. J. Biol. Chem. 276, 43775−43783.

Gall, J.G., 2000. Cajal bodies: the first 100 years. Annu. Rev. Cell Dev. Biol. 16, 273−300.

Garavito, M.F., Narváez-Ortiz, H.Y., Zimmermann, B.H., 2015. Pyrimidine metabolism: dynamic and versatile pathways in pathogens and cellular development. J. Genet. Genomics 42, 195−205.

Gantt, J.S., Arfin, S.M., 1981. Elevated levels of asparagine synthetase activity in physiologically and genetically derepressed Chinese hamster ovary cells are due to increased rates of enzyme synthesis. J. Biol. Chem. 256, 7311−7315.

Gou, K.M., Chang, C.C., Shen, Q.J., Sung, L.Y., Liu, J.L., 2014. CTP synthase forms cytoophidia in the cytoplasm and nucleus. Exp. Cell Res. 323, 242−253.

Gunning, B.E., 1965. The fine structure of chloroplast stroma following aldehyde osmium-tetroxide fixation. J. Cell Biol. 24, 79−93.

Herman, P.K., 2002. Stationary phase in yeast. Curr. Opin. Microbiol. 5, 602−607.

Huh, W.K., Falvo, J.V., Gerke, L.C., Carroll, A.S., Howson, R.W., Weissman, J.S., O'Shea, E.K., 2003. Global analysis of protein localization in budding yeast. Nature 425, 686−691.

Hyman, A.A., Weber, C.A., Julicher, F., 2014. Liquid-liquid phase separation in biology. Annu. Rev. Cell Dev. Biol. 30, 39−58.

Ingerson-Mahar, M., Briegel, A., Werner, J.N., Jensen, G.J., Gitai, Z., 2010. The metabolic enzyme CTP synthase forms cytoskeletal filaments. Nat. Cell Biol. 12, 739−746.

Kim, S.Y., Kim, Y.W., Hegerl, R., Cyrklaff, M., Kim, I.S., 2005. Novel type of enzyme multimerization enhances substrate affinity of oat beta-glucosidase. J. Struct. Biol. 150, 1−10.

Kleinschmidt, A.K., Moss, J., Lane, D.M., 1969. Acetyl coenzyme A carboxylase: filamentous nature of the animal enzymes. Science 166, 1276−1278.

Laplante, M., Sabatini, D.M., 2009. mTOR signaling at a glance. J. Cell Sci. 122, 3589−3594.

Larsen, T.M., Boehlein, S.K., Schuster, S.M., Richards, N.G., Thoden, J.B., Holden, H.M., Rayment, I.I., 2000. Three-dimensional structure of *Escherichia coli* asparagine synthetase B: a short journey from substrate to product. Biochemistry 39, 7330.

Li, H., Huang, Y., Wang, P.Y., Ye, F., Liu, J.L., 2016. Data on dynamic study of cytoophidia in *Saccharomyces cerevisiae*. Data in brief, Submitted.

Liu, J.L., 2010. Intracellular compartmentation of CTP synthase in *Drosophila*. J. Genet. Genomics 37, 281−296.

Liu, J.L., Buszczak, M., Gall, J.G., 2006a. Nuclear bodies in the *Drosophila* germinal vesicle. Chromosome Res. 14, 465−475.

Liu, J.L., Gall, J.G., 2007. U bodies are cytoplasmic structures that contain uridine-rich small nuclear ribonucleoproteins and associate with P bodies. Proc. Natl. Acad. Sci. USA 104, 11655−11659.

Liu, J.L., Murphy, C., Buszczak, M., Clatterbuck, S., Goodman, R., Gall, J.G., 2006b. The *Drosophila melanogaster* Cajal body. J. Cell Biol. 172, 875−884.

Liu, J.L., 2015. May the force be with you: metabolism of arginine and pyrimidines. J. Genet. Genomics 42, 179−180.

Meredith, M.J., Lane, M.D., 1978. Acetyl-CoA carboxylase. Evidence for polymeric filament to protomer transition in the intact avian liver cell. J. Biol. Chem. 253, 3381−3383.

Mouilleron, S., Golinelli-Pimpaneau, B., 2007. Conformational changes in ammonia-channeling glutamine amidotransferases. Curr. Opin. Struct. Biol. 17, 653−664.

Noree, C., Monfort, E., Shiau, A.K., Wilhelm, J.E., 2014. Common regulatory control of CTP synthase enzyme activity and filament formation. Mol. Biol. Cell 25, 2282−2290.

Noree, C., Sato, B.K., Broyer, R.M., Wilhelm, J.E., 2010. Identification of novel filament-forming proteins in *Saccharomyces cerevisiae* and *Drosophila melanogaster*. J. Cell Biol. 190, 541−551.

O'Connell, J.D., Zhao, A., Ellington, A.D., Marcotte, E.M., 2012. Dynamic reorganization of metabolic enzymes into intracellular bodies. Annu. Rev. Cell Dev. Biol. 28, 89−111.

Panosyan, E.H., Wang, Y., Xia, P., Lee, W.N., Pak, Y., Laks, D.R., Lin, H.J., Moore, T.B., Cloughesy, T.F., Kornblum, H.I., Lasky 3rd, J.L., 2014. Asparagine depletion potentiates the cytotoxic effect of chemotherapy against brain tumors. Mol. Cancer Res. 12, 694−702.

Petrovska, I., Nuske, E., Munder, M.C., Kulasegaran, G., Malinovska, L., Kroschwald, S., Richter, D., Fahmy, K., Gibson, K., Verbavatz, J.M., Alberti, S., 2014. Filament formation by metabolic enzymes is a specific adaptation to an advanced state of cellular starvation. eLife 3, e02409.

Saxton, M.J., Jacobson, K., 1997. Single-particle tracking: applications to membrane dynamics. Annu. Rev. Biophys. Biomol. Struct. 26, 373−399.

Sbalzarini, I.F., Koumoutsakos, P., 2005. Feature point tracking and trajectory analysis for video imaging in cell biology. J. Struct. Biol. 151, 182−195.

Schwock, J., Kirchberger, J., Edelmann, A., Kriegel, T.M., Kopperschlager, G., 2004. Interaction of 6-phosphofructokinase with cytosolic proteins of *Saccharomyces cerevisiae*. Yeast 21, 483−494.

Sheth, U., Parker, R., 2006. Targeting of aberrant mRNAs to cytoplasmic processing bodies. Cell 125, 1095−1109.

Sircar, K., Huang, H., Hu, L., Cogdell, D., Dhillon, J., Tzelepi, V., Efstathiou, E., Koumakpayi, I.H., Saad, F., Luo, D., Bismar, T.A., Aparicio, A., Troncoso, P., Navone, N., Zhang, W., 2012. Integrative molecular profiling reveals asparagine synthetase is a target in castration-resistant prostate cancer. Am. J. Pathol. 180, 895−903.

Stahl, G., Salem, S.N., Chen, L., Zhao, B., Farabaugh, P.J., 2004. Translational accuracy during exponential, postdiauxic, and stationary growth phases in *Saccharomyces cerevisiae*. Eukaryot. Cell 3, 331−338.

Strochlic, T.I., Stavrides, K.P., Thomas, S.V., Nicolas, E., O'Reilly, A.M., Peterson, J.R., 2014. Ack kinase regulates CTP synthase filaments during *Drosophila* oogenesis. EMBO Rep. 15, 1184−1191.

Suresh, H.G., da Silveira Dos Santos, A.X., Kukulski, W., Tyedmers, J., Riezman, H., Bukau, B., Mogk, A., 2015. Prolonged starvation drives reversible sequestration of lipid biosynthetic enzymes and organelle reorganization in *Saccharomyces cerevisiae*. Mol. Biol. Cell 26, 1601−1615.

Szklarczyk, D., Franceschini, A., Wyder, S., Forslund, K., Heller, D., Huerta-Cepas, J., Simonovic, M., Roth, A., Santos, A., Tsafou, K.P., Kuhn, M., Bork, P., Jensen, L.J., von Mering, C., 2015. STRING v10: protein-protein interaction networks, integrated over the tree of life. Nucleic Acids Res. 43, D447−D452.

Tastan, Ö.Y., Liu, J.L., 2015a. CTP synthase is required for optic lobe homeostasis in *Drosophila*. J. Genet. Genomics 42, 261−274.

Tastan, Ö.Y., Liu, J.L., 2015b. Visualizing cytoophidia expression in *Drosophila* follicle cells *via* immunohistochemistry. Methods Mol. Biol. 1328, 179−189.

Telford, J.N., Lad, P.M., Hammes, G.G., 1975. Electron microscope study of native and crosslinked rabbit muscle phosphofructokinase. Proc. Natl. Acad. Sci. USA 72, 3054−3056.

Wang, P.Y., Lin, W.C., Tsai, Y.C., Cheng, M.L., Lin, Y.H., Tseng, S.H., Chakraborty, A., Pai, L.M., 2015. Regulation of CTP synthase filament formation during DNA endoreplication in *Drosophila*. Genetics 201, 1511−1523.

Zhang, J., Fan, J., Venneti, S., Cross, J.R., Takagi, T., Bhinder, B., Djaballah, H., Kanai, M., Cheng, E.H., Judkins, A.R., Pawel, B., Baggs, J., Cherry, S., Rabinowitz, J.D., Thompson, C.B., 2014a. Asparagine plays a critical role in regulating cellular adaptation to glutamine depletion. Mol. Cell 56, 205−218.

Zhang, J., Hulme, L., Liu, J.L., 2014b. Asymmetric inheritance of cytoophidia in *Schizosaccharomyces pombe*. Biol. Open 3, 1092−1097.

Zhou, C., Slaughter, B.D., Unruh, J.R., Eldakak, A., Rubinstein, B., Li, R., 2011. Motility and segregation of Hsp104-associated protein aggregates in budding yeast. Cell 147, 1186−1196.

References

1. Graça Raposo, Willem Stoorvoge. Extracellular vesicles: Exosomes, microvesicles, and friends. *J Cell Biol*. 2013. doi:10.1083/jcb.201211138.
2. Tkach M, Th??ry C. Communication by Extracellular Vesicles: Where We Are and Where We Need to Go. *Cell*. 2016;164(6):1226-1232. doi:10.1016/j.cell.2016.01.043.
3. Pettersen Hessvik N, Llorente A. Current knowledge on exosome biogenesis and release. *Cell Mol Life Sci*. 2018;75:193-208. doi:10.1007/s00018-017-2595-9.
4. D'Souza-Schorey C, Schorey JS. Regulation and mechanisms of extracellular vesicle biogenesis and secretion. *Essays Biochem*. 2018;62(2):125-133. doi:10.1042/EBC20170078.
5. Tricarico C, Clancy J, D'Souza-Schorey C. Biology and biogenesis of shed microvesicles. *Small GTPases*. 2017;8(4):220-232. doi:10.1080/21541248.2016.1215283.
6. Juan T, Fürthauer M. Biogenesis and function of ESCRT-dependent extracellular vesicles. *Semin Cell Dev Biol*. 2018;74:66-77. doi:10.1016/j.semcdb.2017.08.022.
7. Christ L, Raiborg C, Wenzel EM, Campsteijn C, Stenmark H. Cellular Functions and Molecular Mechanisms of the ESCRT Membrane-Scission Machinery. *Trends Biochem Sci*. 2017;42(1). doi:10.1016/j.tibs.2016.08.016.
8. Raiborg C, Stenmark H. The ESCRT machinery in endosomal sorting of ubiquitylated membrane proteins. *Nature*. 2009. doi:10.1038/nature07961.
9. Buschow SI, Nolte-'t Hoen ENM, van Niel G, et al. MHC II in Dendritic Cells is Targeted to Lysosomes or T Cell-Induced Exosomes Via Distinct Multivesicular Body Pathways. *Traffic*. 2009;10(10):1528-1542. doi:10.1111/j.1600-0854.2009.00963.x.
10. Stenmark H. Rab GTPases as coordinators of vesicle traffic. *Nat Rev Mol Cell Biol*. 2009;10(8):513-525. doi:10.1038/nrm2728.
11. Ostrowski M, Carmo NB, Krumeich S, et al. Rab27a and Rab27b control different steps of the exosome secretion pathway. *Nat Cell Biol*. 2010;12(1):19-30. doi:10.1038/ncb2000.
12. Hsu C, Morohashi Y, Yoshimura SI, et al. Regulation of exosome secretion by Rab35 and its GTPase-activating proteins TBC1D10A-C. *J Cell Biol*. 2010. doi:10.1083/jcb.200911018.
13. Savina A, Furlán M, Vidal M, Colombo MI. Exosome release is regulated by a calcium-dependent mechanism in K562 cells. *J Biol Chem*. 2003;278(22):20083-20090. doi:10.1074/jbc.M301642200.
14. Alonso R, Rodríguez MC, Pindado J, Merino E, Mérida I, Izquierdo M. Diacylglycerol kinase alpha regulates the secretion of lethal exosomes bearing Fas ligand during activation-induced cell death of T lymphocytes. *J Biol Chem*. 2005;280(31):28439-28450. doi:10.1074/jbc.M501112200.
15. Laulagnier K, Grand D, Dujardin A, et al. PLD2 is enriched on exosomes and its activity is correlated to the release of exosomes. *FEBS Lett*. 2004;572(1-3):11-14. doi:10.1016/j.febslet.2004.06.082.
16. Alonso R, Mazzeo C, Rodriguez MC, et al. Diacylglycerol kinase α regulates the formation and polarisation of mature multivesicular bodies involved in the secretion of Fas ligand-containing exosomes in T lymphocytes. *Cell Death Differ*. 2011;18(7):1161-1173. doi:10.1038/cdd.2010.184.
17. Fader CM, Sánchez DG, Mestre MB, Colombo MI. TI-VAMP/VAMP7 and VAMP3/cellubrevin: two v-SNARE proteins involved in specific steps of the

autophagy/multivesicular body pathways. *Biochim Biophys Acta - Mol Cell Res*. 2009;1793(12):1901-1916. doi:10.1016/J.BBAMCR.2009.09.011.
18. Verweij FJ, Bebelman MP, Jimenez CR, et al. Quantifying exosome secretion from single cells reveals a modulatory role for GPCR signaling. *J Cell Biol*. 2018;217(3):1129-1142. doi:10.1083/jcb.201703206.
19. Stuffers S, Sem Wegner C, Stenmark H, Brech A. Multivesicular Endosome Biogenesis in the Absence of ESCRTs. *Traffic*. 2009;10(7):925-937. doi:10.1111/j.1600-0854.2009.00920.x.
20. Trajkovic K, Hsu C, Chiantia S, et al. Ceramide triggers budding of exosome vesicles into multivesicular endosomes. *Science*. 2008;319(5867):1244-1247. doi:10.1126/science.1153124.
21. Muralidharan-Chari V, Clancy J, Plou C, et al. Article ARF6-Regulated Shedding of Tumor Cell-Derived Plasma Membrane Microvesicles. *Curr Biol*. 19:1875-1885. doi:10.1016/j.cub.2009.09.059.
22. Wang T, Gilkes DM, Takano N, et al. Hypoxia-inducible factors and RAB22A mediate formation of microvesicles that stimulate breast cancer invasion and metastasis. doi:10.1073/pnas.1410041111.
23. Del Piccolo N, Placone J, He L, Agudelo SC, Hristova K. Production of Plasma Membrane Vesicles with Chloride Salts and Their Utility as a Cell Membrane Mimetic for Biophysical Characterization of Membrane Protein Interactions. *Anal Chem*. 2012;84(20):8650-8655. doi:10.1021/ac301776j.
24. Liu M-L, Scalia R, Mehta JL, Williams KJ. Cholesterol-Induced Membrane Microvesicles As Novel Carriers of Damage–Associated Molecular Patterns. *Arterioscler Thromb Vasc Biol*. 2012;32(9):2113-2121. doi:10.1161/ATVBAHA.112.255471.
25. D'Souza-Schorey C, Clancy JW. Tumor-derived microvesicles: shedding light on novel microenvironment modulators and prospective cancer biomarkers. *Genes Dev*. 2012;26(12):1287-1299. doi:10.1101/gad.192351.112.
26. McConnell RE, Higginbotham JN, Shifrin DA, Tabb DL, Coffey RJ, Tyska MJ. The enterocyte microvillus is a vesicle-generating organelle. *J Cell Biol*. 2009;185(7):1285-1298. doi:10.1083/jcb.200902147.
27. Sedgwick AE, Clancy JW, Olivia Balmert M, D'souza-Schorey C. Extracellular microvesicles and invadopodia mediate non-overlapping modes of tumor cell invasion OPEN. 2015. doi:10.1038/srep14748.
28. Schlienger S, Campbell S, Claing A. ARF1 regulates the Rho/MLC pathway to control EGF-dependent breast cancer cell invasion. *Mol Biol Cell*. 2013;25(1):17-29. doi:10.1091/mbc.e13-06-0335.
29. Luga V, Zhang L, Viloria-Petit AM, et al. Exosomes mediate stromal mobilization of autocrine Wnt-PCP signaling in breast cancer cell migration. *Cell*. 2012;151(7):1542-1556. doi:10.1016/j.cell.2012.11.024.
30. Rodríguez M, Silva J, Herrera A, et al. Exosomes enriched in stemness/metastatic-related mRNAS promote oncogenic potential in breast cancer. *Oncotarget*. 2015;6(38). doi:10.18632/oncotarget.5818.
31. Hoshino A, Costa-Silva B, Shen T-L, et al. Tumour exosome integrins determine organotropic metastasis. *Nature*. 2015;527(7578):329-335. doi:10.1038/nature15756.
32. Zhou W, Fong MY, Min Y, et al. Cancer-Secreted miR-105 destroys vascular endothelial barriers to promote metastasis. *Cancer Cell*. 2014;25(4):501-515. doi:10.1016/j.ccr.2014.03.007.
33. Feng Q, Zhang C, Lum D, et al. A class of extracellular vesicles from breast cancer cells activates VEGF receptors and tumour angiogenesis. *Nat Commun*. 2017;8. doi:10.1038/ncomms14450.

34. Clayton A, Tabi Z. Exosomes and the MICA-NKG2D system in cancer. *Blood Cells, Mol Dis*. 2005;34(3):206-213. doi:10.1016/j.bcmd.2005.03.003.
35. Vaupel P. Tumor Hypoxia: Causative Factors, Compensatory Mechanisms, and Cellular Response. *Oncologist*. 2004. doi:10.1634/theoncologist.9-90005-4.
36. King HW, Michael MZ, Gleadle JM. Hypoxic enhancement of exosome release by breast cancer cells. *BMC Cancer*. 2012;12(1):421. doi:10.1186/1471-2407-12-421.
37. Yang W, Sun T, Cao J, Liu F, Tian Y, Zhu W. Downregulation of miR-210 expression inhibits proliferation, induces apoptosis and enhances radiosensitivity in hypoxic human hepatoma cells in vitro. *Exp Cell Res*. 2012. doi:10.1016/j.yexcr.2012.02.010.
38. Goler-Baron V, Assaraf YG. Structure and Function of ABCG2-Rich Extracellular Vesicles Mediating Multidrug Resistance. Joly E, ed. *PLoS One*. 2011;6(1):e16007. doi:10.1371/journal.pone.0016007.
39. Bebawy M, Combes V, Lee E, et al. Membrane microparticles mediate transfer of P-glycoprotein to drug sensitive cancer cells. *Leukemia*. 2009;23(9):1643-1649. doi:10.1038/leu.2009.76.
40. Bao L, Haque A, Jackson K, et al. Increased Expression of P-Glycoprotein Is Associated with Doxorubicin Chemoresistance in the Metastatic 4T1 Breast Cancer Model. *Am J Pathol*. 2011;178(2):838-852. doi:10.1016/j.ajpath.2010.10.029.
41. Lv M, Zhu X, Chen W, et al. Exosomes mediate drug resistance transfer in MCF-7 breast cancer cells and a probable mechanism is delivery of P-glycoprotein. *Tumor Biol*. 2014;35(11):10773-10779. doi:10.1007/s13277-014-2377-z.
42. Szeliga M, Obara-Michlewska M. Glutamine in neoplastic cells: Focus on the expression and roles of glutaminases. *Neurochem Int*. 2009. doi:10.1016/j.neuint.2009.01.008.
43. Elgadi KM, Meguid RA, Qian M, Souba WW, Abcouwer SF. Cloning and analysis of unique human glutaminase isoforms generated by tissue-specific alternative splicing Cloning and analysis of unique human glutaminase isoforms generated by tissue-specific alternative splicing. *Physiol Genomics*. 1999. doi:1/2/51 [pii].
44. DeBerardinis RJ, Cheng T. Q's next: the diverse functions of glutamine in metabolism, cell biology and cancer. *Oncogene*. 2010;29(3):313-324. doi:10.1038/onc.2009.358.
45. Geck RC, Toker A. Nonessential amino acid metabolism in breast cancer. *Adv Biol Regul*. 2016;62:11-17. doi:10.1016/j.jbior.2016.01.001.
46. El Ansari R, McIntyre A, Craze ML, Ellis IO, Rakha EA, Green AR. Altered glutamine metabolism in breast cancer; subtype dependencies and alternative adaptations. *Histopathology*. 2018;72(2):183-190. doi:10.1111/his.13334.
47. Xu J, Chen Y, Olopade OI. MYC and Breast Cancer. *Genes Cancer*. 2010;1(6):629-640. doi:10.1177/1947601910378691.
48. Gao P, Tchernyshyov I, Chang T-C, et al. c-Myc suppression of miR-23a/b enhances mitochondrial glutaminase expression and glutamine metabolism. *Nature*. 2009;458(7239):762-765. doi:10.1038/nature07823.
49. Wise DR, DeBerardinis RJ, Mancuso A, et al. Myc regulates a transcriptional program that stimulates mitochondrial glutaminolysis and leads to glutamine addiction. *Proc Natl Acad Sci*. 2008;105(48):18782-18787. doi:10.1073/pnas.0810199105.
50. van Geldermalsen M, Wang Q, Nagarajah R, et al. ASCT2/SLC1A5 controls glutamine uptake and tumour growth in triple-negative basal-like breast cancer.

Oncogene. 2016;35(24):3201-3208. doi:10.1038/onc.2015.381.
51. Jeon YJ, Khelifa S, Ratnikov B, et al. Regulation of Glutamine Carrier Proteins by RNF5 Determines Breast Cancer Response to ER Stress-Inducing Chemotherapies. *Cancer Cell*. 2015;27(3):354-369. doi:10.1016/j.ccell.2015.02.006.
52. Reynolds MR, Lane AN, Robertson B, et al. Control of glutamine metabolism by the tumor suppressor Rb. *Oncogene*. 2014;33(5):556-566. doi:10.1038/onc.2012.635.
53. Kung HN, Marks JR, Chi JT. Glutamine synthetase is a genetic determinant of cell type-specific glutamine independence in breast epithelia. *PLoS Genet*. 2011;7(8):1002229. doi:10.1371/journal.pgen.1002229.
54. Gupta GP, Nguyen DX, Chiang AC, et al. Mediators of vascular remodelling co-opted for sequential steps in lung metastasis. *Nature*. 2007;446(7137):765-770. doi:10.1038/nature05760.
55. Oskarsson T, Acharyya S, Zhang XH-F, et al. Breast cancer cells produce tenascin C as a metastatic niche component to colonize the lungs. *Nat Med*. 2011;17(7):867-874. doi:10.1038/nm.2379.
56. Alečković M, Wei Y, LeRoy G, et al. Identification of Nidogen 1 as a lung metastasis protein through secretome analysis. *Genes Dev*. 2017;31(14):1439-1455. doi:10.1101/gad.301937.117.
57. Bachmann C, Schmidt S, Staebler A, et al. CNS metastases in breast cancer patients: prognostic implications of tumor subtype. *Med Oncol*. 2015;32(1):400. doi:10.1007/s12032-014-0400-2.
58. Witzel I, Oliveira-Ferrer L, Pantel K, Müller V, Wikman H. Breast cancer brain metastases: biology and new clinical perspectives. *Breast Cancer Res*. 2016;18(1):8. doi:10.1186/s13058-015-0665-1.
59. Weil RJ, Palmieri DC, Bronder JL, Stark AM, Steeg PS. Breast Cancer Metastasis to the Central Nervous System. *Am J Pathol*. 2005;167(4):913-920. doi:10.1016/S0002-9440(10)61180-7.
60. Fidler IJ. The role of the organ microenvironment in brain metastasis. *Semin Cancer Biol*. 2011;21(2):107-112. doi:10.1016/j.semcancer.2010.12.009.
61. Wrobel JK, Toborek M. Blood-brain Barrier Remodeling during Brain Metastasis Formation. *Mol Med*. 2016;22:32-40. doi:10.2119/molmed.2015.00207.
62. Lee B-C, Lee T-H, Avraham S, Avraham HK. Involvement of the chemokine receptor CXCR4 and its ligand stromal cell-derived factor 1alpha in breast cancer cell migration through human brain microvascular endothelial cells. *Mol Cancer Res*. 2004;2(6):327-338. http://www.ncbi.nlm.nih.gov/pubmed/15235108. Accessed November 18, 2018.
63. Avraham HK, Jiang S, Fu Y, Nakshatri H, Ovadia H, Avraham S. Angiopoietin-2 mediates blood-brain barrier impairment and colonization of triple-negative breast cancer cells in brain. *J Pathol*. 2014;232(3):369-381. doi:10.1002/path.4304.
64. Bos PD, Zhang XH-F, Nadal C, et al. Genes that mediate breast cancer metastasis to the brain. *Nature*. 2009;459(7249):1005-1009. doi:10.1038/nature08021.
65. Laplante M, Sabatini DM. mTOR signaling at a glance. *J Cell Sci*. 2009;122:3589-3594. doi:10.1242/jcs.051011.
66. Dibble CC, Manning BD. Signal integration by mTORC1 coordinates nutrient input with biosynthetic output. *Nat Cell Biol*. 2013;15(6):555-564. doi:10.1038/ncb2763.
67. Laplante M, Sabatini DM. MTOR signaling in growth control and disease. *Cell*. 2012;149(2):274-293. doi:10.1016/j.cell.2012.03.017.

68. Ben-Sahra I, Manning BD. mTORC1 signaling and the metabolic control of cell growth. *Curr Opin Cell Biol*. 2017;45:72-82. doi:10.1016/j.ceb.2017.02.012.
69. Chauvin C, Koka V, Nouschi A, et al. Ribosomal protein S6 kinase activity controls the ribosome biogenesis transcriptional program. *Oncogene*. 2014;33(4):474-483. doi:10.1038/onc.2012.606.
70. Düvel K, Yecies JL, Menon S, et al. Activation of a Metabolic Gene Regulatory Network Downstream of mTOR Complex 1. *Mol Cell*. 2010;39(2):171-183. doi:10.1016/J.MOLCEL.2010.06.022.
71. Keith B, Johnson RS, Simon MC. HIF1α and HIF2α: sibling rivalry in hypoxic tumour growth and progression. *Nat Rev Cancer*. 2012;12(1):9-22. doi:10.1038/nrc3183.
72. Porstmann T, Santos CR, Griffiths B, et al. SREBP Activity Is Regulated by mTORC1 and Contributes to Akt-Dependent Cell Growth. *Cell Metab*. 2008;8(3):224-236. doi:10.1016/J.CMET.2008.07.007.
73. Jung CH, Jun CB, Ro S-H, et al. ULK-Atg13-FIP200 Complexes Mediate mTOR Signaling to the Autophagy Machinery. Schmid SL, ed. *Mol Biol Cell*. 2009;20(7):1992-2003. doi:10.1091/mbc.e08-12-1249.
74. deGraffenried LA, Friedrichs WE, Russell DH, et al. Inhibition of mTOR Activity Restores Tamoxifen Response in Breast Cancer Cells with Aberrant Akt Activity. *Clin Cancer Res*. 2004;10(23):8059-8067. doi:10.1158/1078-0432.CCR-04-0035.
75. Beeram M, Tan Q-T, Tekmal R, Russell D, Middleton A, deGraffenried L. Akt-induced endocrine therapy resistance is reversed by inhibition of mTOR signaling. *Ann Oncol*. 2007;18(8):1323-1328. doi:10.1093/annonc/mdm170.
76. Boulay A, Rudloff J, Ye J, et al. Dual Inhibition of mTOR and Estrogen Receptor Signaling In vitro Induces Cell Death in Models of Breast Cancer. *Clin Cancer Res*. 2005;11(14):5319-5328. doi:10.1158/1078-0432.CCR-04-2402.
77. Macaskill EJ, Bartlett JMS, Sabine VS, et al. The mammalian target of rapamycin inhibitor everolimus (RAD001) in early breast cancer: results of a pre-operative study. *Breast Cancer Res Treat*. 2011;128(3):725-734. doi:10.1007/s10549-010-0967-z.
78. Baselga J, Semiglazov V, van Dam P, et al. Phase II Randomized Study of Neoadjuvant Everolimus Plus Letrozole Compared With Placebo Plus Letrozole in Patients With Estrogen Receptor–Positive Breast Cancer. *J Clin Oncol*. 2009;27(16):2630-2637. doi:10.1200/JCO.2008.18.8391.
79. Gonzalez-Malerva L, Park J, Zou L, et al. High-throughput ectopic expression screen for tamoxifen resistance identifies an atypical kinase that blocks autophagy. *Proc Natl Acad Sci*. 2011;108(5):2058-2063. doi:10.1073/pnas.1018157108.
80. Shi J-J, Chen S-M, Guo C-L, Li Y-X, Ding J, Meng L-H. *The MTOR Inhibitor AZD8055 Overcomes Tamoxifen Resistance in Breast Cancer Cells by Down-Regulating HSPB8*. Vol 39.; 2018. www.chinaphar.com. Accessed November 3, 2018.
81. Slamon DJ, Leyland-Jones B, Shak S, et al. Use of Chemotherapy plus a Monoclonal Antibody against HER2 for Metastatic Breast Cancer That Overexpresses HER2. *N Engl J Med*. 2001;344(11):783-792. doi:10.1056/NEJM200103153441101.
82. Nagata Y, Lan K-H, Zhou X, et al. PTEN activation contributes to tumor inhibition by trastuzumab, and loss of PTEN predicts trastuzumab resistance in patients. *Cancer Cell*. 2004;6(2):117-127. doi:10.1016/j.ccr.2004.06.022.
83. Miller TW, Forbes JT, Shah C, et al. Inhibition of Mammalian Target of Rapamycin Is Required for Optimal Antitumor Effect of HER2 Inhibitors against

HER2-Overexpressing Cancer Cells. *Clin Cancer Res*. 2009;15(23):7266-7276. doi:10.1158/1078-0432.CCR-09-1665.
84. Hsu P-Y, Shang Wu V, Kanaya N, et al. Cancer Therapy: Preclinical Dual mTOR Kinase Inhibitor MLN0128 Sensitizes HR þ /HER2 þ Breast Cancer Patient-Derived Xenografts to Trastuzumab or Fulvestrant. 2018. doi:10.1158/1078-0432.CCR-17-1983.
85. Morrow PK, Wulf GM, Ensor J, et al. Phase I/II Study of Trastuzumab in Combination With Everolimus (RAD001) in Patients With HER2-Overexpressing Metastatic Breast Cancer Who Progressed on Trastuzumab-Based Therapy. *J Clin Oncol*. 2011;29(23):3126-3132. doi:10.1200/JCO.2010.32.2321.
86. Jerusalem G, Fasolo A, Dieras V, et al. Phase I trial of oral mTOR inhibitor everolimus in combination with trastuzumab and vinorelbine in pre-treated patients with HER2-overexpressing metastatic breast cancer. *Breast Cancer Res Treat*. 2011;125(2):447-455. doi:10.1007/s10549-010-1260-x.
87. Torres V a, Tapia JC, Rodríguez D a, et al. Caveolin-1 controls cell proliferation and cell death by suppressing expression of the inhibitor of apoptosis protein survivin. *J Cell Sci*. 2006;119(Pt 9):1812-1823. doi:10.1242/jcs.02894.
88. Andre F, Campone M, O'Regan R, et al. Phase I Study of Everolimus Plus Weekly Paclitaxel and Trastuzumab in Patients With Metastatic Breast Cancer Pretreated With Trastuzumab. *J Clin Oncol*. 2010;28(34):5110-5115. doi:10.1200/JCO.2009.27.8549.
89. Andre F, Job B, Dessen P, et al. Molecular Characterization of Breast Cancer with High-Resolution Oligonucleotide Comparative Genomic Hybridization Array. *Clin Cancer Res*. 2009;15(2):441-451. doi:10.1158/1078-0432.CCR-08-1791.
90. Marty B, Maire V, Gravier E, et al. Frequent PTEN genomic alterations and activated phosphatidylinositol 3-kinase pathway in basal-like breast cancer cells. *Breast Cancer Res*. 2008;10(6):R101. doi:10.1186/bcr2204.
91. Lehmann BDB, Bauer J a J, Chen X, et al. Identification of human triple-negative breast cancer subtypes and preclinical models for selection of targeted therapies. *J Clin Invest*. 2011;121(7):2750-2767. doi:10.1172/JCI45014DS1.
92. Beuvink I, Boulay A, Fumagalli S, et al. The mTOR Inhibitor RAD001 Sensitizes Tumor Cells to DNA-Damaged Induced Apoptosis through Inhibition of p21 Translation. *Cell*. 2005;120(6):747-759. doi:10.1016/j.cell.2004.12.040.
93. Wong SW, Tiong KH, Kong WY, et al. Rapamycin synergizes cisplatin sensitivity in basal-like breast cancer cells through up-regulation of p73. *Breast Cancer Res Treat*. 2011;128(2):301-313. doi:10.1007/s10549-010-1055-0.
94. Gonzalez-Angulo AM, Akcakanat A, Liu S, et al. Open-label randomized clinical trial of standard neoadjuvant chemotherapy with paclitaxel followed by FEC versus the combination of paclitaxel and everolimus followed by FEC in women with triple receptor-negative breast cancer†. *Ann Oncol*. 2014;25(6):1122-1127. doi:10.1093/annonc/mdu124.
95. Protter DSW, Parker R. Principles and Properties of Stress Granules. *Trends Cell Biol*. 2016;26(9):668-679. doi:10.1016/j.tcb.2016.05.004.
96. Pedley AM, Benkovic SJ. A New View into the Regulation of Purine Metabolism: The Purinosome. *Trends Biochem Sci*. 2017;42(2). doi:10.1016/j.tibs.2016.09.009.
97. Liu J-L. The Cytoophidium and Its Kind: Filamentation and Compartmentation of Metabolic Enzymes. *Annu Rev Cell Dev Biol*. 2016. doi:10.1146/annurev-cellbio-111315-124907.
98. Liu JL. The enigmatic cytoophidium: Compartmentation of CTP synthase via filament formation. *BioEssays*. 2011. doi:10.1002/bies.201000129.

99. Munder MC, Midtvedt D, Franzmann T, et al. A pH-driven transition of the cytoplasm from a fluid- to a solid-like state promotes entry into dormancy. *Elife*. 2016. doi:10.7554/eLife.09347.
100. Noree C, Sato BK, Broyer RM, Wilhelm JE. Identification of novel filament-forming proteins in *Saccharomyces cerevisiae* and *Drosophila melanogaster*. *J Cell Biol*. 2010. doi:10.1083/jcb.201003001.
101. Narayanaswamy R, Levy M, Tsechansky M, et al. Widespread reorganization of metabolic enzymes into reversible assemblies upon nutrient starvation. *Proc Natl Acad Sci*. 2009. doi:10.1073/pnas.0812771106.
102. Ji Y, Gu J, Makhov AM, Griffith JD, Mitchell BS. Regulation of the Interaction of Inosine Monophosphate Dehydrogenase with Mycophenolic Acid by GTP. *J Biol Chem*. 2006;281(1):206-212. doi:10.1074/jbc.M507056200.
103. Carcamo WC, Satoh M, Kasahara H, et al. Induction of Cytoplasmic Rods and Rings Structures by Inhibition of the CTP and GTP Synthetic Pathway in Mammalian Cells. El-Rifai W, ed. *PLoS One*. 2011;6(12):e29690. doi:10.1371/journal.pone.0029690.
104. Chen K, Zhang J, Tastan ÖY, Deussen ZA, Siswick MYY, Liu JL. Glutamine analogs promote cytoophidium assembly in human and Drosophila cells. *J Genet Genomics*. 2011. doi:10.1016/j.jgg.2011.08.004.
105. Lauritsen I, Willemoës M, Jensen KF, Johansson E, Harris P, IUCr. Structure of the dimeric form of CTP synthase from *Sulfolobus solfataricus*. *Acta Crystallogr Sect F Struct Biol Cryst Commun*. 2011;67(2):201-208. doi:10.1107/S1744309110052334.
106. Hedstrom L. IMP dehydrogenase: structure, mechanism, and inhibition. *Chem Rev*. 2009;109(7):2903-2928. doi:10.1021/cr900021w.
107. Gou K-M, Chang C-C, Shen Q-J, Sung L-Y, Liu J-L. CTP synthase forms cytoophidia in the cytoplasm and nucleus. *Exp Cell Res*. 2014;323(1):242-253. doi:10.1016/j.yexcr.2014.01.029.
108. McPartland R, Wang M, Bloch A, research HW-C, 1974 undefined. Cytidine 5′-triphosphate synthetase as a target for inhibition by the antitumor agent 3-deazauridine. *AACR*. http://cancerres.aacrjournals.org/content/34/11/3107.short. Accessed November 18, 2018.
109. John Calise S, Carcamo WC, Krueger C, Yin JD, Purich DL, L Chan EK. Glutamine deprivation initiates reversible assembly of mammalian rods and rings. 2014. doi:10.1007/s00018-014-1567-6.
110. Petrovska I, Nüske E, Munder MC, et al. Filament formation by metabolic enzymes is a specific adaptation to an advanced state of cellular starvation. *Elife*. 2014;3. doi:10.7554/eLife.02409.
111. Lynch EM, Hicks DR, Shepherd M, et al. Human CTP synthase filament structure reveals the active enzyme conformation. *Nat Struct Mol Biol*. 2017;24(6):507-514. doi:10.1038/nsmb.3407.
112. Ingerson-Mahar M, Briegel A, Werner JN, Jensen GJ, Gitai Z. The metabolic enzyme CTP synthase forms cytoskeletal filaments. *Nat Cell Biol*. 2010. doi:10.1038/ncb2087.
113. McLEAN JE, HAMAGUCHI N, BELENKY P, MORTIMER SE, STANTON M, HEDSTROM L. Inosine 5′-monophosphate dehydrogenase binds nucleic acids in vitro and in vivo. *Biochem J*. 2004. doi:10.1042/bj20031585.
114. Kozhevnikova EN, van der Knaap JA, Pindyurin A V., et al. Metabolic Enzyme IMPDH Is Also a Transcription Factor Regulated by Cellular State. *Mol Cell*. 2012. doi:10.1016/j.molcel.2012.04.030.
115. Juda P, Šmigová J, Kováčik L, Bártová E, Raška I. Ultrastructure of

Cytoplasmic and Nuclear Inosine-5'-Monophosphate Dehydrogenase 2 "Rods and Rings" Inclusions. *J Histochem Cytochem*. 2014. doi:10.1369/0022155414543853.
116. Chang C-C, Jeng Y-M, Peng M, Keppeke GD, Sung L-Y, Liu J-L. CTP synthase forms the cytoophidium in human hepatocellular carcinoma. *Exp Cell Res*. 2017;361(2):292-299. doi:10.1016/j.yexcr.2017.10.030.
117. Ellims PH, Gan TE, Medley G. Cytidine triphosphate synthetase activity in lymphoproliferative disorders. *Cancer Res*. 1983;43(3):1432-1435. http://www.ncbi.nlm.nih.gov/pubmed/6572096. Accessed February 5, 2019.
118. Williams JC, Kizaki H, Weber G, Morris HP. Increased CTP synthetase activity in cancer cells. *Nature*. 1978. doi:10.1038/271071a0.
119. Xu Q, Tu J, Dou C, et al. HSP90 promotes cell glycolysis, proliferation and inhibits apoptosis by regulating PKM2 abundance via Thr-328 phosphorylation in hepatocellular carcinoma. *Mol Cancer*. 2017;16(1):178. doi:10.1186/s12943-017-0748-y.
120. Keppeke GD, Calise SJ, Chan EKL, Andrade LEC. Assembly of IMPDH2-Based, CTPS-Based, and Mixed Rod/Ring Structures Is Dependent on Cell Type and Conditions of Induction. *J Genet Genomics*. 2015. doi:10.1016/j.jgg.2015.04.002.
121. Shapiro RA, Clark VM, Curthoys NP. Inactivation of rat renal phosphate-dependent glutaminase with 6-diazo-5-oxo-L-norleucine. Evidence for interaction at the glutamine binding site. *J Biol Chem*. 1979. doi:10.1093/heapol/czt047 LK - http://limo.libis.be/resolver?&sid=EMBASE&issn=14602237&id=doi:10.1093%2Fheapol%2Fczt047&atitle=The+impact+of+performance+incentives+on+child+health+outcomes%3A+results+from+a+cluster+randomized+controlled+trial+in+the+Philippines&stitle=Health+Policy+Plan&title=Health+policy+and+planning&volume=29&issue=5&spage=615&epage=621&aulast=Peabody&aufirst=John+W.&auinit=J.W.&aufull=Peabody+J.W.&coden=&isbn=&pages=615-621&date=2014&auinit1=J&auinitm=W.
122. Kisner DL, Catane R, Muggia FM. The rediscovery of DON (6-diazo-5-oxo-L-norleucine). *Recent Results Cancer Res*. 1980. doi:10.1007/978-3-642-81488-4_30.
123. Pinkus LM. Glutamine binding sites. *Methods Enzymol*. 1977;46:414-427. http://www.ncbi.nlm.nih.gov/pubmed/909432. Accessed December 27, 2018.
124. Ortlund E, Lacount MW, Lewinski K, Lebioda L. Reactions of Pseudomonas 7A glutaminase-asparaginase with diazo analogues of glutamine and asparagine result in unexpected covalent inhibitions and suggests an unusual catalytic triad Thr-Tyr-Glu. *Biochemistry*. 2000. doi:10.1021/bi991797d.
125. Durán RV, Oppliger W, Robitaille AM, et al. Glutaminolysis Activates Rag-mTORC1 Signaling. *Mol Cell*. 2012;47(3):349-358. doi:10.1016/J.MOLCEL.2012.05.043.
126. Lampa M, Arlt H, He T, et al. Glutaminase is essential for the growth of triple-negative breast cancer cells with a deregulated glutamine metabolism pathway and its suppression synergizes with mTOR inhibition. 2017. doi:10.1371/journal.pone.0185092.
127. Huh W-K, Falvo J V., Gerke LC, et al. Global analysis of protein localization in budding yeast. *Nature*. 2003;425(6959):686-691. doi:10.1038/nature02026.
128. Guaragnella N, Palermo V, Galli A, Moro L, Mazzoni C, Giannattasio S. The expanding role of yeast in cancer research and diagnosis: insights into the function of the oncosuppressors p53 and BRCA1/2. 2013. doi:10.1111/1567-1364.12094.

129. Pereira C, Coutinho I, Soares J, Bessa C, Leão M, Saraiva L. New insights into cancer-related proteins provided by the yeast model. *FEBS J*. 2012;279(5):697-712. doi:10.1111/j.1742-4658.2012.08477.x.
130. Postnikoff SDL, Johnson JE, Tyler JK. The integrated stress response in budding yeast lifespan extension. *Microb Cell*. 2017;4(11):368-375. doi:10.15698/mic2017.11.597.
131. Goffeau A, Barrell G, Bussey H, et al. Life with 6000 genes. *Science (80-)*. 1996. doi:10.1126/science.274.5287.546.
132. Giaever G, Chu AM, Ni L, et al. Functional profiling of the Saccharomyces cerevisiae genome. *Nature*. 2002;418(6896):387-391. doi:10.1038/nature00935.
133. Winzeler EA, Shoemaker DD, Astromoff A, et al. Functional characterization of the S. cerevisiae genome by gene deletion and parallel analysis. *Science (80-)*. 1999. doi:10.1126/science.285.5429.901.
134. Jones GM, Stalker J, Humphray S, et al. A systematic library for comprehensive overexpression screens in Saccharomyces cerevisiae. *Nat Methods*. 2008. doi:10.1038/nmeth.1181.
135. Ghaemmaghami S, Huh WK, Bower K, et al. Global analysis of protein expression in yeast. *Nature*. 2003. doi:10.1038/nature02046.
136. Tsien RY. The Green Fluorescent Protein. *Annu Rev Biochem*. 1998. doi:10.1146/annurev.biochem.67.1.509.
137. Eelen G, Dubois C, Cantelmo AR, et al. *Role of Glutamine Synthetase in Angiogenesis beyond Glutamine Synthesis*. Vol 561.; 2018. doi:10.1038/s41586-018-0466-7.
138. Jewell JL, Kim YC, Russell RC, et al. Differential regulation of mTORC1 by leucine and glutamine. *Science*. 2015;347(6218):194-198. doi:10.1126/science.1259472.
139. Flinn RJ, Yan Y, Goswami S, Parker PJ, Backer JM. The late endosome is essential for mTORC1 signaling. *Mol Biol Cell*. 2010;21(5):833-841. doi:10.1091/mbc.E09.
140. Urbanelli L, Magini A, Buratta S, et al. Signaling Pathways in Exosomes Biogenesis, Secretion and Fate. *Genes (Basel)*. 2013;4:152-170. doi:10.3390/genes4020152.
141. Baietti MF, Zhang Z, Mortier E, et al. Syndecan–syntenin–ALIX regulates the biogenesis of exosomes. *Nat Cell Biol*. 2012;14(7):677-685. doi:10.1038/ncb2502.
142. Albacete-Albacete L, Navarro-Lérida I, Antonio Lopez J, et al. ECM deposition is driven by caveolin1-dependent regulation of exosomal biogenesis and cargo sorting. doi:10.1101/405506.
143. Colombo M, Moita C, van Niel G, et al. Analysis of ESCRT functions in exosome biogenesis, composition and secretion highlights the heterogeneity of extracellular vesicles. *J Cell Sci*. 2013;126(24):5553-5565. doi:10.1242/jcs.128868.
144. Bott AJ, Peng I-C, Fan Y, et al. Oncogenic Myc Induces Expression of Glutamine Synthetase through Promoter Demethylation. *Cell Metab*. 2015;22(6):1068-1077. doi:10.1016/J.CMET.2015.09.025.
145. Commisso C, Davidson SM, Soydaner-Azeloglu RG, et al. Macropinocytosis of protein is an amino acid supply route in Ras-transformed cells. *Nature*. 2013;497(7451):633-637. doi:10.1038/nature12138.
146. Zhao H, Yang L, Baddour J, et al. Tumor microenvironment derived exosomes pleiotropically modulate cancer cell metabolism. *Elife*. 2016;5. doi:10.7554/eLife.10250.
147. Timmerman LA, Holton T, Yuneva M, et al. Glutamine Sensitivity Analysis

Identifies the xCT Antiporter as a Common Triple-Negative Breast Tumor Therapeutic Target. *Cancer Cell*. 2013. doi:10.1016/j.ccr.2013.08.020.
148. Cassago A, Ferreira APS, Ferreira IM, et al. Mitochondrial localization and structure-based phosphate activation mechanism of Glutaminase C with implications for cancer metabolism. *Proc Natl Acad Sci*. 2012. doi:10.1073/pnas.1112495109.
149. Szeliga M, Sidoryk M, Matyja E, Kowalczyk P, Albrecht J. Lack of expression of the liver-type glutaminase (LGA) mRNA in human malignant gliomas. *Neurosci Lett*. 2005. doi:10.1016/j.neulet.2004.10.051.
150. Turner A, McGivan JD. Glutaminase isoform expression in cell lines derived from human colorectal adenomas and carcinomas. *Biochem J*. 2003. doi:10.1042/BJ20021360.
151. Ebi H, Costa C, Faber AC, et al. PI3K regulates MEK/ERK signaling in breast cancer via the Rac-GEF, P-Rex1. *Proc Natl Acad Sci*. 2013;110(52):21124-21129. doi:10.1073/pnas.1314124110.
152. Borisov N, Aksamitiene E, Kiyatkin A, et al. Systems-level interactions between insulin-EGF networks amplify mitogenic signaling. *Mol Syst Biol*. 2009;5:256. doi:10.1038/msb.2009.19.
153. Li Q-L, Gu F-M, Wang Z, et al. Activation of PI3K/AKT and MAPK Pathway through a PDGFRβ-Dependent Feedback Loop Is Involved in Rapamycin Resistance in Hepatocellular Carcinoma. Guan X, ed. *PLoS One*. 2012;7(3):e33379. doi:10.1371/journal.pone.0033379.
154. Tardito S, Oudin A, Ahmed SU, et al. Glutamine synthetase activity fuels nucleotide biosynthesis and supports growth of glutamine-restricted glioblastoma. *Nat Cell Biol*. 2015;17(12):1556-1568. doi:10.1038/ncb3272.
155. Hanahan D, Weinberg RA. Hallmarks of Cancer: The Next Generation. *Cell*. 2011;144(5):646-674. doi:10.1016/J.CELL.2011.02.013.
156. Nordin JZ, Lee Y, Vader P, et al. Ultrafiltration with size-exclusion liquid chromatography for high yield isolation of extracellular vesicles preserving intact biophysical and functional properties. *Nanomedicine Nanotechnology, Biol Med*. 2015;11(4):879-883. doi:10.1016/j.nano.2015.01.003.
157. Lobert VH, Stenmark H. Cell Polarity and Migration: Emerging Role for the Endosomal Sorting Machinery. *Physiology*. 2011;26(3):171-180. doi:10.1152/physiol.00054.2010.
158. SARKAR D, Boukerche H, Su Z-Z, Fisher PB. mda-9/syntenin: recent insights into a novel cell signaling and metastasis-associated gene. *Pharmacol Ther*. 2004;104(2):101-115. doi:10.1016/j.pharmthera.2004.08.004.
159. Boukerche H, Su Z, Emdad L, et al. *mda-9* /Syntenin: A Positive Regulator of Melanoma Metastasis. *Cancer Res*. 2005;65(23):10901-10911. doi:10.1158/0008-5472.CAN-05-1614.
160. Zimmermann P, Zhang Z, Degeest G, et al. Syndecan Recyling Is Controlled by Syntenin-PIP2 Interaction and Arf6. *Dev Cell*. 2005;9(3):377-388. doi:10.1016/J.DEVCEL.2005.07.011.
161. Estrach S, Legg J, Watt FM. Syntenin mediates Delta1-induced cohesiveness of epidermal stem cells in culture. *J Cell Sci*. 2007;120(16):2944-2952. doi:10.1242/jcs.016253.
162. Beekman JM, Coffer PJ. The ins and outs of syntenin, a multifunctional intracellular adaptor protein. *J Cell Sci*. 2008;121(9):1349-1355. doi:10.1242/jcs.026401.
163. Beekman JM, Vervoort SJ, Dekkers F, et al. Syntenin-mediated regulation of Sox4 proteasomal degradation modulates transcriptional output. *Oncogene*. 2012;31(21):2668-2679. doi:10.1038/onc.2011.445.

164. Ghossoub R, Lembo F, Rubio A, et al. Syntenin-ALIX exosome biogenesis and budding into multivesicular bodies are controlled by ARF6 and PLD2. *Nat Commun*. 2014;5(1):3477. doi:10.1038/ncomms4477.
165. Kashyap R, Roucourt B, Lembo F, et al. Syntenin controls migration, growth, proliferation, and cell cycle progression in cancer cells. *Front Pharmacol*. 2015;6(OCT):1-11. doi:10.3389/fphar.2015.00241.
166. Bussolati B, Biancone L, Cassoni P, et al. PAF Produced by Human Breast Cancer Cells Promotes Migration and Proliferation of Tumor Cells and Neo-Angiogenesis. *Am J Pathol*. 2000;157(5):1713-1725. doi:10.1016/S0002-9440(10)64808-0.
167. Gupta R, Toufaily C, Annabi B. Caveolin and cavin family members: Dual roles in cancer. *Biochimie*. 2014;107:188-202. doi:10.1016/j.biochi.2014.09.010.
168. Liu P, Rudick M, Anderson RGW. Multiple Functions of Caveolin-1. *J Biol Chem*. 2002;277(44):41295-41298. doi:10.1074/jbc.R200020200.
169. Svensson KJ, Christianson HC, Wittrup A, et al. Exosome uptake depends on ERK1/2-heat shock protein 27 signaling and lipid raft-mediated endocytosis negatively regulated by caveolin-1. *J Biol Chem*. 2013;288(24):17713-17724. doi:10.1074/jbc.M112.445403.
170. Ko Y-H, Lin Z, Flomenberg N, et al. Glutamine fuels a vicious cycle of autophagy in the tumor stroma and oxidative mitochondrial metabolism in epithelial cancer cells. *Cancer Biol Ther*. 2011;12(12):1085-1097. doi:10.4161/cbt.12.12.18671.
171. Quest AFG, Lobos-González L, Nuñez S, et al. The caveolin-1 connection to cell death and survival. *Curr Mol Med*. 2013;13(2):266-281. http://www.ncbi.nlm.nih.gov/pubmed/23228128. Accessed December 8, 2018.
172. Cokakli M, Erdal E, Nart D, et al. Differential expression of Caveolin-1 in hepatocellular carcinoma: correlation with differentiation state, motility and invasion. *BMC Cancer*. 2009;9:65. doi:10.1186/1471-2407-9-65.
173. Meyer C, Dzieran J, Liu Y, et al. Distinct dedifferentiation processes affect caveolin-1 expression in hepatocytes. *Cell Commun Signal*. 2013;11(1):6. doi:10.1186/1478-811X-11-6.
174. Sommers CL, Byers SW, Thompson EW, Torri JA, Gelmann ER. *Differentiation State and Invasiveness of Human Breast Cancer Cell Lines*. Vol 31.; 1994. https://link.springer.com/content/pdf/10.1007%2FBF00666165.pdf. Accessed December 8, 2018.
175. Koliha N, Wiencek Y, Heider U, et al. A novel multiplex bead-based platform highlights the diversity of extracellular vesicles. *J Extracell Vesicles*. 2016;5(1):29975. doi:10.3402/jev.v5.29975.
176. Wang X, Osada T, Wang Y, et al. CSPG4 Protein as a New Target for the Antibody-Based Immunotherapy of Triple-Negative Breast Cancer. *JNCI J Natl Cancer Inst*. 2010;102(19):1496-1512. doi:10.1093/jnci/djq343.
177. Hsu NC, Nien P-Y, Yokoyama KK, Chu P-Y, Hou M-F. High chondroitin sulfate proteoglycan 4 expression correlates with poor outcome in patients with breast cancer. *Biochem Biophys Res Commun*. 2013;441(2):514-518. doi:10.1016/J.BBRC.2013.10.093.
178. Burrows FJ, Derbyshire EJ, Tazzari PL, et al. Up-regulation of endoglin on vascular endothelial cells in human solid tumors: implications for diagnosis and therapy. *Clin Cancer Res*. 1995;1(12):1623-1634. http://www.ncbi.nlm.nih.gov/pubmed/9815965. Accessed October 23, 2018.
179. Miller DW, Graulich W, Karges B, et al. Elevated expression of endoglin, a component of the TGF-beta-receptor complex, correlates with proliferation of tumor endothelial cells. *Int J cancer*. 1999;81(4):568-572.

http://www.ncbi.nlm.nih.gov/pubmed/10225446. Accessed October 23, 2018.
180. Wikström P, Lissbrant IF, Stattin P, Egevad L, Bergh A. Endoglin (CD105) is expressed on immature blood vessels and is a marker for survival in prostate cancer. *Prostate*. 2002;51(4):268-275. doi:10.1002/pros.10083.
181. Zeng Q, Li W, Lu D, et al. CD146, an epithelial-mesenchymal transition inducer, is associated with triple-negative breast cancer. *Proc Natl Acad Sci*. 2012;109(4):1127-1132. doi:10.1073/pnas.1111053108.
182. Zeng Q, Zhang P, Wu Z, et al. Quantitative proteomics reveals ER-α involvement in CD146-induced epithelial-mesenchymal transition in breast cancer cells. *J Proteomics*. 2014;103:153-169. doi:10.1016/j.jprot.2014.03.033.
183. Jang MH, Kim HJ, Kim EJ, Chung YR, Park SY. Expression of epithelial-mesenchymal transition–related markers in triple-negative breast cancer: ZEB1 as a potential biomarker for poor clinical outcome. *Hum Pathol*. 2015;46(9):1267-1274. doi:10.1016/j.humpath.2015.05.010.
184. Zabouo G, Imbert A-M, Jacquemier J, et al. CD146 expression is associated with a poor prognosis in human breast tumors and with enhanced motility in breast cancer cell lines. *Breast Cancer Res*. 2009;11(1):R1. doi:10.1186/bcr2215.
185. Zhang S, Chen L, Cui B, et al. ROR1 Is Expressed in Human Breast Cancer and Associated with Enhanced Tumor-Cell Growth. Li J, ed. *PLoS One*. 2012;7(3):e31127. doi:10.1371/journal.pone.0031127.
186. Yamaguchi T, Yanagisawa K, Sugiyama R, et al. NKX2-1/TITF1/TTF-1-Induced ROR1 Is Required to Sustain EGFR Survival Signaling in Lung Adenocarcinoma. *Cancer Cell*. 2012;21(3):348-361. doi:10.1016/j.ccr.2012.02.008.
187. Liu Y, Yang H, Chen T, et al. Silencing of Receptor Tyrosine Kinase ROR1 Inhibits Tumor-Cell Proliferation via PI3K/AKT/mTOR Signaling Pathway in Lung Adenocarcinoma. Rich BE, ed. *PLoS One*. 2015;10(5):e0127092. doi:10.1371/journal.pone.0127092.
188. Cui B, Zhang S, Chen L, et al. Targeting ROR1 Inhibits Epithelial-Mesenchymal Transition and Metastasis. *Cancer Res*. 2013;73(12):3649-3660. doi:10.1158/0008-5472.CAN-12-3832.
189. Cheah MT, Chen JY, Sahoo D, et al. CD14-expressing cancer cells establish the inflammatory and proliferative tumor microenvironment in bladder cancer. *Proc Natl Acad Sci*. 2015. doi:10.1073/pnas.1424795112.
190. Sullivan HC, Edgar MA, Cohen C, Kovach CK, HooKim K, Reid MD. The utility of ERG, CD31 and CD34 in the cytological diagnosis of angiosarcoma: an analysis of 25 cases. *J Clin Pathol*. 2015;68(1):44-50. doi:10.1136/jclinpath-2014-202629.
191. Venkataramani V, Kuffer S, Cheung KCP, et al. CD31 expression determines redox status and chemoresistance in human angiosarcomas. *Clin Cancer Res*. 2018. doi:10.1158/1078-0432.CCR-17-1778.
192. Tarrant JM, Robb L, van Spriel AB, Wright MD. Tetraspanins: molecular organisers of the leukocyte surface. *Trends Immunol*. 2003;24(11):610-617. http://www.ncbi.nlm.nih.gov/pubmed/14596886. Accessed October 23, 2018.
193. Levy S, Shoham T. The tetraspanin web modulates immune-signalling complexes. *Nat Rev Immunol*. 2005;5(2):136-148. doi:10.1038/nri1548.
194. Zöller M. Tetraspanins: push and pull in suppressing and promoting metastasis. *Nat Rev Cancer*. 2009;9(1):40-55. doi:10.1038/nrc2543.
195. Hemler ME. Tetraspanin proteins promote multiple cancer stages. *Nat Rev Cancer*. 2014;14(1):49-60. doi:10.1038/nrc3640.
196. Wiklander OPB, Bostancioglu RB, Welsh JA, et al. Systematic methodological

evaluation of a multiplex bead-based flow cytometry assay for detection of extracellular vesicle surface signatures. *Front Immunol*. 2018;9(JUN). doi:10.3389/fimmu.2018.01326.
197. Li C, Cui J-F, Chen M-B, et al. The preclinical evaluation of the dual mTORC1/2 inhibitor INK-128 as a potential anti-colorectal cancer agent. *Cancer Biol Ther*. 2015;16(1):34-42. doi:10.4161/15384047.2014.972274.
198. Liu Z-G, Tang J, Chen Z, et al. The novel mTORC1/2 dual inhibitor INK128 enhances radiosensitivity of breast cancer cell line MCF-7. *Int J Oncol*. 2016;49(3):1039-1045. doi:10.3892/ijo.2016.3604.
199. Fu S-J, Shen S-L, Li S-Q, et al. Hornerin promotes tumor progression and is associated with poor prognosis in hepatocellular carcinoma. doi:10.1186/s12885-018-4719-5.
200. Gutknecht MF, Seaman ME, Ning B, et al. Identification of the S100 fused-type protein hornerin as a regulator of tumor vascularity. *Nat Commun*. 2017;8(1). doi:10.1038/s41467-017-00488-6.
201. Sun Y, Xia Z, Shang Z, et al. Facile preparation of salivary extracellular vesicles for cancer proteomics. *Sci Rep*. 2016;6(December 2015):1-11. doi:10.1038/srep24669.
202. Arellano-Garcia ME, Li R, Liu X, et al. Identification of Tetranectin as a Potential Biomarker for Metastatic Oral Cancer. *Int J Mol Sci*. 2010;11(9):3106-3121. doi:10.3390/ijms11093106.
203. Miki Y, Kidoguchi Y, Sato M, et al. Dual roles of group IID phospholipase A2in inflammation and cancer. *J Biol Chem*. 2016;291(30):15588-15601. doi:10.1074/jbc.M116.734624.
204. Shen C, Yu J, Zhang X, et al. Strawberry Notch 1 (SBNO1) promotes proliferation of spermatogonial stem cells via the noncanonical Wnt pathway in mice. *Asian J Androl*. 2018;0(0):0. doi:10.4103/aja.aja_65_18.
205. De Groot M, Iyer A, Zurolo E, et al. Overexpression of ADK in human astrocytic tumors and peritumoral tissue is related to tumor-associated epilepsy. *Epilepsia*. 2012;53(1):58-66. doi:10.1111/j.1528-1167.2011.03306.x.
206. Tao Y, Wang K, Chen Z, et al. Correlation of five secretory proteins with the nasopharyngeal carcinoma metastasis and the clinical applications. *Oncotarget*. 2017;8(17):29383-29394. doi:10.18632/oncotarget.14725.
207. Yasmin-karim S, King MR, Messing EM, Lee Y. E-selectin ligand-1 controls circulating prostate cancer cell rolling / adhesion and metastasis. 2014;5(23).
208. Koh W-P, Yuan J-M, Sun C-L, et al. *Angiotensin I-Converting Enzyme (ACE) Gene Polymorphism and Breast Cancer Risk among Chinese Women in Singapore 1*. Vol 63.; 2003. http://cancerres.aacrjournals.org/content/canres/63/3/573.full.pdf. Accessed December 20, 2018.
209. Sun L, Guo C, Yuan H, et al. *Overexpression of Carboxypeptidase A4 (CPA4) Is Associated with Poor Prognosis in Patients with Gastric Cancer*. Vol 8.; 2016. www.ajtr.org. Accessed December 20, 2018.
210. Sun L, Wang Y, Yuan H, et al. CPA4 is a Novel Diagnostic and Prognostic Marker for Human Non-Small-Cell Lung Cancer. *J Cancer*. 2016;7(10):1197-1204. doi:10.7150/jca.15209.
211. Zhang J, Lim B, Miller LD, et al. RCP is a human breast cancer–promoting gene with Ras-activating function. 2009;119(8):2171-2183. doi:10.1172/JCI37622DS1.
212. Roeckel N, Woerner SM, Kloor M, et al. High frequency of LMAN1 abnormalities in colorectal tumors with microsatellite instability. *Cancer Res*. 2009;69(1):292-299. doi:10.1158/0008-5472.CAN-08-3314.

213. Yang M, Gao H, Chen P, Jia J, Wu S. Knockdown of interferon-induced transmembrane protein 3 expression suppresses breast cancer cell growth and colony formation and affects the cell cycle. *Oncol Rep*. 2013;30(1):171-178. doi:10.3892/or.2013.2428.
214. Flores IL, Kawahara R, Miguel MCC, et al. EEF1D modulates proliferation and epithelial-mesenchymal transition in oral squamous cell carcinoma. *Clin Sci*. 2016;130(10):785-799. doi:10.1042/CS20150646.
215. Vidak M, Jovcevska I, Samec N, et al. Meta-analysis and experimental validation identified FREM2 and SPRY1 as new glioblastoma marker candidates. *Int J Mol Sci*. 2018. doi:10.3390/ijms19051369.
216. Ohmura G, Tsujikawa T, Yaguchi T, et al. Aberrant Myosin 1b Expression Promotes Cell Migration and Lymph Node Metastasis of HNSCC. *Mol Cancer Res*. 2015;13(4):721-731. doi:10.1158/1541-7786.MCR-14-0410.
217. Hsin K, Yingrou C•, Rong T•, et al. SNX3-dependent regulation of epidermal growth factor receptor (EGFR) trafficking and degradation by aspirin in epidermoid carcinoma (A-431) cells. *Cell Mol Life Sci*. 2012;69:1505-1521. doi:10.1007/s00018-011-0887-z.
218. Bulk E, Ay A-S, Hammadi M, et al. Epigenetic dysregulation of K Ca 3.1 channels induces poor prognosis in lung cancer. doi:10.1002/ijc.29490.
219. Arthurs C, Nazia Murtaza B, Thomson C, et al. Expression of ribosomal proteins in normal and cancerous human prostate tissue. 2017. doi:10.1371/journal.pone.0186047.
220. Samanta S, Pursell B, Mercurio AM. IMP3 protein promotes chemoresistance in breast cancer cells by regulating breast cancer resistance protein (ABCG2) expression. *J Biol Chem*. 2013;288(18):12569-12573. doi:10.1074/jbc.C112.442319.
221. Sato K, Akimoto K. Expression Levels of KMT2C and SLC20A1 Identified by Information-theoretical Analysis Are Powerful Prognostic Biomarkers in Estrogen Receptor-positive Breast Cancer. *Clin Breast Cancer*. 2017;17(3):e135-e142. doi:10.1016/j.clbc.2016.11.005.
222. Lin G, Aranda V, Muthuswamy SK, Tonks NK. Identification of PTPN23 as a novel regulator of cell invasion in mammary epithelial cells from a loss-of-function screen of the 'PTP-ome'. *Genes Dev*. 2011;25(13):1412-1425. doi:10.1101/gad.2018911.
223. Zhang S, Fan G, Hao Y, Hammell M, Wilkinson JE, Tonks NK. Suppression of protein tyrosine phosphatase N23 predisposes to breast tumorigenesis via activation of FYN kinase. *Genes Dev*. 2017;31(19):1939-1957. doi:10.1101/gad.304261.117.
224. Yang J, Min K-W, Kim D-H, et al. High TNFRSF12A level associated with MMP-9 overexpression is linked to poor prognosis in breast cancer: Gene set enrichment analysis and validation in large-scale cohorts. 2018. doi:10.1371/journal.pone.0202113.
225. Gonias SL, Karimi-Mostowfi N, Murray SS, Mantuano E, Gilder AS. Expression of LDL receptor-related proteins (LRPs) in common solid malignancies correlates with patient survival. 2017. doi:10.1371/journal.pone.0186649.
226. Sheu M-J, Hsieh M-J, Chou Y-E, et al. Effects of ADAMTS14 genetic polymorphism and cigarette smoking on the clinicopathologic development of hepatocellular carcinoma. 2017. doi:10.1371/journal.pone.0172506.
227. Takakura K, Shibazaki Y, Yoneyama H, et al. Inhibition of Cell Proliferation and Growth of Pancreatic Cancer by Silencing of Carbohydrate Sulfotransferase 15 In Vitro and in a Xenograft Model. Batra SK, ed. *PLoS One*. 2015;10(12):e0142981. doi:10.1371/journal.pone.0142981.

228. Bhattacharyya S, Feferman L, Tobacman JK, Bhattacharyya S, Feferman L, Tobacman JK. Chondroitin sulfatases differentially regulate Wnt signaling in prostate stem cells through effects on SHP2, phospho-ERK1/2, and Dickkopf Wnt signaling pathway inhibitor (DKK3). *Oncotarget*. 2017;8(59):100242-100260. doi:10.18632/oncotarget.22152.
229. Han M, Xu W. EMP3 is induced by TWIST1/2 and regulates epithelial-to-mesenchymal transition of gastric cancer cells. *Tumor Biol*. 2017;39(7):101042831771840. doi:10.1177/1010428317718404.
230. Bullock N, Potts J, Simpkin AJ. Serine-arginine protein kinase 1 (SRPK1), a determinant of angiogenesis, is upregulated in prostate cancer and correlates with disease stage and invasion. *J Clin Pathol*. 2016;69:171-175. doi:10.1136/jclinpath.
231. Masuda M, Uno Y, Ohbayashi N, et al. TNIK inhibition abrogates colorectal cancer stemness. *Nat Commun*. 2016;7(1):12586. doi:10.1038/ncomms12586.
232. Zhang Y, Zou X, Qian W, et al. Enhanced PAPSS2/VCAN sulfation axis is essential for Snail-mediated breast cancer cell migration and metastasis. *Cell Death Differ*. June 2018:1. doi:10.1038/s41418-018-0147-y.
233. Velusamy T, Palanisamy N, Kalyana-Sundaram S, et al. Recurrent reciprocal RNA chimera involving YPEL5 and PPP1CB in chronic lymphocytic leukemia. *Proc Natl Acad Sci*. 2013;110(8):3035-3040. doi:10.1073/pnas.1214326110.
234. Geyik E, Ziya Igci Y, Pala E, et al. Investigation of the association between ATP2B4 and ATP5B genes with colorectal cancer. *Gene*. 2014;540:178-182. doi:10.1016/j.gene.2014.02.050.
235. Gao J, Arbman G, He L, et al. MANBA polymorphism was related to increased risk of colorectal cancer in Swedish but not in Chinese populations. 2009. doi:10.1080/02841860701644052.
236. Kapil S, Krishan Sharma B, Patil M, et al. *The Cell Polarity Protein Scrib Functions as a Tumor Suppressor in Liver Cancer*. Vol 8.; 2017. www.impactjournals.com/oncotarget/. Accessed December 21, 2018.
237. Liu Y, Liu F, Cao Y, et al. Shwachman-Diamond Syndrome Protein SBDS Maintains Human Telomeres by Regulating Telomerase Recruitment. *CellReports*. 2018;22:1849-1860. doi:10.1016/j.celrep.2018.01.057.
238. Xie D, Wu X, Lan L, et al. Downregulation of TFAM inhibits the tumorigenesis of non-small cell lung cancer by activating ROS-mediated JNK/p38MAPK signaling and reducing cellular bioenergetics. *Oncotarget*. 2016;7(10):4-6. doi:10.18632/oncotarget.7018.
239. Lo U-G, Pong R-C, Yang D, et al. IFN-r-induced IFIT5 promotes epithelial-to-mesenchymal transition in prostate cancer via microRNA processing. *Cancer Res*. 2018. doi:10.1158/0008-5472.CAN-18-2207.
240. Uchiyama B, Saijo Y, Kumano N, et al. Expression of nucleolar protein p120 in human lung cancer: difference in histological types as a marker for proliferation. *Clin Cancer Res*. 1997;3(10):1873-1877. http://www.ncbi.nlm.nih.gov/pubmed/9815576. Accessed December 21, 2018.
241. Dun MD, Chalkley RJ, Faulkner S, et al. Proteotranscriptomic Profiling of 231-BR Breast Cancer Cells: Identification of Potential Biomarkers and Therapeutic Targets for Brain Metastasis. *Mol Cell Proteomics*. 2015;14(9):2316-2330. doi:10.1074/mcp.M114.046110.
242. López-Knowles E, O'Toole SA, McNeil CM, et al. PI3K pathway activation in breast cancer is associated with the basal-like phenotype and cancer-specific mortality. *Int J Cancer*. 2010;126(5):1121-1131. doi:10.1002/ijc.24831.
243. Ueng S-H, Chen S-C, Chang Y-S, et al. Phosphorylated mTOR expression correlates with poor outcome in early-stage triple negative breast carcinomas.

Int J Clin Exp Pathol. 2012;5(8):806-813. http://www.ncbi.nlm.nih.gov/pubmed/23071863. Accessed December 11, 2018.
244. Fan S-J, Snell C, Turley H, et al. PAT4 levels control amino-acid sensitivity of rapamycin-resistant mTORC1 from the Golgi and affect clinical outcome in colorectal cancer. *Oncogene*. 2016;35(23):3004-3015. doi:10.1038/onc.2015.363.
245. Faes S, Demartines N, Dormond O. Resistance to mTORC1 Inhibitors in Cancer Therapy: From Kinase Mutations to Intratumoral Heterogeneity of Kinase Activity. *Oxid Med Cell Longev*. 2017;2017. doi:10.1155/2017/1726078.
246. Rodrik-Outmezguine VS, Okaniwa M, Yao Z, et al. Overcoming mTOR resistance mutations with a new-generation mTOR inhibitor. *Nature*. 2016;534. doi:10.1038/nature17963.
247. Cloughesy TF, Yoshimoto K, Nghiemphu P, et al. Antitumor Activity of Rapamycin in a Phase I Trial for Patients with Recurrent PTEN-Deficient Glioblastoma. Weil RJ, ed. *PLoS Med*. 2008;5(1):e8. doi:10.1371/journal.pmed.0050008.
248. Rodrik-Outmezguine VS, Chandarlapaty S, Pagano NC, et al. mTOR kinase inhibition causes feedback-dependent biphasic regulation of AKT signaling. *Cancer Discov*. 2011;1(3):248-259. doi:10.1158/2159-8290.CD-11-0085.
249. Soares HP, Ni Y, Kisfalvi K, Sinnett-Smith J, Rozengurt E. Different Patterns of Akt and ERK Feedback Activation in Response to Rapamycin, Active-Site mTOR Inhibitors and Metformin in Pancreatic Cancer Cells. Pizzo S V., ed. *PLoS One*. 2013;8(2):e57289. doi:10.1371/journal.pone.0057289.
250. Gerlinger M, Rowan AJ, Horswell S, et al. Intratumor Heterogeneity and Branched Evolution Revealed by Multiregion Sequencing. *N Engl J Med*. 2012;366(10):883-892. doi:10.1056/NEJMoa1113205.
251. Bantscheff M, Schirle M, Sweetman G, Rick J, Kuster B. Quantitative mass spectrometry in proteomics: a critical review. *Anal Bioanal Chem*. 2007;389(4):1017-1031. doi:10.1007/s00216-007-1486-6.
252. Eitan E, Suire C, Zhang S, Mattson MP. Impact of lysosome status on extracellular vesicle content and release. *Ageing Res Rev*. 2016;32:65-74. doi:10.1016/j.arr.2016.05.001.
253. Safaei R, Larson BJ, Cheng TC, et al. Abnormal lysosomal trafficking and enhanced exosomal export of cisplatin in drug-resistant human ovarian carcinoma cells. *Mol Cancer Ther*. 2005;4(10):1595-1604. doi:10.1158/1535-7163.MCT-05-0102.
254. Wang Y, Ding S-J, Wang W, et al. Profiling signaling polarity in chemotactic cells. *Proc Natl Acad Sci U S A*. 2007;104(20):8328-8333. doi:10.1073/pnas.0701103104.
255. Jia W, Gao X-J, Zhang Z-D, Yang Z-X, Zhang G, Zhang Z. *S100A4 Silencing Suppresses Proliferation, Angiogenesis and Invasion of Thyroid Cancer Cells through Downregulation of MMP-9 and VEGF CONCLUSIONS: Our Results Provide Evidence That the Downregulation of S100A4 Using RNAi Technology May Provide an Effective Tool for Thy-Roid Cancer Therapy*. https://www.europeanreview.org/wp/wp-content/uploads/1495-1508.pdf. Accessed December 19, 2018.
256. Tu C-F, Wu M-Y, Lin Y-C, Kannagi R, Yang R-B. FUT8 promotes breast cancer cell invasiveness by remodeling TGF-β receptor core fucosylation. doi:10.1186/s13058-017-0904-8.
257. Sieg DJ, Hauck CR, Ilic D, et al. FAK integrates growth-factor and integrin signals to promote cell migration. *Nat Cell Biol*. 2000;2(5):249-256. doi:10.1038/35010517.

258. Gordon DE, Bond LM, Sahlender DA, Peden AA. A targeted siRNA screen to identify SNAREs required for constitutive secretion in mammalian cells. *Traffic*. 2010;11(9):1191-1204. doi:10.1111/j.1600-0854.2010.01087.x.
259. Gross JC, Chaudhary V, Bartscherer K, Boutros M. Active Wnt proteins are secreted on exosomes. *Nat Cell Biol*. 2012;14(10):1036-1045. doi:10.1038/ncb2574.
260. Kluger HM, Kluger Y, Gilmore-Hebert M, et al. cDNA microarray analysis of invasive and tumorigenic phenotypes in a breast cancer model. *Lab Investig*. 2004;84(3):320-331. doi:10.1038/labinvest.3700044.
261. Wang D, Cai C, Dong X, et al. Identification of multipotent mammary stem cells by protein C receptor expression. *Nature*. 2015;517(7532):81-84. doi:10.1038/nature13851.
262. Yu QC, Song W, Wang D, Zeng YA. Identification of blood vascular endothelial stem cells by the expression of protein C receptor. *Cell Res*. 2016;26(10):1079-1098. doi:10.1038/cr.2016.85.
263. Iwasaki H, Arai F, Kubota Y, Dahl M, Suda T. Endothelial protein C receptor–expressing hematopoietic stem cells reside in the perisinusoidal niche in fetal liver. *Blood*. 2010;116(4):544-553. doi:10.1182/BLOOD-2009-08-240903.
264. Wang D, Liu C, Wang J, et al. Protein C receptor stimulates multiple signaling pathways in breast cancer cells. 2017. doi:10.1074/jbc.M117.814046.
265. Huleihel L, Hussey GS, Naranjo JD, et al. Matrix-bound nanovesicles within ECM bioscaffolds. *Sci Adv*. 2016;2(June):1600502. doi:10.1126/sciadv.1600502.
266. Giusti I, D'ascenzo S, Millimaggi D, et al. Cathepsin B Mediates the pH-Dependent Proinvasive Activity of Tumor-Shed Microvesicles 1. *Neoplasia*. 2008;10:481-488. doi:10.1593/neo.08178.
267. Kiss I, Korpos É, Deák F. Matrilin-2, an extracellular adaptor protein, is needed for the regeneration of muscle, nerve and other tissues Matrilin-2 Modulates the Extracellular Matrix (ECM) Assembly. 2015. doi:10.4103/1673-5374.158332.
268. Carreras CW, Santi D V. The Catalytic Mechanism and Structure of Thymidylate Synthase. *Annu Rev Biochem*. 1995;64(1):721-762. doi:10.1146/annurev.bi.64.070195.003445.
269. Kotoula V, Krikelis D, Karavasilis V, et al. Expression of DNA repair and replication genes in non-small cell lung cancer (NSCLC): a role for thymidylate synthetase (TYMS). *BMC Cancer 2012 121*. 2012;12(1):342. doi:10.1186/1471-2407-12-342.
270. Pestalozzi BC, Peterson HF, Gelber RD, et al. Prognostic importance of thymidylate synthase expression in early breast cancer. *J Clin Oncol*. 1997;15(5):1923-1931. doi:10.1200/JCO.1997.15.5.1923.
271. Popat S, Matakidou A, Houlston RS. Thymidylate synthase expression and prognosis in colorectal cancer: a systematic review and meta-analysis. *J Clin Oncol*. 2004;22(3):529-536. doi:10.1200/JCO.2004.05.064.
272. Flick K, Kaiser P. Protein degradation and the stress response. *Semin Cell Dev Biol*. 2012;23(5):515-522. doi:10.1016/J.SEMCDB.2012.01.019.
273. Mlecnik B, Bindea G, Kirilovsky A, et al. The tumor microenvironment and Immunoscore are critical determinants of dissemination to distant metastasis. *Sci Transl Med*. 2016;8(327):327ra26-327ra26. doi:10.1126/scitranslmed.aad6352.
274. Basler M, Kirk CJ, Groettrup M. The immunoproteasome in antigen processing and other immunological functions. *Curr Opin Immunol*. 2013;25(1):74-80. doi:10.1016/J.COI.2012.11.004.
275. Huang F, Yao Y, Wu J, et al. *Blocking Platelet-Derived Growth Factor-d Inhibits*

Human Lung Cancer Progression. Vol 10.; 2017. www.ijcep.com/. Accessed December 12, 2018.
276. Satow R, Nakamura T, Kato C, et al. Molecular and Cellular Pathobiology ZIC5 Drives Melanoma Aggressiveness by PDGFD-Mediated Activation of FAK and STAT3. 2017. doi:10.1158/0008-5472.CAN-16-0991.
277. Graham TR, Burd CG. Coordination of Golgi functions by phosphatidylinositol 4-kinases. *Trends Cell Biol*. 2011;21(2):113-121. doi:10.1016/j.tcb.2010.10.002.
278. Yeaman C, Ayala MI, Wright JR, et al. Protein kinase D regulates basolateral membrane protein exit from trans-Golgi network. *Nat Cell Biol*. 2004;6(2):106-112. doi:10.1038/ncb1090.
279. Wang YJ, Wang J, Sun HQ, et al. Phosphatidylinositol 4 phosphate regulates targeting of clathrin adaptor AP-1 complexes to the Golgi. *Cell*. 2003;114(3):299-310. http://www.ncbi.nlm.nih.gov/pubmed/12914695. Accessed December 14, 2018.
280. Tokuda E, Itoh T, Hasegawa J, et al. Molecular and Cellular Pathobiology Phosphatidylinositol 4-Phosphate in the Golgi Apparatus Regulates Cell-Cell Adhesion and Invasive Cell Migration in Human Breast Cancer. *Cancer Res*. 2014;74(11):3054-3066. doi:10.1158/0008-5472.CAN-13-2441.
281. Kim YJ, Choi J-S, Seo J, et al. MET is a potential target for use in combination therapy with EGFR inhibition in triple-negative/basal-like breast cancer. doi:10.1002/ijc.28566.
282. Comoglio PM, Giordano S, Trusolino L. Drug development of MET inhibitors: targeting oncogene addiction and expedience. *Nat Rev Drug Discov*. 2008;7(6):504-516. doi:10.1038/nrd2530.
283. Rasheed SAK, Teo CR, Beillard EJ, et al. MicroRNA-31 controls G protein alpha-13 (GNA13) expression and cell invasion in breast cancer cells. *Mol Cancer*. 2015;14(1):67. doi:10.1186/s12943-015-0337-x.
284. Rasheed SAK, Teo CR, Beillard EJ, Voorhoeve PM, Casey PJ. MicroRNA-182 and microRNA-200a control G-protein subunit α-13 (GNA13) expression and cell invasion synergistically in prostate cancer cells. *J Biol Chem*. 2013;288(11):7986-7995. doi:10.1074/jbc.M112.437749.
285. Rasheed SAK, Leong HS, Lakshmanan M, et al. GNA13 expression promotes drug resistance and tumor-initiating phenotypes in squamous cell cancers. *Oncogene*. 2018;37(10):1340-1353. doi:10.1038/s41388-017-0038-6.
286. Lo P-K, Yao Y, Lee JS, et al. LIPG signaling promotes tumor initiation and metastasis of human basal-like triple-negative breast cancer. doi:10.7554/eLife.31334.001.
287. Kanda Y, Osaki M, Onuma K, et al. Amigo2-upregulation in tumour cells facilitates their attachment to liver endothelial cells resulting in liver metastases. *Sci Rep*. 2017;7(October 2016):1-13. doi:10.1038/srep43567.
288. Kuang C-M, Fu X, Hua Y-J, et al. BST2 confers cisplatin resistance via NF-κB signaling in nasopharyngeal cancer. *Nat Publ Gr*. 2017;8. doi:10.1038/cddis.2017.271.
289. Mahauad-Fernandez WD, DeMali KA, Olivier AK, Okeoma CM. Bone marrow stromal antigen 2 expressed in cancer cells promotes mammary tumor growth and metastasis. *Breast Cancer Res*. 2014;16(1). doi:10.1186/s13058-014-0493-8.
290. Meng Y, Wang L, Chen D, et al. LAPTM4B: An oncogene in various solid tumors and its functions. *Oncogene*. 2016;35(50):6359-6365. doi:10.1038/onc.2016.189.
291. Li L, Wei XH, Pan YP, et al. LAPTM4B: A novel cancer-associated gene motivates multidrug resistance through efflux and activating PI3K/AKT signaling.

Oncogene. 2010;29(43):5785-5795. doi:10.1038/onc.2010.303.
292. Benjamin S, Weidberg H, Rapaport D, et al. EHD2 mediates trafficking from the plasma membrane by modulating Rac1 activity. *Biochem J*. 2011;439(3):433-442. doi:10.1042/BJ20111010.
293. Yang X, Ren H, Yao L, Chen X, He A. Role of EHD2 in migration and invasion of human breast cancer cells. *Tumor Biol*. 2015. doi:10.1007/s13277-014-3011-9.
294. Bustelo XR, Ojeda V, Barreira M, Sauzeau V, Castro-Castro A. Rac-ing to the plasma membrane. *Small GTPases*. 2012;3(1):60-66. doi:10.4161/sgtp.19111.
295. Bignotti E, Tassi RA, Calza S, et al. Differential gene expression profiles between tumor biopsies and short-term primary cultures of ovarian serous carcinomas: identification of novel molecular biomarkers for early diagnosis and therapy. *Gynecol Oncol*. 2006;103(2):405-416. doi:10.1016/j.ygyno.2006.03.056.
296. Torrino S, Shen W-W, Blouin CM, et al. EHD2 is a mechanotransducer connecting caveolae dynamics with gene transcription. *J Cell Biol*. 2018;217:4092-4105. doi:10.1083/jcb.201801122.
297. Bonifacino JS, Rojas R. Retrograde transport from endosomes to the trans-Golgi network. *Nat Rev Mol Cell Biol*. 2006;7(8):568-579. doi:10.1038/nrm1985.
298. Grant BD, Donaldson JG. Pathways and mechanisms of endocytic recycling. *Nat Rev Mol Cell Biol*. 2009;10(9):597-608. doi:10.1038/nrm2755.
299. van Dam EM, Stoorvogel W. Dynamin-dependent Transferrin Receptor Recycling by Endosome-derived Clathrin-coated Vesicles. Bonifacino J, ed. *Mol Biol Cell*. 2002;13(1):169-182. doi:10.1091/mbc.01-07-0380.
300. Rychtarcikova Z, Lettlova S, Tomkova V, et al. *Tumor-Initiating Cells of Breast and Prostate Origin Show Alterations in the Expression of Genes Related to Iron Metabolism*. Vol 8.; 2017. www.impactjournals.com/oncotarget. Accessed December 19, 2018.
301. Miller LD, Coffman LG, Chou JW, et al. An iron regulatory gene signature predicts outcome in breast cancer. *Cancer Res*. 2011;71(21):6728-6737. doi:10.1158/0008-5472.CAN-11-1870.
302. Zhu R, Liu Y, Zhou H, et al. Deubiquitinating enzyme PSMD14 promotes tumor metastasis through stabilizing SNAIL in human esophageal squamous cell carcinoma. *Cancer Lett*. 2018;418:125-134. doi:10.1016/j.canlet.2018.01.025.
303. Przybyla LM, Theunissen TW, Jaenisch R, Voldman J. Matrix Remodeling Maintains Embryonic Stem Cell Self-Renewal by Activating Stat3. *Stem Cells*. 2013;31(6):1097-1106. doi:10.1002/stem.1360.
304. Overall CM, Dean RA. Degradomics: Systems biology of the protease web. Pleiotropic roles of MMPs in cancer. *Cancer Metastasis Rev*. 2006;25(1):69-75. doi:10.1007/s10555-006-7890-0.
305. Shen C, Kuo Y, Chen C, Chen M. MMP1 expression is activated by Slug and enhances multi-drug resistance (MDR) in breast cancer. 2017:1-13.
306. Wang K, Cao F, Fang W, et al. *Activation of SNAT1/SLC38A1 in Human Breast Cancer: Correlation with p-Akt Overexpression*.; 2013. doi:10.1186/1471-2407-13-343.
307. Mikaelian I, Malek M, Gadet R, et al. Genetic and pharmacologic inhibition of mTORC1 promotes EMT by a TGF-β-independent mechanism. *Cancer Res*. 2013;73(22):6621-6631. doi:10.1158/0008-5472.CAN-13-0560.
308. Dever TE. Gene-Specific Regulation by General Translation Factors. *Cell*. 2002;108(4):545-556. doi:10.1016/S0092-8674(02)00642-6.
309. Cheng DD, Li SJ, Zhu B, Zhou SM, Yang QC. EEF1D overexpression promotes osteosarcoma cell proliferation by facilitating Akt-mTOR and Akt-bad signaling.

J Exp Clin Cancer Res. 2018;37(1):1-10. doi:10.1186/s13046-018-0715-5.
310. Shan S, Lv Q, Zhao Y, et al. Wnt/β-catenin pathway is required for epithelial to mesenchymal transition in CXCL12 over expressed breast cancer cells. *Int J Clin Exp Pathol*. 2015;8(10):12357-12367.
311. Ali N, Zhang L, Taylor S, Mironov A, Urbé S, Woodman P. Recruitment of UBPY and ESCRT Exchange Drive HD-PTP-Dependent Sorting of EGFR to the MVB. *Curr Biol*. 2013;23(6):453-461. doi:10.1016/j.cub.2013.02.033.
312. Kharitidi D, Apaja PM, Manteghi S, et al. Interplay of Endosomal pH and Ligand Occupancy in Integrin α5β1 Ubiquitination, Endocytic Sorting, and Cell Migration. *Cell Rep*. 2015;13(3):599-609. doi:10.1016/J.CELREP.2015.09.024.
313. Vinet L, Zhedanov A. A 'missing' family of classical orthogonal polynomials. *Oncogene*. 2010;37(14):1857-1868. doi:10.1088/1751-8113/44/8/085201.
314. Zhang L, Zhang S, Yao J, et al. Microenvironment-induced PTEN loss by exosomal microRNA primes brain metastasis outgrowth. *Nature*. 2015;527(7576):100-104. doi:10.1038/nature15376.
315. Lorger M, Felding-Habermann B. Capturing changes in the brain microenvironment during initial steps of breast cancer brain metastasis. *Am J Pathol*. 2010;176(6):2958-2971. doi:10.2353/ajpath.2010.090838.
316. Wilhelm I, Molnár J, Fazakas C, Haskó J, Krizbai IA. Role of the Blood-Brain Barrier in the Formation of Brain Metastases. *OPEN ACCESS Int J Mol Sci*. 2013;14:14. doi:10.3390/ijms14011383.
317. Eichler AF, Chung E, Kodack DP, Loeffler JS, Fukumura D, Jain RK. The biology of brain metastases—translation to new therapies. *Nat Rev Clin Oncol*. 2011;8(6):344-356. doi:10.1038/nrclinonc.2011.58.
318. Puech C, Hodin S, Forest V, et al. Assessment of HBEC-5i endothelial cell line cultivated in astrocyte conditioned medium as a human blood-brain barrier model for ABC drug transport studies. *Int J Pharm*. 2018;551(1-2):281-289. doi:10.1016/j.ijpharm.2018.09.040.
319. Wiklander OPB, Nordin JZ, O'Loughlin A, et al. Extracellular vesicle in vivo biodistribution is determined by cell source, route of administration and targeting. *J Extracell Vesicles*. 2015;4(2015):1-13. doi:10.3402/jev.v4.26316.
320. Serwer L, Hashizume R, Ozawa T, James CD. Systemic and Local Drug Delivery for Treating Diseases of the Central Nervous System in Rodent Models. *J Vis Exp*. 2010;(42):1992. doi:10.3791/1992.
321. Chen W, Hoffmann AD, Liu H, Liu X. Organotropism: new insights into molecular mechanisms of breast cancer metastasis. *npj Precis Oncol*. 2018;2:4. doi:10.1038/s41698-018-0047-0.
322. Groisman GM. Lobular Carcinoma of the Breast Metastatic to the Spleen and Accessory Spleen: Report of a Case. *Case Rep Pathol*. 2016. doi:10.1155/2016/5160180.
323. Nasu H, Miura K, Baba M, et al. Breast cancer metastatic to the kidney with renal vein involvement. *Jpn J Radiol*. 2015;33(2):107-111. doi:10.1007/s11604-014-0386-x.
324. Zhang J, Hulme L, Liu J-L. Asymmetric inheritance of cytoophidia in Schizosaccharomyces pombe. *Biol Open*. 2014. doi:10.1242/bio.20149613.
325. Azzam G, Liu JL. Only One Isoform of Drosophila melanogaster CTP Synthase Forms the Cytoophidium. *PLoS Genet*. 2013. doi:10.1371/journal.pgen.1003256.
326. Campbell SG, Hoyle NP, Ashe MP. Dynamic cycling of eIF2 through a large eIF2B-containing cytoplasmic body: implications for translation control. *J Cell Biol*. 2005;170(6):925-934. doi:10.1083/jcb.200503162.
327. Mcmurray MA, Bertin A, Iii GG, Lam L, Nogales E, Thorner J. Article Septin

Filament Formation Is Essential in Budding Yeast. 2011. doi:10.1016/j.devcel.2011.02.004.
328. Garcia G, Bertin A, Li Z, et al. Subunit-dependent modulation of septin assembly: Budding yeast septin Shs1 promotes ring and gauze formation. *J Cell Biol*. 2011. doi:10.1083/jcb.201107123.
329. Boone AN, Chan A, Kulpa JE, Brownsey RW. Bimodal activation of acetyl-CoA carboxylase by glutamate. *J Biol Chem*. 2000;275(15):10819-10825. doi:10.1074/JBC.275.15.10819.
330. Allen C, Büttner S, Aragon AD, et al. Isolation of quiescent and nonquiescent cells from yeast stationary-phase cultures. *J Cell Biol*. 2006;174(1):89-100. doi:10.1083/jcb.200604072.
331. Thangavelu K, Chong QY, Low BC, Sivaraman J. Structural Basis for the Active Site Inhibition Mechanism of Human Kidney-Type Glutaminase (KGA). *Sci Rep*. 2015;4:1-7. doi:10.1038/srep03827.
332. Lehmann BD, Bauer JA, Chen X, et al. Identification of human triple-negative breast cancer subtypes and preclinical models for selection of targeted therapies. *J Clin Invest*. 2011;121(7):2750-2767. doi:10.1172/JCI45014.
333. Yang L, Venneti S, Nagrath D. Glutaminolysis: A Hallmark of Cancer Metabolism. *Annu Rev Biomed Eng*. 2017;19:163-194. doi:10.1146/annurev-bioeng-071516.
334. Brownsey RW, Zhande R, Boone AN. Isoforms of acetyl-CoA carboxylase: structures, regulatory properties and metabolic functions. *Biochem Soc Trans*. 1997;25(4):1232-1238. doi:10.1042/BST0251232.
335. Kim K-H. REGULATION OF MAMMALIAN ACETYL-COENZYME A CARBOXYLASE. *Annu Rev Nutr*. 1997. doi:10.1146/annurev.nutr.17.1.77.
336. Kleinschmidt AK, Moss J, Lane DM. Acetyl coenzyme A carboxylase: filamentous nature of the animal enzymes. *Science*. 1969;166(3910):1276-1278. doi:10.1126/SCIENCE.166.3910.1276.
337. Meredith MJ, Lane MD. *Acetyl-CoA Carboxylase*. Vol 253.; 1978. http://www.jbc.org/. Accessed August 30, 2018.
338. Hunkeler M, Hagmann A, Stuttfeld E, et al. Structural basis for regulation of human acetyl-CoA carboxylase. *Nature*. 2018;558(7710):470-474. doi:10.1038/s41586-018-0201-4.
339. Ha J, Daniel S, Broyles SS, Kim KH. Critical phosphorylation sites for acetyl-CoA carboxylase activity. *J Biol Chem*. 1994.
340. Magnard C, Bachelier R, Vincent A, et al. BRCA1 interacts with acetyl-CoA carboxylase through its tandem of BRCT domains. *Oncogene*. 2002. doi:10.1038/sj.onc.1205915.
341. Alvarez-Vasquez F, Sims KJ, Voit EO, Hannun YA. Coordination of the dynamics of yeast sphingolipid metabolism during the diauxic shift. *Theor Biol Med Model*. 2007;4:42. doi:10.1186/1742-4682-4-42.
342. Richards NGJ, Kilberg MS. Asparagine Synthetase Chemotherapy. *Annu Rev Biochem*. 2006. doi:10.1146/annurev.biochem.75.103004.142520.
343. Barbosa-Tessmann IP, Chen C, Zhong C, et al. Activation of the Human Asparagine Synthetase Gene by the Amino Acid Response and the Endoplasmic Reticulum Stress Response Pathways Occurs by Common Genomic Elements*. 2000. doi:10.1074/jbc.M000004200.
344. Krall AS, Xu S, Graeber TG, Braas D, Christofk HR. ARTICLE Asparagine promotes cancer cell proliferation through use as an amino acid exchange factor. *Nat Commun*. 2016;7. doi:10.1038/ncomms11457.
345. ASLANIAN AM, FLETCHER BS, KILBERG MS. Asparagine synthetase expression alone is sufficient to induce l-asparaginase resistance in MOLT-4

human leukaemia cells. *Biochem J*. 2001. doi:10.1042/0264-6021:3570321.
346. Zwaan CM, Kaspers GJL, Pieters R, et al. Different drug sensitivity profiles of acute myeloid and lymphoblastic leukemia and normal peripheral blood mononuclear cells in children with and without Down syndrome. *Blood*. 2002. doi:10.1182/blood.V99.1.245.
347. Cui H, Darmanin S, Natsuisaka M, et al. Enhanced expression of asparagine synthetase under glucose-deprived conditions protects pancreatic cancer cells from apoptosis induced by glucose deprivation and cisplatin. *Cancer Res*. 2007. doi:10.1158/0008-5472.CAN-06-2519.
348. Zhang S, Ding K, Shen Q-J, Zhao S, Liuid J-L. Filamentation of asparagine synthetase in Saccharomyces cerevisiae. *PLOS Genet* |. 2018. doi:10.1371/journal.pgen.1007737.
349. Liu B, Field G, Qian S-B. Translational reprogramming in stress response. doi:10.1002/wrna.1212.
350. Netto LES, Antunes F. The Roles of Peroxiredoxin and Thioredoxin in Hydrogen Peroxide Sensing and in Signal Transduction. *Mol Cells*. 2016;39(1):65-71. doi:10.14348/molcells.2016.2349.
351. Irokawa H, Tachibana T, Watanabe T, et al. Redox-dependent Regulation of Gluconeogenesis by a Novel Mechanism Mediated by a Peroxidatic Cysteine of Peroxiredoxin OPEN. 2016. doi:10.1038/srep33536.
352. Mor I, Cheung EC, Vousden KH. Control of glycolysis through regulation of PFK1: Old friends and recent additions. *Cold Spring Harb Symp Quant Biol*. 2011. doi:10.1101/sqb.2011.76.010868.
353. Foe LG, Trujillo JL. Quaternary structure of pig liver phosphofructokinase. *J Biol Chem*. 1980.
354. Webb BA, Dosey AM, Wittmann T, Kollman JM, Barber DL. The glycolytic enzyme phosphofructokinase-1 assembles into filaments. *J Cell Biol*. 2017. doi:10.1083/jcb.201701084.
355. Zampar GG, Kümmel A, Ewald J, et al. Temporal system-level organization of the switch from glycolytic to gluconeogenic operation in yeast. *Mol Syst Biol*. 2013. doi:10.1038/msb.2013.11.
356. François J, Parrou JL. Reserve carbohydrates metabolism in the yeast *Saccharomyces cerevisiae*. *FEMS Microbiol Rev*. 2001. doi:10.1111/j.1574-6976.2001.tb00574.x.
357. Horowitz A, Lapointe JF, Eid R, et al. The human septin7 and the yeast CDC10 septin prevent Bax and copper mediated cell death in yeast. *Biochim Biophys Acta - Mol Cell Res*. 2013. doi:10.1016/j.bbamcr.2013.09.004.
358. Spiliotis ET, Kinoshita M, Nelson WJ. A mitotic septin scaffold required for Mammalian chromosome congression and segregation. *Science*. 2005;307(5716):1781-1785. doi:10.1126/science.1106823.
359. Zhang N, Liu L, Fan N, et al. The requirement of SEPT2 and SEPT7 for migration and invasion in human breast cancer via MEK/ERK activation. *Oncotarget*. 2016;7(38):61587-61600. doi:10.18632/oncotarget.11402.
360. Connolly D, Abdesselam I, Verdier-Pinard P, Montagna C. Septin roles in tumorigenesis. *Biol Chem*. 392:725-738. doi:10.1515/BC.2011.073.
361. Mostowy S, Cossart P. Septins: The fourth component of the cytoskeleton. *Nat Rev Mol Cell Biol*. 2012. doi:10.1038/nrm3284.
362. Kinoshita M. *The Septins*. Vol 4.; 2003. http://genomebiology.com/2003/4/11/236. Accessed September 19, 2018.
363. Liu M, Shen S, Chen F, Yu W, Yu L. Linking the septin expression with carcinogenesis. *Mol Biol Rep*. 2010. doi:10.1007/s11033-010-0009-2.
364. Jiang H, Ouyang H, Zhou H, Jin C. GDP-mannose pyrophosphorylase is

essential for cell wall integrity, morphogenesis and viability of Aspergillus fumigatus. *Microbiology*. 2008. doi:10.1099/mic.0.2008/019240-0.
365. Warit S, Walmsley RM, Stateva LI. Cloning and sequencing of the Candida albicans homologue of SRB1/PSA1/VIG9, the essential gene encoding GDP-mannose pyrophosphorylase in Saccharomyces cerevisiae. *Microbiology*. 1998;144(9):2417-2426. doi:10.1099/00221287-144-9-2417.
366. Li L, Miles S, Melville Z, Prasad A, Bradley G, Breeden LL. Key events during the transition from rapid growth to quiescence in budding yeast require posttranscriptional regulators. doi:10.1091/mbc.E13-05-0241.
367. Grenson M, Hou C. Ammonia inhibition of the general amino acid permease and its suppression in NADPH-specific glutamate dehydrogenaseless mutants of saccharomyces cerevisiae. *Biochem Biophys Res Commun*. 1972;48(4):749-756. http://www.ncbi.nlm.nih.gov/pubmed/4404622. Accessed September 19, 2018.
368. Miller SM, Magasanik B. Role of NAD-linked glutamate dehydrogenase in nitrogen metabolism in Saccharomyces cerevisiae. *J Bacteriol*. 1990;172(9):4927-4935. doi:10.1128/JB.172.9.4927-4935.1990.
369. Wang PY, Lin WC, Tsai YC, et al. Regulation of CTP synthase filament formation during DNA endoreplication in Drosophila. *Genetics*. 2015. doi:10.1534/genetics.115.180737.
370. Aughey GN, Liu J-L. Metabolic regulation via enzyme filamentation. 2016. doi:10.3109/10409238.2016.1172555.
371. Stahl G, Salem SN Ben, Chen L, Zhao B, Farabaugh PJ. Translational Accuracy during Exponential, Postdiauxic, and Stationary Growth Phases in Saccharomyces cerevisiae. *Eukaryot Cell*. 2004;3(2):331-338. doi:10.1128/EC.3.2.331-338.2004.
372. Galdieri L, Mehrotra S, Yu S, Vancura A. Transcriptional Regulation in Yeast during Diauxic Shift and Stationary Phase. doi:10.1089/omi.2010.0069.
373. Davidson GS, Joe RM, Roy S, et al. The proteomics of quiescent and nonquiescent cell differentiation in yeast stationary-phase cultures. Fox TD, ed. *Mol Biol Cell*. 2011;22(7):988-998. doi:10.1091/mbc.e10-06-0499.
374. Mouilleron S, Golinelli-Pimpaneau B. Conformational changes in ammonia-channeling glutamine amidotransferases. *Curr Opin Struct Biol*. 2007;17(6):653-664. doi:10.1016/j.sbi.2007.09.003.
375. Chang C-C, Lin W-C, Pai L-M, et al. Cytoophidium assembly reflects upregulation of IMPDH activity. 2015. doi:10.1242/jcs.175265.
376. Pan M, Reid MA, Lowman XH, et al. Regional glutamine deficiency in tumours promotes dedifferentiation through inhibition of histone demethylation. *Nat Cell Biol*. 2016;18(10):1090-1101. doi:10.1038/ncb3410.
377. Colombo M, Moita C, Van Niel G, et al. Analysis of ESCRT functions in exosome biogenesis, composition and secretion highlights the heterogeneity of extracellular vesicles. *J Cell Sci*. 126:5553-5565. doi:10.1242/jcs.128868.
378. Ratheesh A, Ingle A, Gude RP. Pentoxifylline modulates cell surface integrin expression and integrin mediated adhesion of B16F10 cells to extracellular matrix components. *Cancer Biol Ther*. 2007;6(11):1743-1752. http://www.ncbi.nlm.nih.gov/pubmed/17986856. Accessed December 29, 2018.
379. Rørth P. Fellow travellers: emergent properties of collective cell migration. *EMBO Rep*. 2012. doi:10.1038/embor.2012.149.
380. Davidson GS, Joe RM, Roy S, et al. The proteomics of quiescent and nonquiescent cell differentiation in yeast stationary-phase cultures. 2011. doi:10.1091/mbc.E10-06-0499.